University of Bath

PHD

Computation of Flow Instabilities in Turbine Rim Seals

Horwood, Joshua

Award date:
2019

Awarding institution:
University of Bath

Link to publication

Alternative formats
If you require this document in an alternative format, please contact:
openaccess@bath.ac.uk

Copyright of this thesis rests with the author. Access is subject to the above licence, if given. If no licence is specified above, original content in this thesis is licensed under the terms of the Creative Commons Attribution-NonCommercial 4.0 International (CC BY-NC-ND 4.0) Licence (https://creativecommons.org/licenses/by-nc-nd/4.0/). Any third-party copyright material present remains the property of its respective owner(s) and is licensed under its existing terms.

Take down policy
If you consider content within Bath's Research Portal to be in breach of UK law, please contact: openaccess@bath.ac.uk with the details. Your claim will be investigated and, where appropriate, the item will be removed from public view as soon as possible.

Download date: 05. May. 2023

Computation of Flow Instabilities in Turbine Rim Seals

Joshua Timothy Michael Horwood

A thesis submitted for the degree of Doctor of Philosophy

University of Bath

Department of Mechanical Engineering

June 2019

COPYRIGHT

Attention is drawn to the fact that copyright of this thesis rests with the author. A copy of this thesis has been supplied on condition that anyone who consults it is understood to recognise that its copyright rests with the author and that they must not copy it or use material from it except as permitted by law or with the consent of the author.

This thesis may be made available for consultation within the University Library and may be photocopied or lent to other libraries for the purposes of consultation.

Signature:…….

DECLARATION OF AUTHORSHIP

I am the author of this thesis, and the work described therein was carried out by myself personally, with the exception of the measurement of experimental data, which was carried out by other researchers. Analysis of the experimental data was carried out by myself and is provided to support the computational investigation.

Signature:……..

Abstract

In gas turbines, the ingress of hot annulus gas into cavities between stator and rotor discs is an important topic to engine designers. Rim seals are fitted at the periphery of these cavities to reduce the pressurised purge required to protect vulnerable, highly-stressed engine components. This thesis describes a computational study of ingress and egress through turbine rim seals. The computations were undertaken using time-domain and frequency-domain flow solvers available in DLR's TRACE code. Several turbine configurations, incorporating different vane, blade and rim seal geometries were modelled and validation was performed against existing experimental results available from the University of Bath's 1.5-stage axial turbine test rig.

The circumferential pressure distribution in the annulus was generally well-predicted across all configurations. The circumferential pressure difference, ΔC_p, downstream of the vane was dependent upon the relative positions of the vanes and rim seal, however it was largely unaffected by the presence of the blades.

Egress from the upstream seal was shown to be entrained into the passage vortex. This feature moved radially outward of the hub, promoting little re-ingestion of upstream purge into the downstream wheel-space. Egress from the downstream wheel-space remained hub-bound due to weaker secondary flow features along the downstream vane.

The qualitative features of the flow structure in the seal clearances and wheel-spaces were captured, and a chute seal geometry demonstrated good quantitative prediction of ingress. However, the sealing effectiveness of radial overlap seals was over-predicted and it is speculated that the RANS turbulence model failed to accurately capture flow separation at the seal's corners.

High levels of shear across the rim seals promoted the formation of large-scale structures at the periphery of the wheel-spaces, associated with increased levels of ingress. These transient structures are referred to as instabilities in this thesis. Unsteady time-domain computations showed that the presence and intensity of these structures are dependent upon both geometry and sealing flow rate. Structures were stronger for the upstream wheel-space than the downstream wheel-space due to a higher tangential shear gradient. The computed structures qualitatively reflected that measured in experiments, however their strength was generally over-predicted; this is again believed to be due to deficiencies in the RANS turbulence model.

Comparison of computational domains with circumferential sectors ranging from 30º to 360º indicate that the time-averaged features of the flow are largely unaffected by sector size. However, differences in large-scale flow structures present in the rim seals were pronounced with a 60º

sector, suggesting that modelling an even number of blades in small sector simulations should be avoided.

A bladeless configuration was used to capture large-scale structures from a frequency domain computation for the first time. The harmonic balance solver captured similar behaviour to that of the time-domain solver, but with reduced computational cost. However, a reduction in the computed ingress was attributed to neglecting the transport equations for the higher harmonics of turbulence. Furthermore, in its current form the solver is not able to capture the non-linear interaction between the differing fundamental frequencies associated with blades and the large-scale structures.

The injection of high radius purge from the stator wall was shown to have a strong influence on the flow structure in the wheel-spaces. Increasing the proportion of purge supplied from these discrete positions disrupted the conventional Batchelor flow regime and led to the formation of recirculations. For the rim seal configuration studied, the presence of a buffer cavity restricted the influence of the high radius purge at the rim seal and resulted in no clear impact upon ingress.

Acknowledgements

Firstly, I would like to thank my supervisors, Dr. Mike Wilson, Dr. Carl Sangan and Prof. Gary Lock for their invaluable guidance throughout my PhD. Additionally, I would like to thank Dr. James Scobie for his continued advice and significant involvement in my research.

The project sponsors, Siemens, and in particular Dr. Kunyuan Zhou and Dr. Vincent Peltier are thanked for their support of the research, their technical advice and for making my time in Berlin so enjoyable.

I would also like to express thanks to Dr. Marios Patinios, Fabian Hualca and Dimitris Graikos. Through technical ability and perseverance, they produced high quality experimental data that has been integral to my project.

Dr. Graham Ashcroft is thanked for generously sharing his time and expertise to guide in the operation of TRACE code.

I would like to acknowledge my colleagues from all four corners of 4E 2.27, without whom, my PhD would certainly not have been such an entertaining and rewarding experience.

Finally, I would like to thank my family for their constant support and in particular Florence for the many hours spent listening and offering words of encouragement through the good times and bad.

Contents

List of Figures

List of Tables

Nomenclature

Symbols

A_p	amplitude of unsteady pressure
b	radius of inner shroud
c	concentration of tracer
c_p	specific heat capacity
c_x	axial chord
$\tilde{c}$	mixed-out concentration of tracer
C	velocity relative to vanes
C_d	discharge coefficient
C_F	flow coefficient [$=W/\Omega b$]
C_p	unsteady pressure coefficient [$=A_p/(0.5\rho\Omega^2 b^2)$]
$C_{p,a}$	annulus pressure coefficient [$=(p-\bar{p})/(0.5\rho\Omega^2 b^2)$]
$C_{p,a,inc}$	annulus pressure coefficient for incompressible flow $[=C_{p,a}\sqrt{1-\mathrm{M}^2}/(1-C_{p,a}(\mathrm{M}^2\{1+[(\gamma-1)/2]\mathrm{M}^2\}(\sqrt{1-\mathrm{M}^2}/2)))]$
$C_{p,s}$	stator wall pressure coefficient [$=(p-p_{ref})/(0.5\rho\Omega^2 b^2)$]
C_w	non-dimensional flow rate [$=\dot{m}/\mu b$]
C^*	dilution ratio [$=c_B/(c_B+c_L)$]
D	diameter of pipe
f	frequency
f_d	rotational frequency of disc
$\vec{F}_j$	flux through cell face j
G	gap ratio [$=S/b$]
G_c	seal-clearance ratio [$=s_c/b$]
h	height
i	complex unit
I_T	turbulence intensity
j	cell face index
k	turbulent kinetic energy
l_m	mixing length
$l_1, \ldots, l_4$	length dimensions in wheel-space

L_T	turbulent length scale
m	number of cell faces
$\dot{m}$	mass flow rate
$\dot{m}'$	mass flow rate of re-ingested gas
M	Mach number
n	harmonic index
N	number of large-scale structures
N_f	number of harmonics
p	static pressure
$\bar{p}$	mean static pressure over one vane pitch
q	heat
r	radius
$r_1, \ldots, r_6$	radial dimensions in wheel-space
R	time domain form of computed residuals in Navier-Stokes equations
Re $[a]$	real part of complex quantity a
Re_w	annulus Reynolds number $[=\rho W b/\mu]$
Re_x	Reynolds number over flat plate $[=\rho V x/\mu]$
Re_ϕ	rotational Reynolds number $[=\rho \Omega b^2/\mu]$
R_m	ratio of sealing flow $[=\Phi_{0,H}/\Phi_{0,B}]$
$\widehat{R}_n$	Fourier coefficient form of computed residuals for n^{th} harmonic in Navier-Stokes equations
s	entropy
s_c	seal clearance
$s_{overlap}$	seal overlap
S	axial clearance in wheel-space
S'	Sutherland constant
$\vec{S}_j$	area of cell face j
t	time
T	static temperature
T_0	total temperature
T_1	static temperature upstream of stator
T_2	static temperature downstream of stator
T_3	static temperature downstream of rotor
u_w	near wall friction velocity $[=\sqrt{\tau_w/\rho}]$
U	time domain form of conservative variables in Navier-Stokes equations
$\widehat{U}_n$	Fourier coefficient form of conservative variables for n^{th} harmonic in Navier-Stokes equations

V	velocity; velocity relative to blades; cell volume
W	axial velocity in annulus
x	characteristic length; axial distance from blade leading edge
x_b	axial distance from blade trailing edge
x_s	axial distance from seal leading edge
x_v	axial distance from vane trailing edge
y	pitch-wise distance from blade leading edge
y^+	non-dimensional near wall mesh spacing [$=(\Delta y\, u_w\, \rho)/\mu$]
α	vane inlet/exit angle; angular offset of fast response pressure transducers
β	blade inlet/exit angle; swirl ratio [$=V_\phi/\Omega r$]
γ	ratio of specific heats
Γ_c	ratio of discharge coefficients [$=C_{d,i}/C_{d,e}$]
ΔC_p	non-dimensional pressure difference in annulus [$=\Delta p/0.5\rho\Omega^2 b^2$]
Δp	peak-to-trough pressure difference in annulus
Δp_{seal}	peak-to-trough pressure difference in seal
Δt_a	average lag time between rotating structures
ΔT	temperature difference between two computations
Δy	near wall mesh spacing
ε	sealing effectiveness [$= C_{w,0}/C_{w,e} = \Phi_0/\Phi_e$]
ε_c	concentration-based sealing effectiveness [$=(c-c_a)/(c_0-c_a)$]
ε_t	turbulent dissipation rate
$\overline{\varepsilon_t}$	time-averaged turbulent dissipation rate
ε_T	temperature based sealing effectiveness [$= (\Delta T-\Delta T_a)/(\Delta T_0-\Delta T_a)$]
θ	non-dimensional vane pitch
θ_{chute}	angle of chute seal
λ_T	turbulent flow parameter [$=C_{w,0}Re_\phi^{-0.8}$]
Λ	degree of reaction [$= (T_2-T_3)/(T_1-T_3)$]
μ	dynamic viscosity
ρ	density
τ	pseudo-time
τ_w	shear stress at the wall
Φ_0	sealing flow parameter [$=C_{w,0}/2\pi G_c Re_\phi$]
χ	re-ingestion mass fraction [$=\dot{m}'/\dot{m}_{i,d}$]
ψ	blade loading coefficient [$= (2c_p(T_{01}-T_{03}))/(\Omega r)^2$]
ω	angular frequency of large-scale structures; angular frequency modelled in frequency domain

Ω	angular frequency of rotor

Subscripts

a	annulus
ax	axial clearance
buffer	buffer cavity
B	bore flow
chute	chute seal
d	downstream wheel-space
e	egress
EI	externally induced
H	high radius purge
i	ingress
in	purge inlet
max	maximum
min	minimum
r	radial component
rad	radial clearance
ref	reference
RI	rotationally induced
s	stator wall
seal	rim seal
u	upstream wheel-space
x	axial component
ϕ	tangential component
0	sealing flow

Abbreviations

BPF	blade passing frequency
CCGT	combined cycle gas turbine
CFD	computational fluid dynamics
CFL	Courant-Friedrichs-Lewy
CI	combined ingress
DLR	Deutsches Zentrum für Luft- und Raumfahrt
EI	externally induced
FFT	fast Fourier transform

GRZ	gap recirculation zone
HB	harmonic balance
LDV	laser Doppler velocimetry
LES	large eddy simulation
NLH	non-linear harmonic
PIV	particle image velocimetry
RANS	Reynolds-averaged Navier-Stokes
RI	rotationally induced
RPM	revolutions per minute
SAS	secondary air system
SST	shear stress transport
TET	turbine entry temperature
TRACE	Turbomachinery Research Aerodynamics Computational Environment
URANS	unsteady Reynolds-averaged Navier-Stokes

Chapter 1: Introduction

1.1 The Gas Turbine Engine

As a means of producing mechanical power gas turbines are hugely important to modern society. They can offer high power output from a reliable and efficient machine. In combined cycle operation a large industrial gas turbine such as Siemens' SGT5-8000H (see Figure 1) can produce >600 MW at an efficiency >60%.

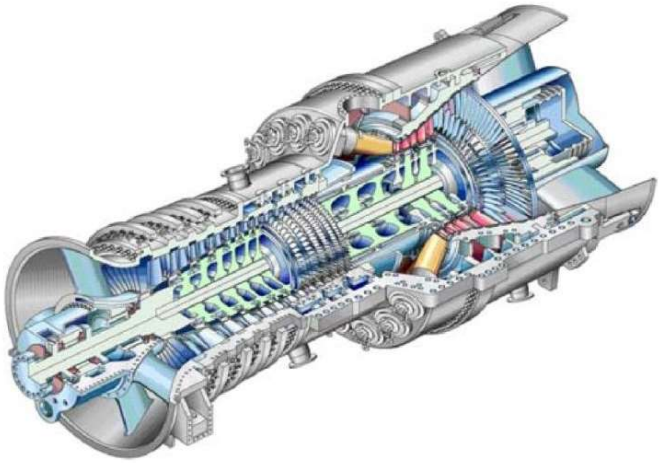

Figure 1: Siemens SGT5-8000H, Diakunchak *et al.* (2008)

Large-scale power generation is only one of a wide range of the applications of gas turbines, they are also used for powering aircraft, marine vehicles, tanks, compressors in gas pipelines, and a host of other small scale power applications.

Whilst much of the early development of gas turbines was driven by the needs of aircraft propulsion, and indeed aero-derivative turbines are used for small-scale power generation, there are several requirements of large-scale industrial gas turbines that lead to considerable differences in their design. Firstly, industrial gas turbines are not restricted by the weight requirements of aircraft engines. Secondly, the operational life of an industrial gas turbine before major overhaul is typically in the order of 100,000 hours, while the figure for aero-engines is generally a small fraction of this. Thirdly, unlike industrial gas turbines, which operate in a relatively steady-state, aircraft engines must operate over flight cycles that cause frequent, significant changes in both environmental conditions and output power. Lastly, an aero gas turbine uses the turbine's exhaust as thrust whereas any kinetic energy in the exhaust of an industrial gas turbine is wasted.

The earliest patent for a gas turbine machine was made in 1791 by John Barber, with a design that would incorporate a reciprocating compressor to drive air into a combustion chamber and

through an impulse turbine, therefore containing the key components of a modern gas turbine. However, it was not until the 20th century that progress was made with operational gas turbines by a number of pioneers, including Rene Armengaud, Charles Lemale and Ægidius Elling. In 1903 Elling created the first successful machine using both a rotary compressor and turbine, it had a power output of approximately 8kW and was designed to power pneumatic tools (Bakken *et al.* (2004)). In the same year, Armengaud and Lemale had also begun successfully testing gas turbines. Their first was adapted from a de Laval steam turbine, operated at 4000rpm and even injected steam upstream of the rotor to cool the blades (Giampaolo (2002)).

By 1939 the first practical large-scale gas turbine had been developed and introduced by Brown Boveri (Hunt (2011)). With a power output of 4 MW and an overall cycle efficiency of 18% the machine was a huge step towards today's gas turbines; a schematic of Brown Boveri's Neuchâtel engine is shown in Figure 2.

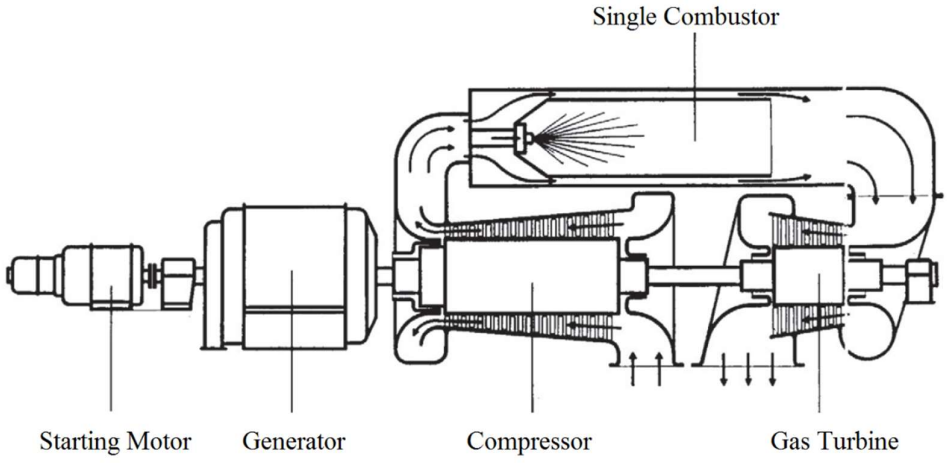

Figure 2: Layout of Brown Boveri's single cycle gas turbine installed at the Neuchâtel power station in 1939 (ASME (1988))

In the 1930's significant development was also being made in gas turbines for aircraft propulsion, led by Hans von Ohain in Germany and Frank Whittle in the United Kingdom. Von Ohain's HeS3 engine became the first to power an aircraft in 1939, and was followed two years later by Whittle's W.1X, both engines using a centrifugal compressor and an axial turbine. By 1945 the Second World War had driven many advancements in gas turbines for aircraft; the Junkers Jumo 004 was an example of this featuring an axial compressor for the first time.

In 1950 the Allies gave permission to Siemens to resume industrial gas turbine development. Their first engine, named VM1, had a similar compressor design to the JUMO 004, a turbine entry temperature (TET) of ~620 °C and a 3-stage axial turbine design. By the late 50's development had accelerated; the 5.6 MW VM5 featured two compressors, a TET of ~700 °C, a recuperator and an efficiency of 29% (Diakunchak *et al.* (2008)).

In the 1960's combined cycle gas turbines (CCGT) became more prominent in large industrial facilities. These use heat recovered from the gas turbine exhaust to power conventional steam turbines, greatly improving overall efficiency. The first GE combined cycle units were installed in 1967. They were the City of Ottawa 11MW FS3 and the Wolverine Electric 21MW FS5 (Hunt (2011)).

Over the last 50 years, improvements in materials, cooling and aerodynamics have allowed higher compressor pressure ratios, TETs, power outputs and improved efficiencies. A comparison of an early gas turbine against a modern equivalent can be seen in Table 1.

	Brown Boveri Neuchâtel Gas Turbine	**Siemens SGT5-9000HL Gas Turbine**
Year launched	1939	2017
Turbine Entry Temperature	550ºC	>1500ºC (estimated)
Compressor Pressure Ratio	4.2:1	24:1
Output (simple cycle)	4 MW	593 MW
Output (combined cycle)	N/A	870 MW
Efficiency (simple cycle)	17.4%	42.8%
Efficiency (combined cycle)	N/A	>63%

Table 1: Comparison of industrial gas turbine operating parameters. Values from Hunt (2011) and Siemens-AG (2018)

1.2 Gas Turbine Theory

At a simple level a gas turbine is composed of three key components: a compressor a combustor and a turbine. Air is drawn into the compressor where it is pressurised, before being heated in a combustion chamber. The resulting high pressure, high temperature mixture of air and exhaust gases is then expanded through a turbine that is coupled back to the compressor. The principle relies upon the ability to extract more energy from the turbine than is required by the compressor. Figure 3 depicts the process for an industrial configuration, in which this is achieved through a generator connected to a second turbine.

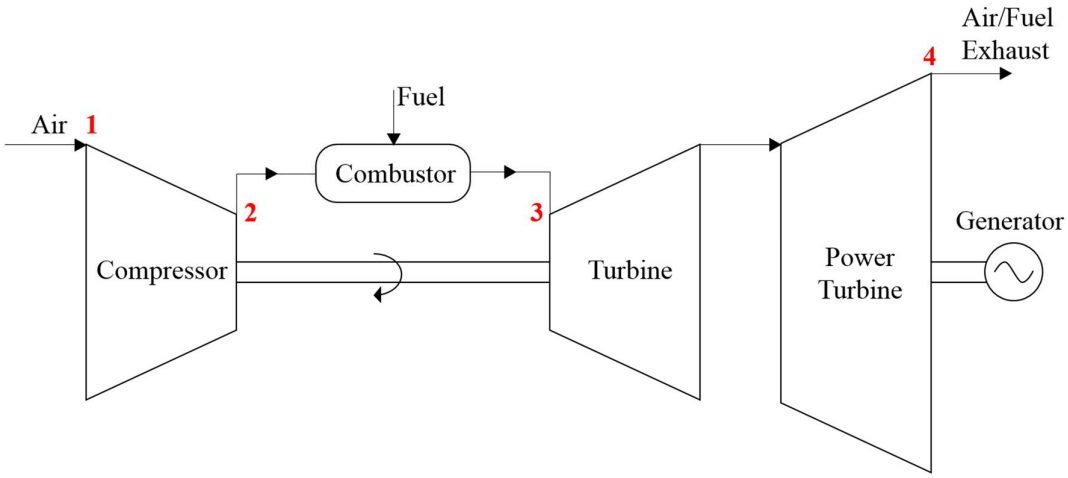

Figure 3: Schematic diagram of an industrial gas turbine cycle

The fundamental thermodynamics of the gas turbine can be understood by considering Figure 4. The solid lines depict the ideal Brayton cycle. Compression of the working fluid occurs between 1 and 2, whilst the addition of energy takes the cycle to position 3, before expansion through the turbine lowers the temperature and pressure of the fluid, leading to position 4. Theoretically, if no heat was added in an ideal cycle, the work extracted from the turbine would match that consumed by the compressor and the machine could simply turn itself over; it is only by virtue of raising the fluid temperature that excess work can be generated by the turbine. However, the non-ideal cycle must also overcome efficiency losses; dashed lines in Figure 4 indicate the non-isentropic processes resulting from frictional and aerodynamic losses.

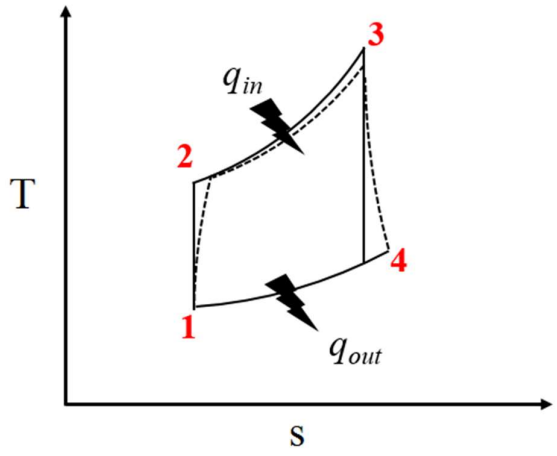

Figure 4: Temperature-entropy diagram for a Brayton cycle (solid and dashed lines indicate ideal and non-ideal cycles respectively)

Turbine manufacturers desire a high cycle efficiency and a high specific work from their machines. In a real engine achieving this is principally dependent upon increasing the pressure ratio achieved during compression, the TET and the component efficiencies. The drive for higher

pressure ratios and TETs can be seen clearly in the comparison between a 1939 turbine and 2017 turbine in Table 1. In large-scale industrial facilities, further efficiency gains are often achieved through operating combined cycle gas turbines (CCGT). This configuration exploits the relatively high turbine exit temperatures to operate an additional steam cycle; extracting additional work for no added fuel burn.

1.3 Secondary Air System

The incremental increase of TETs in gas turbines has driven the design of ever more exotic systems to protect critical components. The network of flow paths and systems that provide this role is often referred to as the secondary air system (SAS). Coolant required for the SAS is typically bled as early as possible in the compressor. However, air from the final compressor stages may be required to cool the first turbine stage, flowing downstream by virtue of the slight pressure drop across the combustion chamber. A typical arrangement of coolant flow paths is depicted in Figure 5.

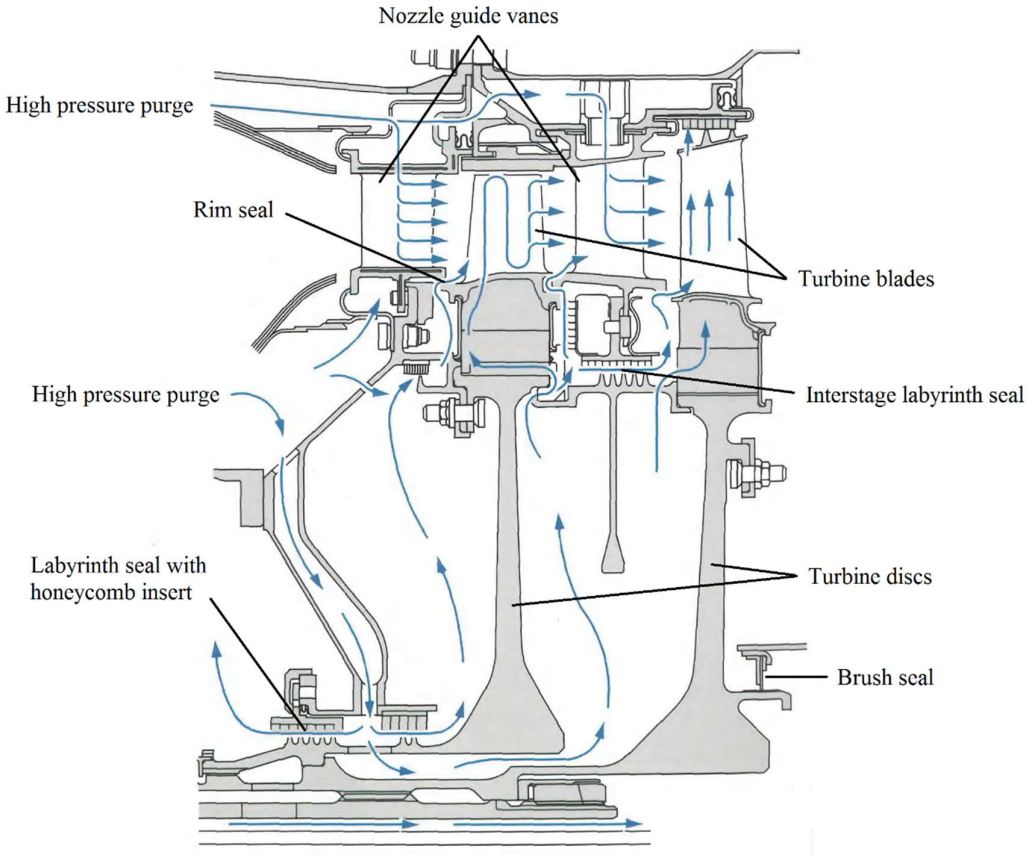

Figure 5: Typical cooling and sealing arrangement of the first two turbine stages of a gas turbine. Adapted from Rolls-Royce (2005)

To direct the secondary flow and prevent leakage, a host of seals and conduits are incorporated into the system. However, one particularly complex aspect of the secondary air system is the need to seal two components that do not rotate at a common speed. Whilst a close clearance may be used and is still potentially considered a seal, numerous more complex solutions are used to increase the resistance to airflow. Figure 6 depicts three common types of rotating seal used in gas turbines; a labyrinth seal, a brush seal and a hydraulic seal.

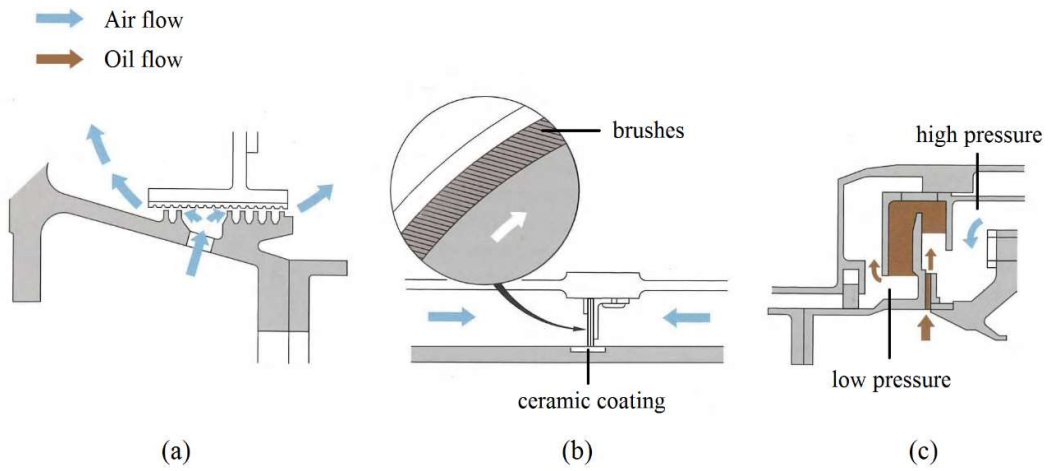

Figure 6: Three rotating seals used in secondary air systems: (a) labyrinth seal, (b) brush seal, (c) hydraulic seal. Adapted from Rolls-Royce (2005)

Labyrinth seals – see Figure 6 (a) – are used in several locations within the SAS. They provide resistance to flow through a series of fins; pressure losses occur through repeated acceleration and expansion of flow over the fin tips. Abradable honeycomb inserts may also be added to allow for rubbing. Typically, brush seals – see Figure 6 (b) – are only used at low radius and consist of a pack of metallic bristles that are permanently in contact with the rotating part. The bristles can deform to allow for axial and radial movement and ceramic coatings are used to protect the rotating surface. Hydraulic seals – see Figure 6 (c) – are implemented between co-rotating shafts. They can potentially prevent all leakage and operate on the basis that a fin on the inner surface is submerged in a fluidic (generally oil) annulus created by rotational forces. Differing pressures are countered by a differing head of oil each side of the fin.

Having bypassed the combustor, a large portion of the purge flow is used to protect the first stage turbine vanes and blades, which are shown in Figure 7. These are subjected to the highest temperatures in the engine and their design has evolved considerably since early designs. Advances in manufacturing and metallurgy have led to a single crystal nickel alloy construction. Whilst this has allowed improved strength retention and creep resistance over those vanes and blades with an equiaxed crystal structure, the metal temperature must remain well below that of the mainstream fluid. This is achieved through a combination of techniques: internal convection

removes heat by passing coolant through ducts in the blade, film cooling provides a protective layer by expelling coolant through holes in the blade surface, and thermal barrier coatings consist of a heat resistant ceramic layer applied to the blade surface.

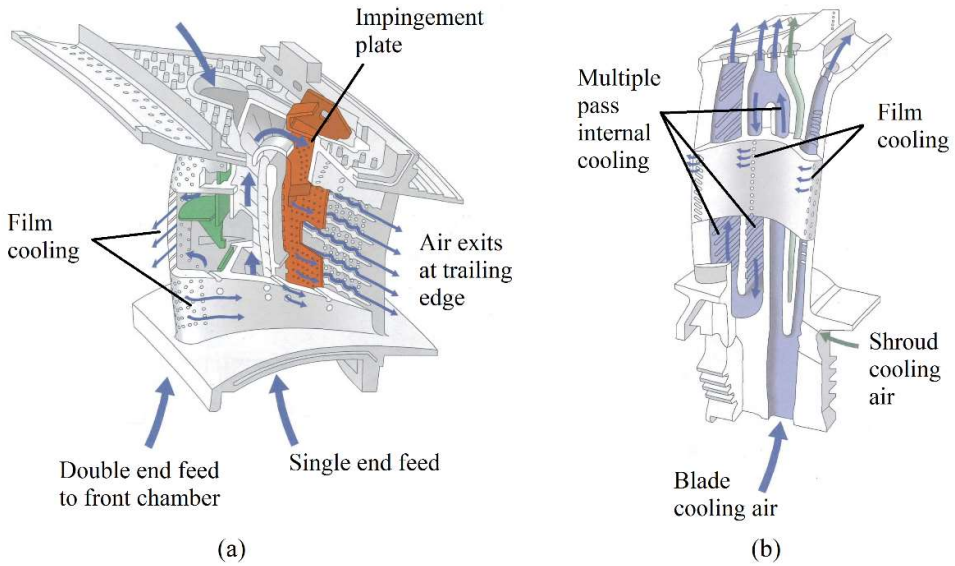

Figure 7: Vane (a) and blade (b) cooling, adapted from Rolls-Royce (2005)

In addition to blade and vane cooling, the problem of hot gas ingress from the annulus to the wheel-space is a subject that is of great importance to the engine designer. To prevent excessive ingress, purge air is supplied through rim seals fitted at the periphery of wheel-spaces between the stator and rotor discs, as shown in Figure 8.

It should be noted that the cavity may not be fully sealed from the annulus flow. In this situation the purge air can provide a cooling role, particularly to the highly stressed rotor discs. Supplying the optimal level of purge requires compromise. If too little purge is supplied, ingested hot gas can significantly reduce the life of components or even cause catastrophic failure. Superfluous use, however, is inefficient; not only because it wastes bleed air but the egress itself is potentially detrimental to the flow structure passing over blades and vanes. As such, a large volume of theoretical, experimental and computational research has been undertaken in recent years to both understand the fundamental physics of ingress and to develop advanced rim seals that reduce purge requirements.

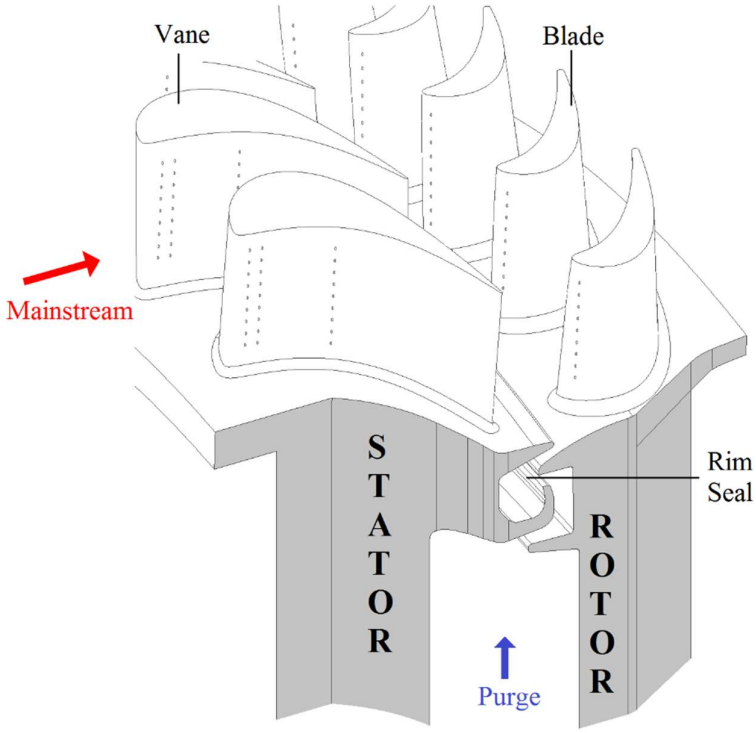

Figure 8: Purge supplied through a rim seal

1.4 Industrial Design of Secondary Air Systems

By their very nature, SASs are composed of a complex set of flow paths. Modelling such a system in its entirety is beyond the feasibility of full 3-D CFD, instead engineers use 1-D flow networks to design and predict how the SAS will behave. This section outlines a basic overview of this approach. For detailed information the reader is referred to Sultanian (2018).

Figure 9 depicts a typical 1-D flow network. These low order models generally consist of a number of components that are connected at junctions (or *chambers* in Figure 9) which are numerically solved for a set of boundary conditions. Components may include, but are not limited to, ducts, orifices, vortices, rotor-stator cavities, rotor-rotor cavities and seals.

The solution process for 1-D networks bears many similarities to conventional CFD; the problem is discretised and equations are solved for the conservation of mass, energy and momentum. Indeed, a duct may be modelled from a sequence of control volumes connected in series, it may handle area changes and the resulting compressible effects such as choking and the formation of normal shocks. However, in addition to any geometric parameters, each component requires empirical or semi-empirical correlations to determine terms such as friction factors or heat transfer coefficients.

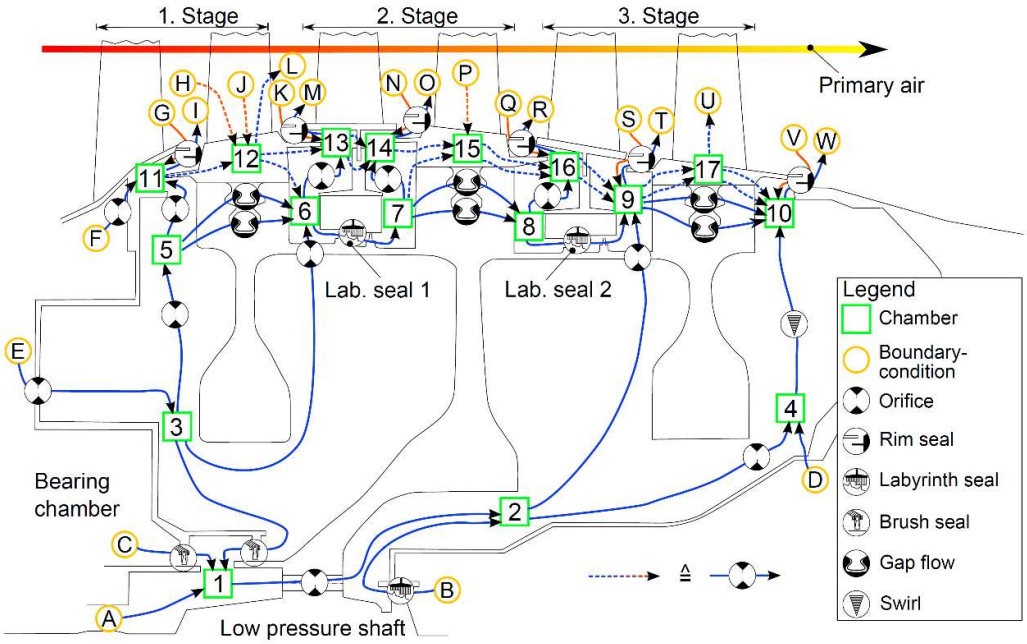

Figure 9: A 1-D flow network used to model a secondary air system Brack and Muller (2014)

Having formed a 1-D flow model, its physical accuracy depends principally upon two conditions, formulating the problem such that the conservation laws are satisfied throughout every element of the network and obtaining empirical correlations from tests that are physically representative. Given the former is based upon solving established laws of flow and heat transfer, the quality of the data used to generate empirical correlations is likely to be the largest source of inaccuracies in the solution.

The development of empirically based models remains a highly active research area, particularly those designed to predict ingress. Sultanian (2018) identified that at the date of publication, investigations into hot gas ingress remained the most active area of research in support of internal air systems, with 1-D modelling gaining plenty of focus. One such model, proposed by Owen (2011b), links ingress to the circumferential peak-to-trough pressure difference in the annulus; requiring empirically determined 'discharge coefficients' to account for particular seal geometries. More detail on this and other 1-D ingress models is provided in 2.2.5.

Despite the implementation of 1-D flow networks to model the SAS, CFD remains an important tool and plays several key roles. Firstly, it can be used to inform input parameters for 1-D models, such as loss coefficients, or in the case of the orifice model of Owen (2011b), the peak-to-trough pressure distribution in the annulus. Secondly, during the detailed design phase it is used to evaluate the merits of multiple solutions; in the case of ingress this might involve a side-by-side comparison of the sealing effectiveness of different seal geometries. Finally, it is also

used to develop a better fundamental understanding of a component's flow physics, resulting in part from the powerful visualisation possible.

1.5 Thesis Aim

The aim of this research is to develop computational models of gas turbine ingress, which can be used to support the development of more efficient gas turbines. The models will provide a broad understanding of the governing fluid dynamics of ingress into cavities upstream and downstream of a rotor. The latter of which is even less well understood than the former. This CFD based research programme will be supported by experimental results gathered during a complementary experimental PhD at the University of Bath.

In order to satisfy the project aim several questions will be addressed during the research:

Q1) Can Reynolds-averaged Navier-Stokes computations be used to capture time-accurate and time-averaged flow features associated with ingress?

Computational models that are geometrically similar to a 1.5-stage turbine rig at the University of Bath will include an upstream wheel-space cavity together with the main gas path. More specifically, an Unsteady Reynolds-averaged Navier-Stokes (URANS) solver will be used to investigate both time-averaged and time-accurate flow features related to ingress, and evaluation will be performed against a range of steady and unsteady measurements available from the test facility.

Q2) How do the fundamental fluid dynamics vary between wheel-space cavities located upstream and downstream of a rotor?

URANS computational models will be extended to include the wheel-space downstream of a rotor disc. Validation will again be performed against the available experimental data and comparisons drawn between the flow physics in both cavities.

Q3) What is the effect of introducing purge at high radius??

High radius purge injection is often neglected in fundamental research but it is speculated that it could have a significant impact in real engines. Computational models will be extended further, to include multiple paths for purge flow.

Q4) Are harmonic balance frequency domain solvers a viable means to accurately compute ingress at a reduced computational cost over conventional URANS solvers?

Frequency domain computations model unsteady perturbations of pre-defined frequencies and have been demonstrated to reduce computational requirements by several orders of magnitude.

Their suitability for cavity flows is not been rigorously demonstrated. Harmonic balance computations will be directly compared and evaluated against results from time-domain simulations.

1.6 Thesis Outline

Chapter 1 presents a brief history of the development of gas turbines along with the fundamental theory behind their operation. The internal flow system and the analysis methods used to design them are introduced to the readers. The aims and objectives of the research, and a list of the published work are also presented.

Chapter 2 provides a review of literature relevant to the present work. An introduction to cavity flows is followed by an overview of fundamental studies into ingress, and the computational work that has attempted to model the phenomenon.

Chapter 3 describes the experimental facility that was modelled and the corresponding flow conditions chosen. The CFD methodology is detailed, including; boundary conditions, grid topology, numerical approaches, convergence and sensitivity studies.

Chapter 4 presents results from Unsteady Reynolds-averaged Navier-Stokes (URANS) computations of the baseline stage. The work includes studying two axial positions of the vane alongside a bladed and a bladeless rotor. The discussion focusses on both the time-averaged and time-accurate fluid dynamics governing ingress.

Chapter 5 details the modelling of the baseline stage using frequency domain computations. The work focuses on a bladeless configuration to simplify the computational methodology, with comparisons performed against similar URANS computations presented in Chapter 4. In addition to the effect of the vanes, the harmonic balance approach attempts to include fundamental frequencies associated with large-scale rim seal instabilities.

Chapter 6 presents results from URANS computations of the increased reaction stage. This configuration includes modified blades, downstream vanes and also analyses time-averaged and time-accurate drivers for ingress into a downstream wheel-space. Further computations presented in this chapter investigated the effect of injecting purge from high radius locations on the stator wall.

Chapter 7 presents URANS computations of a stage that includes a chute seal, twisted blades and stacked vanes. This geometry is scaled from a 1-stage test facility at KTH Royal Institute of Technology, and reports on the first phase of a collaboration to investigate the influence of scaling on ingress in gas turbines. Time-averaged and time-accurate flow structures are discussed in a

similar manner to Chapter 4, however the results present improved agreement with experimental data.

Chapter 8 provides the conclusions of this thesis and recommendations for future computational work into ingress.

1.7 Project Funding

The work presented in this thesis is part of a research programme jointly funded by the UK Engineering and Physical Sciences Research Council (grant number: EP/J014826/1) and Siemens AG.

1.8 Publications

The papers detailed below were published during the course of this research programme. Aspects of Paper 1 and Paper 2 inform all sections of this thesis, but most significantly Paper 1 forms the majority of Chapter 4, whilst paper 2 forms the majority of Chapter 7.

1 **Horwood, J.,** Hualca, F., Scobie, J., Wilson, M., Sangan, C. and Lock, G., 2018, "Experimental and Computational Investigation of Flow Instabilities in Turbine Rim Seals," ASME J. Eng. Gas Turb. Power, 141(1), pp. 011028

2 **Horwood, J.,** Hualca, F., Wilson, M., Scobie, J., Sangan, C., Lock, G., Dahlqvist, J., Fridh, J., 2019, "Flow Instabilities in Gas Turbine Chute Seals," ASME Paper GT2019-90982

To appear in Transactions of the ASME.

3 Hualca, F., **Horwood, J.**, Sangan, C., Lock, G. and Scobie, J., 2019, "The Effect of Vanes and Blades on Ingress in Gas Turbines," ASME Paper GT2019-90987

To appear in Transactions of the ASME.

Paper 1 was also published in Proceedings of ASME Turbo Expo 2018: Turbine Technical Conference and Exposition, under the following title.

4 **Horwood, J.,** Hualca, F., Scobie, J., Wilson, M., Sangan, C. and Lock, G., 2018, "Unsteady Computation of Ingress through Turbine Rim Seals," ASME Paper GT2018-75321

Chapter 2: Literature Review

This chapter outlines previous research undertaken in the field of hot gas ingress through turbine rim seals. Section 2.1 introduces the fundamental flow structures of rotor-stator cavities alongside related non-dimensional parameters. Section 2.2 provides an overview of the fundamental drivers for ingress and the analytical approaches to modelling them. Sections 2.3.1 - 2.3.3 focus predominantly on steady and unsteady computation of ingress, however several supporting experimental investigations are discussed. Section 2.3.4 presents work that has implemented frequency domain solvers to perform computations of unsteady flow in gas turbines at a reduced cost.

2.1 Cavity Flows

2.1.1 Governing Equations

Much of the research into rotor-stator systems uses similar non-dimensional parameters to describe the physical flow characteristics and geometrical features of turbines. This section details the equations for the key parameters relevant to this work.

The rotational Reynolds number is given by equation 2.1, where b and Ω refer to the outer cavity radius and disc speed respectively – see Figure 10.

$$\mathrm{Re}_\phi = \frac{\rho \Omega b^2}{\mu} \tag{2.1}$$

The University of Bath 1.5-stage experimental facility operates at $\mathrm{Re}_\phi \approx 10^6$, whereas typical engines operate at $\mathrm{Re}_\phi \approx 10^7$. Theoretical and experimental work by Sangan *et al.* (2013a) and Sangan *et al.* (2013b) showed ingress levels to be invariant to Re_ϕ but demonstrated that the sealing flow parameter, Φ_0, and the turbulent flow parameter, λ_T, are of great importance in characterising the flow. The boundary layers in the wheel-space depend upon λ_T, while the ingress level is dependent upon Φ_0. These variables are described by equations 2.2 and 2.3, where $C_{w,0}$ is the non-dimensional sealing flow rate (equation 2.4) and G_c is the normalised seal clearance (equation 2.5).

$$\lambda_T = \frac{C_{w,0}}{\mathrm{Re}_\phi^{0.8}} \tag{2.2}$$

$$\Phi_0 = \frac{C_{w,0}}{2\pi G_c \mathrm{Re}_\phi} \tag{2.3}$$

$$C_{w,0} = \frac{\dot{m}_0}{\mu b} \quad \textbf{2.4}$$

$$G_c = \frac{s_c}{b} \quad \textbf{2.5}$$

The swirl ratio, β, refers to the normalised tangential velocity in a rotor-stator system.

$$\beta = \frac{V_\phi}{\Omega r} \quad \textbf{2.6}$$

The flow coefficient C_F is important in governing annulus flow; it is the ratio of axial velocity (W) to the rotor speed and therefore describes the flow angle above the rim seal.

$$C_F = \frac{W}{\Omega b} \quad \textbf{2.7}$$

A concentration-based measure of sealing effectiveness ε_c is often used to describe the level of wheel-space ingress experimentally and computationally. By seeding the purge flow with a tracer (often CO_2 in experiments or a passive scalar in computations) the sealing effectiveness can be calculated as follows:

$$\varepsilon_c = \frac{c - c_a}{c_0 - c_a} \quad \textbf{2.8}$$

where c, c_a and c_0 are the tracer concentrations in the local, annulus and purge flow.

2.1.2 Rotor-Stator Cavities

To gain a deeper understanding into what governs ingress it is important to first understand the fundamental flow structure of rotor-stator cavities. Figure 10 considers such a cavity, which includes a shroud, an axial inlet at the bore and a radial outlet between the shroud and rotating disc. The depicted flow structure was suggested by Batchelor (1951) and is characterised by several distinct zones: a boundary layer on the stator wall; a boundary layer on the rotor wall; a core of fluid in the centre that rotates at an angular velocity between that of the stator and rotor walls. The rotor boundary layer flows radially outwards, entraining fluid from the rotating core; this effect is driven by centrifugal pumping from the disc. The stator wall boundary layer flows radially inwards with an efflux of flow into the core. Additionally, mixing regions exist at inner and outer radii, where purge and ingress flows interact with the main cavity flow.

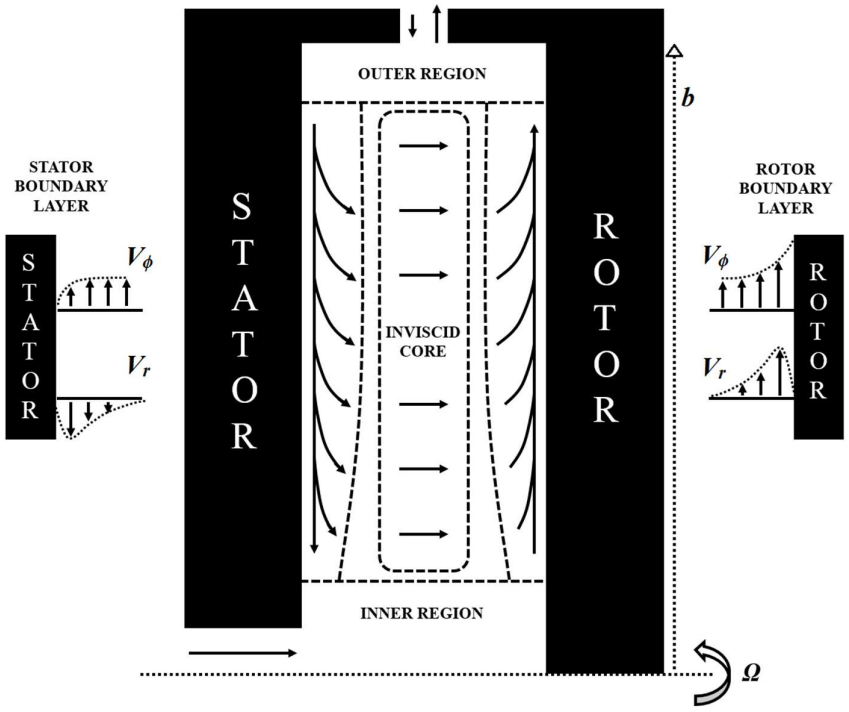

Figure 10: Batchelor flow in a shrouded rotor-stator system

The angular velocity of the core has been found to be dependent on the flow conditions but generally the rotation will be reduced by higher superposed radial purge flow and larger distances between the rotor and stator (Childs (2011)). Indeed with a large enough rotor-stator gap an alternative flow structure, proposed by Stewartson (1953) (and similar to that of a free disc) is valid, where the rotating core does not exist and the tangential velocity approaches zero outside of the rotor wall boundary layer. Whilst Batchelor and Stewartson flow structures are both valid, many studies, including those undertaken by Sangan *et al.* (2014) have shown Batchelor flow to exist at flow conditions and gap ratios, G (the ratio of axial clearance, s, and the outer cavity radius, b), typical of gas turbine rotor-stator cavities.

Daily and Nece (1960) undertook a theoretical and experimental study on enclosed rotor-stator cavities; characterising the flow based on Reynolds number, Re_ϕ, and gap ratio, G. They identified four distinct flow regimes that are depicted in Figure 11 and defined as followed:

Regime I: Laminar Flow, Close Clearance. A continuous velocity exists across the axial gap due to merged rotor and stator boundary layers (Couette flow).

Regime II: Laminar Flow, Large Clearance. The axial gap is greater than the combined thickness of the boundary layers and the stator and rotor. A rotating core exists between the rotor and stator boundary layers where no velocity change is expected to occur.

Regime III: Turbulent Flow, Close Clearance. The turbulent counterpart to regime I; merged stator and rotor boundary layers but at higher Re_ϕ turbulent flow exists on the discs.

Regime IV: Turbulent Flow, Large Clearance. The turbulent counterpart to regime II; separate stator and rotor boundary layers but turbulent flow results from a higher Re_ϕ.

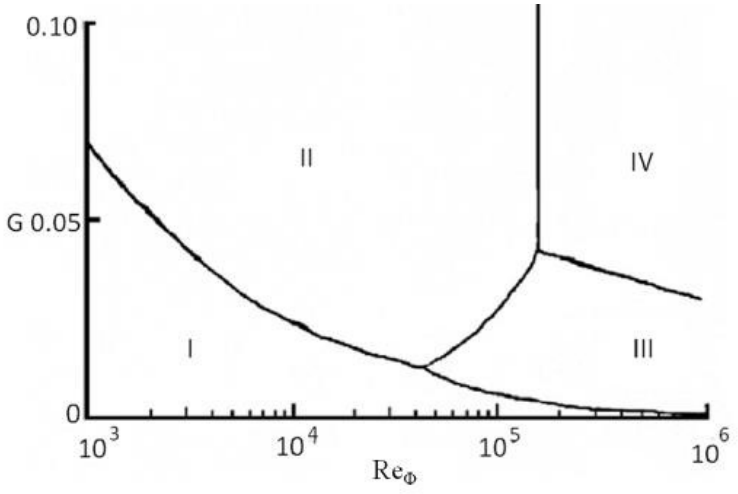

Figure 11: Flow regimes for an enclosed rotor-stator cavity (Daily and Nece (1960))

2.2 Fundamentals of Ingress

Although the problem of gas turbine ingress occurs in an environment with highly unsteady, complex flow interactions, numerous authors have presented work identifying important steady state drivers for ingress. This section presents previous investigations into these phenomena and the different time-averaged techniques used to model, compute and analyse them.

Several studies (e.g. Owen (2011a, b)) have classified three types of ingress; rotationally-induced (RI), externally-induced (EI) and combined ingress (CI), with numerous authors performing fundamental investigations aiming to qualitatively and quantitatively understand their effects.

2.2.1 Rotationally-Induced Ingress

RI ingress occurs due to the rotation of flow inside the wheel-space. This rotation causes a radial pressure gradient, giving the potential for lower pressure in the wheel-space than the annulus (Owen (2011a)). RI ingress therefore occurs even without the presence of blades, vanes or an annulus flow. A simple schematic of RI ingress is shown in Figure 12 (Owen (2011a)).

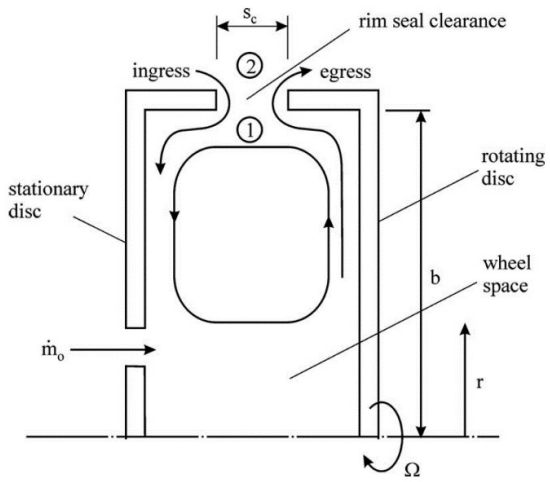

Figure 12 Simplified diagram depicting rotationally-induced ingress through an axial-clearance rim seal (Owen (2011a))

A number of experimental rigs have been developed to demonstrate RI ingress; the first published work was by Bayley and Owen (1970). Their experiments employed a shrouded rotor-stator rig with a variable axial seal clearance and no external flow. Using pressure measurements to determine ingress levels they formed the relationship

$$C_{w,min}=0.61G_c\mathrm{Re}_\phi \qquad 2.9$$

where $C_{w,min}$ is the minimum sealing flow rate required to prevent ingress.

Graber *et al.* (1987) were amongst the first to use a tracer gas to experimentally determine effectiveness. They compared axial and radial seal clearances, identifying that reducing the radial gap between rotor and stator components led to the largest improvement in cooling effectiveness. The work used very low annulus velocities and therefore ingress was believed to be rotationally-induced. Further RI ingress studies were undertaken using the University of Bath 1-stage experimental facility with no axial flow in the annulus (Sangan *et al.* (2013a)); the study presented results that collapse with Reynolds number for both radial and axial seal clearances.

2.2.2 Externally-Induced Ingress

Ingress governed by annulus flow was first demonstrated by Abe *et al.* (1979) with an experimental turbine rig that included vanes along with annulus flow and allowed various rim seal geometries to be tested. The ratio of sealing air velocity to annulus velocity, the rim seal clearance and the shape of the rim seal were all found to affect ingress.

Phadke and Owen (1988) used a rig with blockages in the external annulus to investigate the effect of pressure asymmetries on ingress; they identified that the sealing flow required to prevent any ingress into the wheel-space was independent of the rotational Reynolds number and was

dependant on the peak to trough pressure difference in the annulus. Ingress governed by this annulus pressure asymmetry is what is now commonly referred to as EI ingress and is depicted schematically in Figure 13.

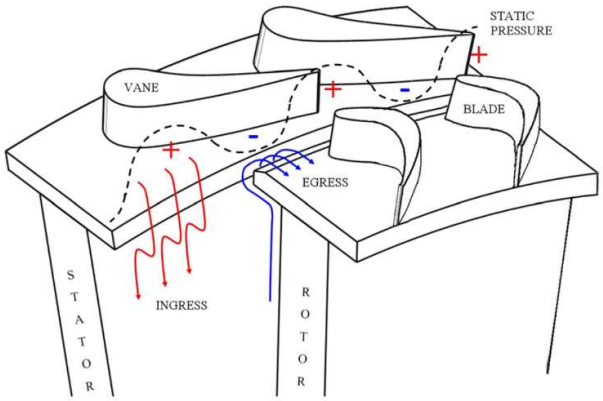

Figure 13 Non-axisymmetric static pressure distribution in annulus driving externally-induced ingress. Red arrows indicate the hot gas entering the wheel-space (ingress) in regions of high pressure relative to the wheel-space and blue arrows indicate cooler flow leaving the wheel-space (egress) in regions of low pressure relative to the wheel-space. (Sangan *et al.* (2013b))

An experimental facility at the University of Sussex capable of achieving Re_ϕ of up to 3×10^6 was first presented by Dadkhah *et al.* (1992). The rig used an external flow without blades or vanes, and a reversible disc assembly allowed investigation of flow upstream and downstream of the rotor. This configuration, suitable for RI ingress investigations was adapted by Chew *et al.* (1994) who ran experiments in a vane only configuration before the rig was further modified for the first published experimental study featuring both vanes and blades by Green and Turner (1994). Green and Turner (1994) showed that the presence of the blades led to a reduction in ingress. The authors suggested this was a result of the blades making the circumferential pressure distribution downstream of the vanes more axisymmetric.

A facility at the University of Aachen, detailed by Bohn *et al.* (1995), included 30 vanes upstream of a rim seal and operated at near engine conditions, with an $Re_\phi = 10^6$ and vane exit Mach numbers up to 0.7. Performing experiments without blades but with vanes at two axial distances from the wheel-space, the authors identified a strong axial decay in the peak-to-trough pressure difference downstream of the vanes. It was suggested this was responsible for higher ingress with the vanes moved closer to the seal. By using laser Doppler velocimetry (LDV) measurements in the wheel-space, it was also shown that under certain conditions ingress could occur not only on the stator but also the rotor. The Aachen rig was later adapted into a 1.5-stage facility, including 62 twisted rotor blades ((Bohn *et al.* (1999)). Bohn *et al.* (2000) compared the bladed and bladeless results from the rig. The peak-to-trough pressure distribution downstream of the vanes was found to increase with the addition of the rotor blades, contradicting with the

reduction in pressure asymmetry found by Green and Turner (1994) when they removed the blades from their configuration. However, the effect on sealing effectiveness from the blades was unclear; two rim seal configurations were tested, the bladed configuration promoted higher ingress levels for the first seal but less for the second seal.

Gentilhomme *et al.* (2003) reported measurements from a single-stage rig using vane and blades, and capable of $Re_\phi = 2.8\times10^6$. It was concluded that vanes, blades, the rim seal and its location all influence ingress.

In contrast to the relatively high Re_ϕ used by Bohn *et al.* (1995), Bohn *et al.* (2000), Chew *et al.* (1994) and Gentilhomme *et al.* (2003), the single-stage turbine rig at Arizona State University (e.g. Roy *et al.* (2007), Zhou *et al.* (2011)) operates at Reynolds numbers up to $Re_\phi = 5.9\times10^5$. Such experimental rigs can offer a benign environment with improved access for instrumentation, flexible and expedient operation, reduced cost, and in some cases greater potential for insight to fundamental fluid dynamics and heat transfer. Roy *et al.* (2007) and Zhou *et al.* (2011) report a combination of particle image velocimetry (PIV) and concentration measurements for various seal geometries. Roy *et al.* (2007) report that distinct regions of instantaneous high and low tangential velocities correspond to ingested annulus fluid and indigenous cavity fluid respectively. It is suggested that the reason these regions do not align directly with the blades or vanes is that the relative position of both is important and varies in the azimuthal direction. They were also less apparent for the case with increased purge. Similar regions were also identified by Zhou *et al.* (2011) which were smeared out in ensemble-averaged velocity contours, as shown in Figure 14.

Sangan *et al.* (2013b) described a 1-stage research facility at the University of Bath that was operated at up to $Re_\phi = 9.68\times10^5$, with 32 vanes and 41 symmetric blades. For two different seal geometries, concentration-based ingress levels are presented alongside profiles of circumferential pressure downstream of the vanes. The peak-to-trough pressure difference at this location is identified as the key driver for ingress. Effectiveness measurements compare well with results from the *orifice model* of Owen (2011b) based on EI Ingress (see 2.2.4). It is suggested that effectiveness can be correlated using the non-dimensional sealing parameter, Φ_0, and in principle these correlations should hold for a geometrically similar engine at the same operating conditions.

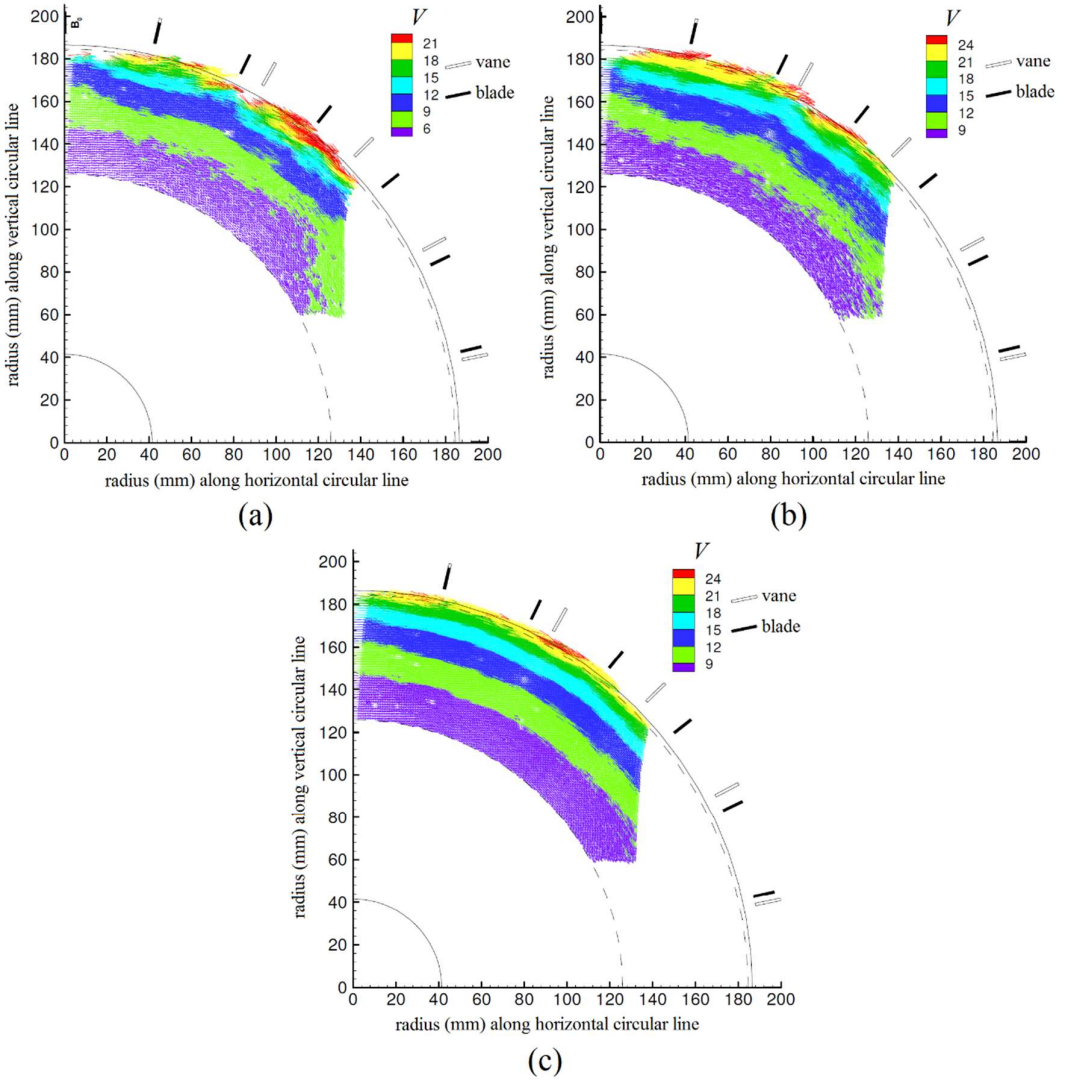

Figure 14: Contours of velocity in the wheel-space from PIV: (a) instantaneous velocities, $Re_\phi = 4.63\times10^5$, $C_{w,0} = 1574$; (b) instantaneous velocities, $Re_\phi = 5.86\times10^5$, $C_{w,0} = 1574$; (c) ensemble-averaged velocities, $Re_\phi = 5.86\times10^5$, $C_{w,0} = 1574$ - adapted from Roy *et al.* (2007), Zhou *et al.* (2011)

The Bath 1.5-stage rig (computed extensively in the present work) was first introduced by Patinios *et al.* (2016). Compared with the earlier single-stage rig (Sangan *et al.* (2013b)), the 1.5-stage facility introduces a downstream wheel-space, loaded blades and an increased annulus height. Similar measurements to those of Sangan were reported, and the *effectiveness equations* of Sangan *et al.* (2013b) (see 2.2.4) were found to fit effectiveness measurements in both the upstream and downstream wheel-spaces (see Figure 15).

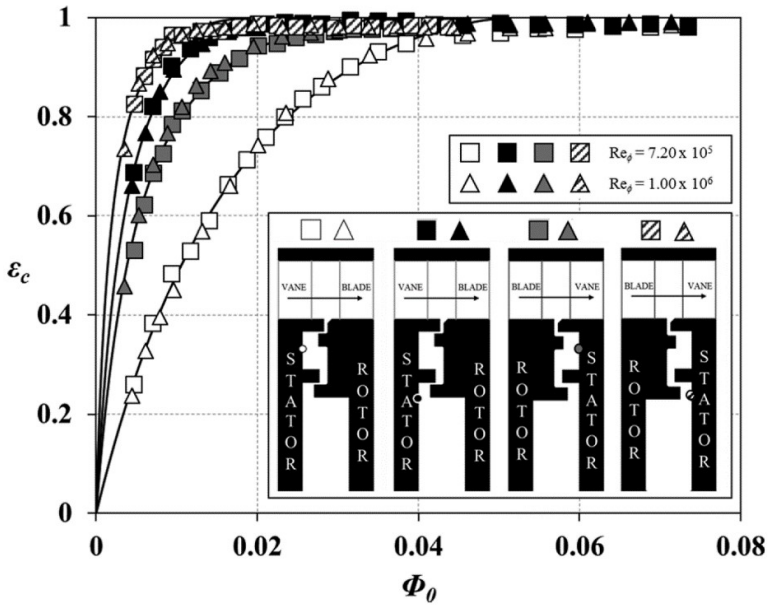

Figure 15: Variation of effectiveness in the upstream and downstream wheel-spaces of the Bath University 1.5-stage rig for $C_F = 0.34$ (Patinios *et al.* (2016))

Zlatinov *et al.* (2016) used a computational model alongside an analytical model to demonstrate that in the presence of a rotating external pressure non-uniformity (such as that caused by rotor blades) pre-swirled purge flow can lead to increased ingress. It is reasoned that swirled purge flow more closely follows the rotor pressure field and responds more readily than non-swirled flow which is influenced by an average of multiple blade passes. The model is also extended to a case where ingress is dominated by an unsteady pressure non-uniformity introduced by stator vanes and finds that under these conditions pre-swirl can reduce ingress levels.

2.2.3 Combined Ingress

Although both EI and RI ingress occur in rotor-stator systems, for basic single overlap seals the dominant effect is generally EI (Owen (2011a)). However, with more advanced seals such as the angel wing seal (see Figure 16) introduced by Scobie *et al.* (2016) the pressure asymmetry from the annulus is largely attenuated in the outer wheel-space and the role RI plays in ingress should not be neglected (Owen (2011a)). The case where EI and RI ingress both play a significant role is often referred to as combined ingress (CI).

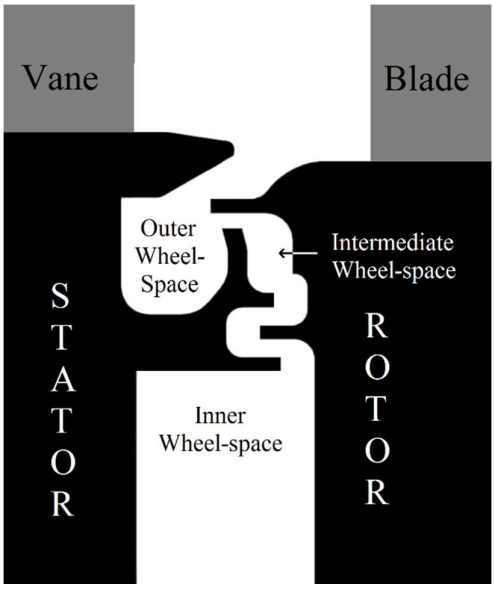

Figure 16: Angel wing rim seal, figure adapted from Scobie *et al.* (2016)

2.2.4 Further Influences on Ingress

In addition to the EI, RI and CI mechanisms described in Section 2.2.1-2.2.3, several other flow effects have been found to influence ingress levels, including the following:

- Large-scale flow instabilities in the rim seal
- Re-ingestion of cooling flow ejected from upstream wheel-spaces
- Wheel-space leakage flows

Large-scale flow instabilities that increase ingress levels have been reported by numerous authors. These phenomena, which are potentially shear driven, are reviewed in Section 2.3.2.

Re-ingestion is the process whereby egress gases that have been ejected from an upstream wheel-space are subsequently entrained into the ingress of a downstream wheel-space. This process can lessen the adverse effect of ingress into the downstream cavity. An experimental investigation of re-ingestion in a turbine stator-well was undertaken by Eastwood *et al.* (2012). Using gas concentration measurements they identified that at engine-representative sealing flow rates, ~7% of the egress from an upstream wheel-space was ingested into the downstream cavity. A complementary computational study by Valencia *et al.* (2012) attempted to model the experimental work using steady and unsteady methods from a range of solvers. The four steady solutions failed to show any significant re-ingestion, while two unsteady solvers fared slightly better, capturing up to 34% of the re-ingestion level measured experimentally.

A further experimental study of re-ingestion was reported by Scobie *et al.* (2018). Their tests included purging both wheel-spaces with the same tracer. Figure 17 illustrates the influence of

egress from the upstream cavity, which is re-ingested into the downstream cavity. An increase in downstream effectiveness of up to 6% can be observed for $\Phi_{0,u} / \Phi_{min,u}$ = 1/2, 1 and 2 relative to the datum case where $\Phi_{0,u} / \Phi_{min,u} = 0$.

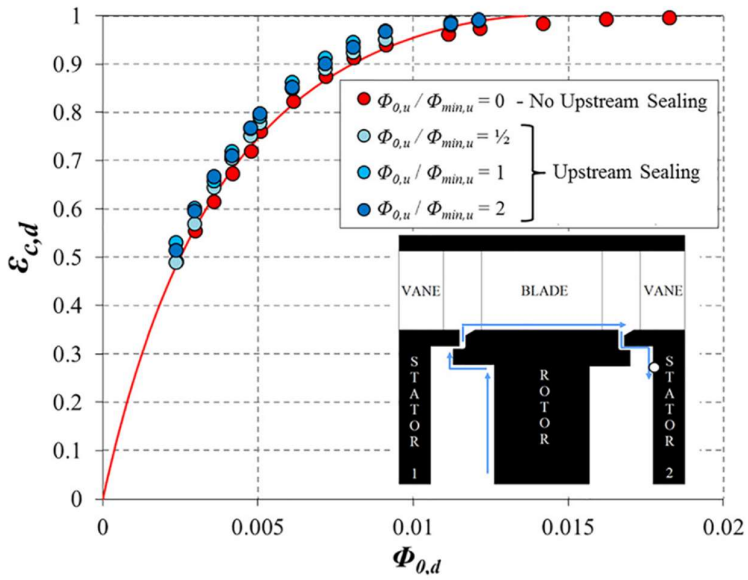

Figure 17: Measured variation of re-ingestion mass fraction with downstream sealing flow rate for three values of upstream sealing flow rate (Scobie *et al.* (2018))

The work of Scobie *et al.* (2018) also defined a re-ingestion mass fraction, χ (see nomenclature), which physically represents the mass fraction of upstream egress entrained into the downstream ingress. The authors found the re-ingestion mass fraction increases with additional downstream purge, as shown in Figure 18. Values of $\chi \sim 0.3$ would be typical at engine sealing flow rates. Additionally, the work found the upstream egress flow does not significantly disturb the fluid dynamics, but simply mixes with the annulus flow.

The majority of ingress studies have neglected the unintended leakage paths that exist in real engine architecture. One such path occurs between the nozzle guide vanes and the ring on which they attach. This leakage, often referred to as *chordal hinge leakage*, exits radially inboard of the rim seal and can form a significant contribution of the egress leaving the wheel-space. The influence of this form of leakage flow was investigated by Patinios *et al.* (2018). By adapting the Bath 1-stage rig it was possible to supply conventional sealing flow from the bore alongside a high radius position (see Figure 19 silhouette) analogous to leakage paths in a real turbine. Results indicated that as the ratio of 'leakage' flow to bore flow increased, the wheel-space flow structure was modified from a conventional Batchelor regime; with a toroidal vortex forming at high radius. The resulting decrease in sealing effectiveness for $0.07 < \Phi_0 < 0.15$ is visible in Figure 19. Additional measurements with the sealing flow delivered through a leakage path in the shroud indicated a significant further reduction in sealing effectiveness.

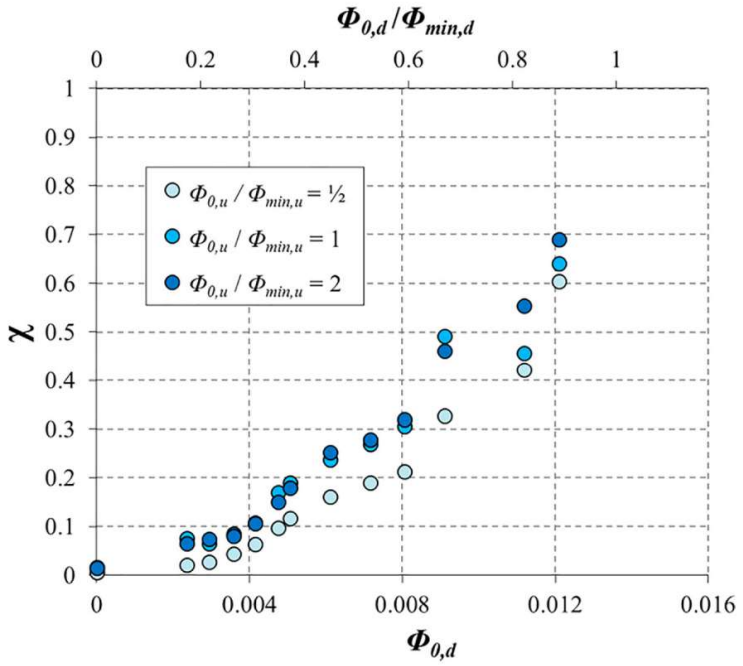

Figure 18: Measured variation of re-ingestion mass fraction with downstream sealing flow rate for three values of upstream sealing flow rate (Scobie *et al.* (2018))

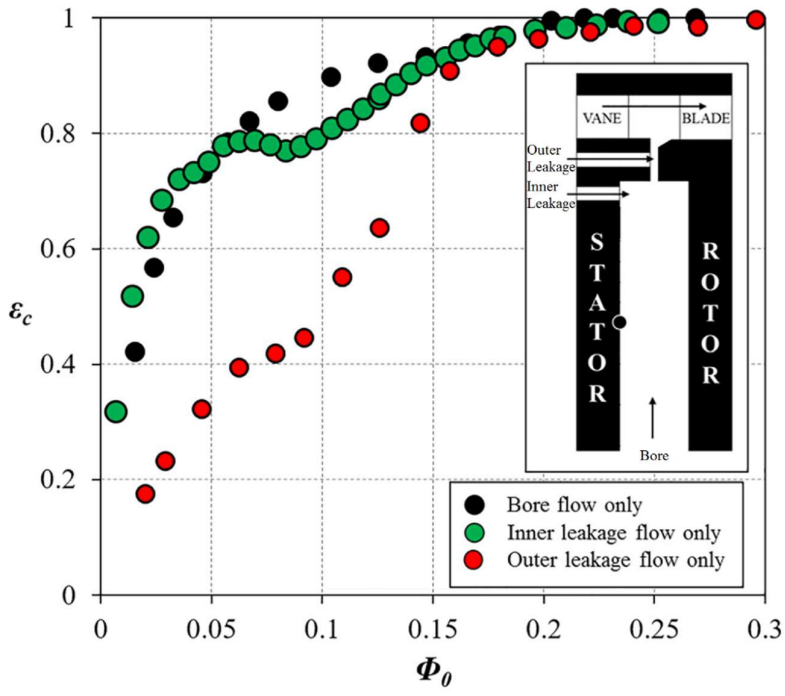

Figure 19: Effect of leakage flow supply on the variation of ε_c with Φ_0, adapted from Patinios *et al.* (2018)

2.2.5 Low Order Modelling

With experimental rigs generally operating at conditions different to engines, there exists a need to scale results from rig to engine. Numerous authors have developed simple theoretical

relationships to predict ingress, often containing empirically gathered coefficients to relate the equations to a specific geometry. These models assume certain simplifications, but nevertheless have the potential to provide relatively fast and cost-effective predictions of ingress.

Most of the theoretical models presented are based on the assumption that ingress is either RI dominated (e.g. Bayley and Owen (1970), Chew *et al.* (1992), Owen (2011a)) or EI dominated (e.g. Chew *et al.* (1994), Johnson *et al.* (2009), Owen (2011b), Phadke and Owen (1988)). The theoretical models of Owen (2011a, b) were solved for RI, EI and CI cases. As clearances are generally very small, these authors treated the rim seal as an orifice through which viscous effects are negligible and ingress is driven by pressure differences between the wheel-space and annulus. Discharge coefficients for ingress and egress, $C_{d,i}$ and $C_{d,e}$, are determined from empirical data for each seal. For the case of EI ingress, $\Phi_{min,EI}$, the minimum sealing flow parameter required to prevent ingress is related to ΔC_p, by

$$\Phi_{min,\ EI} = {}^{2}/_{3}\, C_{d,e} \Delta C_p^{\,1/2} \qquad \textbf{2.10}$$

where ΔC_p is the peak-to-trough annulus pressure distribution defined in the nomenclature. Scobie *et al.* (2015) provide a review of ingress work in which they fit the *orifice models* of Owen (2011a, b) to results from prominent experimental ingress studies in the literature, generally finding the theoretical curves fit well with the experimental data.

Although Owen's full orifice equations were expressed in terms of pressure, for concentration measurements it is convenient to adopt the sealing flow parameter; the resulting *effectiveness equations* were derived by Sangan *et al.* (2013a), Sangan *et al.* (2013b)

The effectiveness equations for EI ingress are expressed as

$$\frac{\Phi_0}{\Phi_{min,\ EI}} = \frac{\varepsilon}{\left[1+\Gamma_c^{-2/3}(1-\varepsilon)^{2/3}\right]^{3/2}} \qquad \textbf{2.11}$$

$$\frac{\Phi_i}{\Phi_{min,\ EI}} = \frac{1-\varepsilon}{\left[1+\Gamma_c^{-2/3}(1-\varepsilon)^{2/3}\right]^{3/2}} \qquad \textbf{2.12}$$

Where subscripts *i* and 0 refer to ingress and sealing flow respectively, and

$$\Gamma_c = \frac{C_{d,i}}{C_{d,e}} \qquad \textbf{2.13}$$

Teuber *et al.* (2013) presented an extrapolation method based on Owen's EI orifice model to scale Φ_{min} from rigs operating at low Mach number to engine. In eqn. 2.10 ΔC_p is influenced by

Mach number whereas $C_{d,e}$ is purely a geometric parameter. Therefore for a geometrically similar engine

$$\frac{\Phi_{min,\ engine}}{\Phi_{min,\ rig}} = \left(\frac{\Delta C_{p,engine}}{\Delta C_{p,rig}}\right)^{1/2} \quad \textbf{2.14}$$

It is suggested $\Phi_{min,rig}$ and $\Delta C_{p,rig}$ are obtained experimentally at incompressible flow conditions and $\Delta C_{p,engine}$ is computed at the elevated Mach number. $\Delta C_{p,engine}$ should then be scaled to incompressible flow conditions for use in equation 2.14. Laitone (1951) proposed equation 2.15, which expresses the relationship between compressible ($C_{p,a}$) and incompressible ($C_{p,a,inc}$) annulus pressure coefficients.

$$\frac{C_{p,a}}{C_{p,a,inc}} = \frac{1}{\sqrt{1\text{-}M^2} + \frac{C_{p,a,inc}}{2}\left(M^2\left[1+\frac{\gamma\text{-}1}{2}M^2\right]\right)\sqrt{1\text{-}M^2}} \quad \textbf{2.15}$$

The advantage of adopting equation 2.14 to calculate the required sealing flow to prevent ingress is that it does not require the direct computation of ingress and could potentially be used with annulus only computations.

Savov and Atkins (2017) developed an alternative low order model by considering a recirculation zone in the seal clearance where annulus and cavity flows are mixed. This region is shown in Figure 20.

The model is based on the notion that this region is modulated by structures of differing length scales and influenced by the purge flow rate. The model treats ingress as turbulent transport driven by eddies of a range of sizes. Similarly to previous models, the prediction of ingress requires the determination of an empirical parameter (this time representing a mixing length), however unlike the previous orifice models ingress is assumed to be largely driven by viscous effects. The authors apply the model to various experimental datasets from the literature, providing generally a good fit and foresee the model being used as a preliminary design tool following further sensitisation.

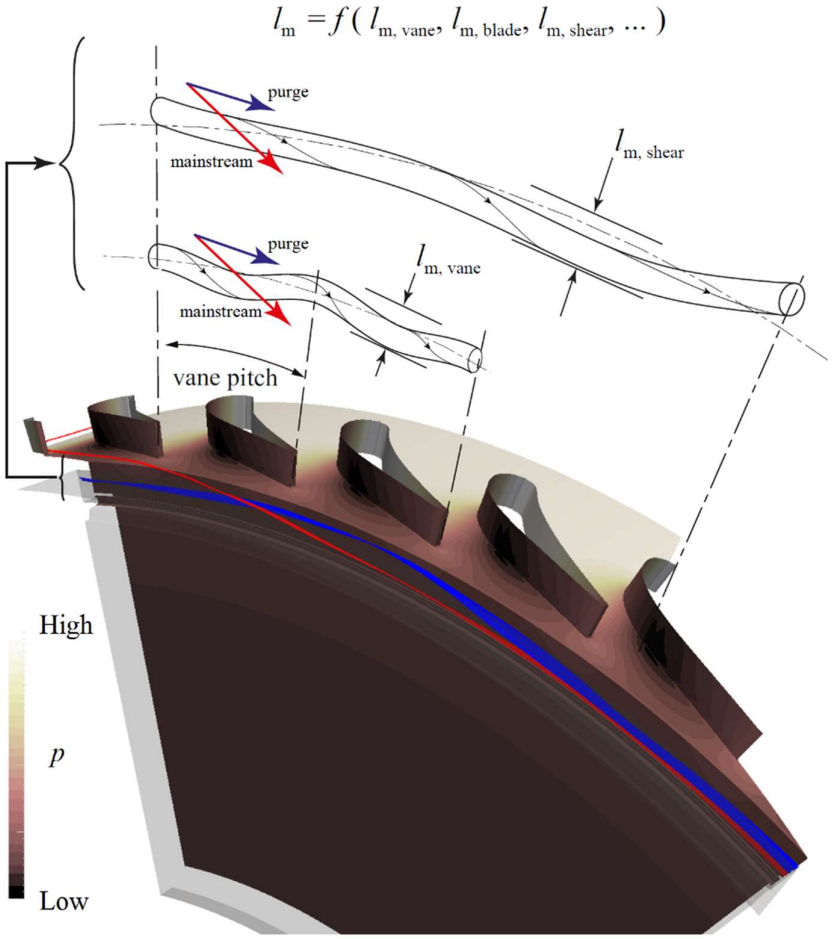

Figure 20: Streamlines of mainstream (red) and rim seal (blue) flow with contours of the pressure coefficient. Schematic of the flow structure indicates modulation of the gap recirculation zone from the vane pressure field and shear-layer instabilities. Adapted from Savov and Atkins (2017)

2.3 Computation of Ingress

2.3.1 Steady Computation of Ingress

Much of the difficulty in modelling gas turbine ingress lies in the problem being inherently highly unsteady in the annulus. Several approaches exist to simplify the problem and enable the use of steady computations in turbomachinery applications. Removing the blades from the computation is perhaps the simplest and allows direct comparison with similar experimental results, but this bladeless approach clearly has a significant effect on the problem. Alternatively, *mixing plane* solutions circumferentially average flow variables between stationary and rotating reference frames or *frozen rotor* solutions include the inertial reference frame but consider only one blade position.

A bladeless approach was adopted by Bohn *et al.* (1999), Green and Turner (1994), Liu *et al.* (2015) and Zhou *et al.* (2013). Whilst Green and Turner (1994) focussed the computational aspect of their predominantly experimental study on the annulus pressure field, Bohn *et al.* (1999) identified a recirculation in the rim seal. A similar recirculation was also identified by Zhou *et al.* (2013), who computed the Bath 1-stage rig detailed by Sangan *et al.* (2013b). However, by comparing unsteady simulations with blades to steady bladeless results they showed the recirculation in the steady case was preventing annulus flow entering the wheel-space, even at low sealing flow rates. By modelling a 'thin seal', the recirculation zone could be removed and a reduced effectiveness, similar to the unsteady model was achieved with 1/20th of the computing time (Figure 21).

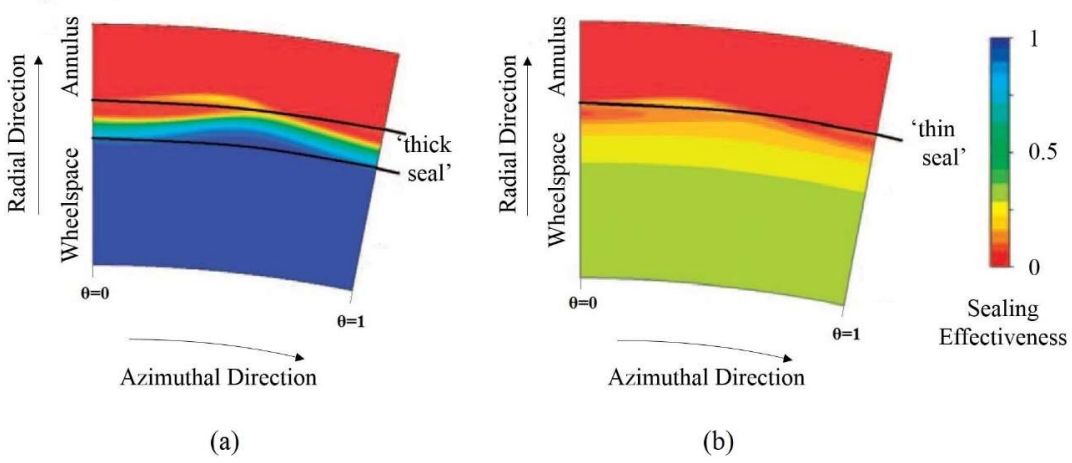

Figure 21 Steady computational results in the r-θ plane at $\Phi_0 = 0.222$, showing the difference in sealing effectiveness for: (a) 'thick seal' geometry; (b) 'thin seal' geometry'. Adapted from Zhou *et al.* (2013)

Liu *et al.* (2015) undertook a similar study to Zhou *et al.* (2013), comparing bladeless RANS simulations with bladed URANS simulations of the Bath rig. They found the computational peak-to-trough pressure distribution to be up to 50% greater than the experimental results, however due to a steep axial decay in the pressure asymmetry, comparisons to computational results 1 mm further downstream gave good correlation. Wheel-space swirl was also predicted well, although without the 'thin seal' approximation of Zhou *et al.* (2013) steady computations greatly under-predicted ingress. The presence of the rotor blades was found to have minimal effect on the annulus pressure distribution. This differs from the conclusions of Bohn *et al.* (2000) but is possibly a reflection of geometrical differences between each of the authors' models.

Mirzamoghadam *et al.* (2008) undertook steady RANS simulations with a mixing plane downstream of the seal. In this configuration, the non-axisymmetric rotor bow wave will not propagate upstream through the stator-rotor interface, therefore the circumferential pressure distribution above the seal is likely to be similar to that of a bladeless configuration. However,

the research did show ingress occurring, even at the highest purge rate tested and found that the presence of vane fillets increased Mach numbers close to the hub, resulting in reduced ingress.

Da Soghe *et al.* (2016) used frozen rotor simulations where, although the rotor is in a separate rotating domain, only one relative position between vanes and blades was considered in each simulation. The computations under-predicted ingress for the radial seal but produced encouraging agreement for the axial seal. The work also demonstrated the thermal buffering effect where Batchelor flow in the wheel-space results in higher rotor wall effectiveness when compared to the stator.

2.3.2 Unsteady Computation and Rim Seal Instabilities

Early computational studies of ingress generally used the steady methods discussed in Section 2.3.1. However, several studies (e.g. (Hills et al., 2002, Laskowski et al., 2011)) have found that unsteady CFD is required to adequately capture the unsteady flows that exist close to rim seals and influence ingress.

Hills *et al.* (2002) computed the University of Sussex ingress rig, comparing results from steady and unsteady CFD to those obtained experimentally. 'Encouraging agreement' was found when the author compared their pressure and concentration results to those from previous work, however despite simulating lower wheel-space sealing effectiveness in unsteady models, the values were still up to 40% higher than in experiments, as shown in Figure 22.

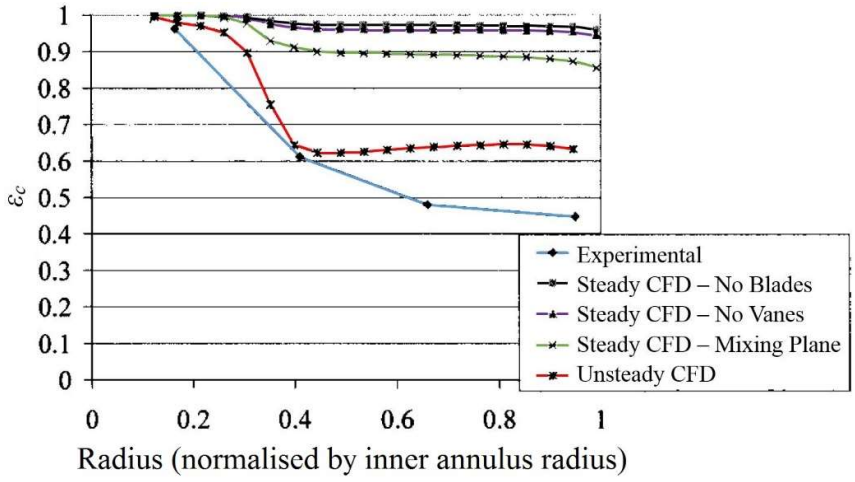

Figure 22 Computational and experimental results for wheel-space sealing effectiveness on the stator wall. Results taken at a $\Phi_0 = 0.02832$, adapted from Hills *et al.* (2002)

One of the most significant challenges in adopting unsteady solvers to compute ingress results from the differing timescales existing in the wheel-space and main gas path flows. Hills *et al.* (2002) found annulus flow would typically converge after ~ 10 blade passes, while low radial

velocities in the cavity (typically ~ 5 m/s) resulted in ~ 200 blade passes being required for a fluid particle to traverse the cavity. To accelerate the convergence of the tracer concentration, Hills *et al.* (2002) suspended the unsteady solution and solved a steady state species concentration equation for the lower wheel-space with fixed velocity and turbulence fields; the unsteady solution was then restarted. Repeated switching from the unsteady solution to a steady solution was used to greatly reduce the computational effort required to reach convergence. Use of the steady solver can be seen by the step changes in tracer concentration in Figure 23.

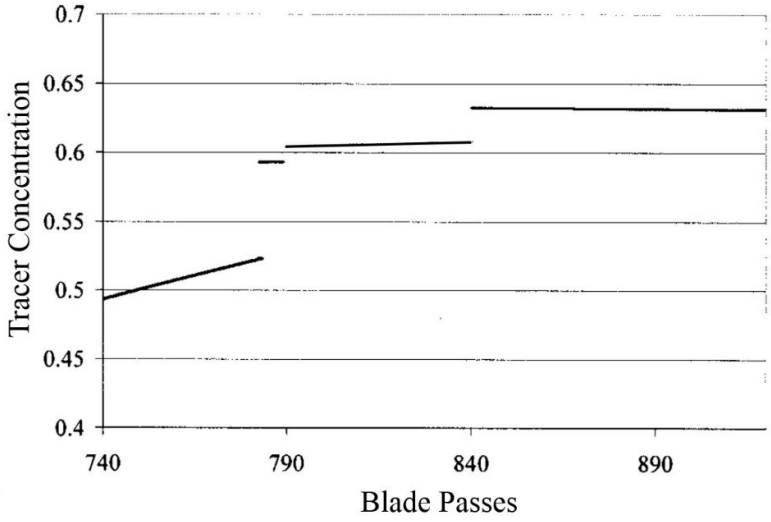

Figure 23 Convergence of the tracer gas concentration on the stator wall at a position r/r_0 =0.41, during an unsteady computation with Φ_0 = 0.02832, adapted from Hills *et al.* (2002)

In addition to the interaction between vanes and blades, recent computational and experimental work has identified large-scale unsteady flow structures in the wheel-space and rim seal, occurring at frequencies unrelated to those of the blades. Figure 24 illustrates data from the literature showing the number of structures identified (N), against their rotational speed relative to the disc (ω/Ω). Most studies, including all experimental investigations, have found between 8 and 30 structures rotating at 75-100% of the disc speed, over a wide range of different geometries and flow conditions. Computational and experimental results from the present work are also included. The breadth of data suggests the structures are physical and not simply an anomaly of one particular experimental facility or computational circumstance. There is a weak negative correlation between the two variables (N and ω/Ω), though further investigation would be required to confirm this relationship.

To the author's knowledge, Cao *et al.* (2004) were the first to demonstrate the existence of the unsteady flow features categorised in Figure 24. Their computations captured low-pressure structures within an axial clearance rim seal, despite removing vanes and blades from the model. These numerical simulations were validated using fast-response pressure transducers, with both experiments and CFD showing $8 < N < 18$ structures rotating at 90-94% of the disc speed. The

authors also showed the characteristics of the rotating structures (N and ω/Ω) were a function of geometry and their intensity was supressed with a reduction in the axial clearance of the seal or an increase in the purge level. Jakoby *et al.* (2004) also conducted ingress computations without blades or vanes; three large, low-pressure regions rotating at 80% of the disc speed were identified, but these structures were suppressed at higher purge flow rates. These structures propagate deep into the cavity, indicating a potential cavity mode. It should be noted that this is distinct from the other instabilities discussed in this review, whilst potentially excited by the same phenomena.

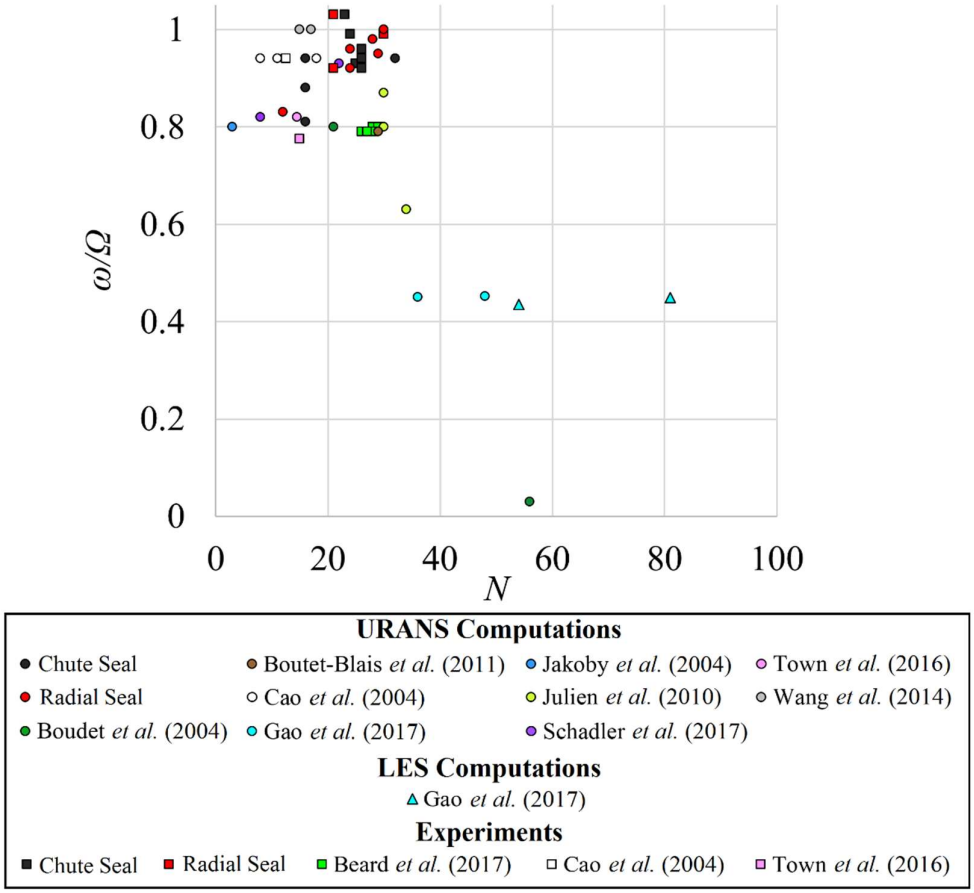

Figure 24: Comparison of rotating low-pressure structures from the present study and from the literature

Boudet *et al.* (2005) and Boudet *et al.* (2006) investigated ingress using unsteady CFD configurations with and without blades. Using a small 13.33º sector they computed rim seal instabilities at 0.44 of the blade passing frequency (BPF), showing these rotating structures disappeared at higher sealing flow rates. They related their findings to Taylor-Couette instabilities and argued that they were supressed at higher purge rates due to a dominant centrifugal flow.

Julien *et al.* (2010) and Boutet-Blais *et al.* (2011) produced numerical simulations based on earlier experimental work by Feiereisen *et al.* (2000), who used a full-scale, half-span

representation of the first stage in a modern high-pressure-ratio turbine. The experiments identified two unsteady structures per-revolution, however this was attributed to eccentricity in the disc. Using a 74º sector model with nine vanes and 12 blades, Julien *et al.* (2010) identified 30-34 large-scale structures rotating at an angular speed slightly less than the disc speed. These structures were strongest at the no-purge and low-purge conditions and led to deep ingress into the wheel-space; in contrast the vane-blade interaction, which dominated at high purge, led to only a shallow penetration of ingress into the upper region of the cavity. Boutet-Blais *et al.* (2011) used sector models with and without vanes or blades and identified $24 < N < 29$ structures rotating around the entire disc. Importantly, the work also showed that a passive scalar-based ingress model compared very well against a temperature-based version and concluded that using a passive scalar in a cold rig was an adequate means to compare rim seal designs.

Rabs *et al.* (2009) studied the existence of Kelvin-Helmholtz instabilities in rim seal flows. They showed that coherent vortex structures were generated due to an unstable shear layer between the purge and tangential annulus flow. Although the presence of vanes and blades supressed these instabilities, they did occur at the highest purge rate tested.

Laskowski *et al.* (2011) modelled a stationary cascade rig that included five stator vanes, a wheel-space and five cylinders representing the leading edge of the rotor blades. They demonstrated that the interaction between the vane wake and rotor bow wave results in an unstable shear layer above the rim seal, which gives rise to ingress. This effect was not present in steady computations, but was captured by their unsteady computations of the rig.

Chilla *et al.* (2013) discussed the formation of Kelvin-Helmholtz instabilities in the *chute* seal of a realistic turbine configuration. These instabilities (depicted in Figure 25) were governed by the velocity deficit of the sealing flow relative to the mainstream and could be stabilised by increasing the sealing tangential velocity or the sealant mass flow. The work also showed that the rim seal unsteadiness is shed into the rotor hub endwall at a frequency below the vane passing frequency, and could lead to increased loss within the turbine stage, emphasising the importance of rim seal flow when analysing profiled end-walls. Similarly, the influence of egress exiting a chute seal was noted in the earlier study of Boudet *et al.* (2006), who reported the swirl angle of the egress impinging upon the blade row was modulated by the sealing flow rate. With greater purge rates leading to higher fluctuations in swirl at the blade leading edge; this influence was even found downstream of the blades where distorted radial profiles of stagnation temperature were observed.

Large eddy simulations (LES) of ingress were performed by O'Mahoney *et al.* (2011) and O'Mahoney *et al.* (2012) using the same geometry as earlier studies by Boudet *et al.* (2005) and Boudet *et al.* (2006). The work found LES showed an improved prediction of ingress relative to

URANS. However, it should be noted that even the smallest LES computation required 20 days on 256 processors, while the corresponding URANS computation took just 14 days on 32 processors.

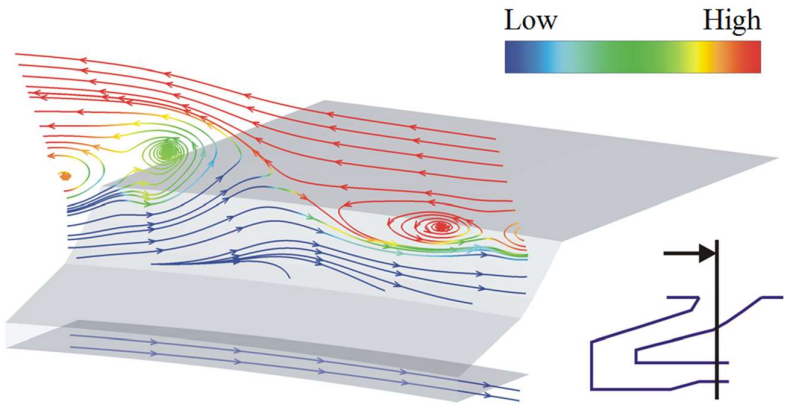

Figure 25: Instantaneous streamlines on an axial plane through a rim seal, coloured by static temperature (Chilla *et al.* (2013))

Full 360º URANS computations of ingress were conducted by Wang *et al.* (2014). They identified 15-17 rotating pressure structures circumferentially distributed around the seal region. The structures moved at approximately the disc speed and the authors concluded that they were a significant driver for ingress. Mirzamoghadam *et al.* (2014) suggested that the six revolutions computed were insufficient for the structures to stabilize and also used 360º URANS numerical simulations for the same rig (albeit with a different seal geometry). They computed 6-8 structures, which were still evolving after 16 disc revolutions.

Subsequent work by other authors continued the use of sector models and also identified large rotating structures. Using a 99.31º sector with eight vanes and ten blades, Town *et al.* (2016) identified 14.5 structures moving at 81.7% of the disc speed; this compared well to the 15 structures rotating at 77.5% of the disc speed measured in their corresponding experiments. However, the work makes no mention of sealing effectiveness and results are only presented at one operating condition. The authors also state that the experimental data would benefit from increased scrutiny.

A purely experimental study by Savov *et al.* (2017) tested two different seal configurations, with and without blades, over a range of conditions. The work identified a band of frequencies in the rim seal at $f/f_d \sim$ 20-40, that were attributed to an unstable shear layer, as also identified by Rabs *et al.* (2009). For a single lip rim seal, the unsteadiness was found to be suppressed by the presence of the blades, as shown in Figure 26, again reflecting the previous findings of Rabs *et al.* (2009). Savov *et al.* (2017) measured lower sealing effectiveness and intensified spectral activity at lower disc speeds (where the shear between annulus and wheel-space flows would be

higher) and decreasing unsteadiness with decreasing ingress at higher disc speeds, thus giving an indication of the importance of these unsteady structures.

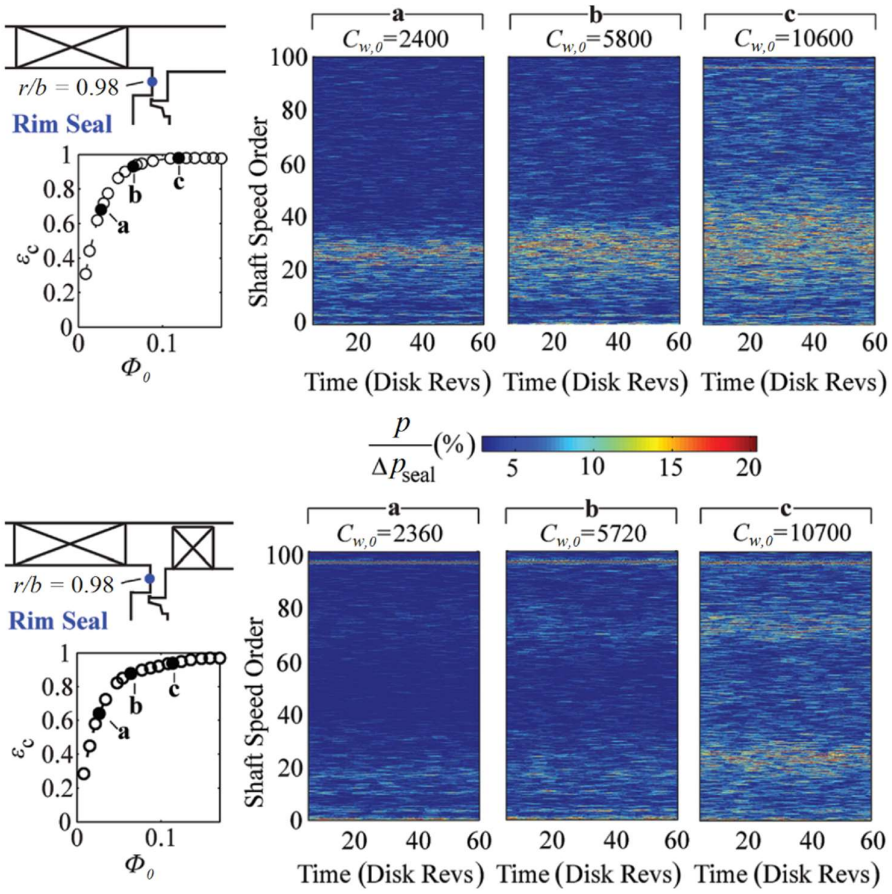

Figure 26: Spectrograms of unsteady pressure in a single lip rim seal with and without rotor blades at $Re_\phi = 4.9 \times 10^6$: (a) low effectiveness, (b) medium effectiveness, (c) high effectiveness (adapted from Savov *et al.* (2017))

Beard *et al.* (2017) conducted an experimental study on a turbine rig without blades or vanes, investigating solely the unsteady pressure field in the rim seal and cavity. The strongest unsteadiness was measured towards the outer periphery of the rim seal where a broad spectrum of activity was identified. The number of low-pressure structures within the rim seal were shown to reduce from $N = 28/29$ to 26/27 as the purge level was reduced from its maximum level down to zero. The structures were measured to rotate at 80% of the disc speed and this was insensitive across the conditions tested. Gao *et al.* (2017) later performed a RANS, URANS and LES study of the experiments conducted by Beard *et al.* (2017). The LES study used a 13.33º sector and captured approximately the same peak frequency at 23.5 times the disc speed; however, while the experiments showed this corresponded to 29 low-pressure structures rotating at 80% of the disc speed, the computations determined 54 structures rotating at 43.5% of the disc speed.

Gao *et al.* (2018) extended the study of Gao *et al.* (2017) and also assessed the time-averaged flow within the overlapping gap of the chute seal. The RANS computations showed conventional rotor-stator behaviour: where the flow in the rotor boundary layer migrates outwards, and the flow in the stator boundary layer migrates inwards. However, the LES and URANS computations revealed a mean flow vortex structure rotating in the opposite direction to convention, with differences most pronounced for the LES (see Figure 27). This vortex structure within the seal has been referred to as a gap recirculation zone (GRZ) by Bohn *et al.* (1999), Ko and Rhode (1992) and Savov and Atkins (2017). With the latter showing it is modulated by structures of differing length scales (see Figure 20), before becoming supressed and subsequently 'blown out' at high purge levels (see Figure 28). Savov and Atkins (2017) also noted that although not explicitly discussed, the GRZ could be observed in other studies, including that of Chilla *et al.* (2013).

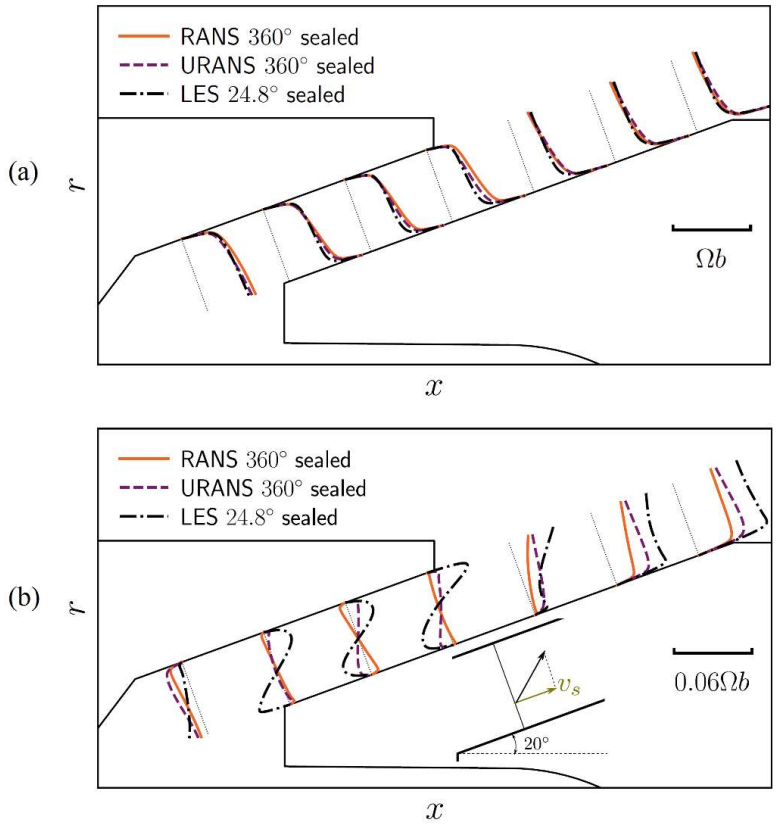

Figure 27: Profiles of mean tangential velocity (a) and stream-wise velocity (b) across an overlapping chute seal for RANS, URANS and LES computations (Gao *et al.* (2018))

A combined experimental and computational study focussing on the influence of the unsteady rim seal/cavity flow on the annulus flow was presented by Schadler *et al.* (2017). The CFD model identified 8-22 pressure structures rotating at 82-93% of the disc speed and as in previous studies (e.g. Boudet *et al.* (2005), Chilla *et al.* (2013), Jakoby *et al.* (2004), Julien *et al.* (2010)), this low-

frequency unsteadiness was found to disappear at the highest purge rates. Schadler *et al.* (2017) also identified that the rim seal unsteadiness could give rise to non-negligible noise emission within the range of human perception.

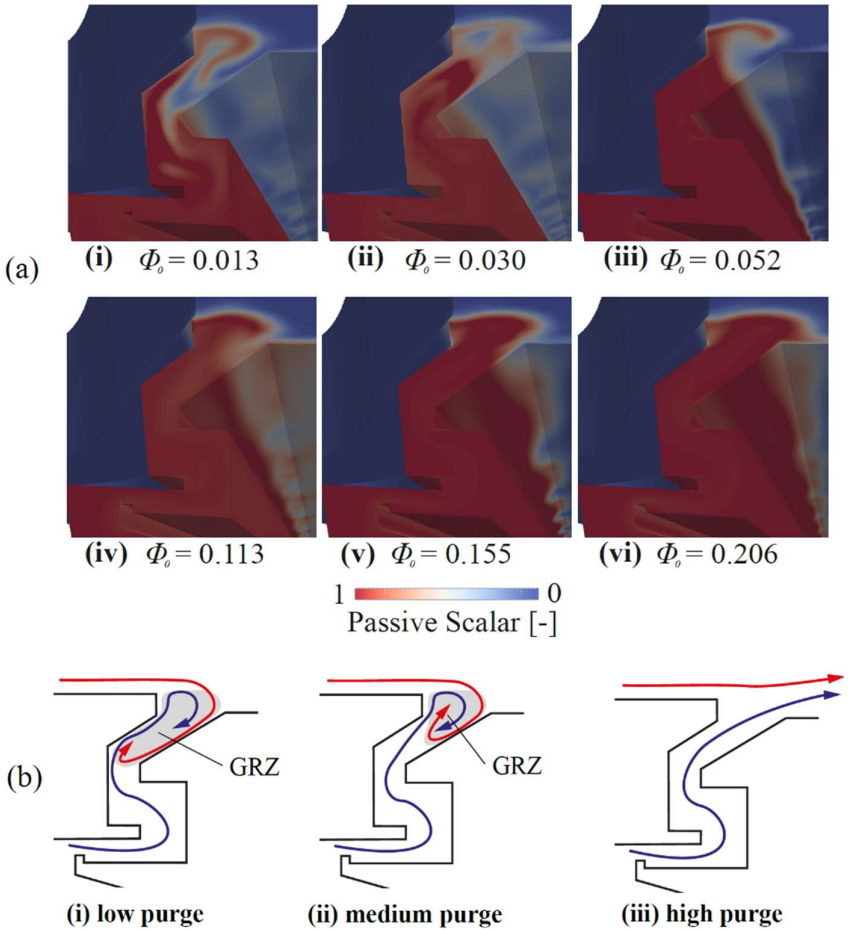

Figure 28: (a) Contours of passive scalar concentration illustrating the blow-out of the GRZ (note purge flow seeded with scalar, mainstream unseeded), (b) schematic illustration of GRZ blow-out with increasing purge (Savov and Atkins (2017))

To the authors' knowledge, Pogorelov *et al.* (2018) was the first publication reporting a study of ingress using LES in a 360º model. A novel Cartesian meshing approach yielded results that compared well with time-averaged experimental data. Additionally, a frequency at 18 times the disc speed was identified, corresponding to 27 structures rotating at 0.66 of the disc speed. These structures are visualised in Figure 29. The authors suggest they are driven by shear layer instabilities in the seal. A further acoustic mode, found to rotate in the opposite direction to the disc, was driven by the interaction of the shear instabilities with the flow downstream of the stator vanes. Unfortunately, no unsteady experimental data was available for validation and the demanding computational requirement limited the simulations to a single flow condition for two seal configurations.

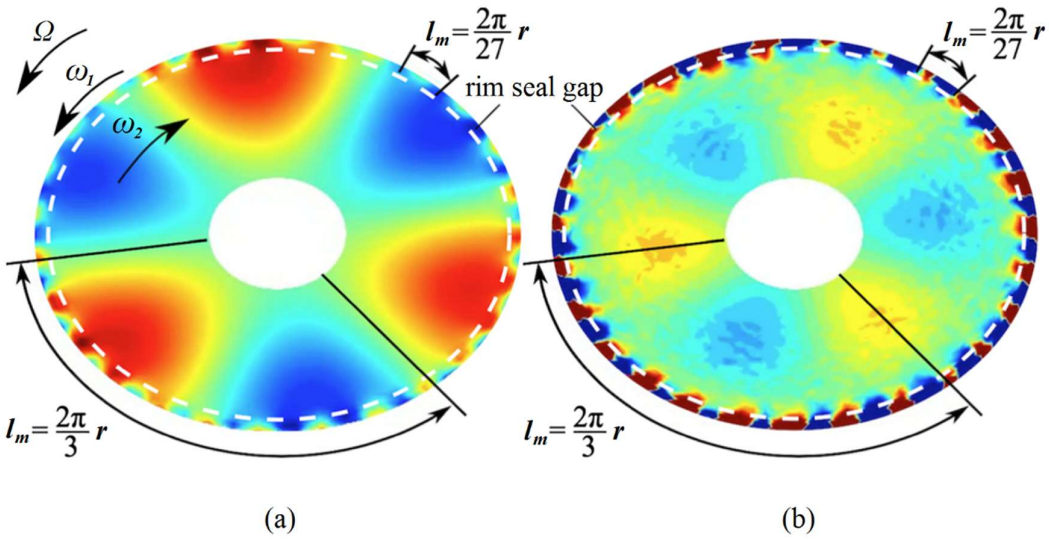

Figure 29: Extracted wheel-space modes at f/f_d ~18 from a 360° LES simulation: (a) pressure amplitude, (b) radial velocity amplitude. Adapted from Pogorelov *et al.* (2018)

2.3.3 Influence of Computational Sector Size

Section 2.3.2 discussed the presence of rotating flow structures in the rim seal region; these may be larger than the blade pitch and rotate asynchronously to the rotor. These large-scale structures were identified by both experiment and computation, and their existence is believed to influence ingress. Numerous authors (see Figure 24) have explored this phenomenon. Given the presence of these structures, the choice of computational sector size (e.g. 30º, 90º, 360º) is an important consideration to avoid enforced periodicity influencing the simulation. This section highlights the results from authors who have investigated the influence of sector size.

Cao *et al.* (2004) compared axisymmetric meshes of 360º and 90º. The time-averaged behaviour was largely unchanged between the cases and despite the increased amplitudes of unsteady structures, the overall behaviour was similar (see Figure 30). Contrastingly, Jakoby *et al.* (2004) showed three large regions of low pressure found in a 360º simulation that were not captured in a small 22.5º sector due to the enforced periodicity. This is perhaps unsurprising given the 120º occupied by each pressure lobe.

Boutet-Blais *et al.* (2011) compared results from a 180º sector without vanes or blades, alongside a 24º sector with blades and vanes, finding significantly smaller lobes. The larger sector model identified $24 < N < 28$ structures rotating around the entire disc, while 29 were computed for the smaller sector.

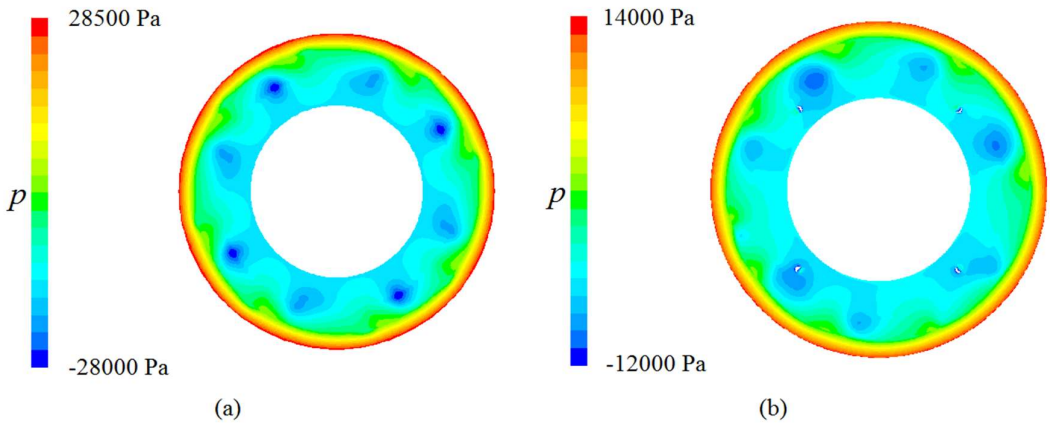

Figure 30: Computed contours of pressure in the wheel-space of the Alstom test rig: (a) 90° domain, (b) 360° domain. Figure adapted from Cao *et al.* (2004)

Zhou *et al.* (2011) speculated that the under-prediction of ingress in their computations of the rig at Arizona State University was due to the use of a 14.4º sector that was unable to capture the rotating low-pressure zones predicted by 360º CFD. Wang *et al.* (2014) later computed the full disc, identifying the presence of 15-17 low-pressure zones (at low purge) in the rim seal that were previously absent, precipitating increased ingress and lower stator-wall effectiveness in comparison to the sector model.

Several authors have performed LES of ingress; here sector size is of even greater importance due to the inherently larger computational requirements. O'Mahoney *et al.* (2011) and O'Mahoney *et al.* (2012) performed LES and URANS computations on various domains between 13.33º and 360º in size, concluding that 'URANS simulations on larger sector models, initialized from a smaller sector model, showed little change in the frequency and amplitude of the unsteady pressure variations or ingestion.' They also suggested that sector size is not as important as turbulence modelling in the prediction of rim seal flows. Gao *et al.* (2018) compared LES models of 13.3º and 24.8º, as well as URANS models of 24.8º and 360º (albeit without vanes or blades): they drew a similar conclusion to O'Mahoney *et al.* (2012), with sector size showing little influence on both the time-averaged and unsteady flow characteristics.

Table 2 details the aforementioned studies comparing large-scale structures in differing sector sizes. It can be seen that only when the sector is significantly smaller than the size of the instability (highlighted in red) has the computation of structures been significantly influenced.

Author	Large Sector Model		Small sector model	
	Sector Size (°)	*N*	Sector Size (°)	*N*
Cao *et al.* (2004)	360	11	90	8
Jakoby *et al.* (2004)	360	3	22.5	0
Boutet-Blais *et al.* (2011)	180	28, 24	24	29
Zhou *et al.* (2013), Wang *et al.* (2014)	360	15, 17	14.4	0
Gao *et al.* (2018)	360	47	24.8	44

Table 2: Comparison of large-scale structures in differing sector sizes

2.3.4 Frequency Domain Computations

The flow structure in turbomachinery is both temporally and spatially periodic in nature. Often temporal oscillations occur at harmonics of either the blade passing frequency (BPF) or the frequency of rotation of the rotor. This means that the problem is well suited to being solved in the frequency domain. The basis of these frequency domain methods is that the variables in the governing Navier-Stokes equations can be represented by a Fourier series in time with spatially varying coefficients. Frequency domain methods have the potential to offer a level of fidelity similar to URANS solvers with a computational cost that is at least one to two orders of magnitude lower (Hall *et al.* (2002)).

2.3.4.1 Theoretical Development of Frequency Domain Methods

Much of the early work on frequency domain methods was based on the time-linearised harmonic model. Hall and Crawley (1989) used this method to analyse the unsteady aeroelastic behaviour of blades. The method assumes that the unsteady perturbations are small relative to the time-averaged flow and are proportional to $e^{j\omega t}$, allowing the governing flow equations to be linearised about the steady mean flow. The equations formed are similar to those used in conventional CFD, however the time derivative terms, $\partial/\partial t$, are replaced with the $i\omega$ operator. The equations can then be discretised and solved using a pseudo-time-marching method. Acceleration techniques such as multigrid, more commonly used with steady simulations, can also be implemented. The major drawback of a time-linearised approach is the inability to capture nonlinear unsteady effects, which are likely to be crucial to accurately modelling ingress.

To address the shortcomings of the time-linearised method, a nonlinear harmonic (NLH) method was initially demonstrated for 2-dimensional inviscid Euler equations by Ning and He (1998) and subsequently for the 2-dimensional Navier-Stokes equations by He and Ning (1998).

The method brings similar advantages to time-linearised methods, but the solution of the time-averaged flow is directly coupled to the solution of the first order harmonic, allowing modelling of dynamic nonlinearities.

He and Ning produced results that quite accurately modelled the unsteady nonlinearities in the flow, however their method neglected the coupling between high order harmonics, and unsteadiness was not considered in the turbulence model.

Harmonic balance methods that address some of the shortcomings of He and Ning's method were proposed by Hall *et al.* (2002) and McMullen *et al.* (2002). These methods both compute the flow variables at a number of discrete times over one blade pass with the use of a pseudo time-marching scheme. A discrete Fourier transform is then used to transfer the flow solution to the frequency domain. The slight difference between the 'Time-Spectral' method of Hall *et al.* (2002) and the 'Non-linear Frequency Domain' method of McMullen *et al.* (2002) is that the first stores the time domain solutions (at several instances in time) whereas the latter stores the frequency domain solution (as Fourier coefficients). A process flowchart showing the solution method proposed by McMullen *et al.* (2002) can be seen in Figure 31. It should be noted that the process of calculating the residuals is undertaken in the time domain, therefore standard flux and discretisation schemes are implemented.

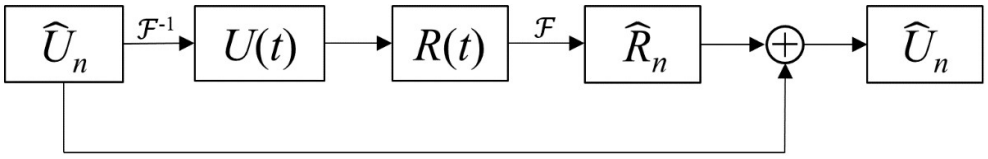

Figure 31 Process flowchart for a nonlinear frequency domain method. $\hat{U}_n$ and $U(t)$ represent the Fourier coefficient form and time-level form of the conservation terms in the Navier-Stokes equations, while $\hat{R}_n$ and $R(t)$ represent the residual terms in the same forms. Adapted from McMullen *et al.* (2002)

All the harmonic methods discussed here have been developed because they offer the potential to reduce computational effort. For similar meshes, a harmonic balance solution retaining N_f harmonics will be computationally equivalent to $2N_f + 1$ steady solutions (He (2010)). This in itself is likely to provide a significant reduction in computing time, however a second reduction can exist by virtue of using phase-lag boundary conditions over conventional periodic boundary conditions. Phase-lag boundary conditions allow adjacent vane and blade rows to be computed with different sector sizes, therefore domains can be reduced in size to a single vane and blade passage.

Erdos *et al.* (1977) first proposed a phase lag boundary condition method whereby the parameters at the periodic interfaces are stored for one blade pass so that one side of the interface can lag the other; the parameters are then updated as the solution is marched forward in time. A

second approach was suggested by Giles (1988) where the computational time plane was inclined in the azimuthal direction, meaning zero phase shift is required at the periodic interfaces. However, a number of limitations with these methods were identified by He (1990), including: a large storage cost associated with the method of Erdos *et al.* (1977) and a limited range of suitable frequencies for the method of Giles (1988). He (1990) proposed a 'shape correction' method that is based on modelling the periodic interfaces using a fundamental frequency which is phase shifted at one side of the interface. The model was subsequently generalised by He (1992) to allow multiple fundamental frequencies. This approach avoids the limitations of the previous two methods and is based in the frequency domain, so is well suited for implementation with harmonic balance methods.

Further details on the formulation of harmonic balance methods can be found in Appendix A. Reviews of the development of harmonic balance methods have also been published by He (2010) and Hall *et al.* (2013).

2.3.4.2 Application of Frequency Domain Methods

Early harmonic balance codes developed in academia (e.g. Hall *et al.* (2002), He and Ning (1998)) have not been widely available to industry, however in recent years harmonic balance solvers have been incorporated into several commercial CFD packages. Research undertaken by Honeywell (e.g. Mirzamoghadam *et al.* (2012)) and GE (e.g. Green *et al.* (2014a)) has used Numeca's FINE™/Turbo software, while other published work has used STAR-CCM+ (Custer *et al.* (2012)) and DLR's TRACE code (Frey *et al.* (2014)).

A number of studies using harmonic balance solvers have been undertaken to model annulus flow without a wheel-space. Custer *et al.* (2012) modelled the annulus from the Aachen 1.5-stage gas turbine rig, comparing time-marching and harmonic balance solutions using STAR-CCM+. Once issues surrounding pressure reflections off the inlet boundary were addressed, little difference was found between blade surface pressures of the time domain solution and the three harmonic frequency domain solution. The latter also provided a tenfold reduction in the computational effort. A large part of this was due to the phase-lag boundary conditions that allowed a single vane/blade passage model to be implemented in the harmonic balance model, while the time-marching solution required a six vane, seven blade sector.

Subramanian *et al.* (2013) simulated a two-stage annulus only configuration using the harmonic balance solver in STAR-CCM+. They investigated the unsteady pressures and concluded that 'acceptable accuracy' could be obtained by retaining only the harmonics from interactions with adjacent rows. This 'nearest neighbour' approach provided a reduction in computational effort greater than an order of magnitude when compared to the 'all blade row'

method (in which all vane and blade interactions are considered in the entire model). The same rig geometry was later used by Marpu *et al.* (2015), who showed the harmonic balance method could efficiently model the complex unsteady effects from blade cooling flows.

Annulus only studies using the TRACE harmonic balance solver have been undertaken by numerous studies, including Frey *et al.* (2014), Junge *et al.* (2015), Frey *et al.* (2017) and Kügeler *et al.* (2018). The first of these showed a number of comparisons between time-marching and harmonic balance computations, indicating good agreement between blade surface pressures when four harmonics from adjacent blade row interactions were retained but poor agreement with only two harmonics. Junge *et al.* (2015) investigated the importance of including interactions from non-adjacent blade rows in large multistage configurations (in this case a 4.5 stage compressor). Unlike in the earlier multistage turbine simulations of Subramanian *et al.* (2013), the authors concluded that these interactions in the compressor substantially impact the unsteady flow field. The influence of these 'scattered modes' can be seen in Figure 32. It can be seen that beyond the second stator, the vane wake is not accurately passed to the downstream rotor when only adjacent vane and blade modes are considered.

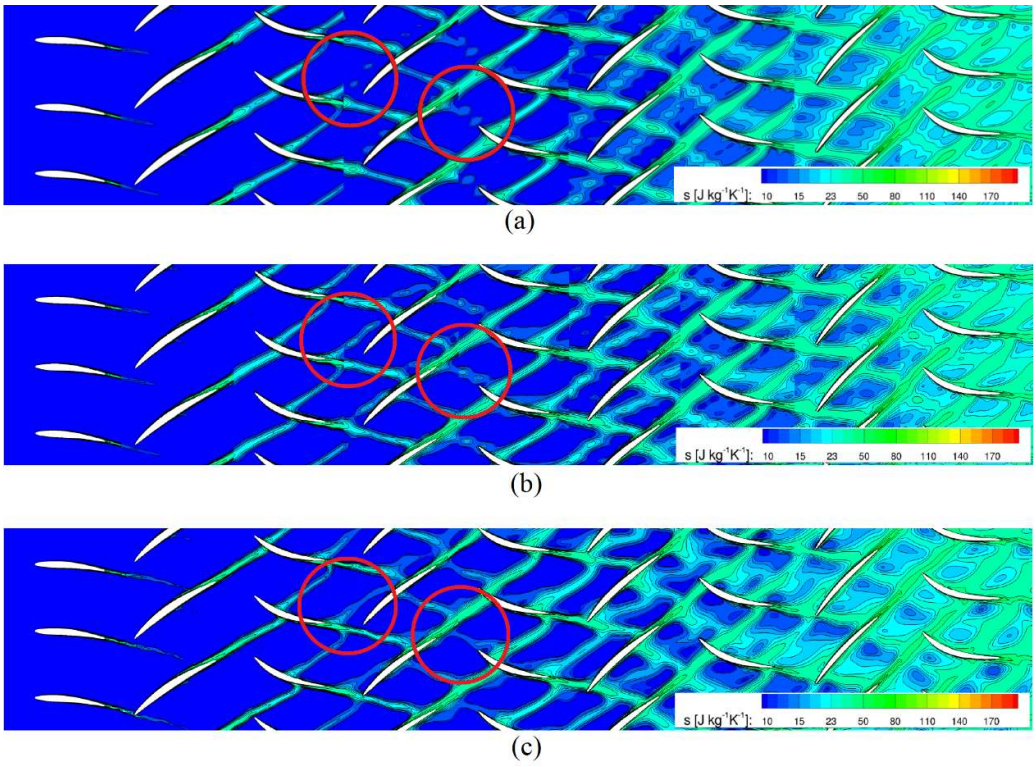

Figure 32: Entropy in 4.5 stage axial compressor, computed using: (a) harmonic balance solution with modes from adjacent rows only, (b) harmonic balance solution with additional scattered modes included, (c) time-domain solution. Figure adapted from Junge *et al.* (2015)

Further multi-stage phenomena such as *clocking* and *indexing* were investigated by Frey *et al.* (2017). The term clocking refers to the relative position of rotors or stators and indexing refers to

the aperiodic effects resulting from differing vane or blade counts. The work demonstrates an aperiodic flow by modelling a large inlet pressure distortion; finding efficient computations from a single vane harmonic balance model can accurately capture the results from more computationally expensive simulations (Figure 33). The ability to simulate such large-scale disturbances that are not periodic with vanes or blades could also form an important part in ingress calculations given the recent research into large-scale rim seal instabilities (see 2.3.2).

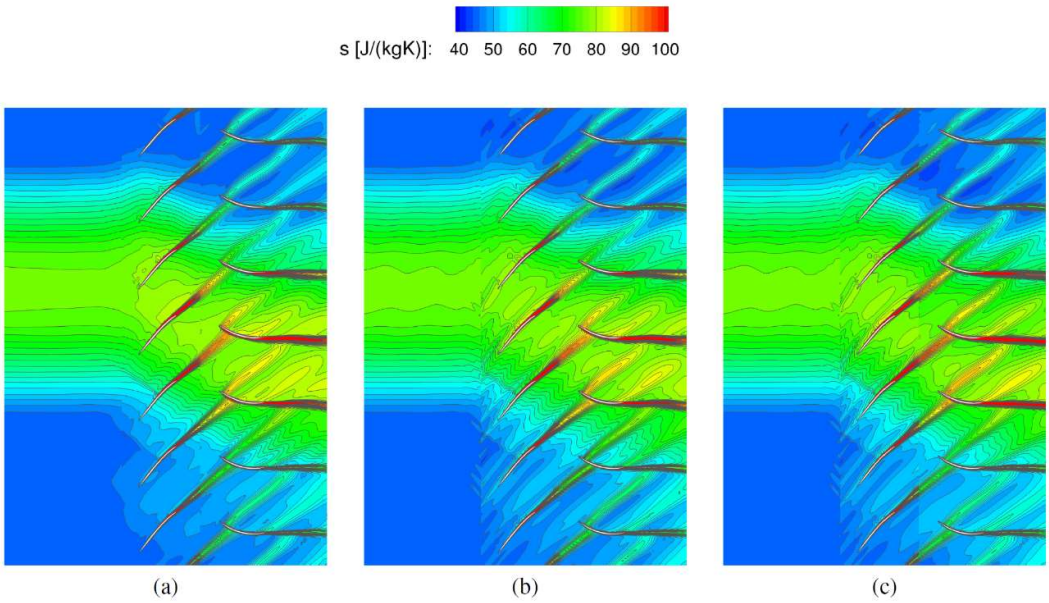

Figure 33: Entropy distribution through a one-stage fan with an aperiodic inlet condition: (a) time-domain solution, (b) harmonic balance solution with full annulus stator, (c) harmonic balance solution with a single stator. Figure from Frey *et al.* (2017)

A harmonic balance approach to modelling ingress was adopted by Mirzamoghadam *et al.* (2012). This study used the FINE Turbo solver and retained three harmonics of the vane/blade passing frequencies in the solution. The author compared three seal geometries, but no comparison to a conventional unsteady time-marching solution was made and the work included very limited comparison to proprietary test data. However, the author did report that the error in upper rim cavity thermal effectiveness was just 1% at the highest sealing flow rates and 8% at the lowest sealing flow rates.

Harmonic balance computations of Ohio state university's 1-stage test facility were evaluated in a series of papers. The high Mach number facility allows investigation of rim seal flows, however, the first study in the series by Green *et al.* (2014a) compared time-marching and harmonic balance computations of an annulus only model using Numeca FINE™/Turbo. As with the solvers discussed previously, good agreement was generally found between the approaches. A further paper evaluated harmonic balance computations that included an upstream wheel-space (Green *et al.* (2014b)). The structured grid used in the study contained approximately 2.3 million

nodes to model the vane-blade-vane passage and 1.4 million nodes in the cavity. Near wall y^+ values were between 1 and 10 and the Spalart-Allmaras turbulence model was used. However, no grid or turbulence model sensitivity studies were performed as the authors used 'default values' wherever possible to mimic industry turbine design processes. The harmonic balance setup modelled three harmonics of the adjacent vane/blade passing frequencies. Stage-exit temperature and pressure profiles from both steady and harmonic computations showed good agreement with experimental data, however the shape and magnitude of profiles close to the annulus hub and seal demonstrated weaker agreement. The paper does not quantify ingress, and temperature comparisons are likely to be highly influenced by the isothermal wall conditions that were based on various discrete measurements. This may explain why the results showed no significant difference in temperature profiles between the steady and harmonic computations.

2.4 Summary

A wealth of research has been undertaken to investigate gas turbine ingress. This chapter has highlighted the most prominent studies, discussing the experimental and computational approaches used to model the problem, alongside the mechanisms that govern the flow phenomena.

Much work has categorised the phenomena as rotationally-induced (RI), externally-induced (EI) or more recently combined ingress. However, numerous studies have identified instabilities that occur at frequencies unrelated to those of the vanes or blades as a key driver of ingress. This process is not yet well understood and literature on the subject formed a large focus of the chapter. Reviewing a breadth of studies has shown that typically 8-30 instabilities may exist around a disc, often rotating at just less than the disc speed. Whilst their cause is not yet proven, it has been suggested they are a consequence of the shear between annulus and wheel-space flows.

The vast majority of ingress research has investigated wheel-space cavities upstream of a rotor. Only a few studies have been published that investigate ingress into a downstream cavity and to the author's knowledge none of these include detailed analysis of the unsteady flow; there is clearly scope for specific research in this area.

Early computations of ingress generally adopted steady RANS methods, however with ever-increasing computational power, researchers have been more readily able to perform URANS and LES simulations. These methods allow powerful insight into what is inherently an unsteady problem. Despite this, no authors have yet demonstrated a reliable means to accurately compute ingress, and best-practice methodologies have not been established.

Unsteady simulations of ingress have often been found to be computationally expensive, consequently there exists a desire to develop more efficient methods. The suitability of reduced sized sector models to capture large-scale structures remains a question, however authors have begun investigating the use of frequency domain solvers to greatly reduce costs. Two studies using harmonic balance methodologies to compute wheel-space cavity flows were identified, however neither attempted to model the rim seal instabilities that have been found to occur at frequencies unrelated to vanes or blades.

Chapter 3: Computational Methodology

This chapter details the CFD modelling approach adopted for all results reported in this thesis. Computations were undertaken using the Turbomachinery Research Aerodynamics Computational Environment (TRACE) code v9.0.411, a CFD package developed at the German Aerospace Center's (DLR) Institute of Propulsion Technology in Cologne, Germany. The compressible flow solver used a finite volume approach to solve the Reynolds-averaged Navier–Stokes (RANS) equations. Computations were run using the Balena High Performance Computing Service at the University of Bath, with cases typically solved on four Intel E5-2650 v2 nodes (64 cores in total).

Computations were based on geometry from the University of Bath's 1.5-stage test rig, discussed in detail by Patinios *et al.* (2016). A range of time-averaged and time-accurate experimental measurements are used for validation purposes, however experiments were not undertaken by the author of this thesis.

Three main turbine configurations are modelled in this thesis: a *baseline stage*, incorporating the original two-dimensional vane and blade profiles designed by Siemens; an *increased reaction stage*, similar to the baseline but with the blade profile modified to increase the degree of reaction; and a stage adopting a *chute seal, twisted blades and stacked vanes*. This final stage is based upon vane, blade and seal geometries scaled from the experimental facility at KTH Royal Institute of Technology (Dahlqvist and Fridh (2017)). Table 3 outlines significant parameters for each of the three configurations. This includes the velocity triangle parameters depicted in Figure 34.

Across the turbine configurations adopted, *double radial overlap* seals were studied in wheel-spaces upstream and downstream of a rotor and a *chute* seal was studied in an upstream wheel-space only. Silhouettes of the wheel-spaces are depicted in Figure 35, with the labelled dimensions detailed in Table 4. Duplicate dimensions across the similar upstream and downstream wheel-spaces have been omitted.

The experimental facility modelled during this study is outlined in Section 3.1 while details of the computational setup are outlined in Sections 3.2-3.5.

Parameter	Baseline Stage	Increased Reaction Stage	Chute Seal, Twisted Blade, Stacked Vanes
Vane/Blade/Vane Count	32/48/32*	32/48/32	48/60/0
Wheel-Spaces Studied	Upstream	Upstream and Downstream	Upstream
RPM	4000	4000	5181
Rotational Reynolds Number, Re_ϕ	1.0×10^6	1.0×10^6	1.3×10^6
Axial Reynolds Number, Re_w	4.0×10^5	4.0×10^5	4.6×10^5
Flow Coefficient, C_F	0.41	0.41	0.35
Vane Exit Mach Number, M	0.44	0.44	0.5
Reaction, Λ	0.14	0.27	0.17
Blade Loading Coefficient, ψ	3.1	3.7	2.8
Non-Dimensional Sealing Parameter, Φ_0	$0 \rightarrow 0.1$	$0 \rightarrow 0.1$	$0 \rightarrow 0.1$
Turbulent Flow Parameter, λ_T	$0 \rightarrow 0.11$	$0 \rightarrow 0.11$	$0 \rightarrow 0.11$
Vane 1 Inlet Angle, α_1 (˚)	0	0	0
Vane 1 Exit Angle, α_2 (˚)	76	76	77
Blade Inlet Angle, β_2 (˚)	56	56	56
Blade Exit Angle, β_3 (˚)	63	68	55
Vane 2 Inlet Angle, α_3 (˚)	-10	21	-25
Vane 2 Exit Angle, α_4 (˚)	N/A	52	N/A
Blade Velocity, Ωr (*m/s*)	87	87	113
Vane 1 Inlet Axial Velocity, W_1 (*m/s*)	30	30	33
Vane 1 Exit Axial Velocity, W_2 (*m/s*)	36	36	38
Vane 1 Exit Velocity, C_2 (*m/s*)	145	147	174
Blade Inlet Velocity, V_2 (*m/s*)	64	66	69
Blade Exit Axial Velocity, W_3 (*m/s*)	41	42	59
Blade Exit Velocity, V_3 (*m/s*)	90	111	104
Vane 2 Inlet Velocity, C_3 (*m/s*)	41	45	65
Vane 2 Exit Axial Velocity, W_4 (*m/s*)	N/A	38	N/A
Vane 2 Exit Velocity, C_4 (*m/s*)	N/A	62	N/A

Table 3: Turbine parameters for each of the main configurations studied, velocity triangle parameters given at mid-span (* downstream vane row not modelled)

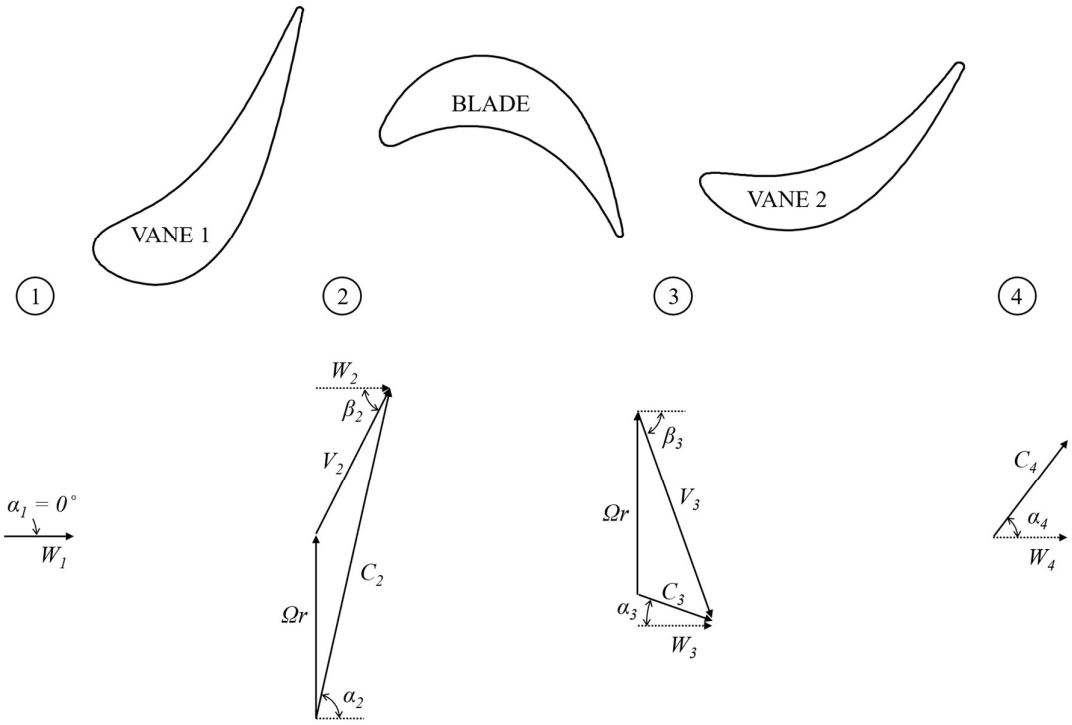

Figure 34: Velocity triangles

Geometric Parameter	Dimension	Geometric Parameter	Dimension
b	190.00 mm	r_1	122.00 mm
h_a	25.00 mm	r_2	116.81 mm
h_{seal}	5.00 mm	r_3	118.70 mm
h_{buffer}	16.50 mm	r_4	106.8 mm
h_{chute}	0.88 mm	r_5	101.61 mm
S	20.00 mm	r_6	96.29 mm
S_{buffer}	11.00 mm	r_{in}	53.50 mm
S_{chute}	15.20 mm	l_1	54.90 mm
$s_{c,ax}$, $s_{c,in}$	2.00 mm	l_2	99.99 mm
$s_{c,rad}$	1.28 mm	l_3	76.90 mm
$s_{c,chute}$	2.11 mm	l_4	90.00 mm
$s_{overlap}$	1.86 mm	θ_{chute}	70°
r_{chute}	6.59 mm		

Table 4: Wheel-space dimensions

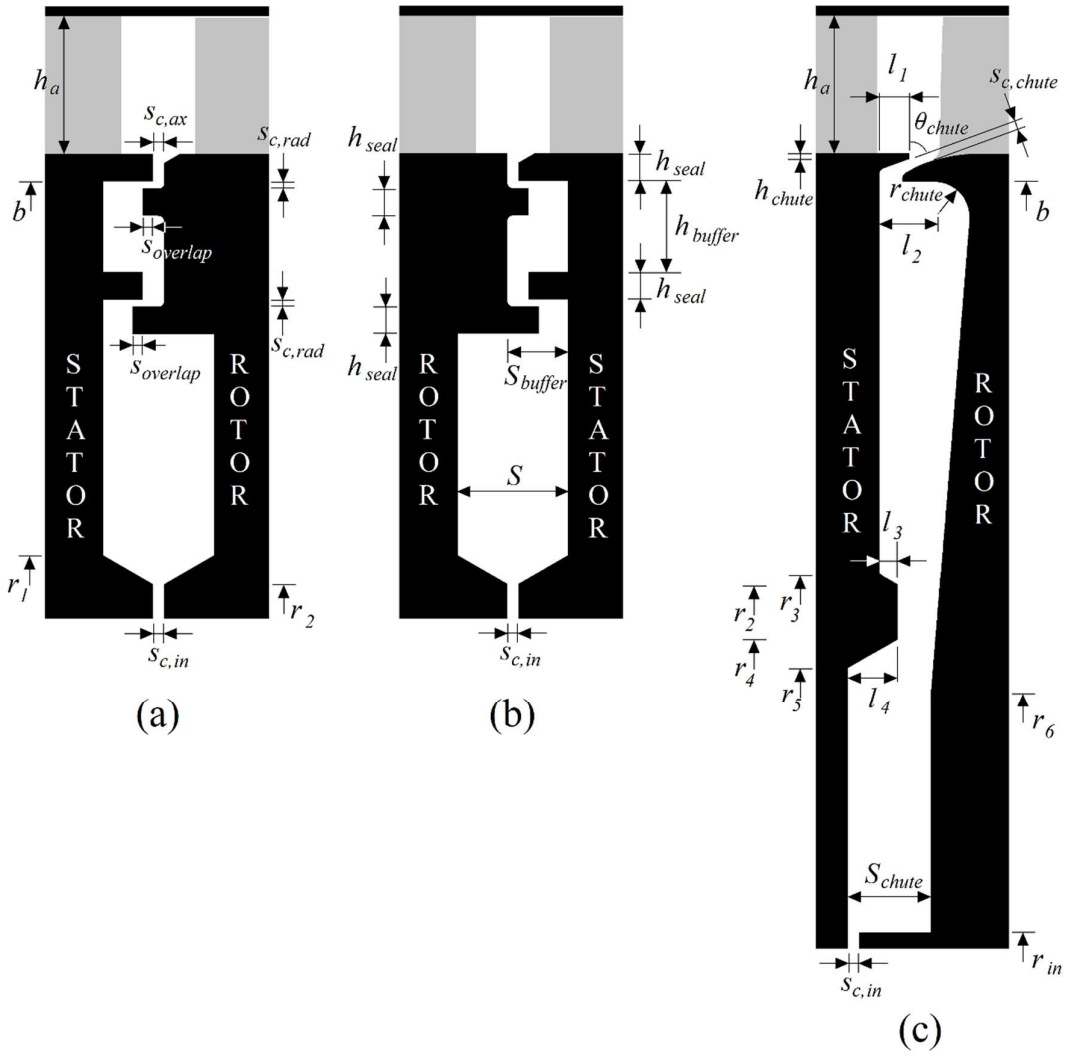

Figure 35: Cavity geometries: (a) upstream and (b) downstream wheel-spaces with double radial-clearance seals, (c) upstream wheel-space with chute seal

3.1 Bath 1.5-Stage Experimental Rig

A brief overview of the experimental facility is given here; full details of the rig design and capabilities have been presented by Patinios *et al.* (2016) and Scobie *et al.* (2018).

The experimental facility was specifically designed to study ingress into the wheel-space cavities of an axial turbine. Incorporating a wide-range of instrumentation and designed in a modular fashion, the rig offers an expedient and inexpensive means of evaluating a range of advanced rim seal concepts. The facility operates at fluid-dynamically scaled conditions at relatively low Reynolds numbers. Experiments match engine-representative values of the turbulent flow parameter (λ_T) and sealing flow parameter (Φ_0) which govern the wheel-space flow structure and levels of ingress respectively (Owen and Rogers (1989)).

Flexibility of the seal, vane and blade geometries is an important feature of the facility. The turbine geometries were designed by Siemens, replicating operational engines, albeit with simplified prismatic blading for the baseline and increased reaction turbines. The diameter of the disc to the underside of the rim seal shroud is 380 mm and the height of the annulus is 25 mm. The rig exhausts to atmospheric pressure.

A cutaway view of the rig test section, revealing the location of the key measurement instrumentation in the upstream wheel-space, is shown in Figure 36. Similar instrumentation was located in the downstream wheel-space when investigating the increased reaction stage. Taps on the annulus hub allowed measurement of a circumferential distribution of static pressure downstream of the first vane row and upstream of the second vane row. The radial distributions of static and total pressure in the wheel-spaces were acquired using taps on the stator wall and probes in the core; this enabled measurements of the radial distribution of swirl. The taps and probes also provided measurements of concentration-based sealing effectiveness by seeding the purge flow with 1% CO_2.

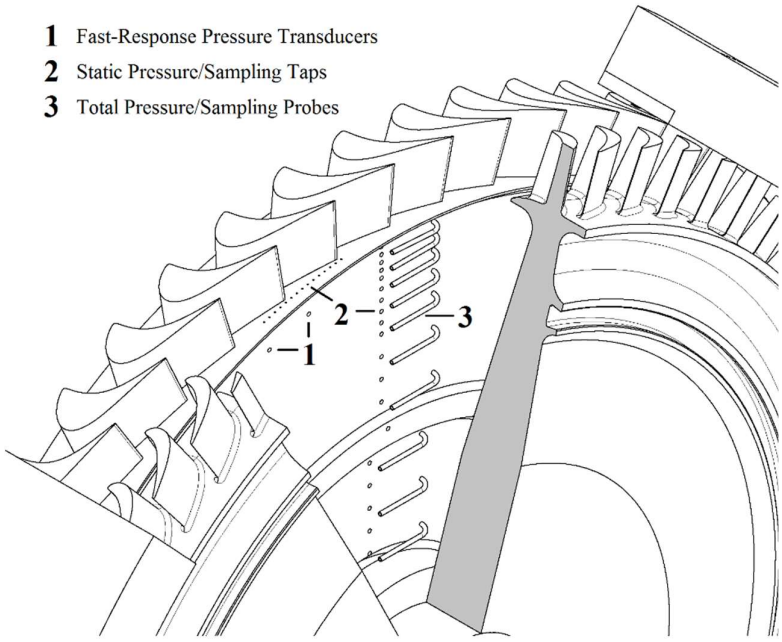

Figure 36: Experimental test section and instrumentation

A pair of Kulite XCS-062 pressure transducers were used to measure unsteady pressure fluctuations in the outer wheel-space. By circumferentially offsetting these and performing phase analysis of the signals, the rotational speed of any large-scale structures could be calculated. The transducers were sampled at 100 kHz, and a 50 kHz low-pass filter was fitted upstream of the data-acquisition system to prevent aliasing. The transducer had a manufacturer-quoted resonant

frequency of 150 kHz, which was significantly higher than the 5.2 kHz BPF at the highest rotational Reynolds number tested.

For the baseline stage only, concentration measurements were also collected along a radial traverse of the mainstream annulus and into the rim seal region. The probe was a simple, miniature, stainless-steel hypodermic tube of 1.0 mm outer diameter. A larger hypodermic tube (1.7 mm diameter) was used by Scobie *et al.* (2018) to demonstrate the probe and gas-extraction rate did not influence the data collected.

3.2 Boundary Conditions and Computed Domains

3.2.1 Baseline Configuration

The computed domain and boundary conditions for the baseline case are shown in Figure 37. A single vane and blade sector is presented, however these were duplicated to form a two vane, three blade 22.5° sector for URANS computations. A sliding non-matching grid interface was defined between the stationary and rotating domains, allowing unsteady coupling of field variables in two dimensions. This stator-rotor interface was placed 1 mm (= s_c/2) upstream of the seal. This avoided locating the interface in the highly unstable region immediately downstream of the seal and left the wheel-space in the rotating domain. A non-matching grid interface was used in the tip-clearance to improve cell quality through the rotor passage. Sealant flow enters at low radius before entering the main wheel-space. Mass flow, total temperature, turbulence intensity, turbulent-length scale and flow angles were specified at this inlet. Inlet swirl was estimated as 0.5, although an extended narrow section was modelled to allow Couette flow to develop properly before entering the main wheel-space. The same parameters were defined at the stage inlet, with total pressure specified rather than mass flow rate. Static pressure was specified at stage exit. Both stage inlet and stage exit used non-reflecting boundary conditions and all walls were assumed adiabatic.

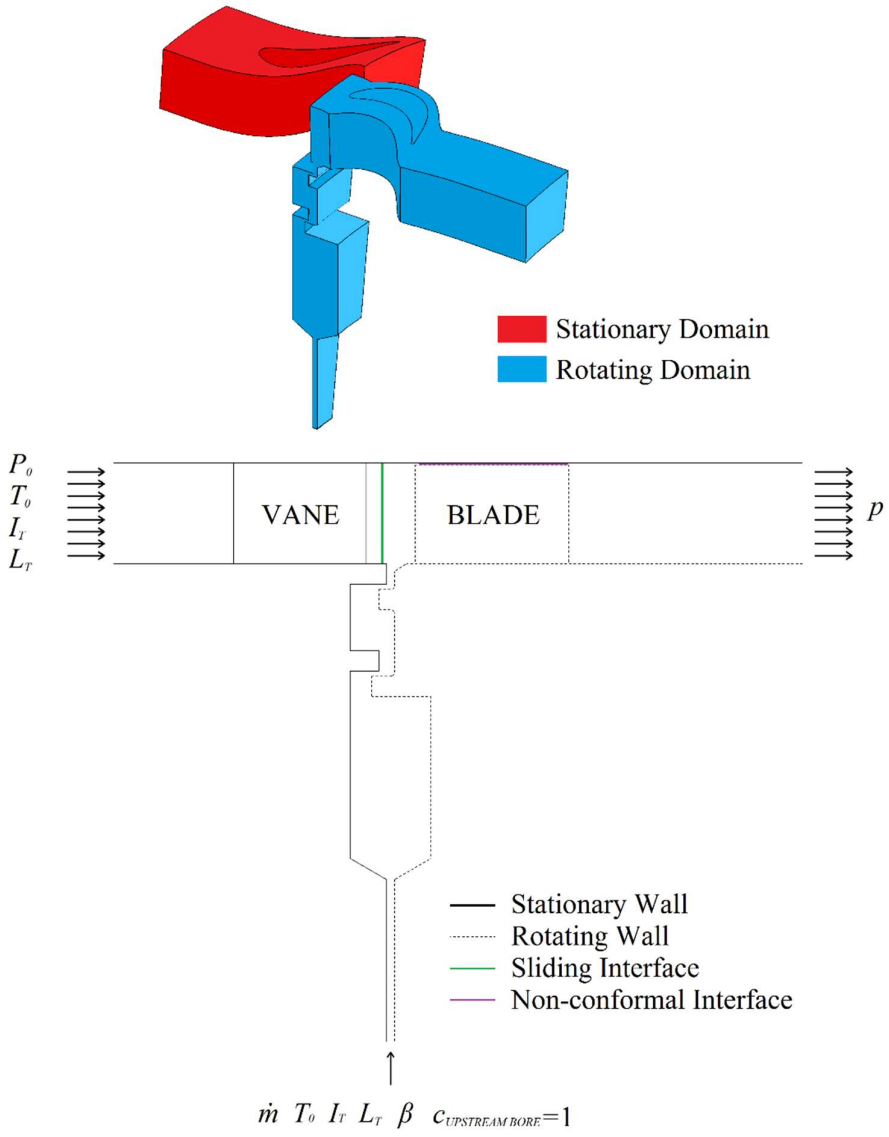

Figure 37: Computed domains and boundary conditions for the baseline stage

Two validation studies were undertaken to confirm the length of annulus and wheel-space inlets were sufficient not to significantly influence the flow in regions of critical interest. The numerical settings and meshes used for these preliminary studies were consistent with those outlined in Section 3.3 and 3.5.

To investigate the influence of the purge inlet, two wheel-space domains were computed using the steady RANS solver in TRACE. The first used the proposed extended inner seal configuration, while the second included a lower wheel-space cavity that was an accurate geometric representation of the experimental rig, but comes at increased computational cost. Both simulations were run at $Re_\phi = 1\times10^6$, with $\lambda_T = 0.052$. Profiles of axial, radial and tangential velocity at a common radius of $r/b = 0.668$ are depicted in Figure 38 (a), (b) and (c) respectively.

Velocities are circumferentially averaged and normalised against Ωr. The data can be seen to collapse between the two computations, indicating that simplifying the purge inlet does not significantly affect the flow in the upper cavity.

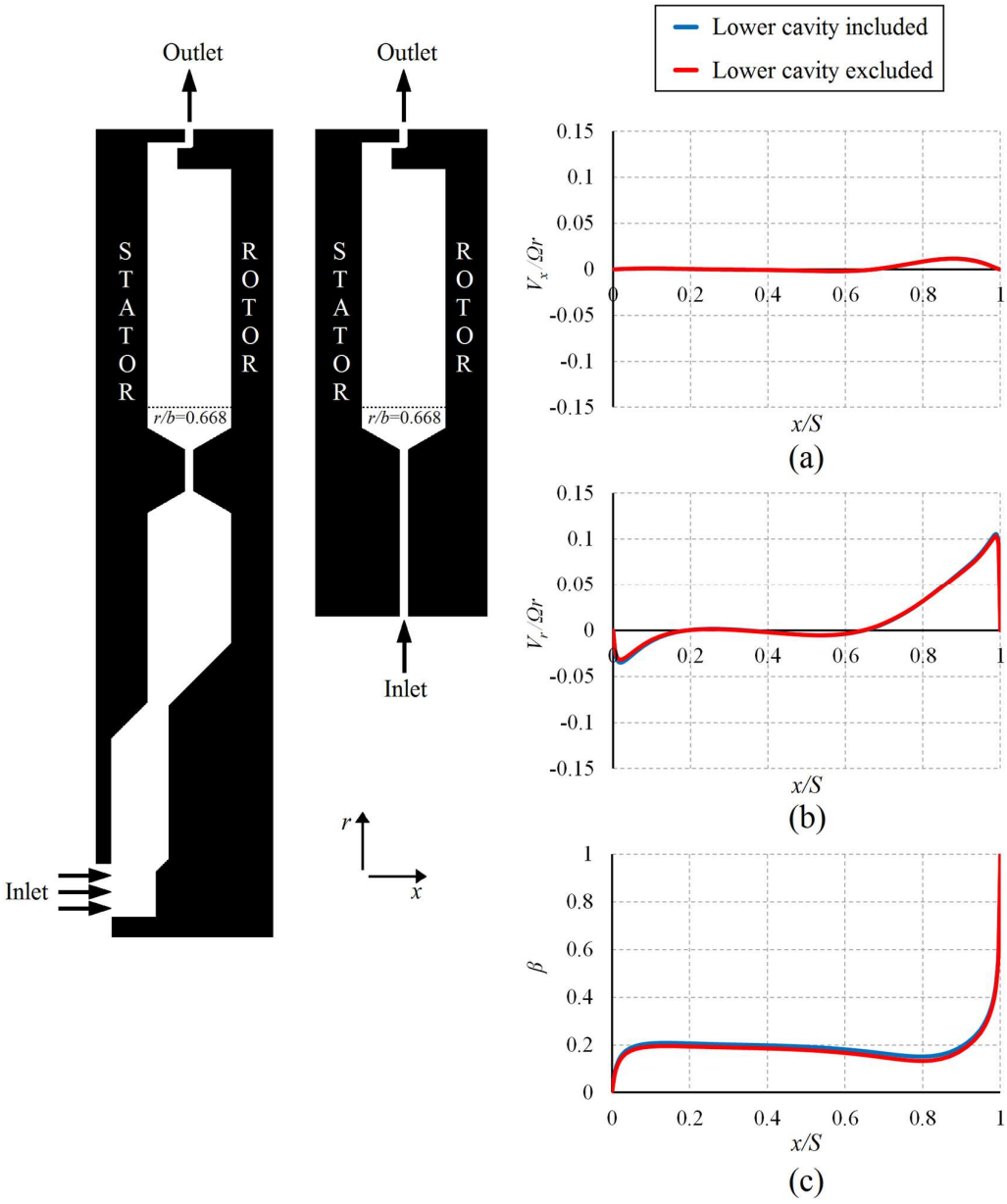

Figure 38: Profiles of axial (a), radial (b) and tangential (c) velocity at a non-dimensional radius of r/b=0.668 for two wheel-space configurations (Re_ϕ =1×10^6, λ_T=0.052)

The influence of annulus inlet length was studied by comparing two steady state *mixing plane* computations of the mainstream flow. The models extended upstream of the vane by one and eight times the axial chord respectively. The longer inlet required an additional non-conformal grid interface to allow for a transition from pipe flow to annular flow that occurs in the

experimental rig. The two domains are depicted in Figure 39 (a) and (b). Computations were carried out at $Re_\phi = 1\times10^6$ with $C_F = 0.41$. Figure 39 (c) shows the circumferential variation in pressure on the hub, 3.5mm downstream of the vane. The inscribed silhouette shows this position, with flow from left to right. The non-dimensional pressure coefficient is defined in the nomenclature and the data is presented over a single vane passage. Data from the two computations are in close agreement, showing the pressure field in this critical location is insensitive to the two inlet configurations. Similar agreement was found in other locations downstream of the vane and the shorter inlet was therefore deemed adequate for more complex unsteady computations including a wheel-space.

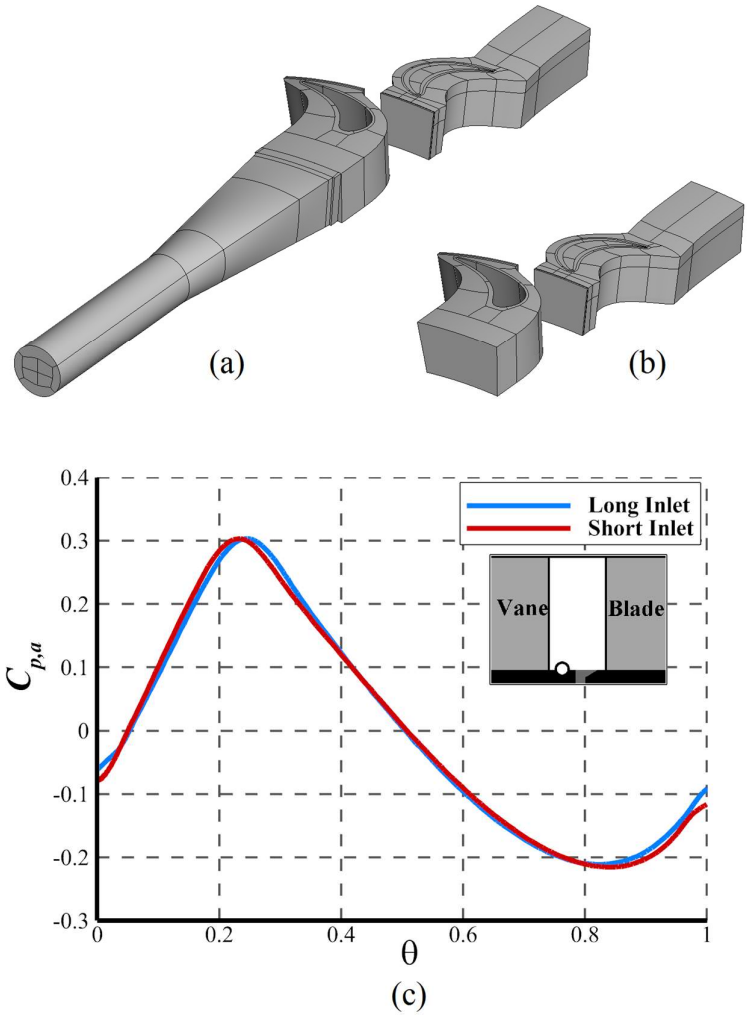

Figure 39: Comparison of inlet lengths: computed domains of the long inlet model (a) and short inlet model (b), alongside circumferential distributions of pressure coefficient downstream of the vane (c) ($Re_\phi = 1\times10^6$, C_F=0.41)

3.2.2 Additional Configurations

Once the baseline configuration was established, further changes to boundary conditions and computational domains were required for additional configurations: a bladeless version of the baseline stage; an increased reaction stage; an increased reaction stage incorporating high radius purge; and a stage incorporating a chute seal, twisted blades and stacked vanes. The boundary conditions for each of these cases are similar to the baseline configuration, however the differences are discussed here.

The computed domain and boundary conditions for the bladeless case are shown Figure 40. With the absence of the blade, all geometry (including the wheel-space) was contained within a single stationary domain, this also removes both non-conformal grid interfaces that were present in the baseline stage. Despite the 11.25° periodicity depicted, URANS computations were computed with a 22.5° sector so as to allow fair comparison with similarly sized bladed cases.

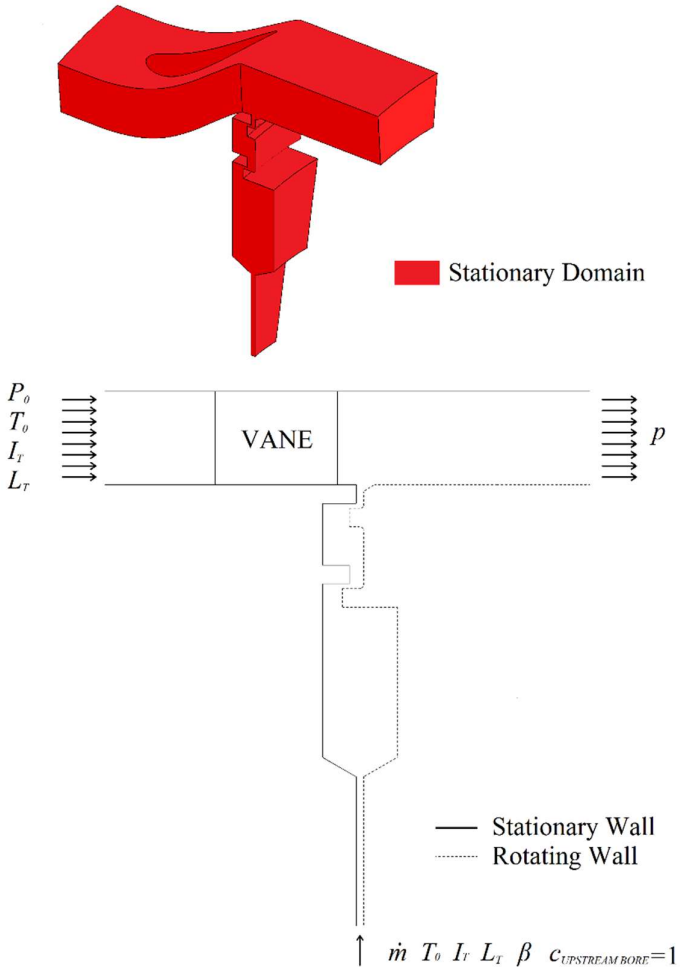

Figure 40: Computed domain and boundary conditions for the bladeless baseline stage

The increased reaction stage incorporated a further wheel-space and vane downstream of the rotor. This results in an additional non-conformal rotor-stator interface, which was placed 1 mm upstream of the downstream rim seal. Unlike the upstream wheel-space, the downstream wheel-space was located in a stationary frame of reference. Purge again entered through an extended inner seal geometry similar to that of the upstream wheel-space and similar inlet parameters were defined. The boundary conditions and the computed domains are shown in Figure 41, although the 22.5° sector used for URANS computations contained two upstream vanes, three blades and two downstream vanes.

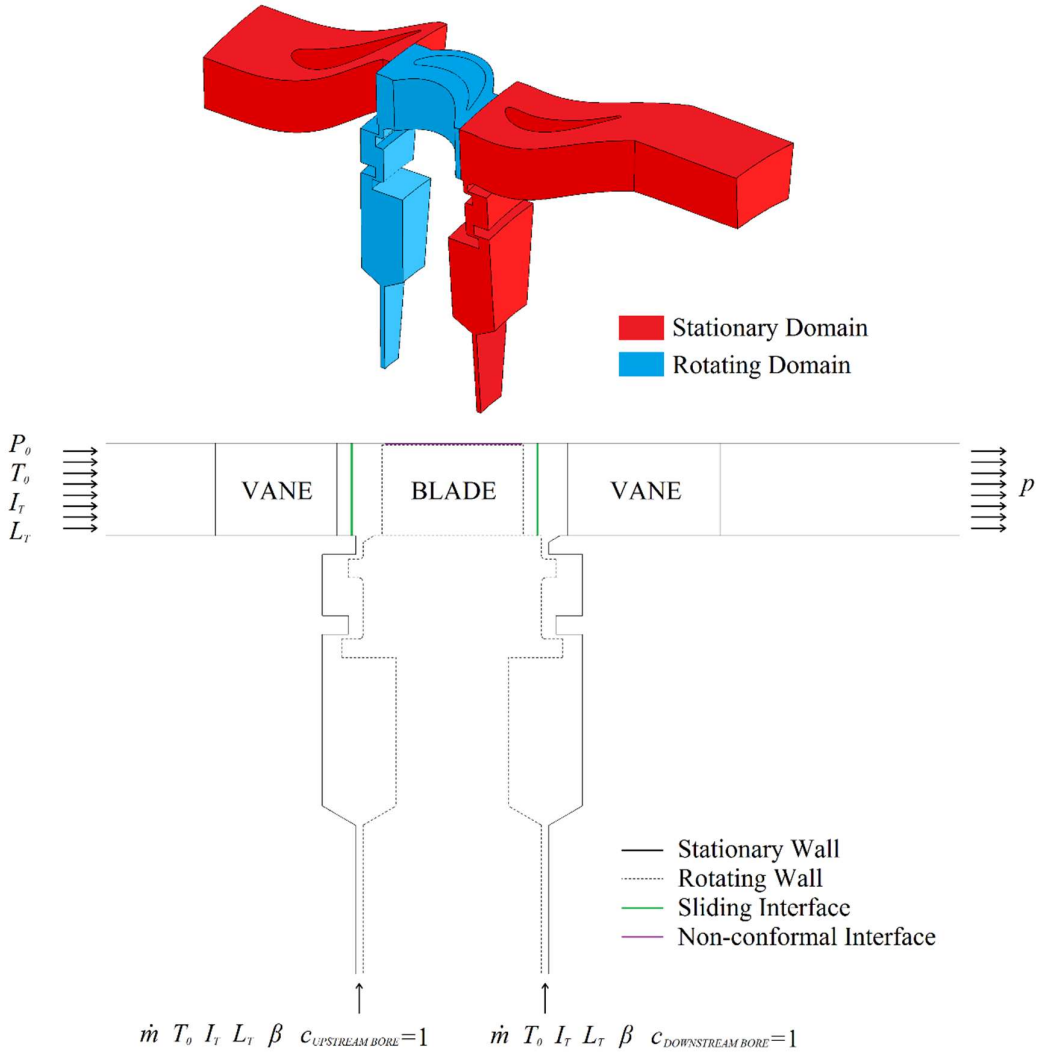

Figure 41: Computed domains and boundary conditions for the increased reaction stage

Several changes to the setup depicted in Figure 41 were required to model high radius purge injection in the upstream and downstream wheel-space of the increased reaction stage. The modified cavities included 32 and 16 circumferentially distributed pipes in the upstream and downstream stator walls respectively. A 22.5° sector is depicted in Figure 42, reflecting the

periodicity of the modified downstream wheel-space. An additional sliding rotor-stator interface, located at the inner radial seal was necessary to place the upstream high radius inlet pipes in a stationary reference frame. Steady simulations of a simple wheel-space, with and without this interface, showed no discernible difference in the computed flow fields. Due to solver constraints, further non-conformal interfaces were also required in each of the inlet pipes, as discussed in Section 3.5.2.

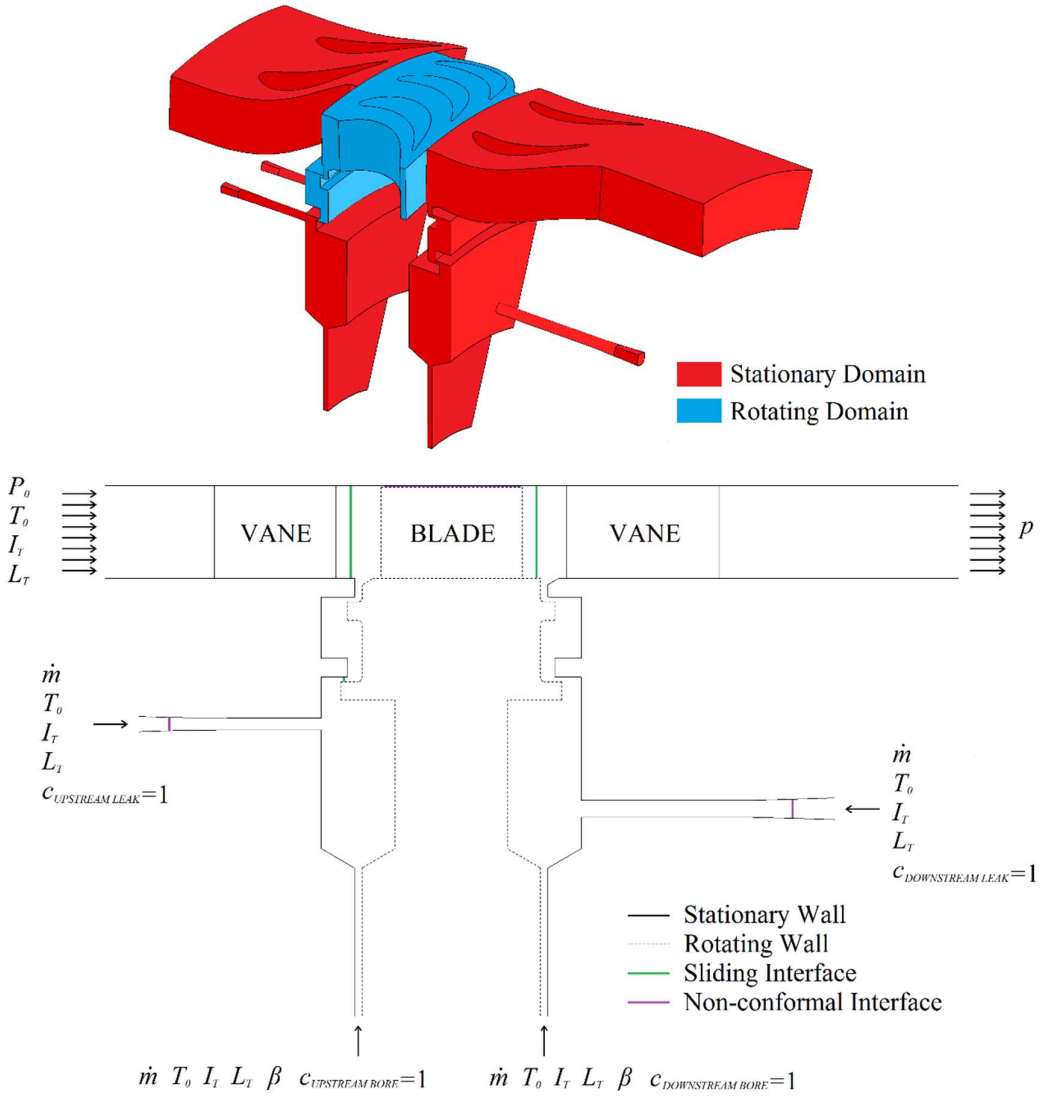

Figure 42: Computed domains and boundary conditions for the increased reaction stage with high radius purge

Figure 43 shows the boundary conditions and computational domains for a stage featuring a chute seal, twisted blades and stacked vanes. The setup is similar to that of the baseline case, however numerous sector sizes were computed, as detailed in Chapter 7.

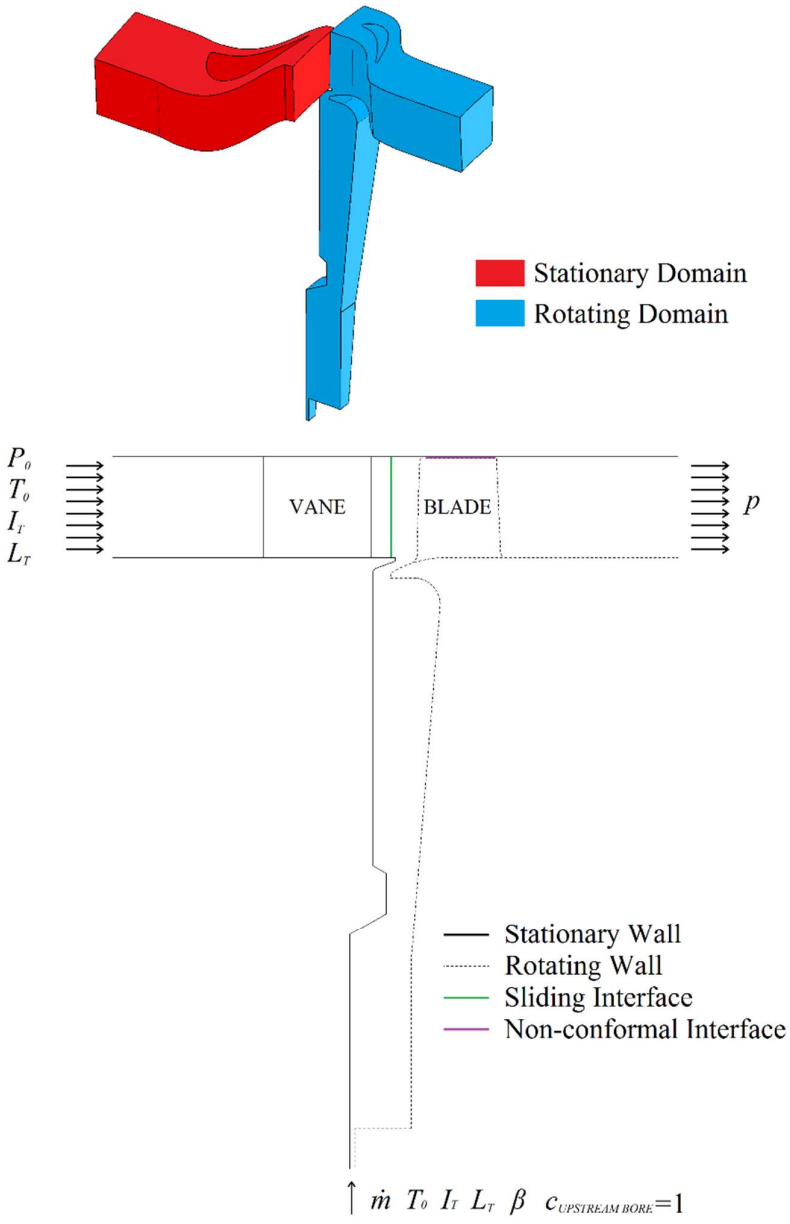

Figure 43: Computed domains and boundary conditions for the stage incorporating a chute seal, twisted blades and stacked vanes

3.3 Numerical Approach

The compressible Reynolds-averaged Navier-Stokes (RANS) solver used a finite-volume approach, with the second-order Fromm and Euler backward schemes chosen for spatial and temporal discretization respectively.

A Courant Friedrich Levy (CFL) number of 100 for used for steady and unsteady RANS computations, however for reasons of stability, harmonic balance computations required reduced

values of 10. The dual time-stepping scheme used for URANS simulations, employed 3840 timesteps per revolution with 20 sub-iterations per timestep. These numbers were deemed appropriate following a timestep sensitivity study which compared the unsteady results from URANS simulations with 1536, 2304, 3072, 3840 and 4608 timesteps per revolution. The study was undertaken for the baseline geometry, with monitor data extracted in the annulus, rim seal and upstream wheel-space. Large differences in the amplitudes of unsteady pressure and velocity fields were observed with fewer than 3840 timesteps per revolution, however the unsteady features were judged to be invariant to further increasing the timesteps per revolution from 3840 to 4608.

Dynamic viscosity, μ, was computed using Sutherland's law:

$$\mu = \mu_{ref} \frac{T_{ref}+S'}{T+S'} \left(\frac{T}{T_{ref}} \right)^{3/2} \qquad \textbf{3.1}$$

where μ_{ref}, T_{ref} are references for viscosity and temperature which used values of 1.72×10^{-5} kg/ms and 273 K, respectively. S' is the Sutherland constant, for which a value of 110 K was used.

Transport equations for a passive scalar (analogous to the CO_2 in the experiments) were computed for each sealing flow. For cases with multiple purge flows, the use of separate passive scalars allowed the ratio of different sealing flows to be calculated at any location.

TRACE supports several RANS turbulence models, including formulations of the k-ω model detailed by Wilcox (1988) and the SST k-ω model by Menter *et al.* (2003). Both are fundamentally two-equation models that use the Boussinesq hypothesis to relate the Reynolds stresses to an eddy viscosity term. However in Wilcox's model, the specific turbulent dissipation rate tends to zero in the freestream, and the solution is highly sensitive to the small non-zero values that are used. The SST k-ω model addresses this issue by using a blending function to transition to a less sensitive k-ε formulation with increasing distance from the wall. TRACE also supports the SSG/LRR Full Reynolds Stress Model (RSM), which unlike two equation models, can account for the anisotropic nature of turbulence (Eisfeld (2004)). This is achieved by modelling each of the six Reynolds stress terms separately, along with a seventh transport equation for the specific turbulent dissipation rate.

The potentially improved prediction of turbulence from an RSM model over a two-equation model is countered by the increased computational cost from the additional transport equations. Therefore, a sensitivity study was conducted to ascertain the importance of this higher order modelling approach. Similar computations using the RSM and SST k-ω were conducted, with the latter also employing the Kato-Launder modification to limit the production of turbulent kinetic energy (Kozulovic *et al.* (2004)). The study used the baseline stage, however computations were

undertaken early in the work programme and differences in flow conditions and geometry exist when compared to simulations presented elsewhere in this thesis: a single radial overlap seal geometry was used (see silhouettes in Figure 44) and the simulations were run at $Re_\phi \sim 7.2\times10^5$, $C_F \sim 0.39$ and $\Phi_0 \sim 0.016$. The URANS computations were also undertaken using a grid with $y^+ \approx 1$ at all solid boundaries, as TRACE's RSM solver does not permit the use of wall-functions.

Figure 44 shows direct comparisons of time-averaged results using the RSM model (red lines) and SST k-ω model (blue lines): (a) and (b) present profiles of circumferential and radial pressure in the annulus and wheel-space respectively, while Figure 44 (c) depicts wheel-space swirl; precise locations are indicated in the adjacent silhouettes. All profiles indicate negligible differences between results from the two turbulence models. However, the solutions did not reach convergence of the passive scalar, due to the prohibitively large computational effort required. Therefore, it was not possible to compare ingress levels. This problem was not apparent for the double radial overlap seal, which was adopted for subsequent computations of the baseline stage.

Figure 45 shows unsteady pressure for both the RSM model (a) and the SST k-ω model (b) at three monitor locations close to the rim seal. The 10,000 timesteps represent the final 2.6 revolutions of each simulation; data was recorded in the rotating reference frame. The dominant periodic behaviour is a result of large-scale unsteady structures within the seal. Slight differences are seen in the magnitude and frequency of the structures observed between the two turbulence models. However, the plots still give reasonable confidence that despite the inability to perform direct comparisons of scalar concentration, ingress levels are unlikely to be significantly influenced by the turbulence model.

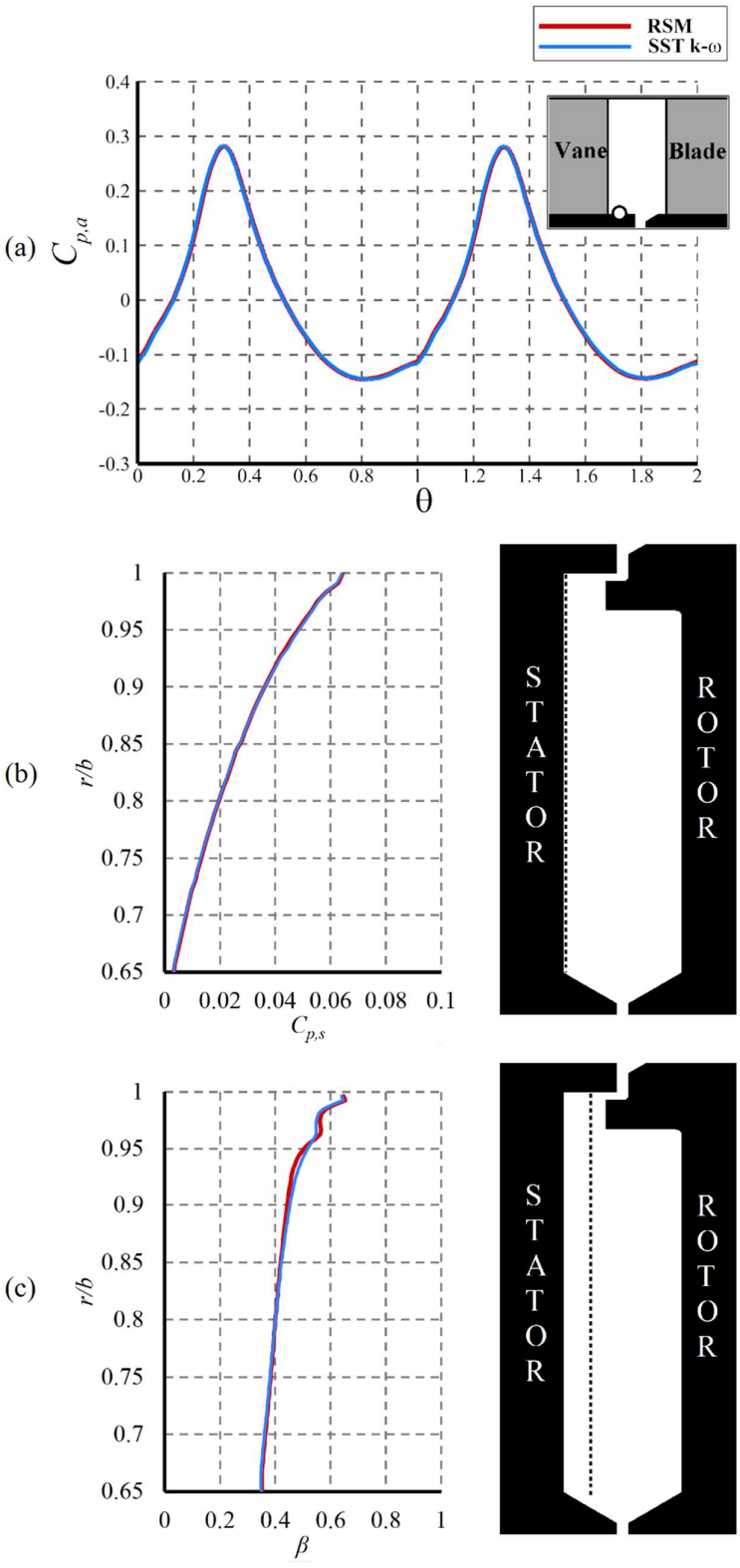

Figure 44: Comparisons of time-averaged results using a Full Reynolds Stress Turbulence model and the Shear Stress Transport *k-ω* turbulence model: (a) circumferential distribution of time-averaged annulus pressure, (b) radial distribution of stator wall pressure coefficient, (c) radial distribution of wheel-space swirl. ($Re_\phi = 7.2 \times 10^5$)

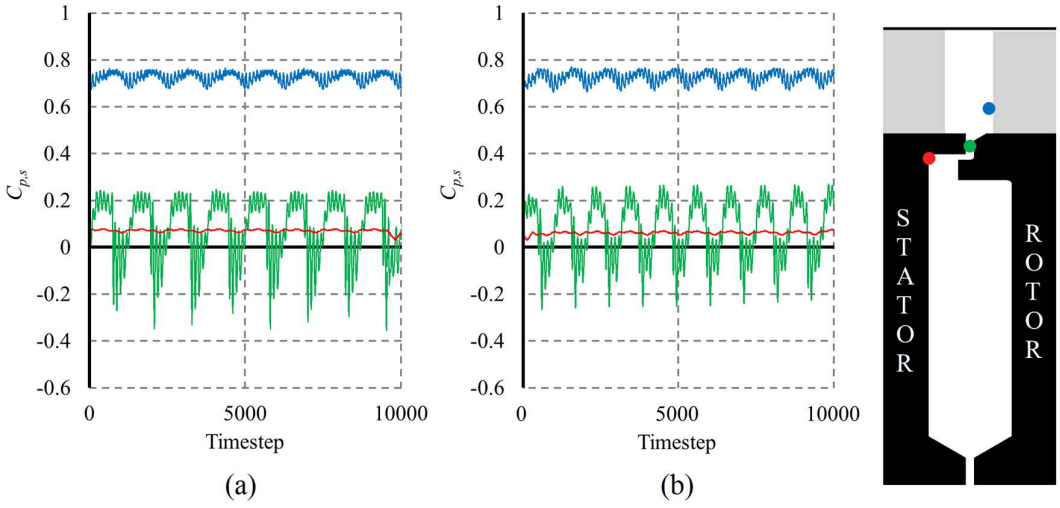

Figure 45: Unsteady pressure coefficient at three locations for computations using (a) a Full Reynolds Stress Turbulence model and (b) the Shear Stress Transport *k-ω* turbulence model. ($Re_\phi = 7.2 \times 10^5$)

Numerous frequency spectra are presented in each of the results chapters of this thesis, the majority of which are used to analyse the unsteady pressure. To generate these spectra for CFD results, data was extracted over the final computed revolution of the disc. For locations in the stationary domains this was achieved by simply inserting monitor points at the locations of interest prior to running the simulation. However, locations in the rotating domain required post-processing to extract data in a stationary frame of reference. This was performed using 240 equally spaced timesteps over the final computed revolution of the disc, for which each timestep was rotated to its time-resolved physical position and duplicated over 360 degrees (using the TRACE post-processing tool POST). This modified data set was then imported into Tecplot 360 EX 2015 where time-resolved data was extracted at locations defined in the stationary frame of reference. Once the raw unsteady data had been extracted, the spectra could then be generated using the FFT function available in Matlab. This function performs a direct Fourier transform of a signal of specified length and was implemented directly on the 240 data points without averaging. From the output of this function the two-sided and single-sided spectrum can be computed. Similar spectra were also generated using data measured directly from the experimental rig. This data was sampled at 100 kHz over 10 seconds using the Kulite XCS-062 fast response pressure transducers, it was processed using the same FFT function as the CFD data, again without any prior averaging.

3.4 Initialisation and Convergence

Steady mixing-plane solutions were used to initialise each of the 22.5º and 30º sector unsteady calculations. Once converged these were duplicated and used to initialise the unsteady larger-

sector models. The unsteady models were subsequently computed for a minimum of seven revolutions of the rotor to allow flow changes to develop fully. Larger sector models (such as the 60º, 90º and 360º models with the chute seal geometry, and the 67.5º model for the baseline geometry) were initialised from converged smaller sector models. Average residual levels were $< 10^{-6}$ and maximum residual levels $< 10^{-3}$. All solutions achieved a change in concentration-based sealing effectiveness, ε_c, of less than 0.01 over 20,000 timesteps alongside periodic, unchanging behaviour in other variables. The relatively slow convergence of the passive scalar is a consequence of the large difference in time-scales between annulus and cavity flows, which results in slow convection of the scalar around the wheel-space. This also results in the highest computational costs occurring for the lowest purge flow cases; at $\Phi_0 = 0.05$, the 30º sector with a chute seal required > 30 revolutions. Figure 46 shows the corresponding passive scalar convergence at the four wheel-space locations depicted in the silhouette. In this case the convergence criteria of < 0.01 change in ε_c over 20,000 timesteps was not alone deemed sufficient and additional judgement was used to ensure further computation could not result in a change of ε_c greater than 0.01.

The case depicted in Figure 46 required ≈ 60,000 core hours. For comparison, an additional 10 revolutions computed with the 360º model required ≈ 320,000 core hours. It should be noted that the computational effort did not scale linearly with sector size, however this was chiefly due to parallelizing the larger problems onto 192 cores rather than the 64 used for other cases.

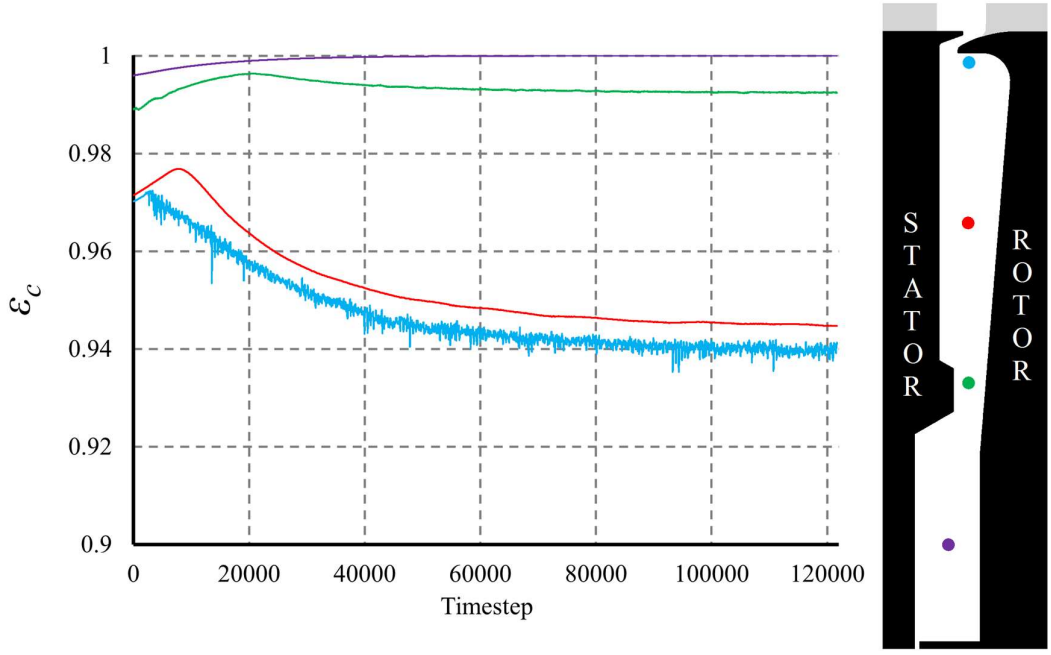

Figure 46: Passive scalar convergence at four wheel-space locations for a 30° sector, with $\Phi_0 = 0.05$ and $Re_\phi = 1.3 \times 10^6$

Further monitor data, depicting the convergence of the passive scalar on the stator wall for all cases using the chute seal geometry is depicted in Figure 47. It can be seen that the 30˚/60˚/360˚ models were initialised from the converged 30˚ sector model.

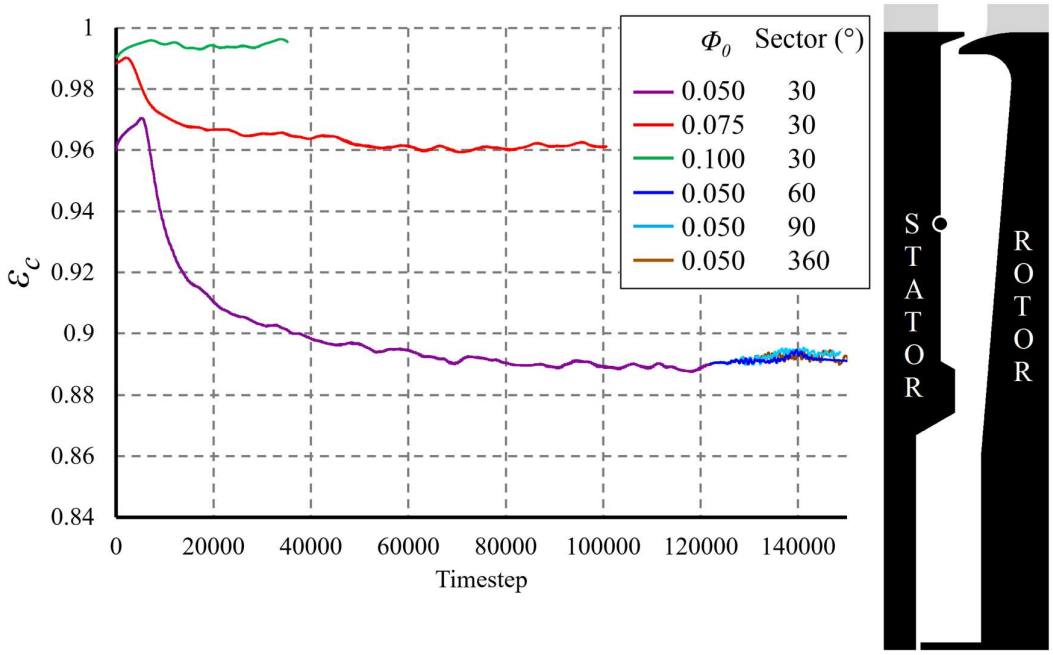

Figure 47: Passive scalar convergence at *r/b* =0.8 on the stator wall for all cases using the chute seal geometry ($Re_\phi = 1.3 \times 10^6$).

3.5 Grid

The structured grids in the present study consisted entirely of hexahedral cells and were developed using a combination of Numeca's Autogrid5 (NUMECA-International (2019a)) and IGG software (NUMECA-International (2019b)). Autogrid5 is a powerful turbomachinery specific meshing tool that was used to generate the main gas path and axisymmetric wheel-space meshes. IGG was later used to add the non-axisymmetric high radius purge inlets and improve cell quality within the cavity. Section 3.5.1 details the meshing of the baseline stage, while Section 3.5.2 outlines the changes required for subsequent grids.

3.5.1 Baseline Configuration

The mainstream grid topologies are shown in Figure 48. Due to the high camber of the aerofoils, the vane and blade outlets, along with blade inlet adopt 'J-grid' topologies, where cell rows aligned with the passage are turned to the azimuthal direction at inlet/outlet. Additional 'O-grids' were used around the vane and blade surfaces. A non-conformal grid interface in the tip clearance of the rotor allowed improved cell quality in the blade passage.

The cavity mesh was created in the meridional plane and revolved to form a matching connection with the rotor domain. The topology is depicted in Figure 49, with the inset views highlighting regions around the seal and purge inlet.

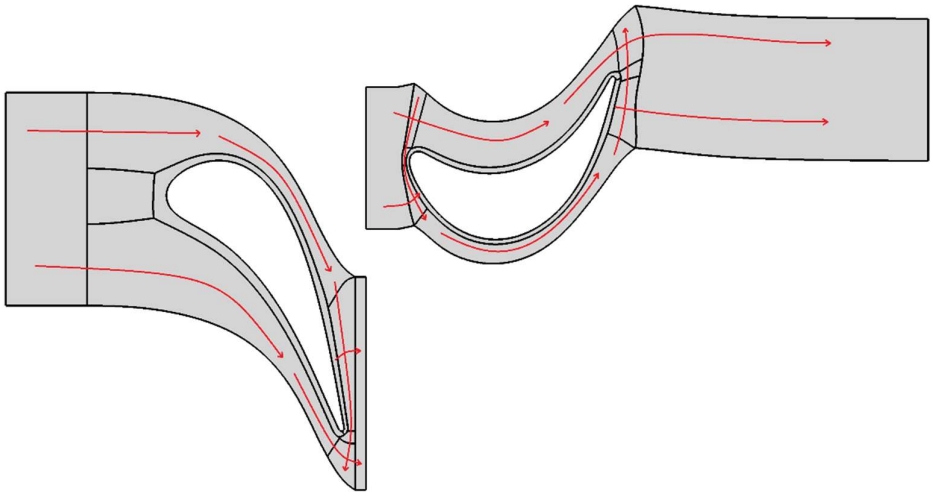

Figure 48: Annulus grid topology for the baseline stage, red arrows indicate the alignment of element rows

A grid independence study was undertaken using three grids based on the same topology. A refinement factor of 1.5 was used in all directions between each grid level. The medium resolution mesh used a near wall $y^+ \approx 1$ within the wheel-space and on the annulus hub, while a larger value of $y^+ \approx 25$, requiring wall functions, was employed on the aerofoil and shroud surfaces. In the radial direction, the vane and blade passages incorporated 49 and 65 nodes respectively, while in the azimuthal direction there are 77 across the outlet of the vane domain and 65 across the outlet of the blade domain. The radial blade tip gap is spanned by 15 nodes, there are 45 across the seal clearance and 68 across the outer part of the wheel-space. Several detailed views of this medium resolution grid are shown in Figure 50. Direct comparisons to other grids in the literature are difficult due to the different flow conditions and geometries tested. However, studies of a similar low Reynolds number facility detailed by Wang *et al.* (2014) and Mirzamoghadam *et al.* (2014) claim grid independence with generally coarser grids. As an example, the ~13° rotor passage reported by these authors used 30 and 33 elements in the radial direction, along with 66 and 26 elements in the azimuthal direction. Wang *et al.* (2014) also used 44 elements across the outer wheel-space, while Mirzamoghadam *et al.* (2014) does not report this parameter.

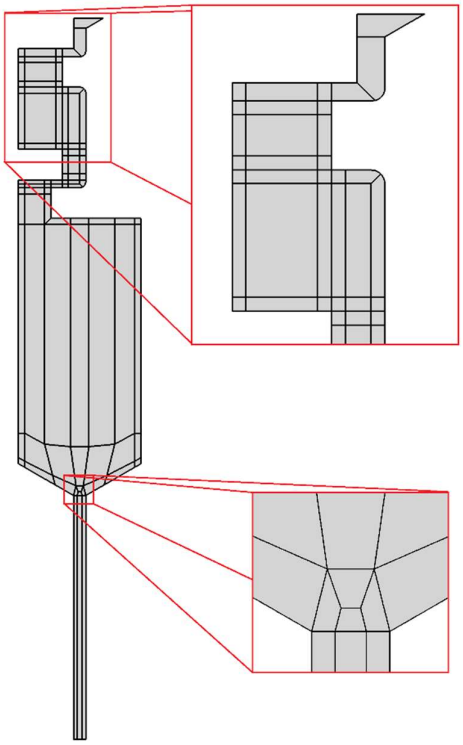

Figure 49: Wheel-space grid topology for the baseline stage

The single passage meshes used for the grid independence study contained 0.50×10^6, 1.84×10^6 and 6.91×10^6 cells. Due to the high cost involved in computing the finest mesh, the study used steady computations, with a mixing-plane between stationary and rotating domains. Computations were run at $Re_\phi = 1 \times 10^6$, with $\lambda_T = 0.030$, typical of the cases explored in this work. Profiles of annulus pressure coefficient, wheel-space pressure coefficient and wheel-space swirl are depicted in Figure 51 (a), (b) and (c) respectively. The circumferential distribution of annulus pressure was recorded 1.5 mm downstream of the vane trailing edge (as depicted in the inscribed silhouette) and good agreement is shown across all grid levels. The wheel-space profiles were circumferentially averaged from the positions shown by the dashed lines in the radially aligned silhouettes. No significant change can be observed between results from the fine and medium resolution grids but the coarse grid shows up to 8% higher swirl and up to 10% higher pressure coefficient. Therefore, the medium resolution mesh was deemed most appropriate for subsequent computations. Once duplicated to form a 22.5° sector the medium resolution mesh contained 5.24×10^6 cells.

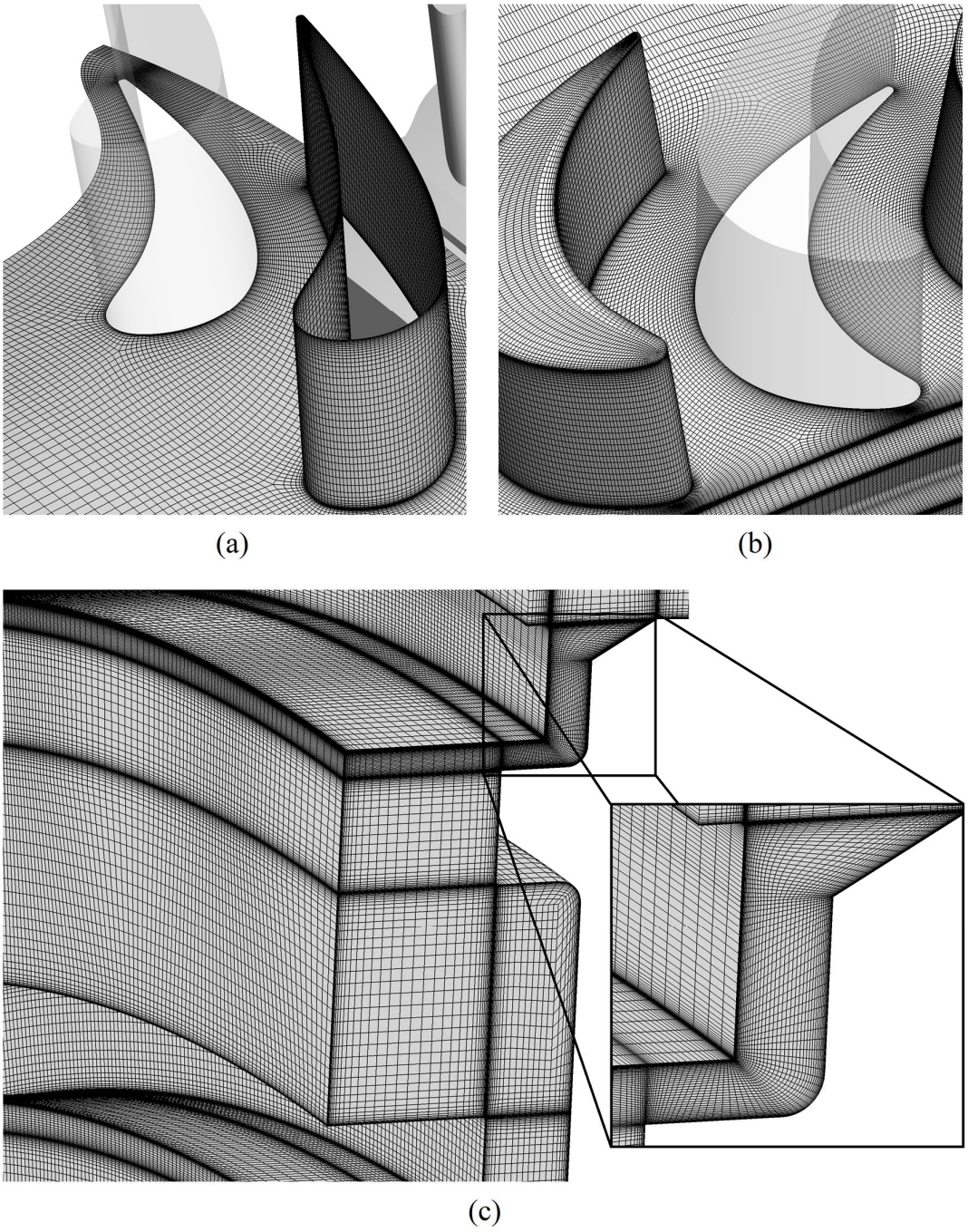

Figure 50: Mesh detail for the baseline stage: (a) vane row, (b) blade row, (c) rim seal

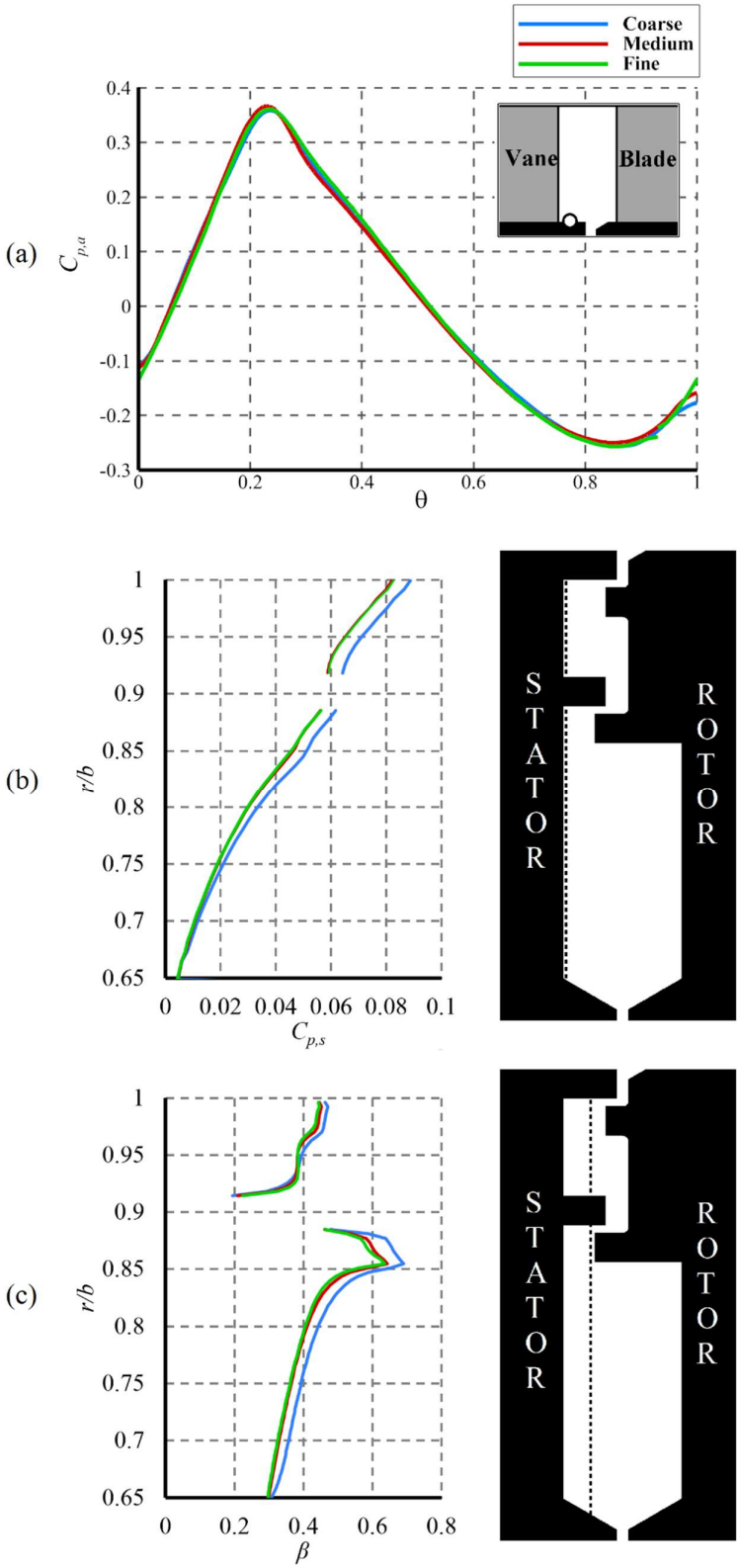

Figure 51: Sensitivity to mesh resolution: (a) circumferential variation of annulus pressure, (b) radial variation of stator wall pressure, (c) radial variation of wheel-space swirl. ($Re_\phi = 1.0 \times 10^6$)

3.5.2 Additional Configurations

The bladeless version of the baseline stage contained a simple arrangement of highly orthogonal cells downstream of the seal, whilst the upstream vane and wheel-space meshes remained unchanged.

The increased reaction stage incorporated an extra downstream vane row; grid detail is shown in Figure 52 and the 'J-grid' topology, similar to that of the upstream vane is apparent. The radial direction was spanned by 48 nodes while there were 66 circumferentially distributed cells at inlet. The downstream wheel-space mesh is a mirror of the upstream. No significant changes were made to either the upstream wheel-space, vane or blade, and the single passage mesh contained 3.36×10^6 cells. A mesh dependency study, similar to that of the baseline stage was undertaken and again profiles swirl and pressure were showed no significant differences between medium and fine meshes. The medium resolution grid was chosen for further computations.

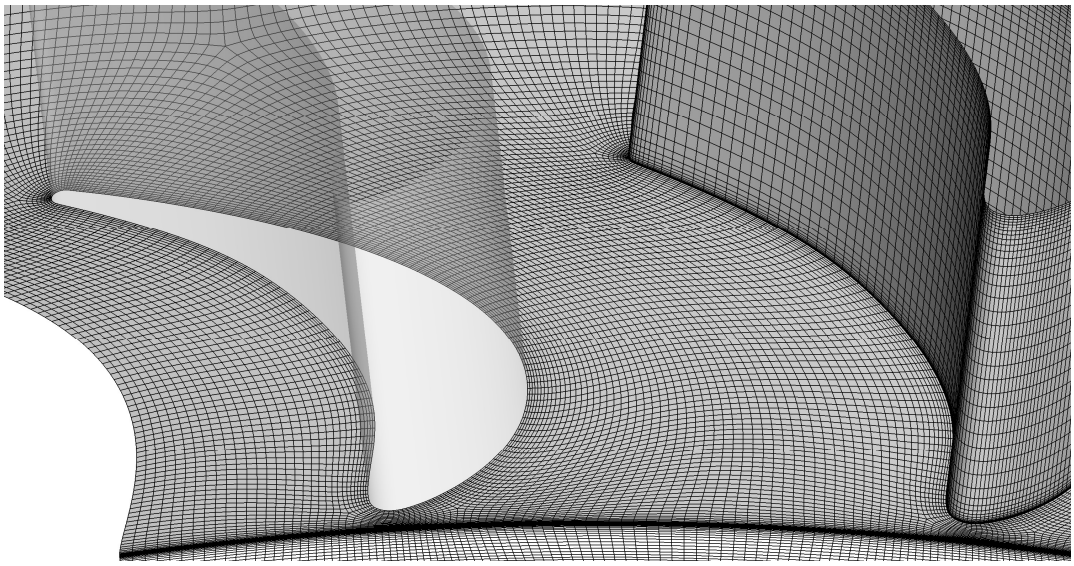

Figure 52: Mesh detail for the downstream vane of the increased reaction turbine

Discrete inlet pipes in both the upstream and downstream cavities required modification of the standard wheel-space meshes; as shown for the upstream and downstream wheel-spaces in Figure 53 (a/b). 'O-grids' were used in each of the circular pipe geometries, with this topology propagating axially across the wheel-space. However, due to restrictions in TRACE, inlet boundary conditions must contain only a single block face. Therefore, the circular cross-section of inlet pipe transitions to a quadrilateral with curvilinear sides at the inlet face. This allows the use of a single hexahedral block at this location which interfaces with the 'O-grid' topology used in the main pipe section further downstream. The length of the circular section of the inlet is 10 D; allowing pipe flow to fully develop before entering the wheel-space.

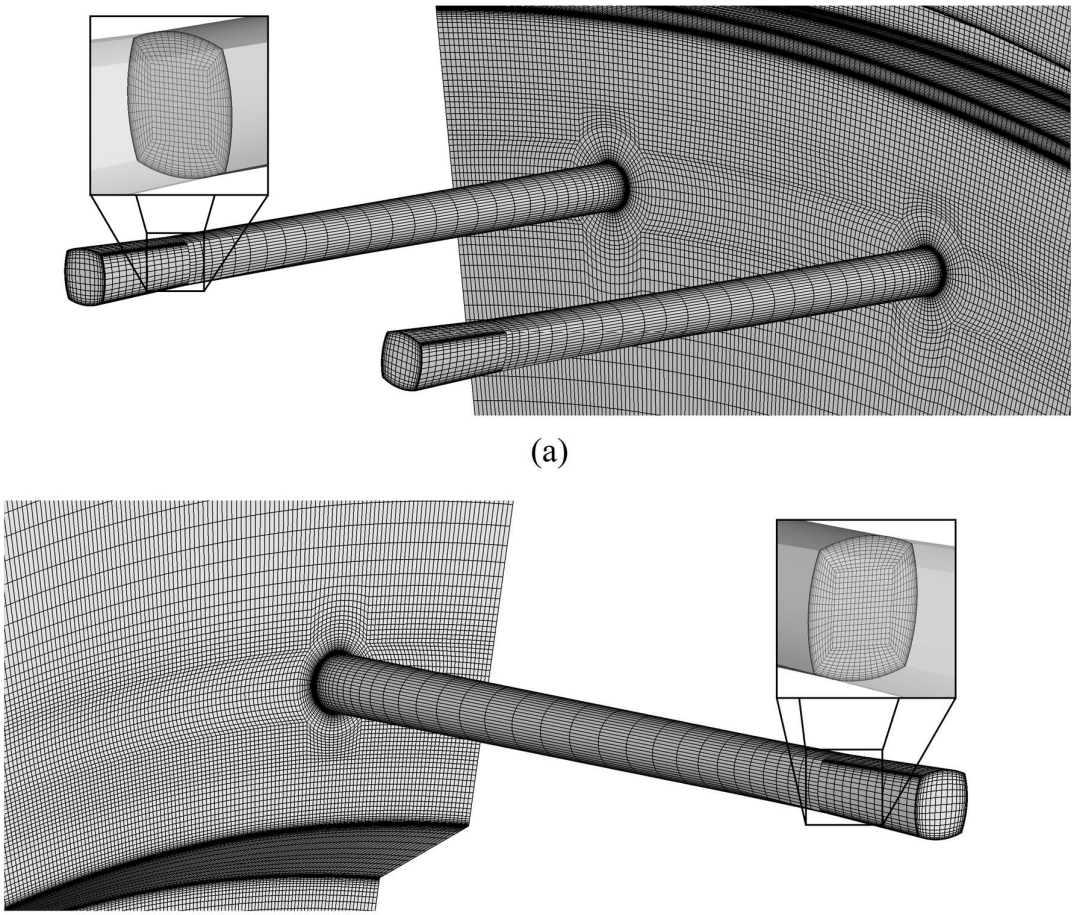

Figure 53: Mesh detail for the high radius inlet pipes: (a) upstream wheel-space, (b) downstream wheel-space

Figure 54 shows mesh detail for the stage featuring a chute seal, twisted blades and stacked vanes. The mesh parameters and cell counts are all based on those of the baseline stage.

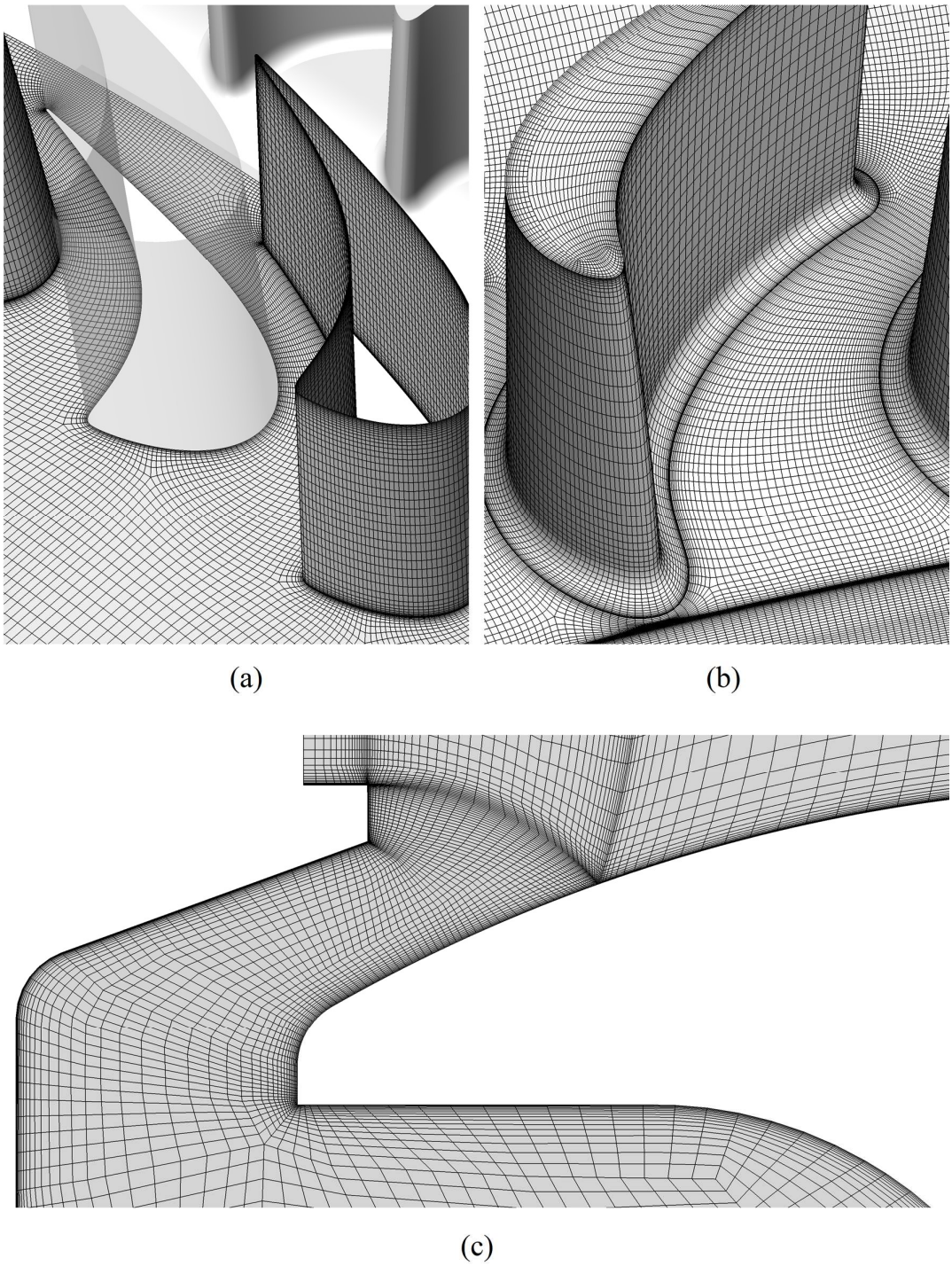

Figure 54: Mesh detail of modified stage: (a) stacked vanes, (b) twisted blades, (c) chute seal

Chapter 4: Baseline Stage

This chapter presents a discussion of results that used the Baseline stage geometry and flow conditions detailed in Chapter 3. Time-averaged results from the annulus and rim seal, in additional to those from a wheel-space upstream of the rotor are discussed in detail in Section 4.1. This includes analysis of pressure, sealing effectiveness and velocity distributions. Further analysis of the unsteady flow phenomena is presented in Section 4.2; this focusses on large-scale structures in the rim seal and their influence on ingress. Section 4.3 investigates the specific influence of the vanes and blades. The influence of axial vane position on the circumferential variation in annulus pressure distribution is described. Additionally, results from the standard bladed rotor configuration are compared to those gathered with a bladeless rotor, but with otherwise similar geometry and flow conditions; differences in annulus pressure, level of ingress level and unsteady behaviour are discussed.

A range of computational results are presented in this chapter, however it should be noted that the numerous experimental data sets that are included for validation were not measured by this author. The work presented in this chapter is based in large part on that presented by Horwood *et al.* (2018) and Hualca *et al.* (2019).

4.1 Time-Averaged Flow Characteristics

4.1.1 Annulus Pressure

The circumferential variation in time-averaged pressure on the hub, immediately upstream of the seal is shown in Figure 55. The non-dimensional pressure ($C_{p,a}$) is defined in the nomenclature. The silhouette indicates the measurement position, with flow from left to right. The two computational vane pitches represent the distribution across the full 22.5º sector model, while the experimental results represent two instrumented vane pitches in the rig separated by 180º. The agreement between experimental and computational data is very good and provides validation that the pressure field in the annulus is captured well in this model. This is important as several authors (including Owen (2011b)) have assumed a relationship between the peak-to-trough pressure difference and the level of ingress. The data presented is taken at $\Phi_0 = 0.03$, although similarly good agreement was found at the other sealing flow rates computed. Note that Patinios *et al.* (2016) suggest that $C_{p,a}$ is virtually independent of Re_ϕ (demonstrated for $7.2\times10^5 \leq \mathrm{Re}_\phi \leq 1.0\times10^6$) for a constant flow coefficient.

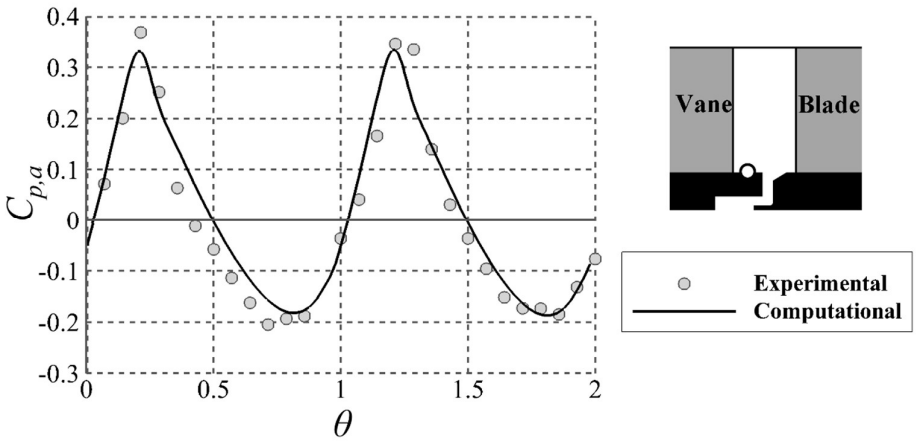

Figure 55: Circumferential distribution of pressure coefficient in annulus over two non-dimensional vane pitches ($\Phi_0 = 0.029$)

4.1.2 Annulus and Rim Seal Effectiveness

Effectiveness is based on the local concentration of CO_2 relative to the concentration of CO_2 in the sealing (purge) flow and annulus, as defined by equation 2.8. Clearly, $\varepsilon_c = 1$ at all locations in a fully-purged wheel-space with no ingress. Figure 56 shows the computed contours of effectiveness and streamlines at a sealing flow rate where the wheel-space is fully purged. Egress from the wheel-space is entrained into the passage vortex with a strong influence near the suction surface of the blade. The egress is seen to clearly provide a tangible cooling effect to the rotor hub; as it migrates through the blade passage it mixes with the annulus flow, causing a gradual reduction in effectiveness. The interaction of the egress and passage vortex would likely introduce aerodynamic losses, and although not the focus of this investigation, this was discussed further by Schreiner *et al.* (2019).

The radial movement of the egress and its entrainment into the passage vortex is illustrated in Figure 57. In Figure 57 (a) a computed isosurface of 5% effectiveness illustrates migration of the egress as it traverses the rotor passage. This time-averaged result is shown in the rotating frame of reference. In Figure 57 (b) the computation is compared with experimental data from the concentration probe (described in Section 3.1), shown as radial traverses of effectiveness both upstream and downstream of the blade. For direct comparison, computational data was extracted at the same locations relative to the vane (circumferential position indicated by the lower right-hand plot, axial positions 3.5 mm upstream and downstream of the blade) over one disc revolution, and then time-averaged. The vertical axis is the non-dimensional radius which extends from $r/b = 1$ under the blade platform to $1.03 \leq r/b \leq 1.16$ across the annulus of height $h = 25$ mm. Scobie *et al.* (2018) demonstrated that data collected with the two different-sized probes (outer

diameters 1.0 and 1.7 mm) collapse to a single curve; further, experimental data collected at two operating points show the concentration profiles are invariant with Re_ϕ.

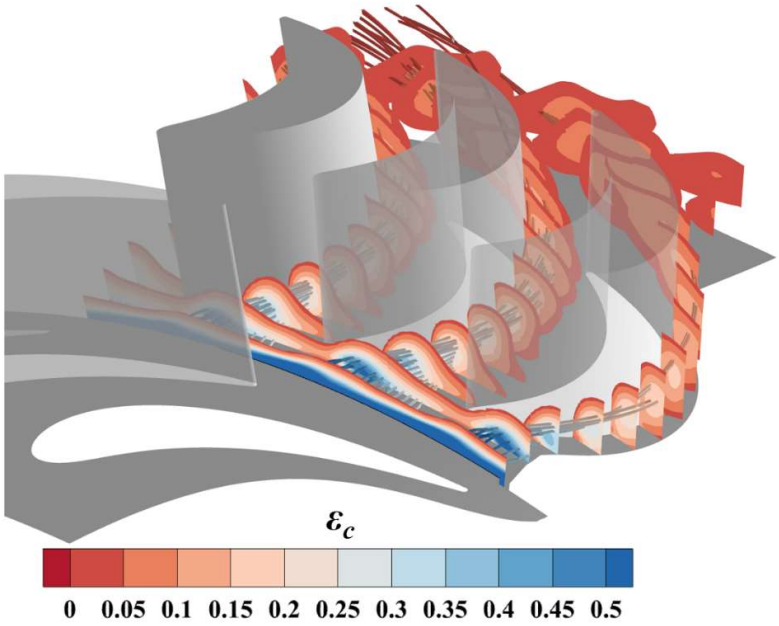

Figure 56: Time-averaged contours of concentration-based effectiveness through the annulus (clipped to > 3%), with time-averaged stream-traces originating from the seal ($\Phi_0 = 0.104$)

The downstream radial traverse shows good qualitative agreement and captures the radial movement of egress. The computational traverse upstream also captures ε_c well for $r/b > 1.04$, however there is a large over-prediction for $r/b < 1.04$.

Figure 58 shows computed and measured concentration effectiveness (ε_c) for a radial traverse from the annulus into the centre-line of the seal clearance. The circumferential location is the same as that presented in Figure 57. Three sealing flow rates were used: $\Phi_0 = 0.021$, 0.029 and 0.050. The data on the left is aligned with the right-hand-side silhouette of the seal and contours of the computed distribution of effectiveness for $\Phi_0 = 0.021$. The data shows $\varepsilon_c = 0$ in the annulus with an increase in effectiveness through the rim seal-clearance as the ingress mixes with the egress pumped up the rotor.

The computations over-predict the measured levels of effectiveness in the rim seal and do not reproduce the penetration of gas from the annulus into the rotating flow. It is speculated that this is a consequence of the inadequacy of a RANS turbulence model. More realistic simulation may be found with LES, as discussed by Chilla *et al.* (2013).

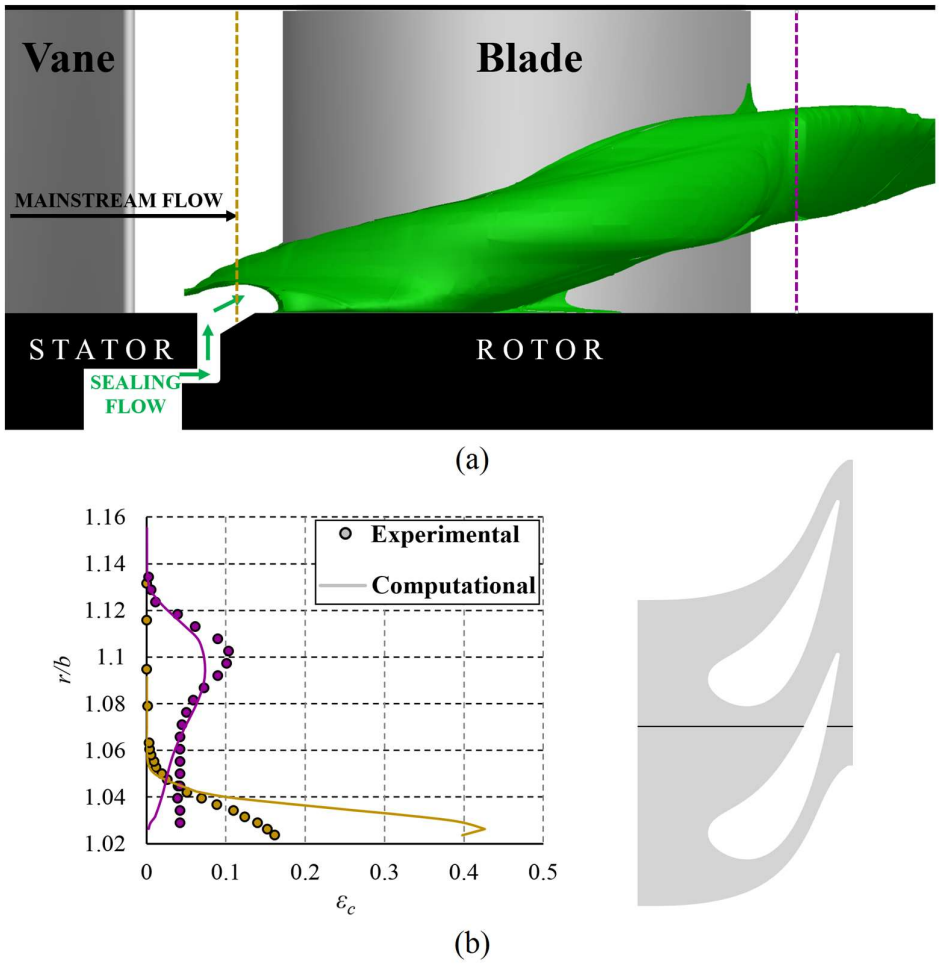

Figure 57: Time-averaged sealing effectiveness through the annulus for Φ_0 = 0.104: isosurface of 5% effectiveness (a), radial traverses of effectiveness upstream and downstream of the blade (b), lower-right silhouette indicates the circumferential position of traverses relative to the vane

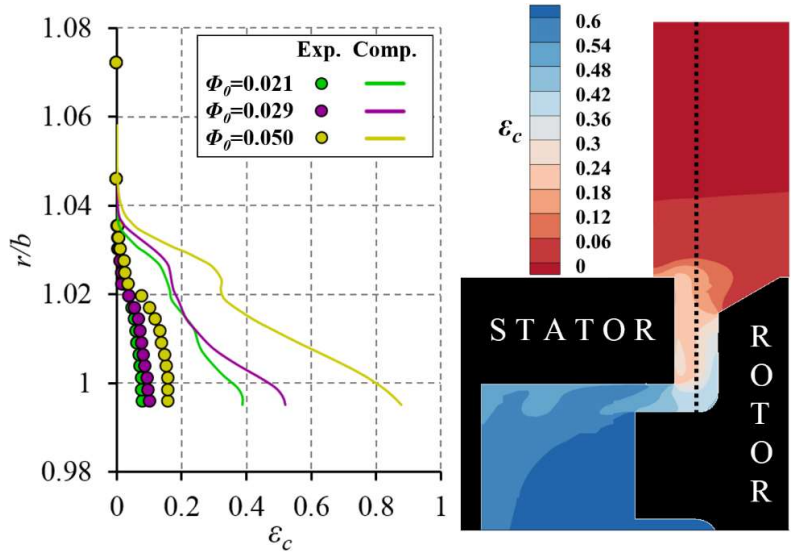

Figure 58: Concentration-based sealing effectiveness through the seal: radial traverse measurements into the seal (left), contours of computational distribution at Φ_0 = 0.021 (right)

4.1.3 Wheel-Space

In this section numerical simulations of concentration-effectiveness (ε_c) and swirl in the wheel-space are compared with experiments.

Both experimentally and computationally, the inner wheel-space is fully sealed ($\varepsilon_c = 1$) for $\Phi_0 > 0.02$. A decision to restrict computations to a range above this value was based on previous work; experience identified the slow convection of ingested fluid through the inner wheel-space led to prohibitively-large computational effort required to reach convergence. Ingress into the outer wheel-space occurred for $\Phi_0 < 0.05$.

Figure 59 (a/b) show the radial variation of ε_c for $\Phi_0 = 0.021$ and 0.029 respectively. Discrete measurements were taken on the stator disc (circle symbols) and in the rotating-core (triangle symbols); computed results are shown as solid and dotted lines respectively. A silhouette of the overlapping seal is included alongside the figure with superposed contours of computed ε_c; the silhouette is aligned with the radial position in the ordinate. There is good qualitative agreement between shapes of experimental and computational curves, but with an overall under-prediction of ingress.

The figures illustrate an abrupt increase in sealing effectiveness from $\varepsilon_c = 0$ in the annulus across the outer seal. There is a further increase in effectiveness across the inner seal, with no penetration of ingress to a fully-sealed inner wheel-space where $\varepsilon_c = 1$. The experiments show the concentration on the stator disc is invariant with radius for $r/b < 0.96$, with essentially complete mixing between ingress and egress as the ingested fluid enters the wheel-space as the source for the stator boundary layer. The computations do not quite simulate this uniform commixture. The effectiveness in the core is influenced by high-concentration fluid from the rotor boundary layer which is pumped radially outwards. The flow structure differs from the classical Batchelor flow where an inviscid core of fluid moves axially from the stator to rotor boundary layers.

Similar observations can be made in both Figure 59 (a) and (b). As expected, ε_c increases with increasing Φ_0 (hence λ_T) and the purge flow pressurises the wheel-space relative to the annulus.

Figure 60 shows the variation of effectiveness with Φ_0 in both the inner ($r/b < 0.85$) and outer wheel-spaces, with concentration measurements made on the stator disc at $r/b = 0.958$ and 0.85 respectively. In all cases ε_c increases with increasing Φ_0, as the sealing flow pressurises the wheel-space and reduces ingress through the rim seal. In addition to the computed operating point outlined in Table 3 ($Re_\phi \sim 1.0 \times 10^6$), experimental data were also collected at $Re_\phi \sim 7.4 \times 10^5$ and are shown to collapse onto individual curves.

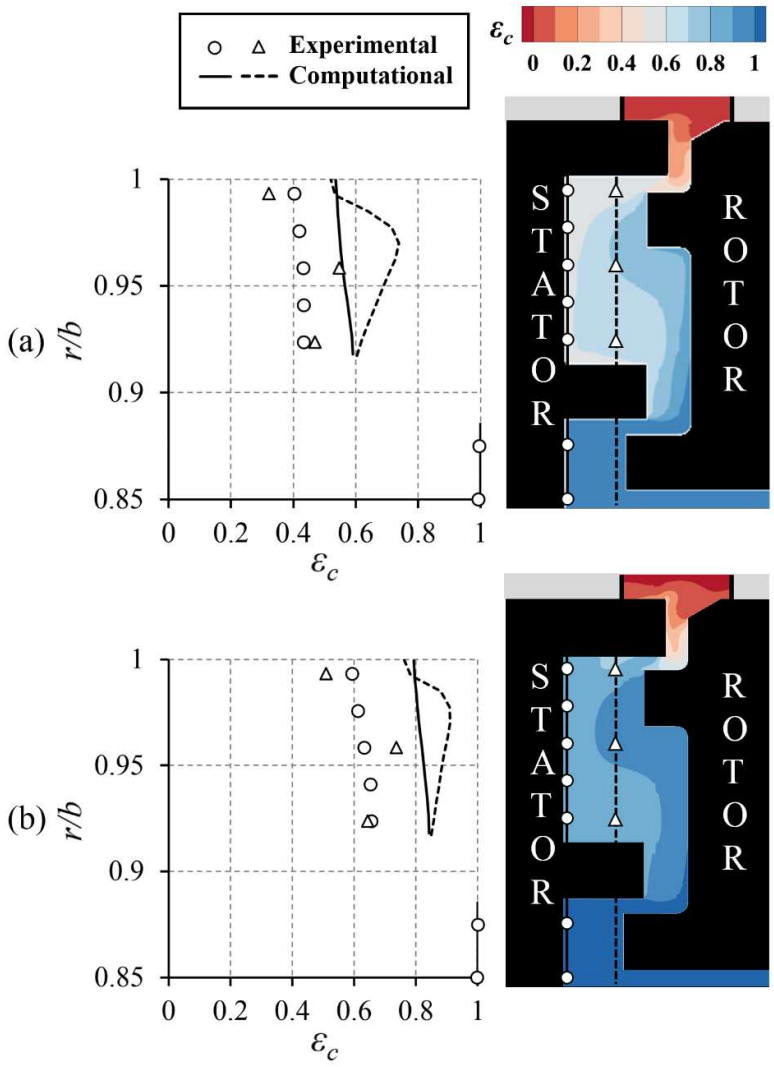

Figure 59: Concentration-based sealing effectiveness in the wheel-space: (a) $\Phi_0 = 0.021$, (b) $\Phi_0 = 0.029$

As discussed above there is an under-prediction of ingress in the outer wheel-space and the CFD has not captured the inflection or *kink* in the experimental data between $0.05 < \Phi_0 < 0.07$. The ε_c - Φ_0 curve does not follow the form predicted by the theoretical model of Owen (2011b) and Sections 4.2 and 4.3 discuss this further in the context of unsteady flow structures identified in the rim seal. Similar shaped curves have been published by Boudet *et al.* (2005), Clark *et al.* (2017), Gentilhomme *et al.* (2003) but the authors do not discuss what drives the phenomenon.

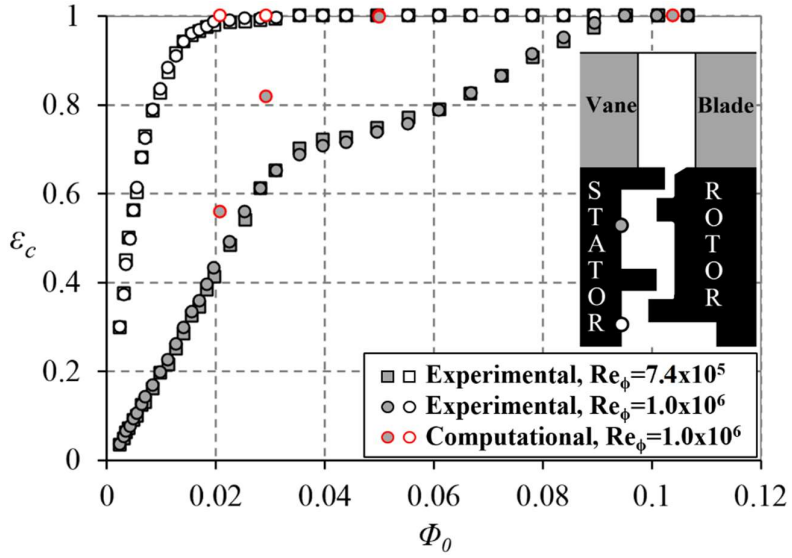

Figure 60: Variation in wheel-space concentration effectiveness with non-dimensional sealing parameter

Profiles of swirl (β) in the wheel-space and into the annulus are shown in Figure 61 for four sealing flow rates. As expected, increasing the turbulent flow parameter reduces the corresponding swirl level. There is good general agreement between experiment and computation, with the exception of r/b = 0.993. However, at this outer wheel-space location there may be sensitivity to probe measurements in proximity to the boundary layers. The figure also indicates the high levels of shear found in the outermost region of the seal that potentially give rise to large-scale rotating structures, as discussed in 4.2.

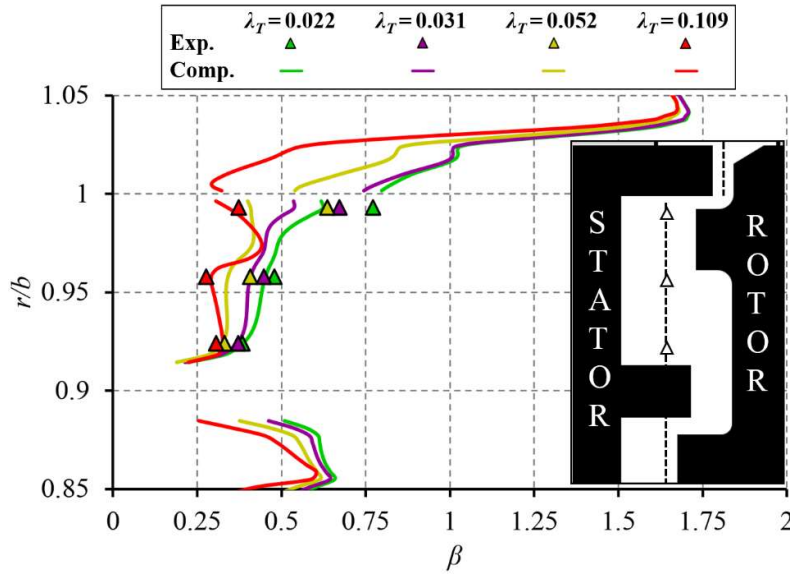

Figure 61: Variation in swirl through the outer wheel-space

4.2 Unsteady Flow Characteristics

As discussed in the literature review and illustrated in Figure 24, numerous computational and experimental studies have identified unsteady flow structures with the potential to influence ingress. Both the cause and effect of this phenomenon are not well understood.

Spectra of the pressure at r/b = 0.993 on the stator disc are presented in Figure 62 for four purge flow rates. The top silhouette indicates the monitoring point and the pressure amplitudes have been normalised, as detailed in the nomenclature. The frequencies were normalised by the rotational disc frequency, f_d.

In Figure 62, f / f_d = 48 corresponds to the blade passing frequency (BPF). Peaks at this frequency are seen across all sealing flow rates, but have a higher amplitudes at higher purge. At the two lowest purge conditions (a/b), low frequencies (i.e. f / f_d ~ 13 to 14) dominate the spectrum; their intensity diminishes with increasing sealing flow, suggesting rotating structures are associated with ingress at low purge. Flow visualisation shows these energy peaks correspond to N = 16 low-pressure structures rotating at 0.85 of the disc speed, which is consistent with data from the literature presented in Figure 24.

As the sealing flow rate is increased to Φ_0 = 0.050 (c), the low-frequency energy significantly reduces in magnitude and the frequency increases slightly to f / f_d ~ 15, corresponding to the N = 16 low-pressure structures rotating at ω / Ω = 0.94. A second harmonic of this frequency also strengthens due to strength of the BPF at this purge. Note that the additional peak frequencies (at f / f_d = 34, 35 and 33 in Figure 62 (a/b/c) respectively) result from non-linear combinations of low frequencies and the BPF: (a) 34 = 48-14, (b) 35 = 48-13, and (c) 33 = 48-15. A similar interaction between frequencies was observed by Boudet *et al.* (2005) in FFTs of their computations. At the highest purge (Φ_0 = 0.104) no clear frequency peaks exist below the normalised BPF, although there is a broad spectrum of activity at reduced magnitude.

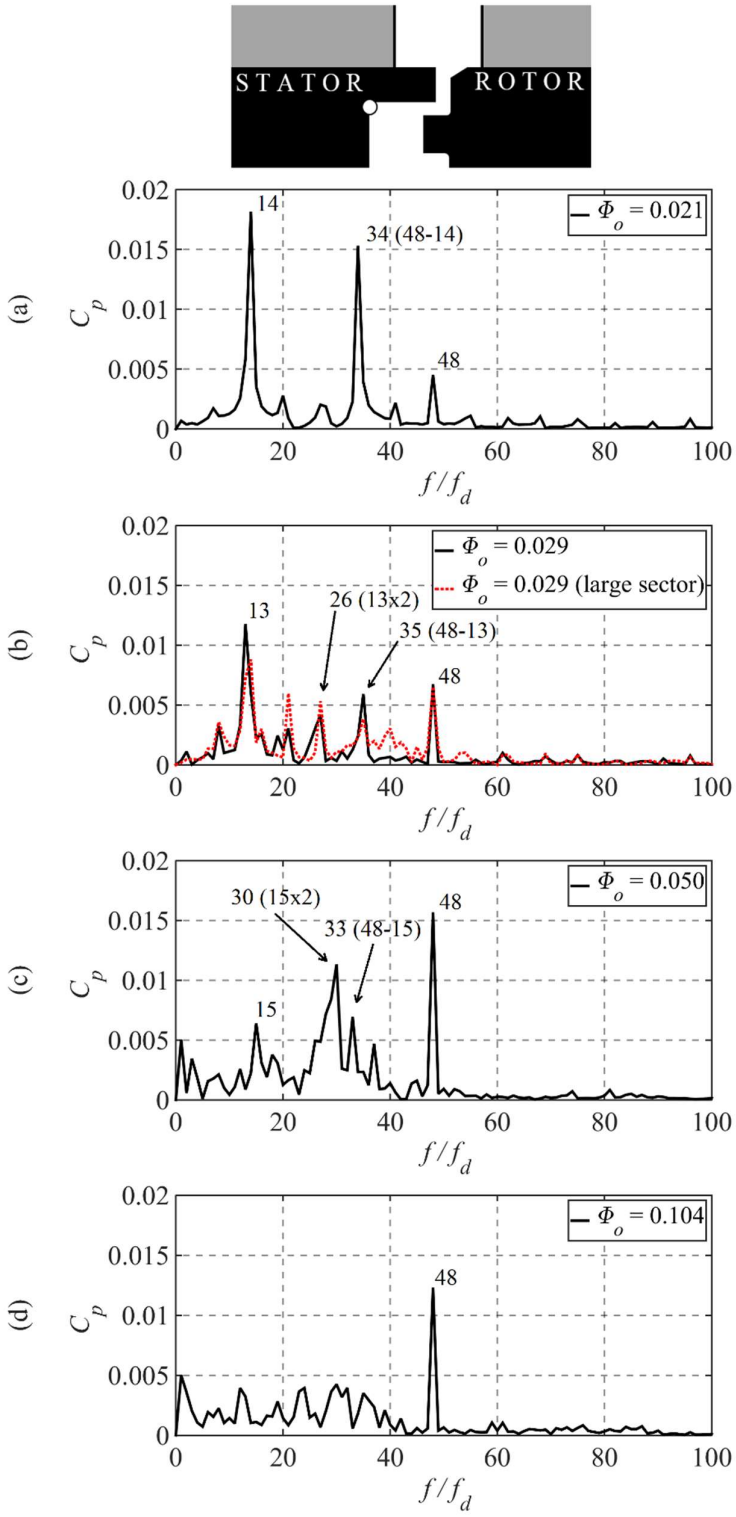

Figure 62: Fast Fourier transforms of computed stator wall pressure at *r/b* = 0.993

To investigate the influence of the 22.5º sector, an enlarged 67.5º sector was used to compute the intermediate purge case with $\Phi_0 = 0.029$. The simulation was initialised from the converged 22.5º model, which was duplicated to form the larger sector. The larger model was then run for a

further five revolutions, allowing changes in the unsteady flow structure to form. There was no significant change to the computed level of ingress and the FFT analysis for the two sectors (shown in Figure 62 (b)) was largely similar. Furthermore, $N = 16$ was dominant for both sector sizes. This is the greatest common divisor of blade and vane count, therefore indicating that vanes and blades may not only supress the unsteady structures, as shown by Rabs *et al.* (2009) and Savov *et al.* (2017), but may also influence their count. The speed, size and number of unsteady flow structures occurring in a full 360º model is not known, however the quantitative similarities between the 22.5º and 67.5º sectors provides a degree of confidence that sector models can be used in numerical simulations of ingress. A further investigation, which does include comparison to a 360º model, was undertaken for the chute seal geometry and is detailed in Chapter 7.

Fast Fourier transforms of unsteady pressure at various radial locations through the seal are shown in Figure 63. The top silhouette indicates the four colour-coded monitoring points. All data presented is for $\Phi_0 = 0.021$, as the strongest unsteadiness occurs at low purge. The same frequencies identified at $r/b = 0.993$ on the stator disc exist at higher radii through the seal, with additional high frequencies in locations closer to the annulus. Note that Figure 62 (a) and Figure 63 (a) present the same data but the different scale in Figure 63 allows the greater unsteadiness found within the seal to be clearly shown. As discussed above, additional frequencies are attributed to non-linear combinations of the fundamental low frequency and the BPF. Unsurprisingly, the strength of the normalised blade passing frequency is magnified at monitoring points closer to the blade row. Interestingly, the dominant low frequency ($f/f_d = 14$) is strongest in the axial clearance, where the annulus flow first interacts with the wheel-space flow. This is consistent with the large-scale structures being created by the shear between two flows; here the highly-swirled flow immediately downstream of the vane meets the relatively low-swirling egress in the outer part of the seal.

The formation of Kelvin-Helmholtz instabilities in a shear layer (which Rabs *et al.* (2009) suggested could drive rim seal structures), is depicted schematically in Figure 64. If the two layers are assumed inviscid and separated by an infinitely thin vortex sheet of uniform vorticity, any small perturbation will cause a slight billowing of the vortex sheet as shown by Figure 64 (a/b). However, this billowing results in localised regions of higher and lower pressure as the local velocities decrease and increase respectively. This fundamentally unstable state, where the local changes in pressure act to increase the size of the billowing, is shown in Figure 64 (c). The two layers quickly wrap into a large vortex. This phenomenon can occur at different length scales, with smaller vortices encompassed by larger ones, as shown by Figure 64 (e).

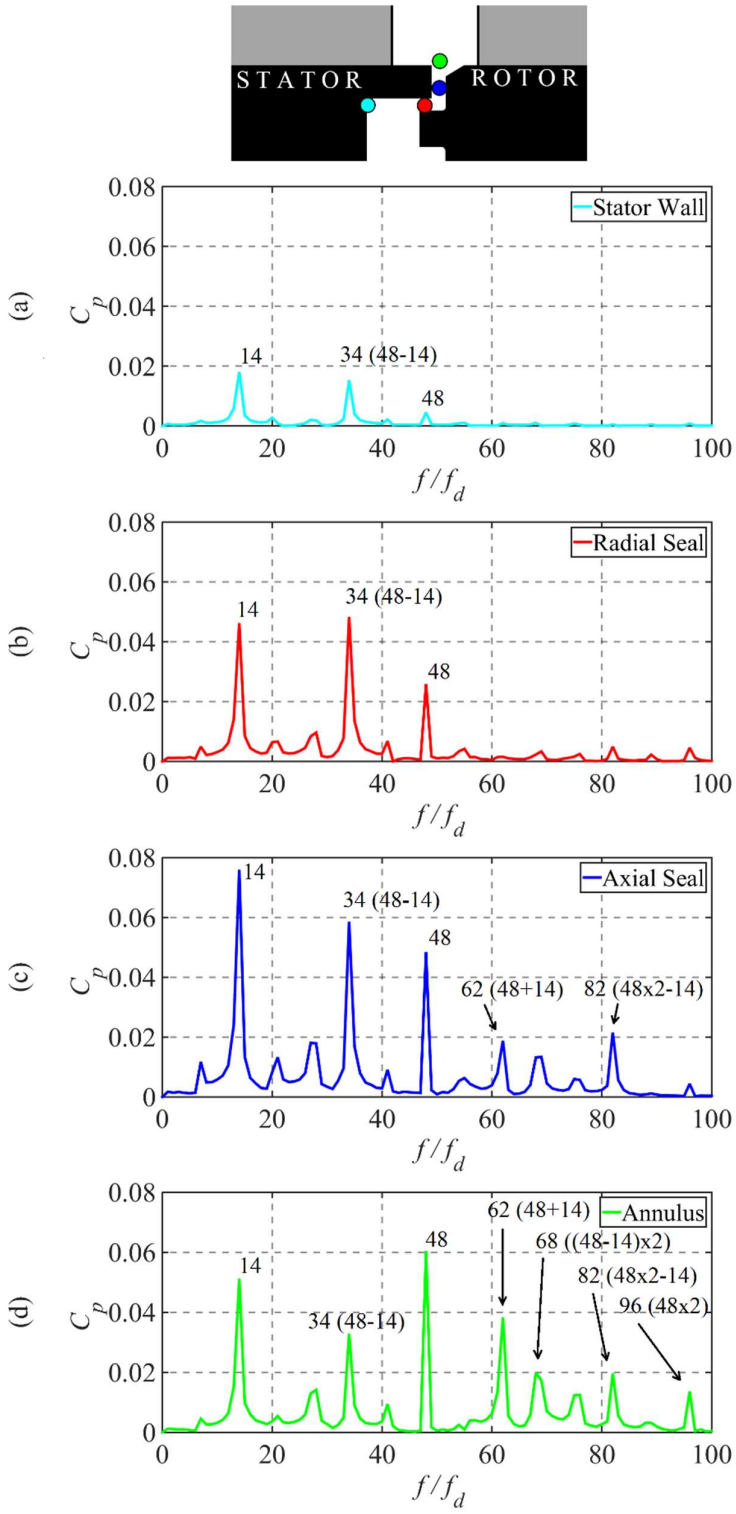

Figure 63: Fast Fourier transforms of computed pressure at four locations through the seal for $\Phi_0 = 0.021$

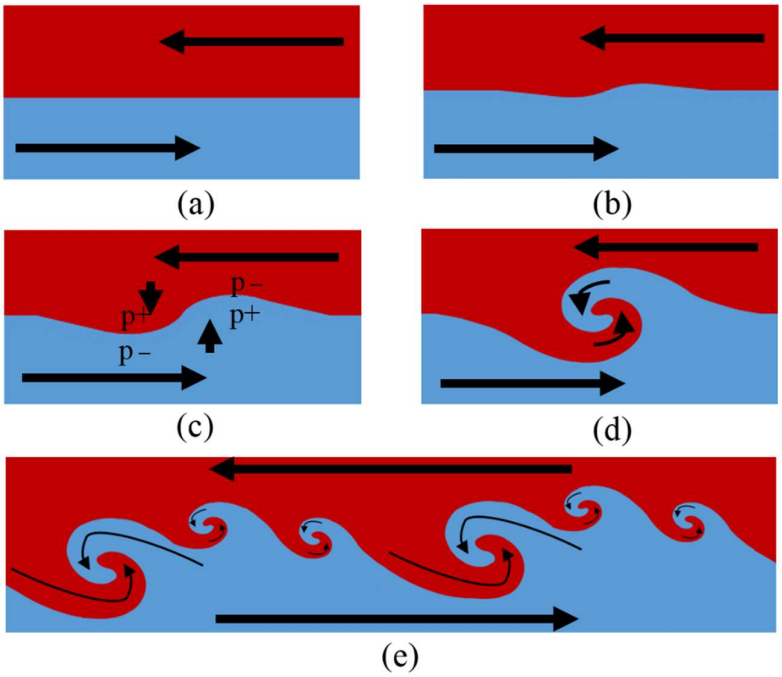

Figure 64: Formation of Kelvin-Helmholtz instabilities

Vortical flow structures similar to Kelvin-Helmholtz instabilities have been captured in the numerical simulations, as shown in Figure 65. This figure shows contours of effectiveness and streamlines on different planes *through* the seal, as indicated by the dotted line in the silhouette. The instantaneous flow fields are taken in the rotating frame and therefore the wheel-space and annulus flows appear to counter rotate. The computational sector has been duplicated for post-processing and two results for different purge flow rates are shown.

Six individual structures form at both sealing flow rates, corresponding to low pressure regions aligned with the blade passages; these are relatively stable and rotate at the disc speed. However, at the low sealing flow rate (Figure 65 (a)) these smaller structures appear to coalesce into larger structures. It is this larger unstable structure that rotates at just less than the disc speed and drives ingress deeper into the wheel-space. For $\Phi_0 = 0.021$, $N = 16$ and $\omega/\Omega = 0.85$, Figure 65 (b) shows that these larger structures are completely suppressed at the higher purge and the six smaller vortical structures are reduced in size. Savov and Atkins (2017) discuss a gap recirculation zone (GRZ) in the seal clearance, the size of which is influenced by the purge flow rate. At high purge the GRZ is blown out and it is speculated this phenomenon influences the structures shown here.

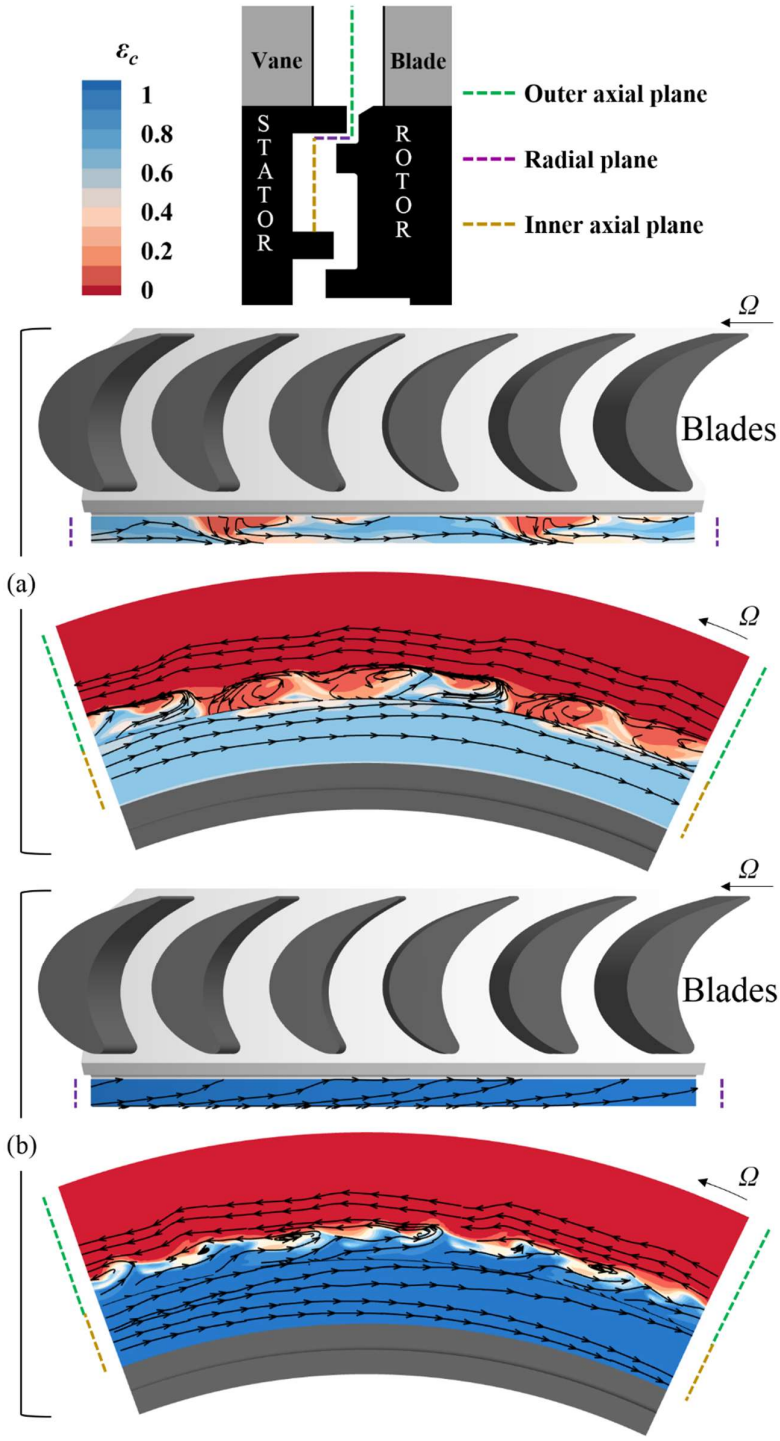

Figure 65: Instantaneous contours of effectiveness through the rim seal with streamlines taken in the rotational frame and with the stator hidden: (a) $\Phi_0 = 0.021$, (b) $\Phi_0 = 0.104$

Experimental measurements of the unsteady pressure field at $r/b = 0.993$ on the stator disc are shown in Figure 66, in the form of an FFT analysis similar to that used for the computations presented in Figure 62. Data was recorded by Fabian Hualca but post-processed by the present author. Data is shown for five purge flow rates and the two rotational Reynolds numbers presented

in Figure 60 (7.4×10^5 / 1.0×10^6). At the common flow coefficient ($C_F = 0.41$) the normalised frequencies at which the spectral activity occurs are largely invariant with Re_ϕ. The experiments were conducted with and without the total pressure probes shown in Figure 36, to confirm they had no measurable effect on the unsteady phenomena. The experiments exhibit unsteady pressure fluctuations at frequencies significantly below the BPF, similar to those observed computationally. For the experiments $f / f_d \sim 25$, for the computations $f / f_d \sim 14$. As with the computations, the amplitude of the low-frequency energy reduces with increasing purge (apart from the case $\Phi_0 = 0.050$ as discussed below) and is largely supressed at $\Phi_0 = 0.104$.

The rotational speed (ω/Ω) and number (N) of the structures were determined from two transducers circumferentially displaced by an angle $\alpha = 8°$, using a phase analysis approach proposed by Beard *et al.* (2017). Data was recorded at 100 kHz for 10 s, with the signals divided into single revolutions of the disc and filtered to remove frequencies outside the region of interest. The filter was applied by first transferring the data to the frequency domain (using a direct Fourier transformation), before applying a bandpass filter, and finally performing an inverse Fourier transformation. The bandpass filter was centred at the peak frequency corresponding to the large-scale structures, typically with a pass band of $2 \times f_d$. The filtered signals from each pressure transducer were then cross-correlated for each disc revolution. A histogram recording the lag-time from the peak in each cross-correlation was then populated to determine the lag time (Δt_α) between the transducers, leading to the rotational speed of the structures ($\omega = \alpha/\Delta t_\alpha$). The number of structures around the circumference (N) follows from the normalised frequency (f / f_d) and rotational speed (ω/Ω). The data is presented in Table 5 with the corresponding computational values. It should be noted that no rotating structures are identified at $\Phi_0 = 0.104$.

At the three lowest sealing flow rates the spectral activity at $f / f_d \sim 25$ (*i.e.* ~ 0.52 of the BPF) corresponds to 25/26 structures rotating at 0.92-0.96 of the disc speed. These can be compared to the 16 structures determined from the computations. Curiously there is a magnification of the low-frequency activity at $\Phi_0 = 0.050$, as shown in Figure 66 (d). This behaviour is distinct from that measured over the range $\Phi_0 = 0.01$-0.03, as $f / f_d = 24$ precisely (*i.e.* half the blade count) and the corresponding structures are calculated, within experimental uncertainty, to rotate at the disc speed ($\omega/\Omega = 1$). The existence of these structures, which are associated with regions of reduced pressure, is believed to be linked to the inflection in the effectiveness curve shown in Figure 60, given the occurrence of both at $\Phi_0 = 0.050$. It is speculated that they become reinforced by the synchronously rotating blade pressure field. Furthermore, the amplitude of the unsteady pressure corresponding to these structures is sudden and significant, and would be expected to have an influence on the effectiveness level depicted in Figure 60. Section 4.3.2 presents a comparison with bladeless results and discusses the influence of the blade over the aforementioned inflection in further detail.

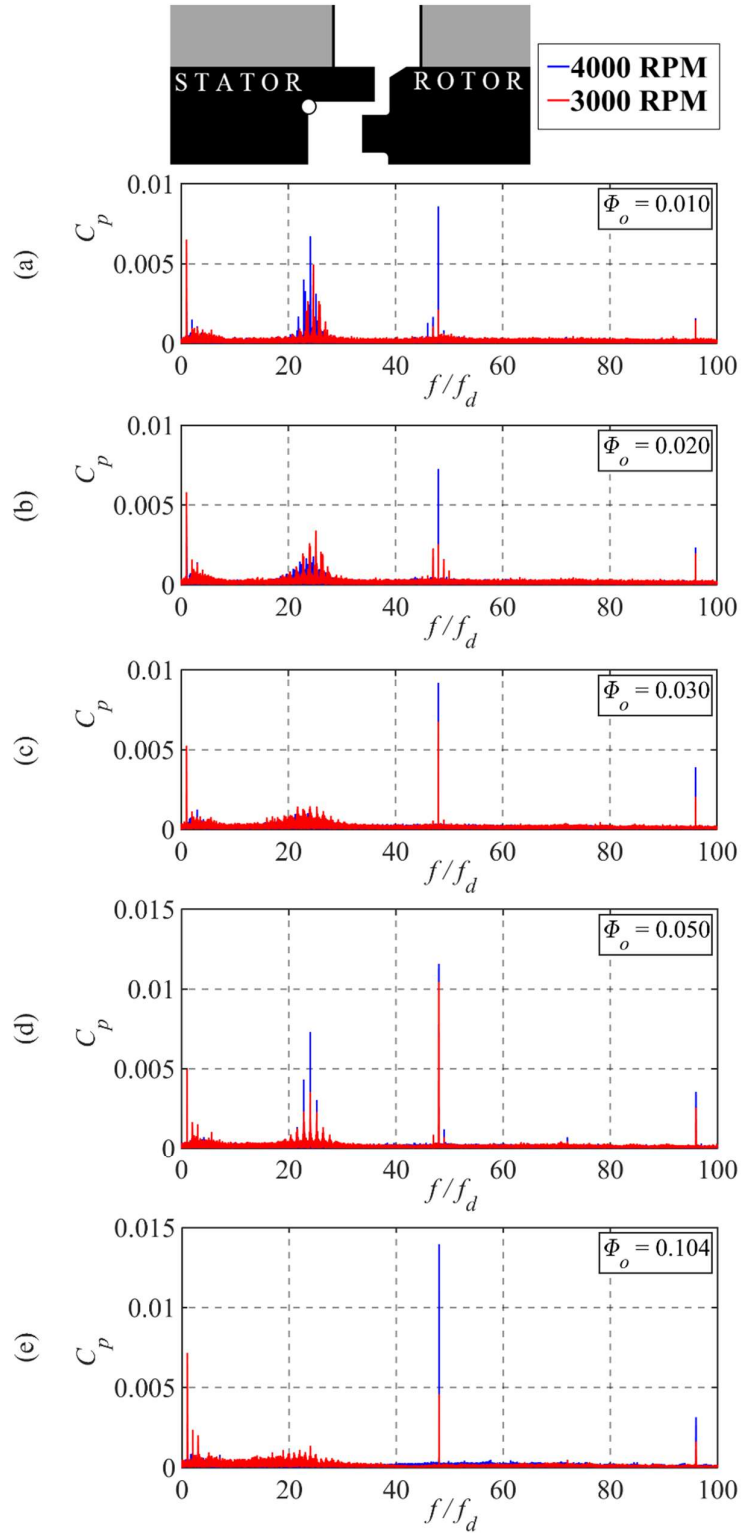

Figure 66: Fast Fourier transforms of experimental stator wall pressure at *r/b* = 0.993

Case	Rotor Speed (RPM)	Non-Dimensional Sealing Parameter (Φ_0)	Number of Structures (N)	Rotational Speed of Structures (ω/Ω)
Comp.	4000	0.021	16	0.88
Comp.	4000	0.029	16	0.81
Comp.	4000	0.050	16/32	0.94
Comp	4000	0.104	N.A.	N.A
Exp.	4000	0.010	26	0.93
Exp.	4000	0.020	26	0.93
Exp.	4000	0.030	25	0.93
Exp.	4000	0.050	24	0.99
Exp.	4000	0.104	N.A.	N.A
Exp.	3000	0.010	26	0.94
Exp.	3000	0.020	26	0.96
Exp.	3000	0.030	26	0.92
Exp.	3000	0.050	23	1.03
Exp.	3000	0.104	N.A.	N.A.

Table 5: Comparison of large-scale flow structures for the baseline stage: experiment and computation

The fundamental unsteady behaviour measured in the rig appears to have been captured by the computations, although differences between the computational and experimental results include the following: different numbers of unsteady structures around the disc (N = 16/32 in computations, N = 24-26 in experiments); frequencies measured at 1-3 times the disc-passing frequency that are attributed to imperfections in the disc; and a second measured harmonic of the BPF. The additional peaks in the computational frequency spectrum created from non-linear combinations of low frequencies and the BPF are not seen experimentally. The significantly higher resolution of the experimental FFTs is a result of data being recorded over 500 revolutions, where the computational data could only be sampled over a single revolution.

4.3 Influence of the Vane and Blade

The baseline configuration, discussed in sections 4.1 and 4.2, considered only one vane position alongside a rotor fitted with 48 blades. This section studies the effect of the axial position of the vanes upon the annulus pressure distribution and more broadly the overall effect of removing blades from the turbine configuration.

4.3.1 Vane Position

Figure 67 shows the peak-to-trough annulus pressure difference against axial position in the annulus. This data is presented at the annulus hub, with solid lines and symbols representing computed and measured results in a stationary reference frame and the dotted lines representing computed data from the rotating reference frame. Furthermore, in addition to the baseline vane position (blue data), the relationships are shown for a case where the distance between vane trailing edge and seal has been halved (red data). For each instance, the axial spacing between the vane, seal and blade is depicted by the colour-coded, geometrically aligned silhouettes. All data is taken for $\Phi_0 = 0.03$.

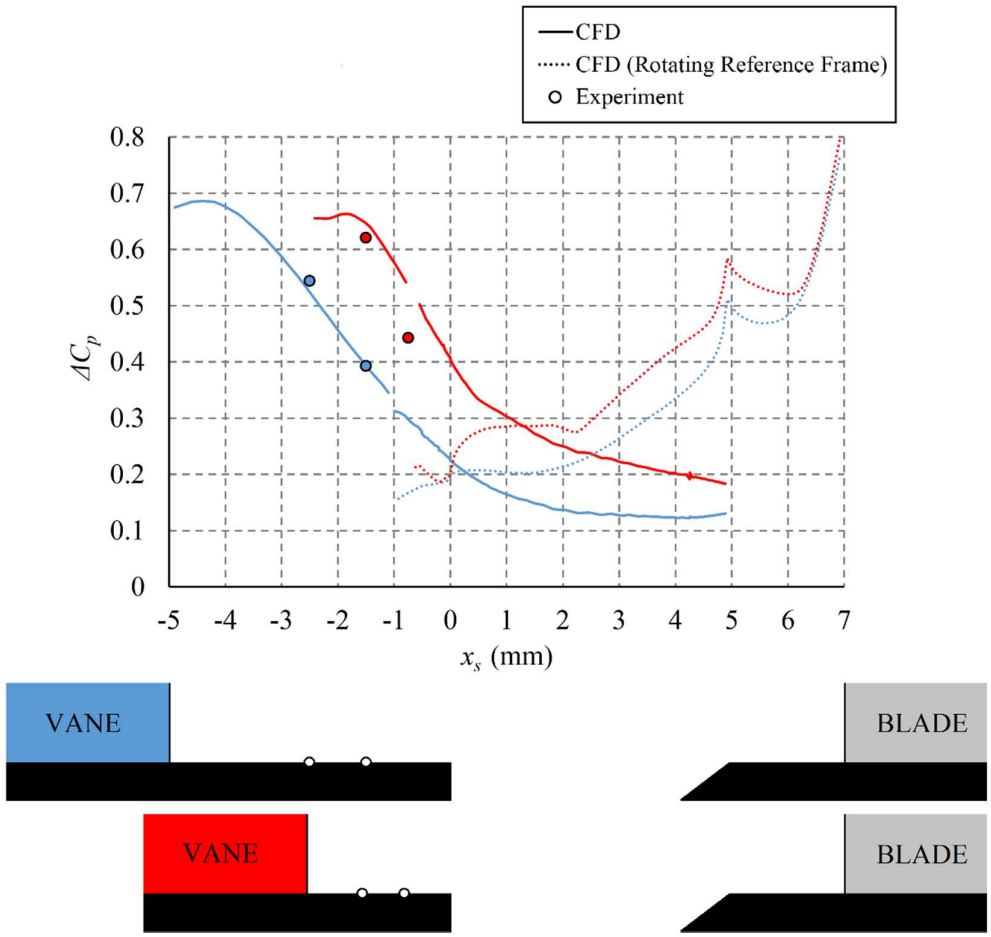

Figure 67: Variation in ΔCp on the annulus hub for two axial distances between the vane and seal. Data aligned with the seal leading edge ($\Phi_0 = 0.029$)

Considering the stationary frame of reference, ΔC_p is shown to decay downstream of the vane trailing edge for both vane positions. However, in the rotating reference frame ΔC_p is driven by the blade bow wave, and therefore decreases with upstream distance from the blade leading edge. Typically, turbine designers locate the rim seal equidistant from the vane and blade to minimise the circumferential pressure variation in the reference frame of both the vane and the blade. Figure

67 demonstrates that with a reduced distance between vane and seal, the magnitude of ΔC_p increases at positions close to the seal, both experimentally and computationally. For the baseline vane position (blue data), the experimental data is well predicted. However, for the modified vane position the agreement is poorer, and a reliable prediction of ΔC_p at $x_s = 0$ cannot be made. This discrepancy highlights the difficulty in achieving accurate computation of the flow fields related to ingress.

Figure 68 depicts the data from Figure 67 in an alternative form. Rather than presenting the horizontal axis as distance from the seal leading edge, distance is shown taken from the vane trailing edge. This demonstrates that in the stationary reference frame, the rate of decay in ΔC_p with axial distance from the vane is steeper when the vane is located closer to the seal. It is perhaps surprising that for at a given distance downstream of the vanes, the magnitude of ΔC_p is not common for the two cases. Section 4.3.2 reveals that the presence of blades does not significantly influence the peak-to-trough pressure distribution on the stator hub platform and therefore it is the presence of the seal and the ingress/egress that modify ΔC_p in this region.

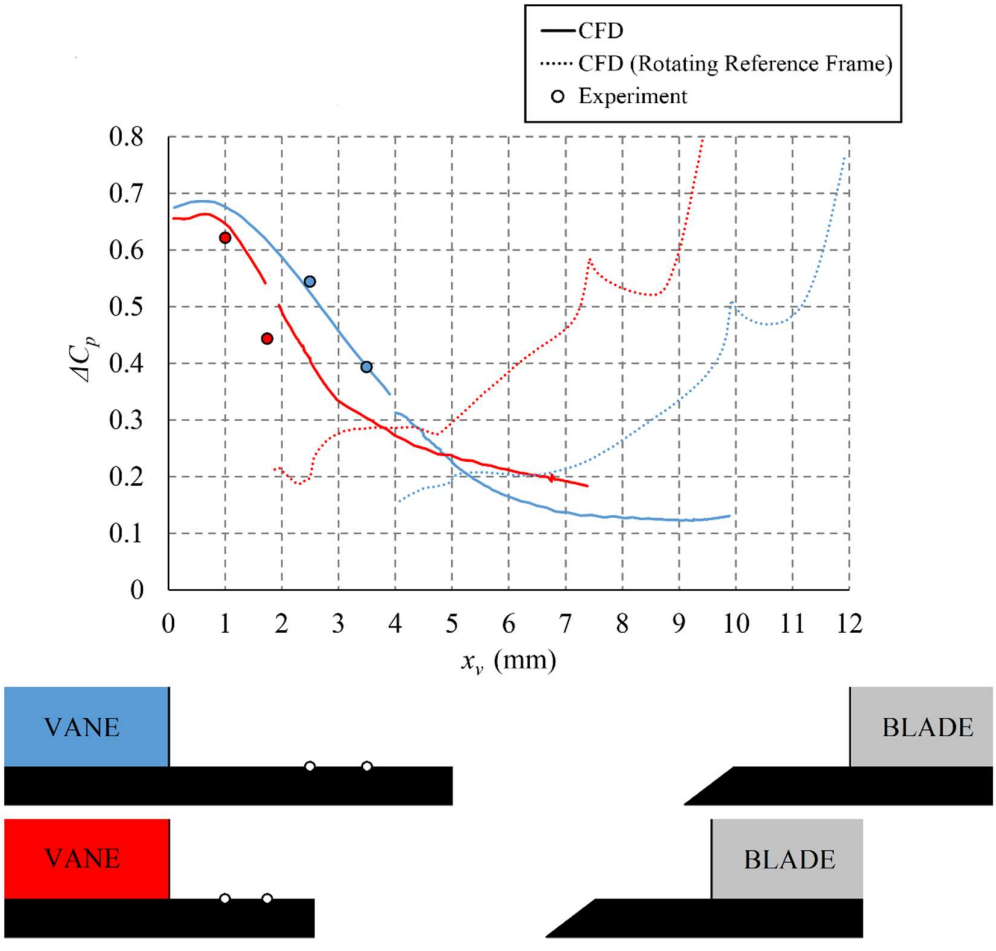

Figure 68: Variation in ΔCp on the annulus hub for two axial distances between the vane and seal. Data aligned with the vane trailing edge (Φ_0 = 0.029)

4.3.2 Bladeless Rotor

The objective of the work presented here was to isolate the effect of the blades in order to understand their influence on ingress. To achieve this, simulations similar to those already discussed in this chapter were produced, but with blades removed from the model. These were computed at $\Phi_0 = 0.021, 0.029, 0.104$. Unlike several previous studies that exploited the lack of rotating blades to run steady RANS simulations (e.g. Bohn *et al.* (1999), Zhou *et al.* (2013)), the present work adopted URANS computations to allow investigation of unsteady flow phenomena.

Figure 69 depicts the circumferential peak-to-trough annulus pressure (ΔC_p) at the annulus hub versus axial position, x_s. All data is shown for the stationary frame. The plot is similar in form to Figure 68, however computational results for the bladed case (solid line) are compared directly to those of the bladeless case (dashed line). Corresponding experimental data is shown by the circles and triangles, respectively. The results are axially aligned with the silhouette and shown for $\Phi_0 = 0.029$, although similar trends were identified at $\Phi_0 = 0.021$ and 0.104. The computational profiles are validated by excellent agreement with experimental data. The results demonstrate that the presence of the rotor blades does not significantly influence ΔC_p over the stator hub (i.e. $x_s < 0$). Conversely, further downstream (i.e. $x_s > 0$), the pressure distribution from the blade becomes a stronger influence and the divergence of ΔC_p in the bladed case demonstrates an increased vane-blade interaction.

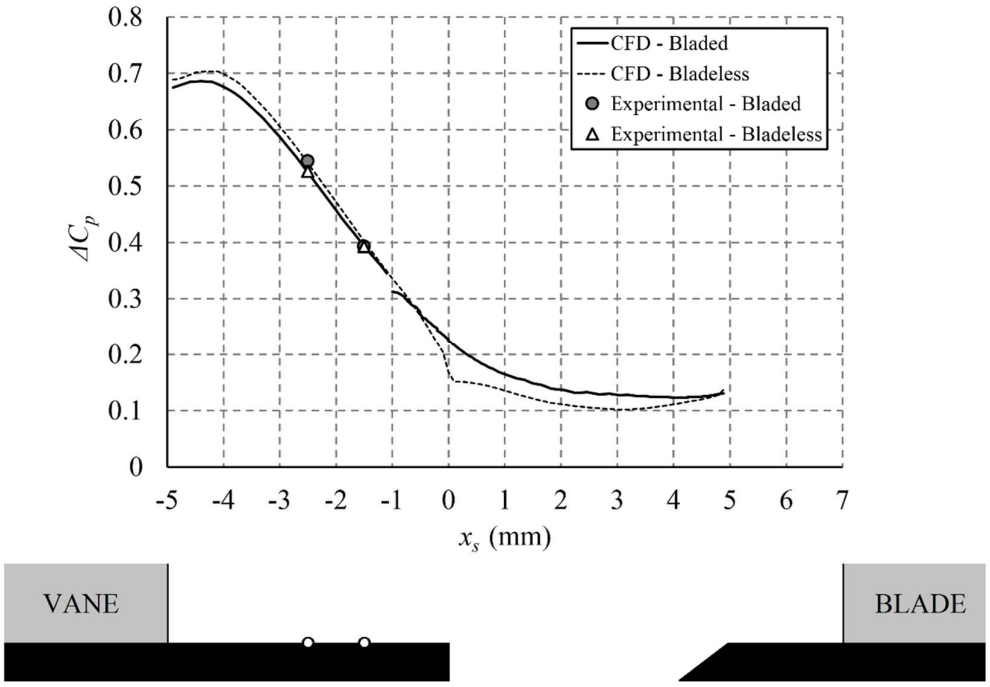

Figure 69: Peak-to-trough pressure distribution in the annulus for bladed and bladeless configurations ($\Phi_0 = 0.029$)

Figure 70 compares the variation of effectiveness with Φ_0 for bladed (white symbols) and bladeless (grey symbols) configurations. Measurements were made at r/b = 0.958 on the stator wall. For both the bladed data (also presented in Figure 60) and bladeless data, experiments were conducted at Re_ϕ ~7.4×10^5, and Re_ϕ ~1.0×10^6, with results found to collapse with Reynolds number.

The general computational under-prediction of ingress, visible in Figure 70, is described in Section 4.1.3, as is the inflection in the experimental data for the bladed case. The experimental data confirms that this inflection in the relationship between Φ_0 and ε_c is caused by the blades, with bladeless results demonstrating monotonic, conventional behaviour. Experimentally the rotor blades are found to increase ingress in this region ($0.03 < \Phi_0 < 0.09$). A similar reduction in ingress is seen computationally at Φ_0 = 0.021 and 0.029. However, it should be noted that an increase in sealing effectiveness resulting from the inclusion of blades conflicts with the findings of Green and Turner (1994), who suggested the blades served to smooth the circumferential annulus pressure distribution, driving lower ingress. In the present study it is believed that the reduction of ingress is driven by a modification to the unsteady flow phenomena, discussed in the context of Figure 71 and Figure 72 below.

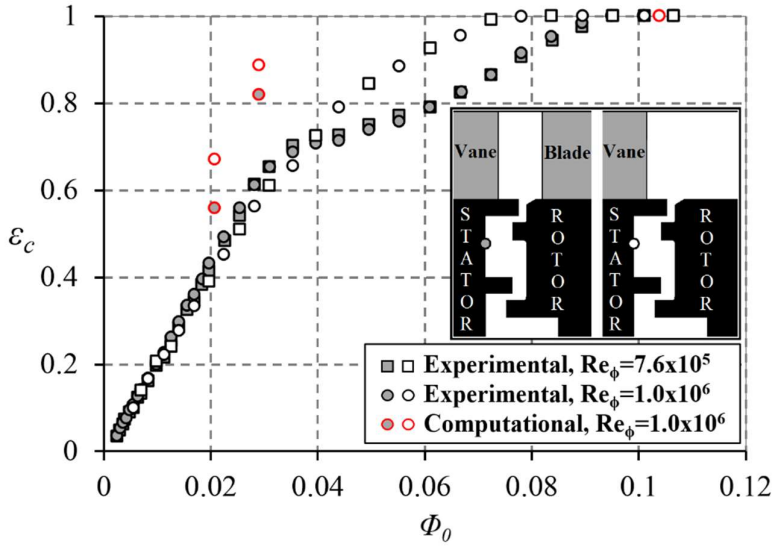

Figure 70: Variation in wheel-space concentration effectiveness with non-dimensional sealing parameter for bladed and bladeless configurations

Figure 71 shows fast Fourier transforms of computed stator wall pressure at r / b = 0.993 for bladed (black line) and bladeless (red line) cases. Data for the bladed cases is duplicated from Figure 62 but presented alongside bladeless results for purposes of direct comparison. Increasing sealing flow rates are shown through plots (a), (b) and (c). Frequencies have been normalised against disc speed, pressure amplitudes have been normalised as detailed in the nomenclature and the silhouette indicates the monitoring location. It should be noted that for bladeless cases, the

stationary reference frame of the wheel-space allowed pressure to be easily monitored at fixed locations; the higher resolution bladeless FFTs represent data from the final eight computed disc revolutions. Figure 72 depicts FFTs which are broadly similar to those in Figure 71, but represent experimental data. Experimental results for the bladeless configuration were only available at Re_ϕ ~7.4×10^5, rather than the computed Re_ϕ ~1.0×10^6, however Figure 66 indicates that for the bladed case, with a common C_F,the measured unsteadiness is broadly invariant to these Re_ϕ. It is assumed this is also the case for the bladeless configuration.

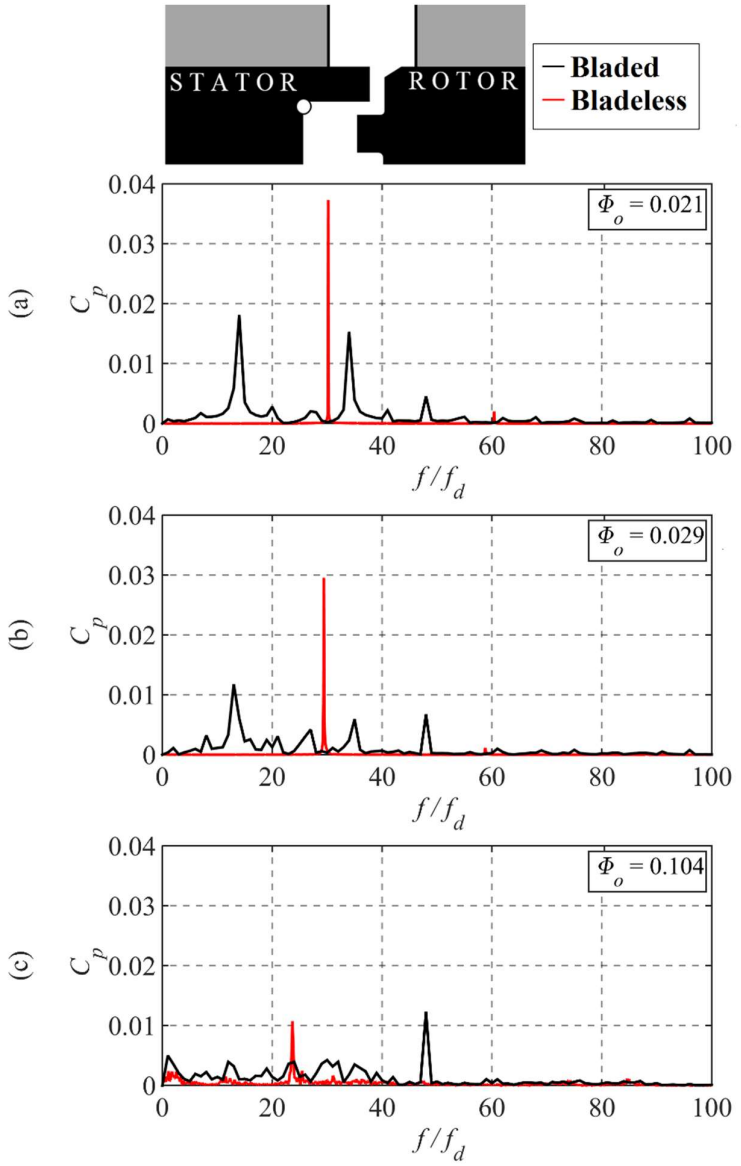

Figure 71: Fast Fourier transforms of computed stator wall pressure at r/b = 0.993 and Re = 1.0×10^6 for bladed and bladeless configurations

Figure 71 and Figure 72 show that, as expected, the BPF ($f/f_d = 48$) is no longer present for the bladeless configurations. However, computationally, experimentally and across all purge

rates, the spectrum of unsteady activity at frequencies below the BPF is replaced by activity at a single distinct frequency of $f/f_d \sim 30$. The rotational speed and number of the large-scale rotating structures corresponding to these frequencies is tabulated in Table 6. Values from experiment were calculated using the same phase analysis approach outlined in Section 4.2.

From Table 6, with the blades removed, the number of structures, N, is increased. It is speculated that the removal of the blades also increases the stability of the large-scale structures, resulting in their energy being distributed across a narrower frequency band and leading to increased peak magnitudes in the FFTs. This increased stability is also reflected at $\Phi_0 = 0.104$, where the large-scale structures are no longer 'blown out' in both computational and experimental bladeless results.

Broadly speaking the bladeless computations show good agreement with experiment, capturing many of the flow features measured across the range of tested sealing flow rates. However, the bladeless computations do not show a reduction in rotational speed, ω, or a change in the number of structures, N, with increasing purge, as the experiments do. This may be attributable in part to the sector domain and the associated periodic boundary conditions.

Section 4.2 attributed the inflection in the experimental Φ_0 vs ε_c curve for bladed data (see Figure 60 and Figure 70) to an increase in the magnitude of low frequency activity at $\Phi_0 = 0.050$. It was speculated that this is a result of synchronous superposition of the rotating pressure fields from the large-scale structures and the rotating blades. This theory would suggest both the inflection and the magnification of low frequency activity would disappear when blades are removed. Figure 70 and Figure 72 (c) demonstrate this is indeed the case. It is therefore reasonable to assume that to computationally capture the aforementioned inflection, CFD would need to accurately capture the precise number and rotational speed of the large-scale structures with varying Φ_0.

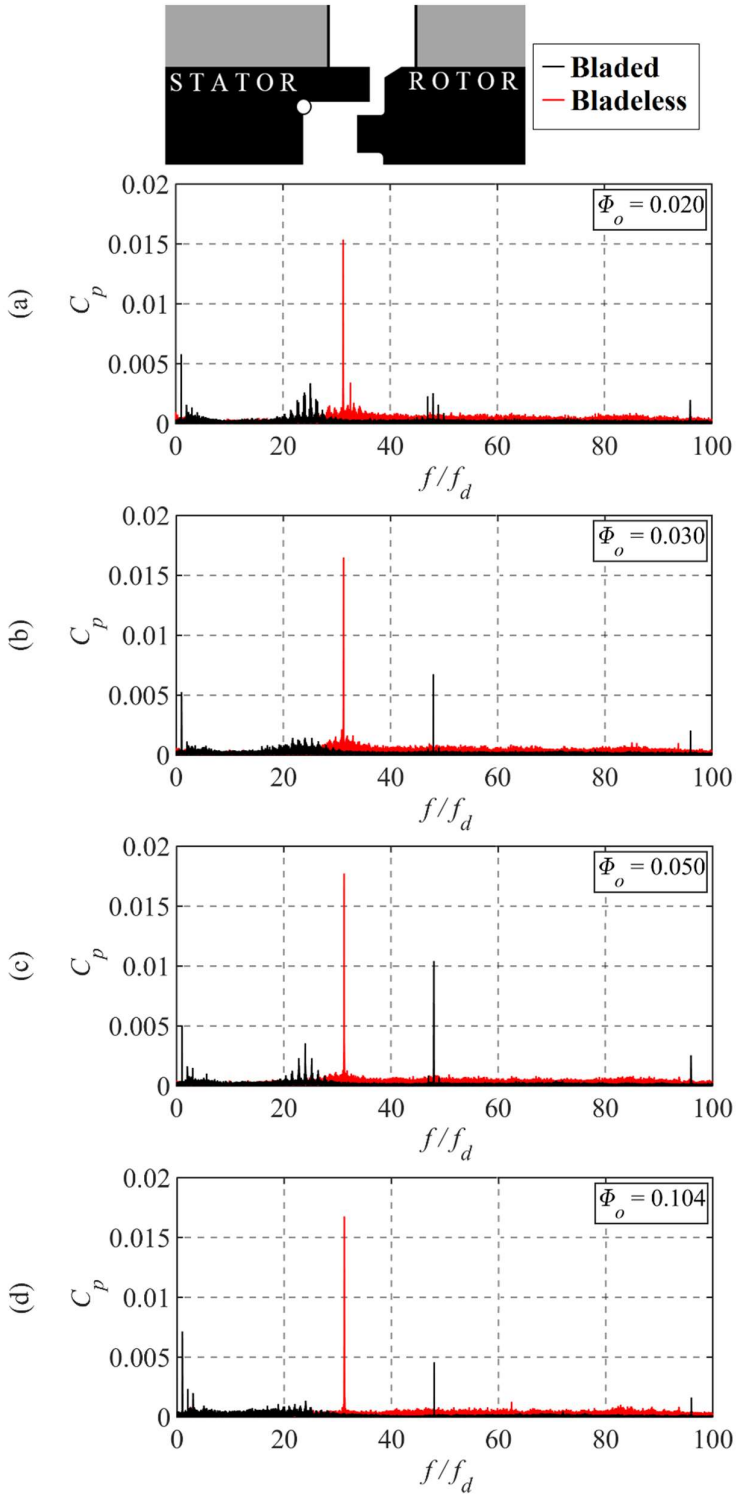

Figure 72: Fast Fourier transforms of experimental stator wall pressure at r/b = 0.993 and 7.4 × 10^5 for bladed and bladeless configurations

Case	Rotor Speed (RPM)	Non-dimensional Sealing Parameter (Φ_0)	Number of Structures (N)		Rotational speed of Structures (ω/Ω)	
			Bladed	Bladeless	Bladed	Bladeless
Comp.	4000	0.021	16	32	0.88	0.94
Comp.	4000	0.029	16	32	0.81	0.92
Comp	4000	0.104	N.A.	32	N.A	0.74
Exp.	3000	0.020	26	34	0.96	0.89
Exp.	3000	0.030	26	36	0.92	0.85
Exp.	3000	0.050	23	37	1.03	0.82
Exp.	3000	0.104	N.A.	39	N.A.	0.79

Table 6: Comparison of large-scale flow structures the bladed and bladeless baseline stage: experiment and computation

4.4 Summary

The object of this chapter was to evaluate and analyse URANS simulations of the baseline geometry used in the Bath University 1.5-stage experimental rig. The computed domain included the first vane and blade rows, separated by a wheel-space cavity that incorporates a radial clearance rim seal at the periphery.

Evaluation of the simulations was performed against a variety of time-averaged and time-accurate experimental measurements. Time-averaged measurements of annulus pressure and wheel-space swirl demonstrated good agreement with computation. Comparison of concentration measurements from a probe, radially traversed into the seal clearance, indicated that the CFD under-predicted the penetration of annulus gas into the rim seal; potentially a result of the turbulence model failing to accurately capture the separated flow in this location. Further comparison with time-accurate pressure measurements, close to the rim seal, showed good qualitative agreement, with the simulations identifying similar large-scale rotating structures that vary in strength, rotational speed and number, with sealing flow rates.

Analysis of the annulus pressure distribution in the stationary frame of reference indicated that the peak-to-trough pressure difference, ΔC_p, is not solely dependent upon the axial distance downstream of the vane, and can show a stronger axial-decay in the presence of the rim seal and the associated ingress/egress flows. Additionally, the egress flow exiting the rim seal is quickly wrapped into the passage vortex and can provide tangible cooling to the blade.

The computations revealed strong tangential shear gradients through the rim seal. It is hypothesised that these give rise to instabilities, which ultimately drive regions of low-pressure that may be larger than a single blade or vane passage, causing increased ingress. Bladed computations identified 16 low-pressure structures rotating at approximately 0.85 of the disc speed, however their existence is highly sensitive to sealing flow rate and they were supressed at high purge.

Further investigation compared the conventional bladed configuration, to that without blades. The circumferential pressure difference, ΔC_p, on the stator hub was unaffected by the presence of the blades, however the bladeless configuration led to a reduction in ingress at certain Φ_0 values. FFTs of the bladeless computations showed that at all sealing flow rates, the spectrum of activity below the BPF (present only in the bladed configurations) was replaced by a single distinct frequency of increased magnitude. This distinct frequency was indicative of rotating structures with a greater stability that were higher in number. Experimentally, the presence of blades was shown to cause an inflection in the relationship between Φ_0 and ε_c; computing this feature would require accurate simulation of both the speed, ω, and the number, N, of large-scale structures around the disc.

Chapter 5: Frequency Domain Computations

This chapter discusses the application of harmonic balance (HB) computations to model the unsteady flow field in gas turbine rim seals. Turbomachinery is well suited to frequency domain CFD methods due to the periodicity of the flow, both geometrically and temporally. The approach has the potential to greatly reduce computational cost over conventional time domain simulations.

The ability to accurately capture unsteady annulus flow fields using nonlinear frequency domain codes is well proven (e.g. Custer *et al.* (2012), Frey *et al.* (2014), Subramanian *et al.* (2013)), however less success has been demonstrated when modelling the problem of gas turbine ingress. Chapters 4, 6 and 7 of the present thesis include much discussion on large-scale structures present in turbine rim seals. It is considered important that these phenomena are captured in order to accurately compute ingress. This presents a clear challenge to frequency domain solvers, given that the unsteadiness is not forced at a known frequency and may vary with flow conditions. Anecdotally, the HB solver in DLR TRACE has been used to capture Von Kármán vortices resulting from flow over a cylinder, however, to the author's knowledge HB solvers have not been used to capture naturally occurring unsteadiness in gas turbines.

Section 5.1 details the numerical methodology used for HB computations, with corresponding results presented in 5.2 and 5.3. Section 5.4 provides a broader discussion of the considerations for future HB ingress computations, in addition to a summary of the work completed so far.

5.1 Modelling Approach

To simplify the problem of capturing large-scale rim seal structures, the initial computational work presented here uses the baseline stage fitted with the bladeless rotor discussed in Section 4.3.2. URANS results from this configuration showed unsteady activity at harmonics of a distinct frequency, rather than the broader spectra associated with bladed computations. This behaviour lends itself to simplified frequency domain simulations. Additionally, the absence of rotor blades means the whole stage can be modelled in a single stationary domain and the challenge of coupling the vane-blade interaction frequencies is not present.

The FFTs displayed in Figure 71 showed wheel-space pressure in bladeless URANS computations. Instabilities were strongest at $\Phi_0 = 0.021$; in order to provide the best opportunity for similar structures to form, this value of Φ_0 was used for the HB computations presented here. Figure 73 shows FFTs of the URANS computation at $\Phi_0 = 0.021$, this time depicting data from the axial clearance of the rim seal, where unsteadiness is strongest. Plots (a) – (f) depict spectra for normalised values of pressure, velocity, turbulent kinetic energy and turbulent dissipation rate.

Across all variables, activity occurs at $f/f_d = 30.2$, and at higher harmonics of this frequency. The accuracy of a HB solution is clearly dependent on the number of harmonics, N_f, retained in the solution. However, the computational cost is proportional to $2N_f + 1$. In Figure 73 activity above the 3rd harmonic is not significant for pressure and velocity fields, therefore the HB computations presented here retain three harmonics with the same fundamental frequency. Plots (d) and (e) indicate that higher harmonics contribute more significantly to the fluctuations in turbulence, however it is common practice to model only the zeroth harmonic of the turbulence field in HB computations (e.g. Frey *et al*. (2014)); this approach was adopted for the computations presented in Section 5.2. It is also the default for TRACE v9.0.411 and results in improved stability, this is discussed further in Section 5.3.

Theoretically, a single vane passage model can be adopted for HB computations, however to retain commonality with the URANS computations (used for direct comparison) the same 22.5 degree mesh with two vanes was adopted. Where possible the HB computations also used the same numerical methods: the SST k-ω turbulence model was employed with the Kato-Launder limiter, the second-order Fromm scheme was chosen for spatial discretization and Sutherland's law was used for computing viscosity. For reasons of stability, a reduced CFL number of 10 was required (URANS computations used 100). A passive scalar transport equation, used to trace ingress in the URANS models, was not included in HB computations presented in Section 5.2. This was for reasons of stability and is discussed further in Section 5.3. Monitor points were also not available for the harmonic balance computations, although the capability was later introduced in v9.1.519. HB computations were initialised from converged RANS solutions and achieved average residual levels ~ 10^{-5} (N.B. URANS achieved < 10^{-6}).

Figure 74 depicts maximum and average residuals (top) alongside contours of non-dimensional pressure amplitude, C_p, after (a) 20,000, (b) 40,000, (c) 60,000 and (d) 100,000 timesteps in a harmonic balance computation. The contours depict pressure amplitude for $f/f_d = 30.2$, the fundamental frequency, and are shown on the annulus hub and wheel-space walls. Residuals appear relatively stable between 10,000 < Timestep < 30,000, however Figure 74 (a) indicates that after 20,000 timesteps no significant unsteadiness has formed at the fundamental frequency. Between 30,000 < Timestep < 55,000, there is a distinct change in behaviour with larger average residuals and falling maximum residuals. This is the range at which the large-scale structures form. Figure 74 (b) shows that after 40,000 timesteps non-zero values of C_p exist in the seal region. Beyond 55,000 timesteps, there is little variation in residuals. Figure 74 (c) and (d) indicate no significant change in the amplitude of pressure at $f/f_d = 30.2$, between 60,000 and 100,000 timesteps. They also show that the strength of the unsteadiness is at a maximum in the outer part of the rim seal, as expected. Results from this computation are discussed further and compared directly to those of the similar URANS simulation in Section 5.2.

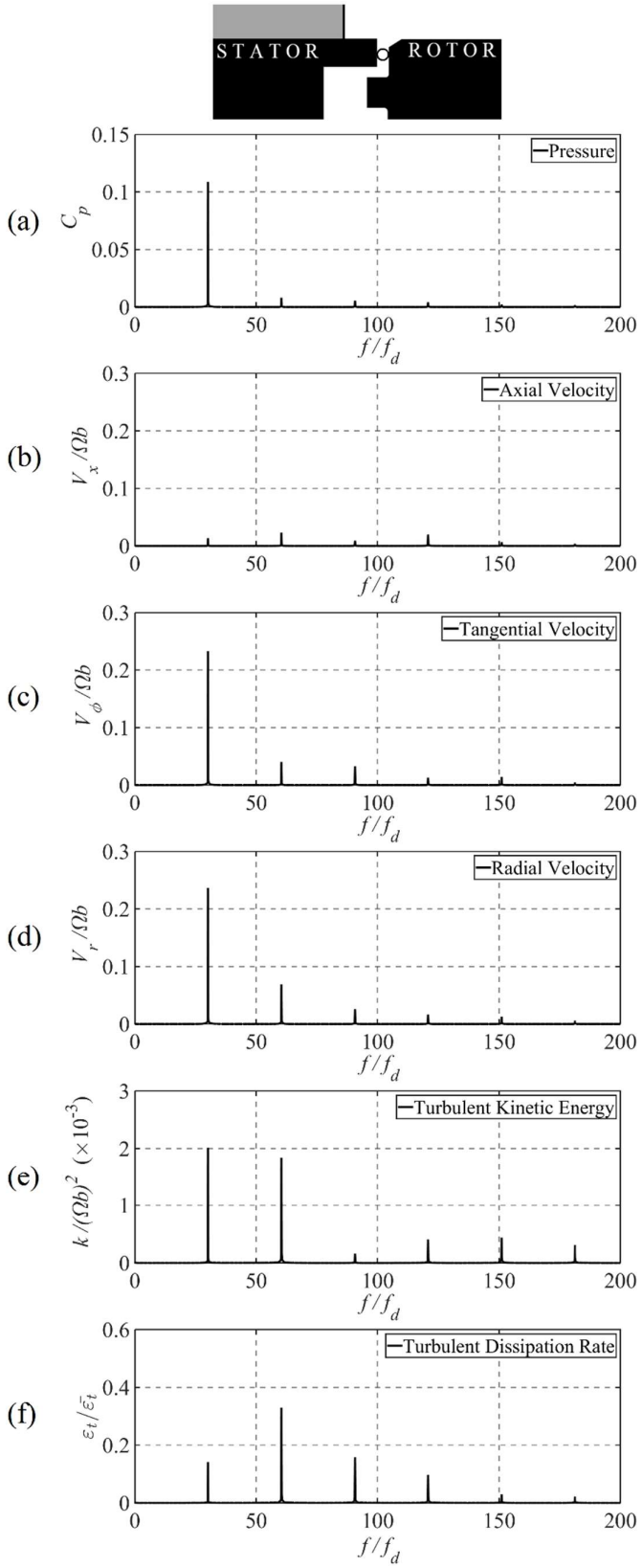

Figure 73: FFTs of computed variables within the seal for time-domain URANS computations of the bladeless configuration

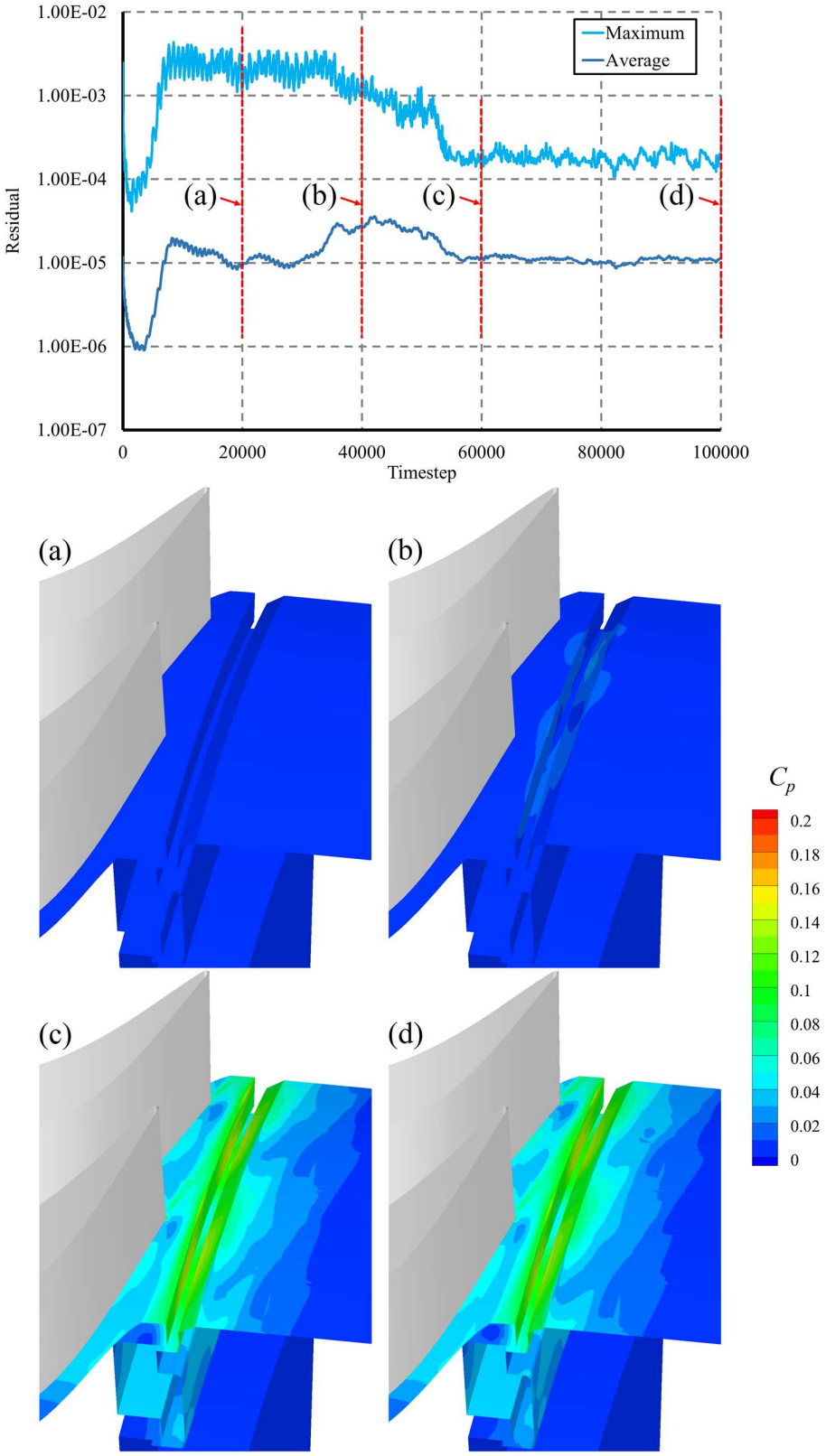

Figure 74: Formation of large-scale structures. Mean and maximum residuals (top), alongside contours of unsteady pressure amplitude at $f/f_d = 30.2$ after; (a) 20,000, (b) 40,000, (c) 60,000 and (d) 100,000 timesteps

5.2 Time-Averaged and Time-Accurate Flow Characteristics

Figure 75 depicts the circumferential pressure difference downstream of the vanes, ΔC_p, against axial position. The results are shown at the hub (r/b = 1.026) and data from the zeroth harmonic of the HB computation is shown alongside time-averaged URANS data. For both computations, Φ_0 = 0.021 and $Re_\phi = 1.0\times10^6$. A decay in ΔC_p with increasing distance from the vanes was discussed in Section 4.3.2 and is again clearly apparent. However, the figure also demonstrates strong agreement between the two computations. Despite the two data sets being based upon the computed steady flow, the correlation is encouraging given that the unsteadiness above the rim seal is likely to have nonlinear effects on the flow field.

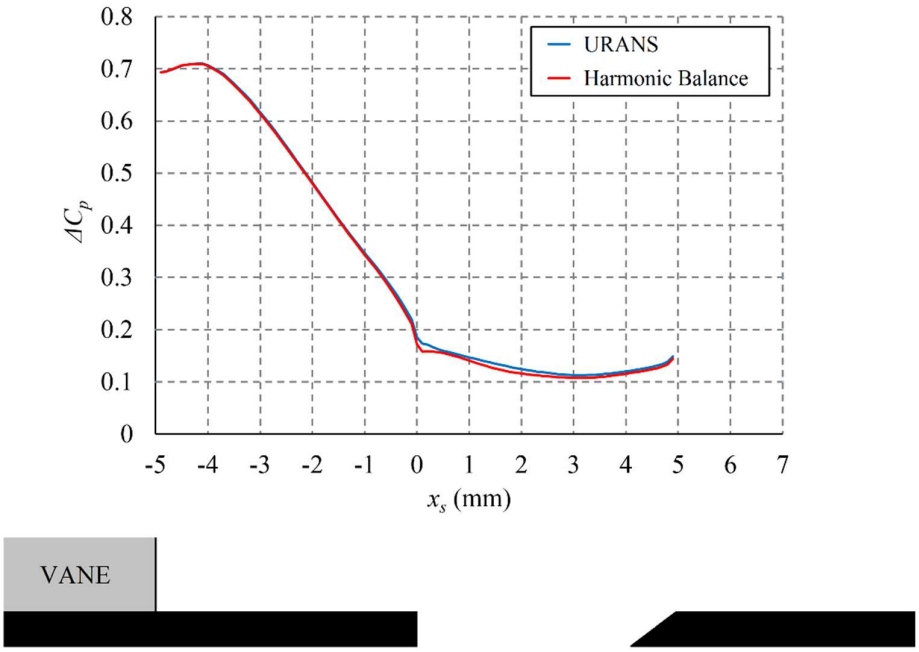

Figure 75: Peak-to-trough pressure distribution at the annulus hub for harmonic balance and URANS computations (Φ_0 = 0.021)

Figure 76 compares the radial profile of swirl, β, between HB and URANS computations. The location of the profiles are indicated by the solid lines in the radially aligned silhouette, spanning the outer wheel-space and the rim seal. Slight discrepancies are present in the rim seal, however the results correlate well, and again indicate that the harmonic balance computation is equivalent to the time-domain simulation when capturing the mean flow field.

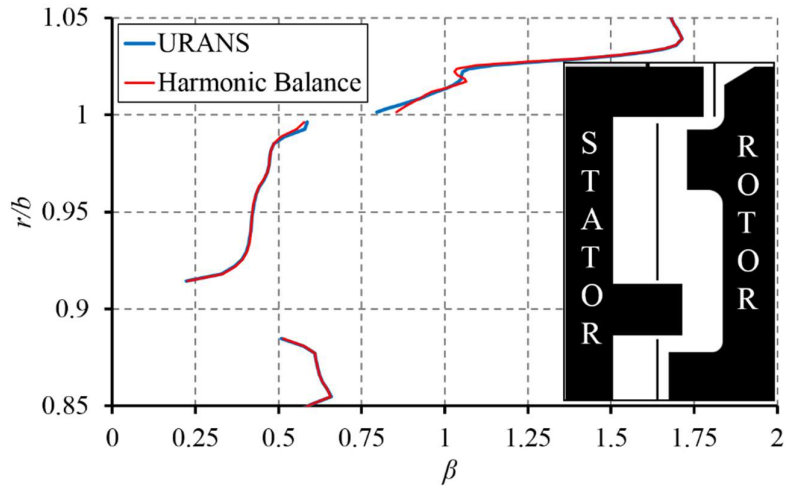

Figure 76: Variation in swirl for harmonic balance and URANS computations ($\Phi_0 = 0.021$)

The unsteady behaviour of the URANS and HB computations can be compared using contours of unsteady pressure amplitude, C_p. Figure 77 (a), (b) and (c) depict these for the first, second and third harmonics of the of the fundamental frequency, $f/f_d = 30.2$. In each case the left plot shows URANS results whilst the right plot depicts HB results. Contours are applied to the hub and wheel-space walls and the URANS results are based on a Fourier transformation of the final computed revolution.

Figure 77 confirms that the unsteadiness is strongest in the outer region of the rim seal. The fundamental amplitude is a result of 32 large-scale structures rotating at $\omega/\Omega = 0.94$ around the rim seal. These structures are thought to be driven by high levels of shear between the wheel-space and annulus flows, but the presence of the blades can have a strong influence, generally reducing their stability (see Section 4.3.2). In Figure 77, across all harmonics, C_p is periodic in the azimuthal direction, this time indicating the impact of the vanes on the unsteady flow field. This behaviour is captured across both URANS and harmonic balance simulations and reflects good overall agreement between the unsteady flow fields. However, Figure 77 does show a slight increase in the strength of unsteady perturbations for the HB simulation, this is most obvious at the two higher harmonics ((b) and (c)). This is believed to be due to the simplified HB model neglecting higher harmonics of the turbulence transport equations and is discussed further in Section 5.3.

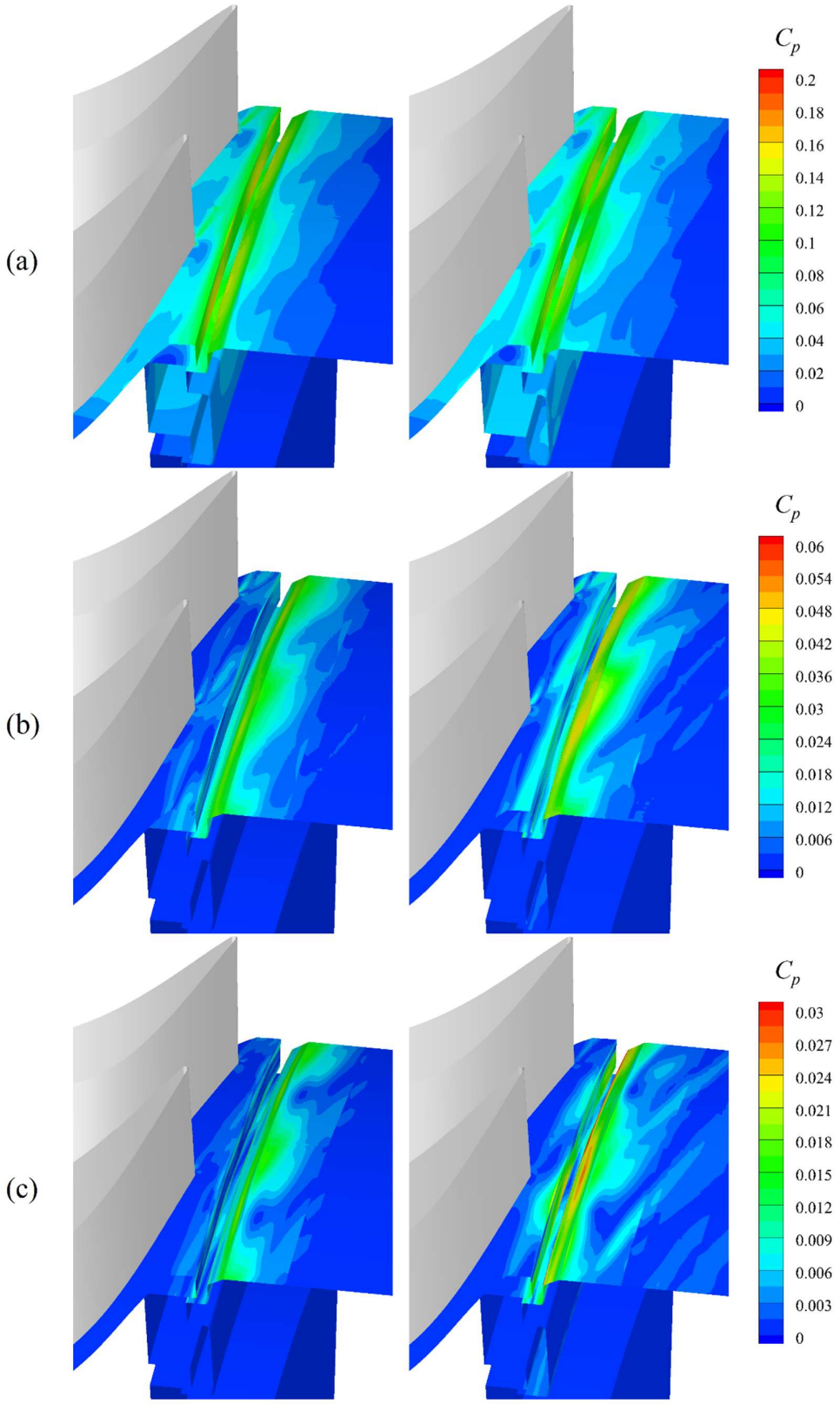

Figure 77: Contours of unsteady pressure amplitude in URANS (left) and harmonic balance (right) simulations; (a) f/f_d = 30.2, (b) f/f_d = 60.4, (c) f/f_d = 90.6 (Φ_0 = 0.021)

5.3 Modelling Ingress

A passive scalar transport equation, which has been used to trace ingress in conventional computations, was not included in the initial HB computation presented in Section 5.2. Figure 78 depicts maximum and average residuals for this computation, alongside those from a case with all three harmonics of the passive scalar and turbulence model equations activated. With the additional harmonics enabled the residuals suddenly increase and the solution becomes unstable after ~ 35,000 timesteps, corresponding to the large-scale structures forming in the initial HB computation. The maximum residuals were found to be located within the rim seal. Turbulence variables should only be defined in the positive range and can often change by several magnitudes. Kügeler *et al.* (2018) highlight that modelling this turbulence field with a relatively small number of harmonics (typically <5) can lead to overshoots (known as the *Gibbs effect*) with nonphysical negative values that de-stabilise the solution. Despite efforts to increase the stability with additional damping factors and 1st order spatial discretization, it was not possible to produce a stable solution with the higher harmonics enabled.

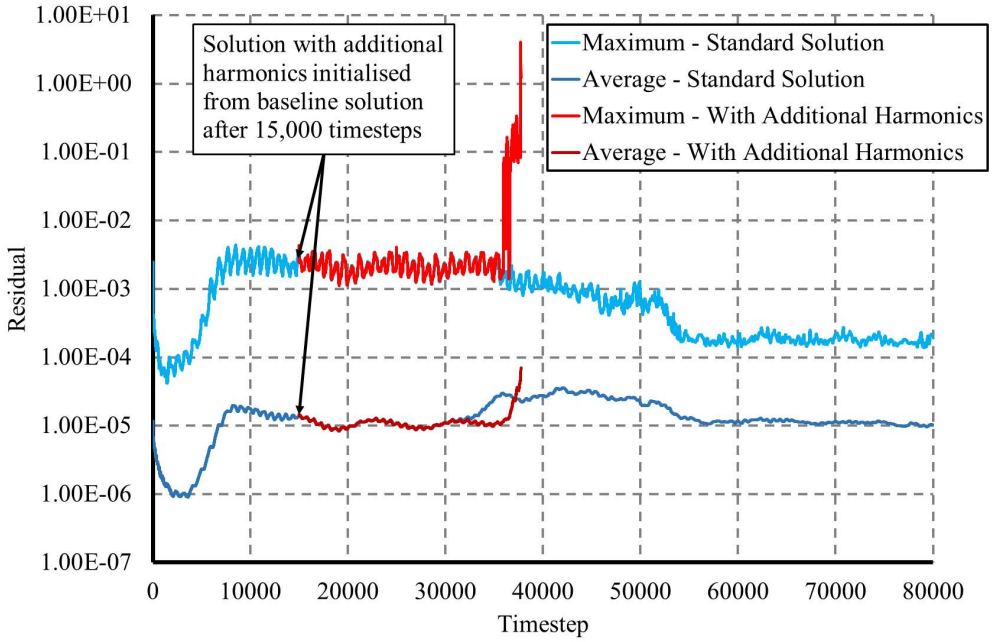

Figure 78: Stability of harmonic balance computations

It would be desirable to model the higher harmonics (above zeroth harmonic) of the passive scalar without the higher turbulence harmonics that were found to reduce stability. Unfortunately, this is not possible in TRACE v9.0.411, therefore an alternative method to measure ingress was explored.

It is possible to measure ingress based upon on the difference between local, purge and annulus temperatures. However, this method requires isolation of the temperature rise from frictional heating on the rotor and stator surfaces; something that is not easily achieved in the relatively complex double radial seal used here.

An alternative temperature based effectiveness, ε_T, can be calculated in a similar manner to the concentration-based effectiveness (equation 2.8) by comparison of two computations with different annulus inlet temperatures. This measure of effectiveness can be calculated as follows:

$$\varepsilon_T = \frac{\Delta T - \Delta T_a}{\Delta T_0 - \Delta T_a} \qquad \textbf{5.1}$$

where the ΔT, ΔT_a and ΔT_0 are the local, annulus and purge temperature differences between the computations. The method works on the basis that a small change in annulus inlet temperature does not significantly alter the fluid dynamics but provides a known difference in the temperature of ingress in each of the two computations. For the present study the URANS and HB (without additional harmonics) computations were re-computed with a 10 K differential in annulus inlet temperature.

Figure 79 depicts radial profiles of sealing effectiveness on the stator wall for URANS (blue) and HB (red) computations. The solid lines depict temperature based effectiveness, ε_T, whilst the additional dashed line represents concentration-based effectiveness, ε_c, available for the URANS simulation only. The profiles of ε_T and ε_c for the URANS computation collapse, giving confidence in the temperature based approach for measuring effectiveness. However, whilst the HB and URANS computations show the same reduction in effectiveness with radius, there is significantly more ingress measured in the time-marching computation. It is speculated that this results from neglecting the harmonics of turbulence in the HB model. This is discussed in the context of Figure 80 below.

Figure 80 depicts contours of normalised turbulent kinetic energy, $k/(\omega b)^2$, on a circumferential plane depicted in the isometric view. Plots (a) and (b) depict the zeroth harmonic of the HB and URANS simulations respectively. Plots (c), (d) and (e) depict the first, second and third harmonics of the fundamental frequency $f/f_d = 30.2$, for the URANS simulation. The URANS results are based on a Fourier transformation of the final computed revolution and all plots use a common scale.

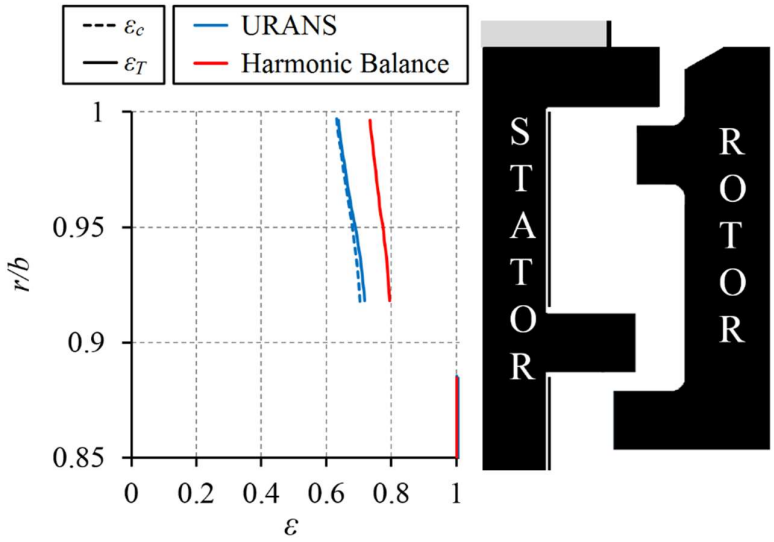

Figure 79: Radial profiles temperature and concentration-based sealing effectiveness on the stator wall for URANS and harmonic balance simulations ($\Phi_0 = 0.021$)

The higher harmonics in Figure 80 (c), (d) and (e) indicate the fluctuations in turbulence that are not included in the harmonic balance computation. The amplitude of the first harmonic in the axial clearance of the rim seal is ~0.015 and is of similar magnitude to the time-averaged value, indicating that the normalised turbulent kinetic energy varies between close to zero and ~ 0.03. The amplitude of the second and third harmonics are reduced relative to the first, but still significant.

Interestingly, the zeroth harmonic of the URANS simulation, (b), displays significantly higher levels of turbulent kinetic energy within the rim seal, when compared to the HB computation, (a). This suggests that the interaction between harmonics has a nonlinear effect on the average field. It is this reduction in turbulence from the HB model that is believed to drive less ingress through the rim seal and indicates that the harmonics of turbulence should be included if HB simulations are to capture the same physical effects as URANS simulations.

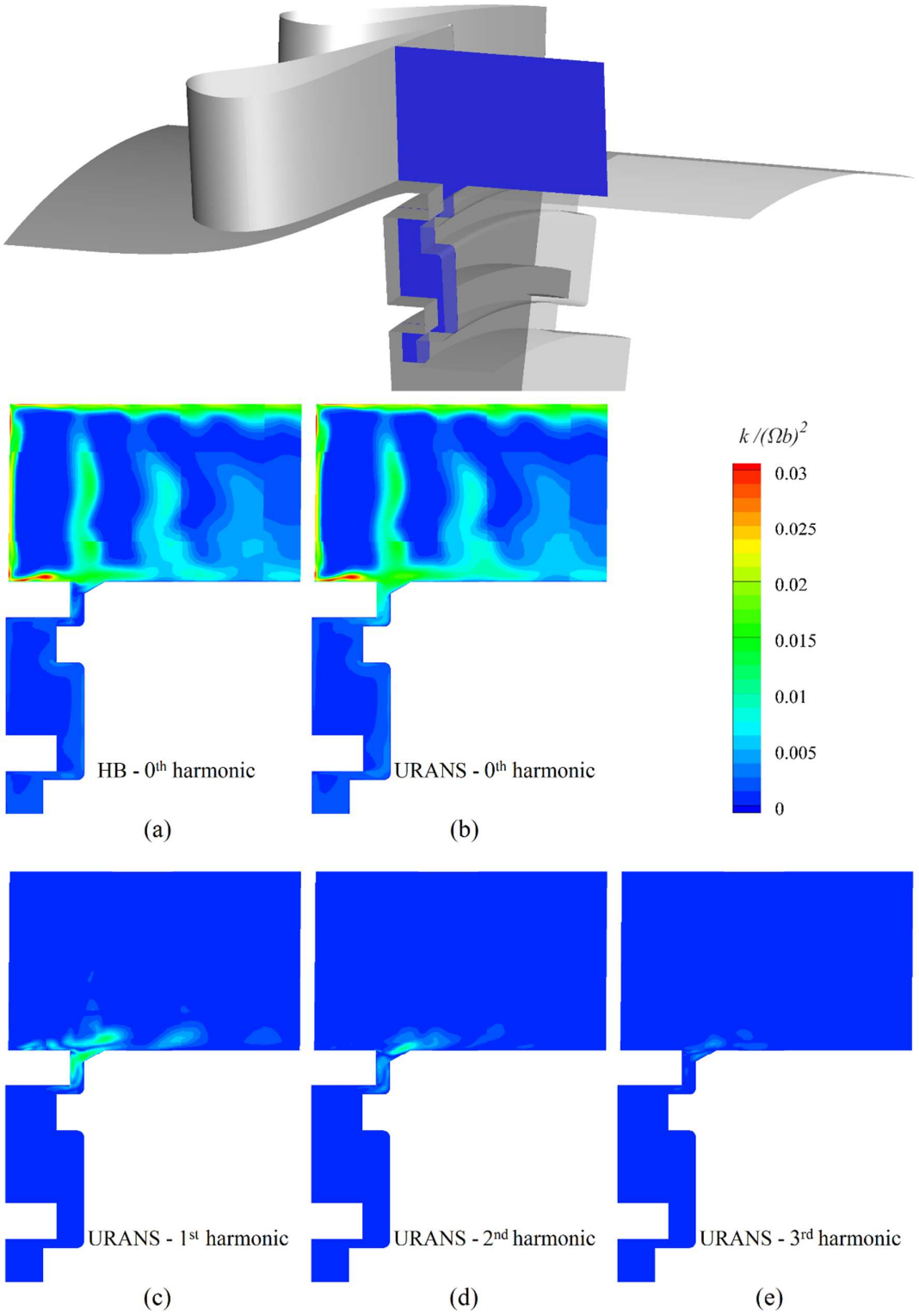

Figure 80: Contours of normalised turbulent kinetic energy in URANS and harmonic balance simulations ($\Phi_0 = 0.021$)

5.4 Summary and Future Considerations

This chapter has presented nonlinear frequency domain computations using the harmonic balance solver in TRACE v9.0.411. Large-scale rotating rim seal structures have been captured using a frequency domain solver for the first time. The behaviour of these instabilities was shown to be very similar to those computed from a time-marching URANS case, but were achieved with a reduced computational cost.

Stable HB solutions have not been demonstrated with the higher harmonics of the turbulence model included. Furthermore, comparison to URANS simulations indicates that ignoring the nonlinear unsteady effects associated with these harmonics may cause a reduction in computed ingress.

Computations have so far only been undertaken for one flow condition and with a simplified bladeless rotor. It is likely that the introduction of a bladed rotor, which requires both a non-matching grid interface and the additional coupling between vane and blade passing frequencies, will challenge the stability of the solution. Moreover, if the fundamental frequencies from vane-blade interactions were to differ from those of the large-scale structures, they would need to be modelled in separate 'harmonic sets'. Whilst the solver can model multiple harmonic sets, they are only coupled through the zeroth harmonic and therefore any nonlinear interactions between the higher harmonics of the two sets are neglected (Kügeler *et al.* (2018)). It is not possible to be certain of the consequences for the solution, however, given that both the vanes and blades have been shown to influence large-scale structures, the effect may be significant. It should also be noted that the presence of blades has been shown to drive a wider spectrum of unsteadiness (see Chapter 4), rather than the distinct frequencies present in Figure 73. It is unclear how neglecting much of this spectra would influence ingress.

The frequencies defined in the HB computations were informed by URANS simulations. However, further investigation is required to understand the sensitivity of ingress to the selected frequencies and more broadly to understand how purge flow rate and annulus conditions may influence large-scale structures. Ultimately, to be a valuable tool HB computations must be able to adopt frequency information, preferably from an analytical relationship based on the geometry and flow conditions of the turbine, but more realistically from experiment. Whilst this is achievable it does limit the suitability of the computations.

The fundamental reason for adopting a frequency domain solver is the potential reduction in computational effort. Table 7 lists the approximate computational cost of the bladeless HB and URANS simulations which used the 22.5° sector models, alongside estimated costs for a 360° URANS calculation and an 11.25° HB calculation. The computed cases were run on 64 cores

using the University of Bath cluster as described in Chapter 3. From the table it can be seen that the 22.5° HB model provides only a 35% reduction in computational effort over the similarly sized URANS model. This reduction is modest due to the reduced CFL (10) required for stability of the HB solution and the common mesh used in both cases. The reduction would be higher if the single vane/blade sector HB model – possible due to the phase-lag boundary conditions - was compared to the full 360° URANS. However, it should be noted that the additional higher harmonics of turbulence and the harmonics associated with vane and blade interactions would almost double the computational cost of HB simulations.

Computation	Core hours
URANS – 22.5° sector	~ 13,000
URANS – 360° sector	~ 208,000*
Harmonic Balance (3 harmonics) – 22.5° sector	~ 8,500
Harmonic Balance (3 harmonics) – 11.25° sector	~ 4,250*

Table 7: Computational cost of simulations (* indicates estimated time)

Overall, encouraging progress has allowed harmonic balance solvers to capture large-scale structures associated with ingress, however several key challenges must be addressed if they are to be used to reliably compute ingress with the same fidelity as conventional URANS simulations. Additionally, when compared to reduced sector time-domain models, HB computations may provide only modest improvements in computational cost.

Chapter 6: Increased Reaction Stage

This chapter presents results for a computed 1.5-stage turbine incorporating two stator rows either side of a rotor. The upstream vane profile adopted for the work here is the same as that of the baseline stage, however the blade row was modified to achieve a higher degree of reaction and a second downstream stator row was also included. Ingress into the wheel-space cavities upstream and downstream of the rotor is considered. The study was also extended to consider the influence of injecting purge from high radius holes in the stator wall. Previous research (e.g. Zhang *et al.* (2017) and Patinios *et al.* (2018)) has shown these flows, which are entirely possible in a real turbine, can influence the wheel-space flow structure and ingress levels. The geometry and setup of all computations discussed in this chapter are detailed in Chapter 3.

The degree of reaction expresses the fraction of expansion that occurs across the rotor compared to the stage. Turbine designers make an informed choice on the degree of reaction based upon their requirements. Steam turbines often operate with pressure ratios over 1000:1 and therefore impulse blading ($\Lambda = 0$) may be desired in the high pressure stages to minimise blade tip clearance losses (Saravanamuttoo *et al.* (2017)). However, industrial gas turbines operate with much lower pressure ratios (e.g. 24:1 for Siemens SGT5-9000HL (Siemens-AG (2018))) and may find improved efficiencies with increased reaction. The blade profiles of the modified turbine stage were designed by Siemens and are intended to be more representative of industrial gas turbines. A direct comparison of the baseline and increased reaction blading is depicted in Figure 81.

Degree of reaction can be calculated based upon the following relationship:

$$\Lambda = \frac{T_2 - T_3}{T_1 - T_3} \qquad \textbf{6.1}$$

where T_1 and T_2 represent temperatures upstream and downstream of the stator, and T_3 represents the temperature downstream of the rotor.

Computed profiles of spanwise reaction across the full annulus are depicted for both the baseline and increased reaction stages in Figure 82. The non-dimensional radius, *r/b*, and reaction, Λ, are displayed on the ordinate and abscissa respectively. In both computations $\Phi_{0,u} = 0.029$ and the results are based upon temporally and circumferentially-averaged data. It can be seen that outside the boundary layers the reaction increases from $\Lambda \sim 0.14$ for the baseline stage to $\Lambda \sim 0.27$ for the modified stage. The figure also shows very similarly shaped profiles between configurations; a result of only modest changes to the blade profile and consequently to the secondary flow field.

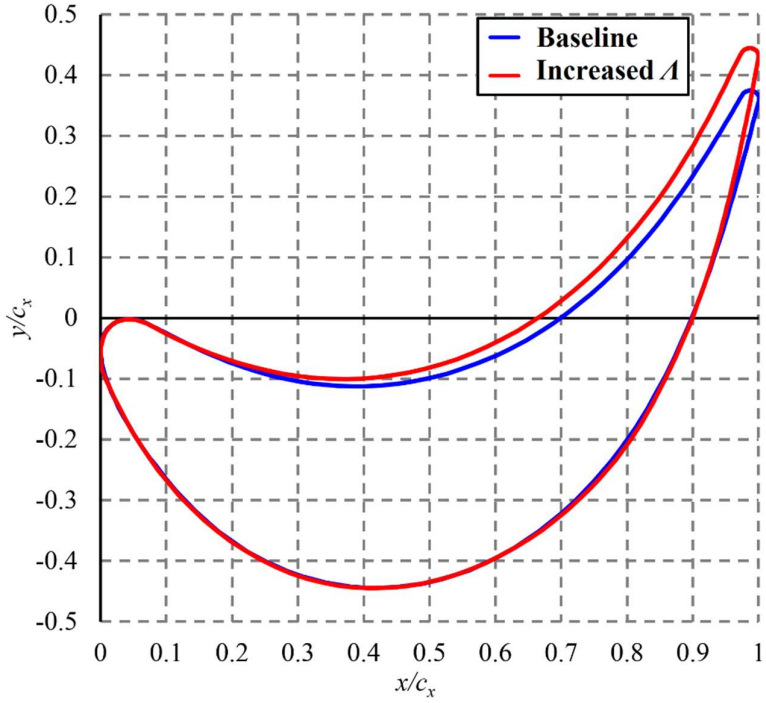

Figure 81: Blade profiles for the baseline and increased reaction configurations

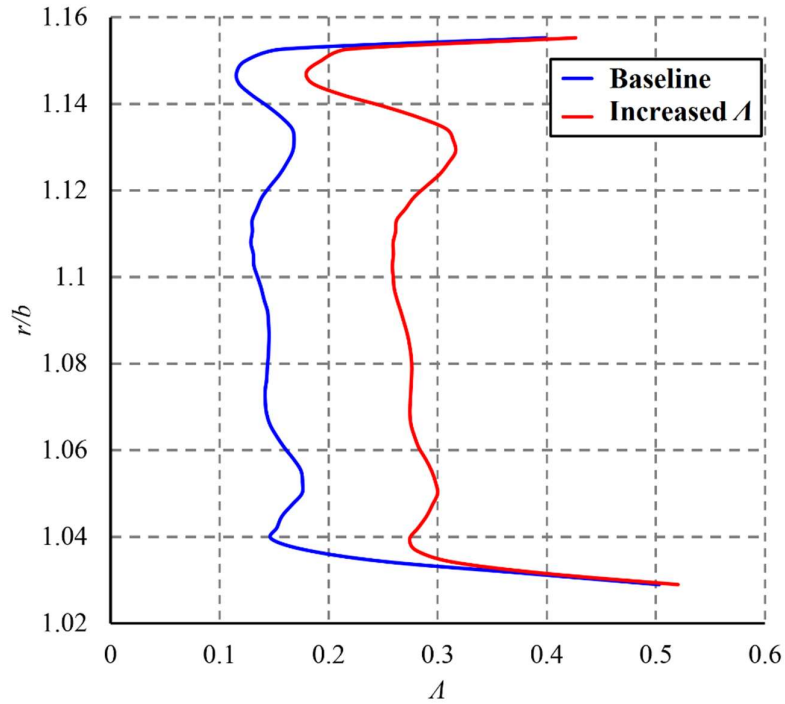

Figure 82: Spanwise profiles of Λ across annulus ($\Phi_{0,u}$ = 0.029)

Further comparisons between the baseline and increased reaction stages are presented in Section 6.1, which investigates the influence of the increased reaction blading on ingress into the

upstream wheel-space. Section 6.2 discusses ingress into the downstream wheel-space, while Section 6.3 looks at the impact of high radius purge in both the upstream and downstream cavities. Computed results are compared to a limited range of experimental data, including measurements of pressure in the annulus and of ingress at two wheel-space locations. At the time of writing, further steady and unsteady experimental data, of the type discussed for the baseline stage, was unavailable for comparison. It should also be noted that all experimental data presented is provided for validation purposes and was not measured by the present author.

6.1 Upstream Cavity

Figure 83 presents the circumferential distribution of annulus pressure coefficient, $C_{p,a}$, on the hub, as depicted in the silhouette. Discrete symbols represent experimental data, whilst the continuous lines show computed results. Red and blue data sets depict the increased reaction and baseline configurations respectively, as is the case for all figures in this section.

Computationally, no change is observed between the two configurations. This is to be expected given that the steady pressure field on the hub is not believed to be influenced by the blade; indeed Chapter 4 showed that removing the blade made no difference to the peak-to-trough pressure difference, ΔC_p, at this location. Experimentally, a slight increase in ΔC_p is observed with the increased reaction blading, however this is within the bounds of experimental uncertainty and the results still demonstrate relatively good agreement with computation.

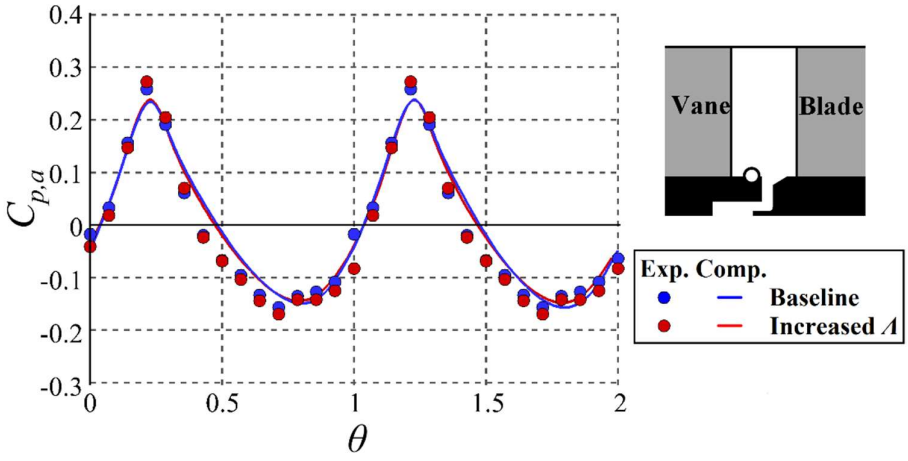

Figure 83: Circumferential distribution of pressure coefficient in the annulus over two non-dimensional vane pitches ($\Phi_{0,u}$ = 0.029)

Figure 84 depicts the variation in concentration-based effectiveness with sealing flow parameter, $\Phi_{0,u}$, on the stator disc at r/b = 0.958. Data from the increased reaction stage are contrasted to baseline stage results duplicated from Chapter 4. Computational and experimental results demonstrate broadly similar trends and the general under-prediction of computed ingress

remains for the increased reaction stage. Relative to the baseline results at $\Phi_{0,u}$ = 0.021, 0.029 and 0.050, the computations show ~3% increase in ingress. Experimentally, a slight increase in ingress is also shown, and the inflection in the curve (discussed in Chapter 4) occurs at a higher value of $\Phi_{0,u}$, suggesting a change in unsteady behaviour. Measurements of unsteady pressure were not available at the time of writing, however the increase in ingress is discussed in the context of FFTs of computed pressure below.

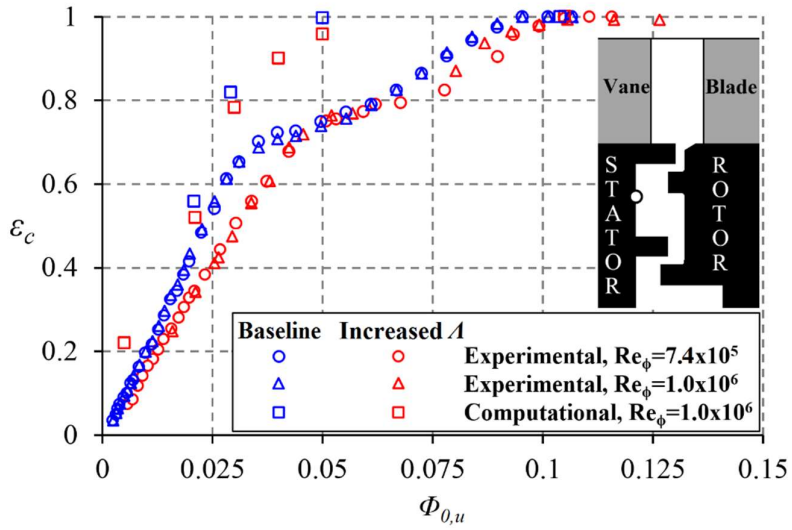

Figure 84: Variation in upstream wheel-space concentration effectiveness with non-dimensional sealing parameter

FFTs of computed pressure within the axial seal are presented in Figure 85. Unsteady results for the baseline geometry have again been presented alongside those of the increased reaction geometry; frequencies and amplitudes are normalised in a similar manner to previous FFTs. Four purge flow rates are shown, and the silhouette indicates the monitoring point. The analysis was performed over the final computed revolution of the disc using the methodology outlined in Chapter 4.

Across all four purge rates, activity at the BPF (f/f_d = 48) is largely unchanged between the two turbine configurations, also strengthening at higher purge as previously discussed. Considering the effect of increased reaction at $\Phi_{0,u}$ =0.021 and 0.029, activity below the BPF is dominated by the same frequencies, which correspond to the same number of large-scale structures rotating at approximately the same speed (detailed in Table 8). However, a clearer difference between frequencies is observed at $\Phi_{0,u}$ = 0.05. For the increased reaction geometry, pressure fluctuations are more clearly defined with distinct activity at f/f_d = 13, corresponding to 16 structures rotating at ω/Ω ~ 0.81. Broadly speaking the amplitude of unsteady pressure fluctuations across the three lowest sealing flow rates is increased for the increased reaction blading, although this is most apparent at $\Phi_{0,u}$ = 0.05. It is this increase in unsteadiness that is

thought to drive the higher computed levels of ingress in Figure 84. Figure 85 (d) shows that at $\Phi_{0,u} = 0.104$ the unsteady activity for the increased reaction turbine is very similar to that of the baseline case, with a broader spectrum of unsteady activity at reduced magnitude. At this sealing flow rate both turbine configurations are fully sealed.

Non-dimensional Sealing Parameter ($\Phi_{0,u}$)	**Number of Structures (N)**	**Rotational speed of Structures (ω/Ω)**
	Baseline / Increased Λ	**Baseline / Increased Λ**
0.021	16 / 16	0.88 / 0.88
0.029	16 / 16	0.81 / 0.88
0.050	16/32 / 16	0.94 / 0.81
0.104	N.A. / N.A.	N.A. / N.A.

Table 8: Comparison of upstream large-scale flow structures for the baseline stage and increased Λ stages

Figure 86 shows profiles of swirl extending from the axial seal clearance radially outward across the annulus, as depicted by the adjacent silhouette. Again, red and blue profiles display results for the increased reaction and baseline configurations. The reduction in swirl with increasing radius is a result of vane geometries having a constant cross-section across their span. The large shear gradient across the seal, observed previously in Figure 61, is also apparent. Additionally, the figure illustrates an increase in swirl across the full span of the annulus for the increased reaction blading; an effect seen across all sealing flow rates, although only shown for $\Phi_{0,u} = 0.029$ here. It is speculated that it is the increased shear gradient above the seal that drives the higher levels of low-frequency unsteadiness observed in Figure 85 and the higher ingress shown in Figure 84. The difference in ingress caused by a slight change in annulus swirl gives an indication of the sensitivity of the problem, particularly in regards to the formation of large-scale structures.

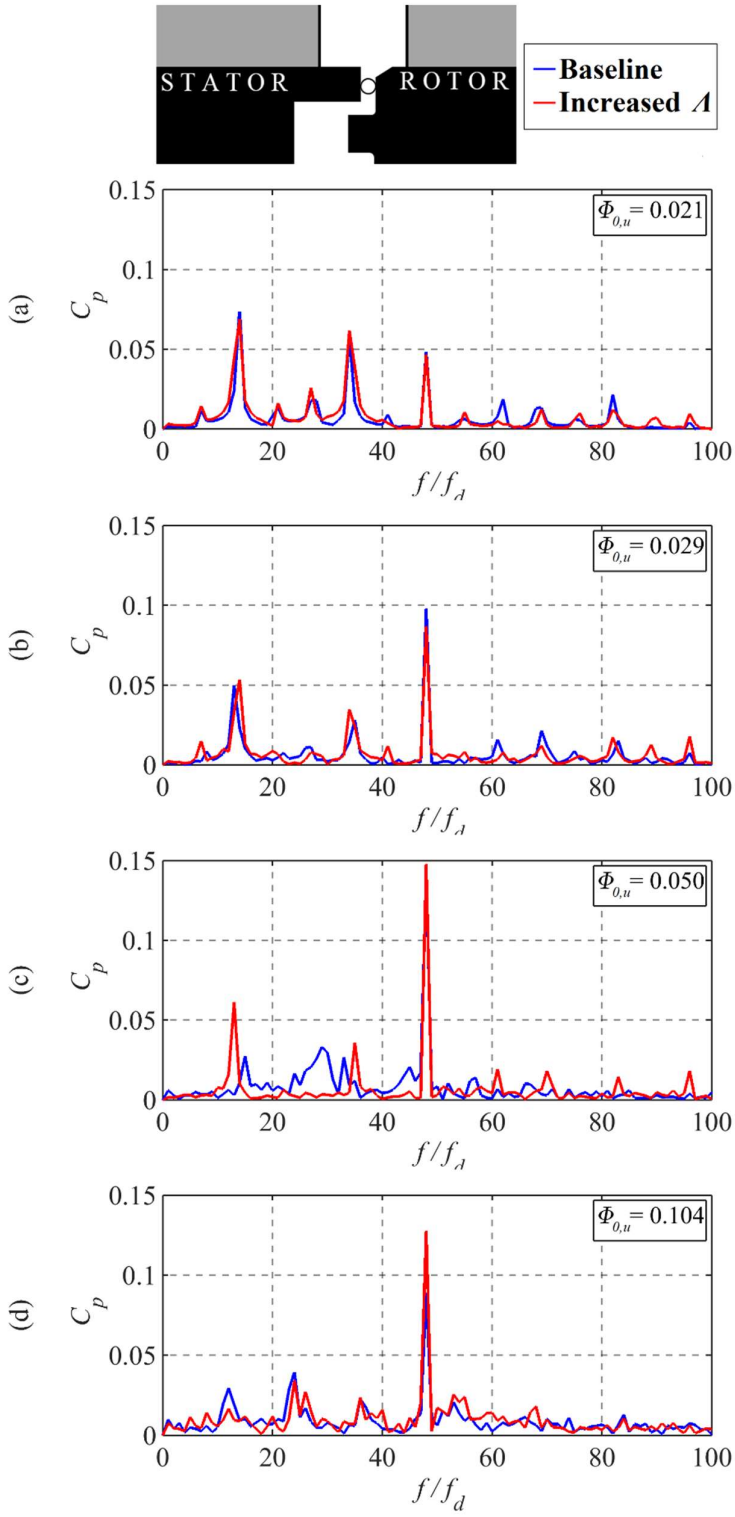

Figure 85: Fast Fourier transforms of computed pressure in the axial clearance of the upstream rim seal

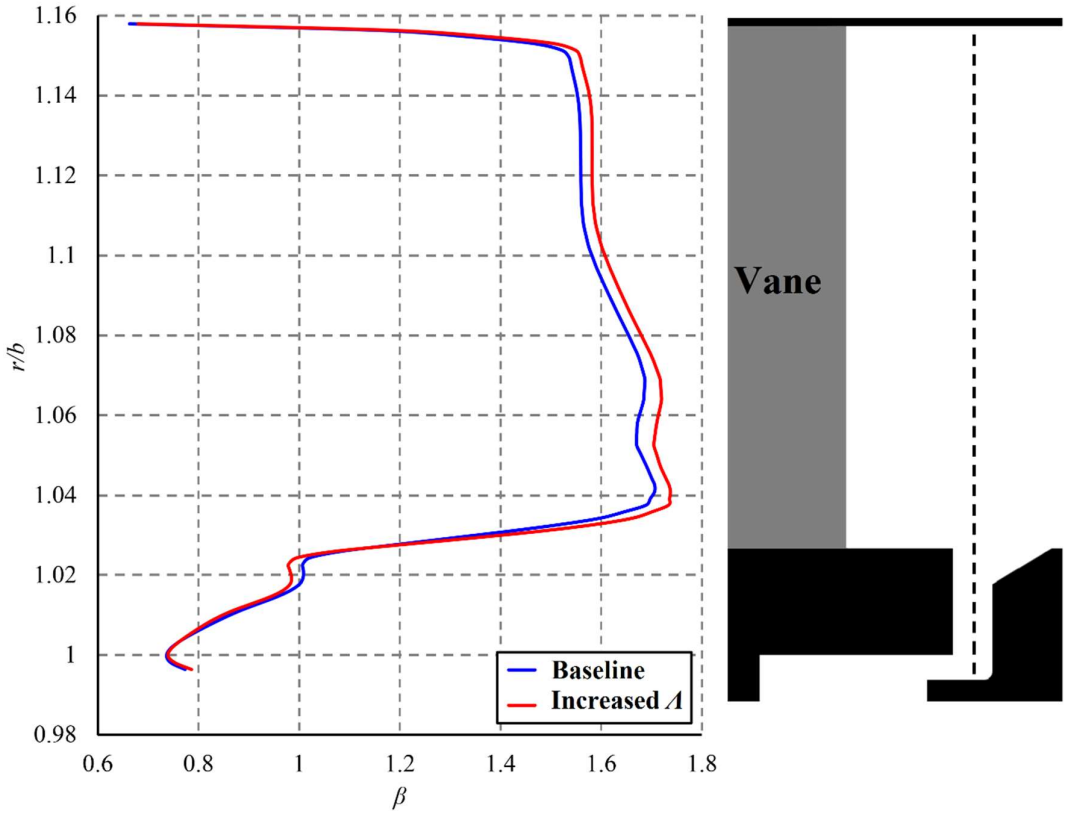

Figure 86: Spanwise profiles of swirl across annulus ($\Phi_{0,u}$ = 0.02)

6.2 Downstream Cavity

Ingress into the wheel-space cavity downstream of a rotor has not previously been studied to the same extent as ingress into the upstream wheel-space. At low radius, within the downstream cavity, the conventional flow structure of any rotor-stator system must exist, however, through the critical rim seal region, the fluid dynamics can differ to an upstream cavity as a result of a differing annulus flow field. Previous authors have also shown that the egress flow from an upstream wheel-space can influence sealing effectiveness in a downstream wheel-space (e.g. Scobie *et al.* (2018)). This section analyses time-averaged and time-accurate results to investigate ingress in a downstream cavity.

6.2.1 Annulus

Figure 87 presents the circumferential peak-to-trough pressure difference, ΔC_p, downstream of the baseline and increased reaction rotor blades. The abscissa represents axial distance from the blade trailing edge and is aligned with the silhouette below. Computed data is shown for a constant r/b = 1.026, corresponding to the annulus hub. Dashed lines represent ΔC_p in the rotating reference frame (i.e. the effect of the blades) and the solid line represents ΔC_p in the stationary

frame (i.e. the effect of the vanes). Results from the baseline (blue) and increased reaction (red) stages show ΔC_p in the rotating frame decays with axial distance from the blade, however the overall magnitude is increased for the increased reaction stage. It is speculated that this could drive higher levels of ingress into a downstream wheel-space, however with the computed baseline stage including only an upstream wheel-space, this could not be investigated further.

The downstream vanes, present in the increased reaction computations only, are analogous to the downstream blades for the upstream wheel-space, which were shown to have little influence on ΔC_p (see Figure 69). It is therefore thought likely that the downstream vanes have little effect on the rotational frame ΔC_p in Figure 87. However, it should also be noted that the seal clearance, which is again only present in the increased reaction computations, could itself influence ΔC_p, as was the case for the upstream wheel-space (see Figure 68).

Experimental data is depicted by the red circle in Figure 87. The result shows good agreement with the computed curve; however, it should be noted that the measurements were located on the chamfer downstream of the seal clearance (as depicted in the silhouette) and are therefore at a slightly reduced radius relative to the computed data. A direct comparison of the computed and measured circumferential pressure at this measurement location is shown in Figure 88.

In Figure 88 the discrete circles (experiment) and continuous line (computation) depict $C_{p,a}$ over two non-dimensional vane pitches. The computed profiles are shown for $\Phi_{0,d} = 0.01$ and 0.016. Experimental data was only available for $\Phi_{0,d} = 0.0$, but the small variation in computed $C_{p,a}$ at differing sealing flow rates indicates purge has only a minor influence. Considering this, the computed data show reasonable agreement with experiment, capturing the shape of the distribution well but with a slightly reduced peak-to-trough difference.

Figure 89 shows time-averaged contours of effectiveness and streamlines depicting egress from the downstream seal. For the depicted case $\Phi_{0,d} = 0.04$, corresponding to an almost fully sealed wheel-space. The contours show the isolated effect of downstream egress, and are clipped to $\varepsilon_c > 3\%$.

The flow through the downstream stator exhibits weaker secondary flow structures than the rotor due to reduced solidity and vane loading. The baseline stage showed upstream egress to be driven radially outward as it was entrained into the blade passage vortex (see Figure 56 and Figure 57). However, in Figure 89 the downstream egress remains hub-bound and within the suction-side leg of the horseshoe vortex, providing modest cooling at low radius only.

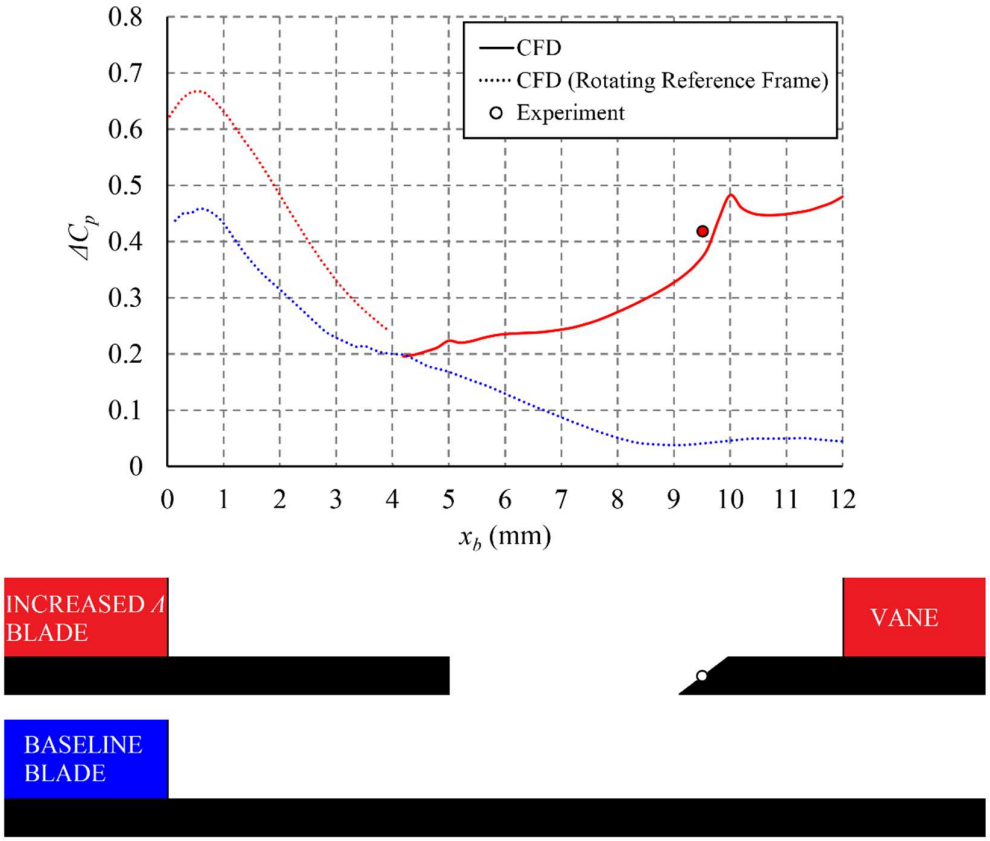

Figure 87: Variation in ΔCp on the annulus hub downstream of the baseline and increased reaction blading. Computed for $\Phi_{0,u} = 0.029$, $\Phi_{0,d} = 0.01$ and measured for $\Phi_{0,u} = 0.00$

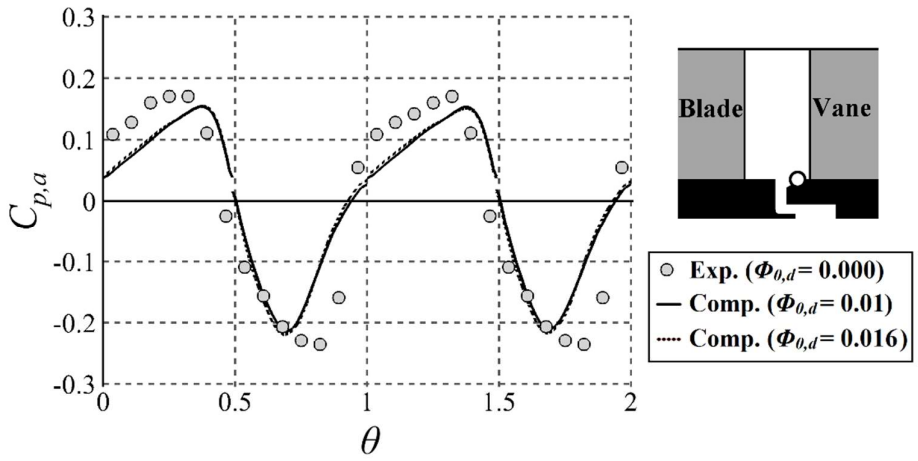

Figure 88: Circumferential distribution of pressure coefficient in annulus over two non-dimensional vane pitches

No significant re-ingestion of upstream egress into the downstream wheel-space was observed in any computations; over the wide range of upstream and downstream sealing flow rates studied the concentration of upstream tracer found in the downstream wheel-space was < 0.1%. This is believed to be due to the strong radial migration of egress through the rotor passage, which

prevents the flow from mixing in the downstream seal region. Despite this finding, it should be noted that for the baseline stage the computations under-predicted the quantity of hub-bound egress flow measured downstream of the rotor (shown in Figure 57 (b)). A similar effect for the increased reaction configuration would likely result in a computational under-prediction of re-ingestion.

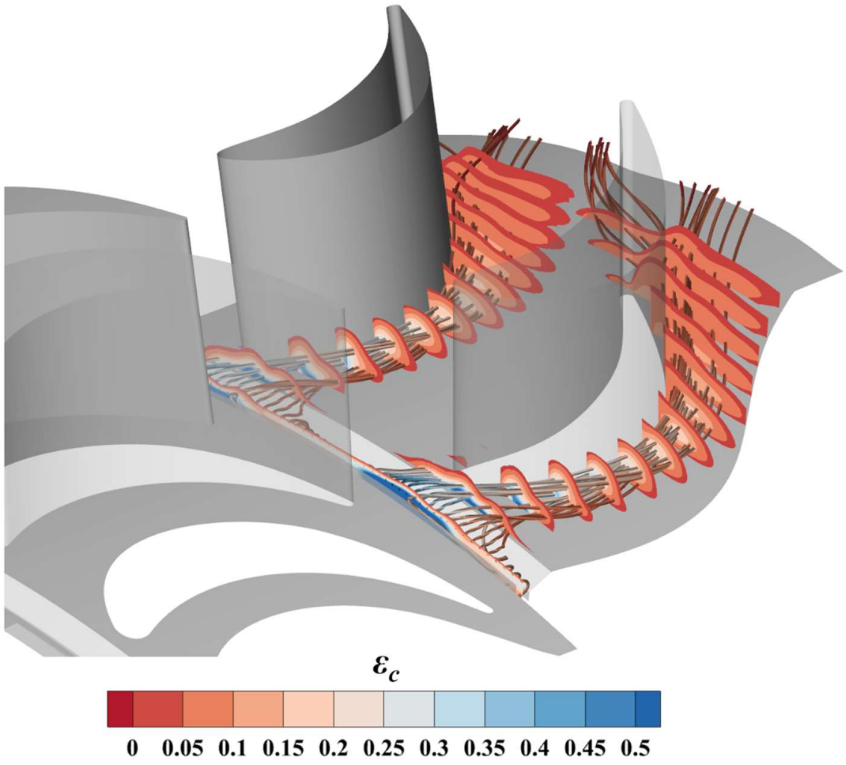

Figure 89: Sealing effectiveness through the downstream stator row (planes are clipped to $\varepsilon_c > 3\%$), with stream-traces originating from the seal: (a) ($\Phi_{0,u} = 0.104$, $\Phi_{0,d} = 0.04$)

6.2.2 Rim Seal and Wheel-Space

In this section, computed levels of ingress are compared to experiment, and numerical predictions of swirl and unsteady pressure are discussed.

The sealing effectiveness in the downstream wheel-space is depicted in Figure 90 for Φ_0 = 0.003 and 0.01. Radial profiles of effectiveness on the stator (solid lines) and in the core (dashed lines) are aligned with the adjacent contour plots.

The figures show abrupt increases in sealing effectiveness from annulus to the outer wheel-space and from the outer wheel-space to the inner wheel-space. At Φ_0 = 0.01 the inner wheel-space is almost fully sealed (ε_c = 0.99), however, at Φ_0 = 0.003, significant ingress into the lower wheel-space, where convection of the passive scalar is relatively slow, led to an approximate eight

fold increase in the computed revolutions required to reach satisfactory convergence of the passive scalar (18 revolutions for $\Phi_0 = 0.01$ versus 150 for $\Phi_0 = 0.003$).

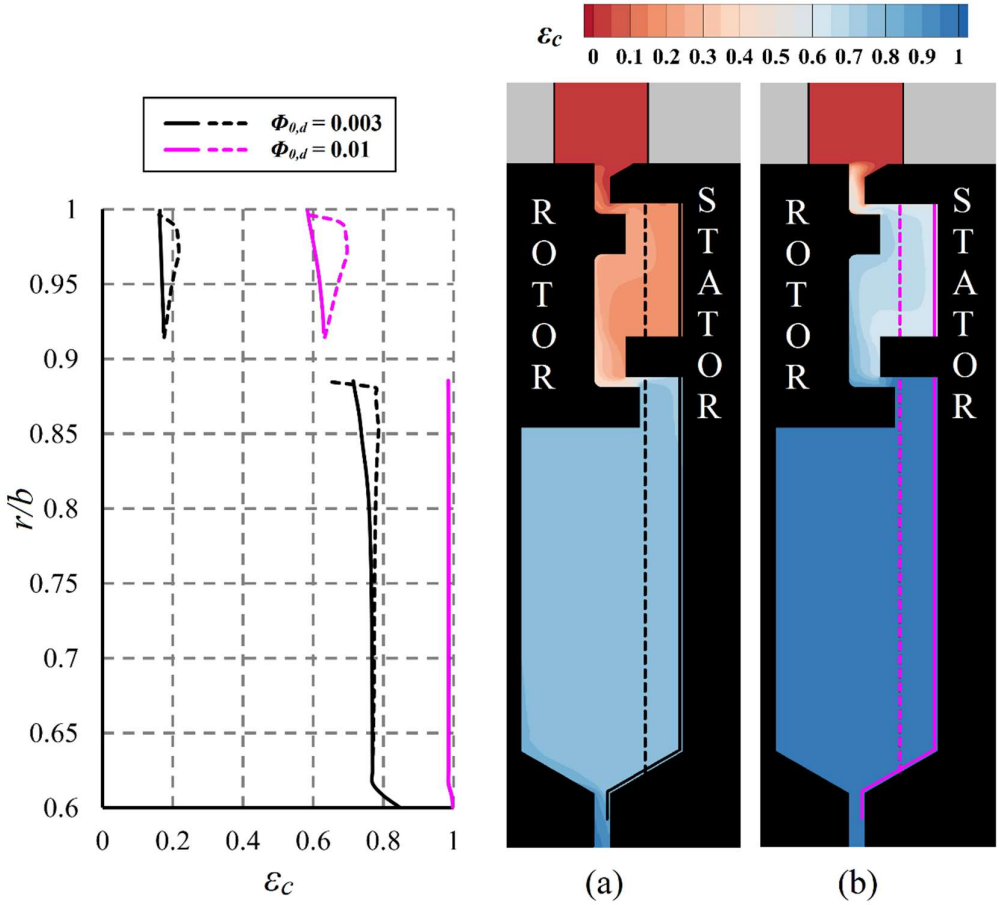

Figure 90: Concentration-based sealing effectiveness in the downstream wheel-space: (a) $\Phi_{0,d} = 0.003$, (b) $\Phi_{0,d} = 0.010$

The flow structure is consistent with that of a similar upstream wheel-space, as discussed in 4.1.3. Scalar concentration on the stator wall is largely invariant with radius as the ingested fluid is entrained into the stator wall boundary layer, which flows radially inwards. In the outer wheel-space, the core and wall concentrations diverge as the core effectiveness is affected by the rotor boundary layer, which is pumped radially outwards. A similar phenomenon can also be observed at the outer radius of the inner wheel-space, where at $\Phi_0 = 0.003$ the concentration in the core is again influenced by the rotor boundary layer.

Experimental profiles of sealing effectiveness against radius for the downstream wheel-space were unavailable at time of the writing, however the measured variation in sealing effectiveness with Φ_0 is compared to computation at two radial locations in Figure 91; $r/b = 0.85$ (white filled symbols) and 0.958 (grey filled symbols), as shown in the silhouette.

Computed results at $Re_\phi = 1\times10^6$ are indicated by red circles, while measured data at $Re_\phi = 1\times10^6$ and 7.4×10^5 are depicted by black circles and squares respectively. The two sets of experimental data collapse, suggesting an invariance with Re_ϕ.

The computational results follow a qualitatively similar trend to the measured data, however a strong under-prediction of computed ingress can be observed at both radial positions. This sort of under-prediction has been common in previous studies of ingress (e.g. Zhou *et al.* (2011)), but is more apparent for the downstream wheel-space than for the upstream wheel-space in the present study. The precise reason is unknown, however it is speculated that deficiencies in the ability of the RANS turbulence model to capture the separated flow through the angular rim seal are at least partly responsible.

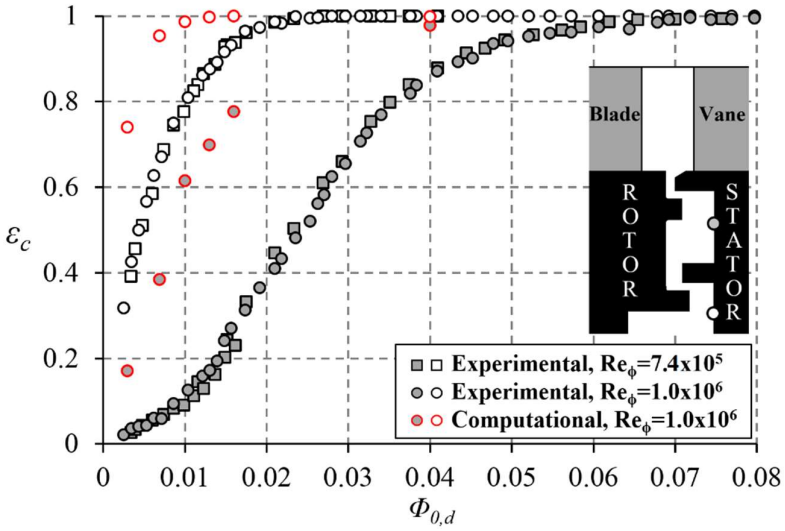

Figure 91: Variation in downstream wheel-space concentration effectiveness with non-dimensional sealing parameter

By comparing Figure 91 with the corresponding figure for the upstream wheel-space (Figure 84) we see that both computationally and experimentally the downstream wheel-space shows generally increased sealing effectiveness for a given value of Φ_0. Additionally, the inflection seen experimentally in the upstream Φ_0 - ε_c relationship is not present for the downstream wheel-space. It is believed that this, combined with the general reduction in downstream effectiveness, may in part be due to the existence of weaker large-scale structures through the downstream seal.

FFTs of computed unsteady pressure in the downstream rim seal are presented in Figure 92. Frequencies and amplitudes are normalised as per previous FFTs. Six purge flow rates are shown, ranging from Φ_0 = 0.003–0.04. As the downstream rim seal is contained within a stationary computational domain (unlike the upstream seal), data did not require the transformation from a rotating reference frame. Therefore, FFTs with a higher frequency resolution were easily obtained

using data from the final six revolutions of each computation rather than the single revolution used for analysis of the upstream seal.

In Figure 92, similarities exist with the unsteady behaviour presented for the upstream seal (Figure 85): across all sealing flow rates the BPF (f/f_d = 48) is observed and at the lower sealing flow rates activity at a reduced frequency exists, corresponding to N =16 large-scale structures rotating at less than the disc speed. Furthermore, the structures are supressed at the highest sealing flow rate, potentially having been 'blown out' from the seal. Activity at f/f_d = 96 corresponds to a harmonic of the BPF and additional peaks in the FFTs, found at all but the highest purge, can also be attributed to non-linear interactions of the BPF and a dominant low frequency (f/f_d ~ 6).

Despite the similarity in behaviour with the upstream seal, numerous important differences exist. In the downstream rim seal the amplitude of low frequency activity, C_p, remained < 0.02 across the sealing flow rates studied, whereas in the upstream seal, values > 0.05 were identified at the lower purge rates. Additionally, in the downstream seal the BPF does not significantly strengthen with increasing sealing flow rate but remains $0.018 < C_p < 0.03$. In the upstream seal, increasing values of C_p (> 0.1) at the BPF were attributed to the effect of increased levels of egress impinging on the blade leading edge. The impingement of downstream egress flow onto the stationary vane is not an unsteady effect and is not evident in the FFTs.

Figure 93 shows FFTs of unsteady pressure at four locations through the downstream rim seal, as indicated by the colour coded silhouette. All data is presented for Φ_0 = 0.01. The frequencies identified in the axial clearance of the rim seal, are identified at all locations. Unsurprisingly, the BPF is strengthened closer to the blades, but the low frequency behaviour is strongest in the axial clearance of the rim seal. This suggests that the large-scale structures are driven by shear between the annulus and wheel-space, and is consistent with the findings of Chapter 4.

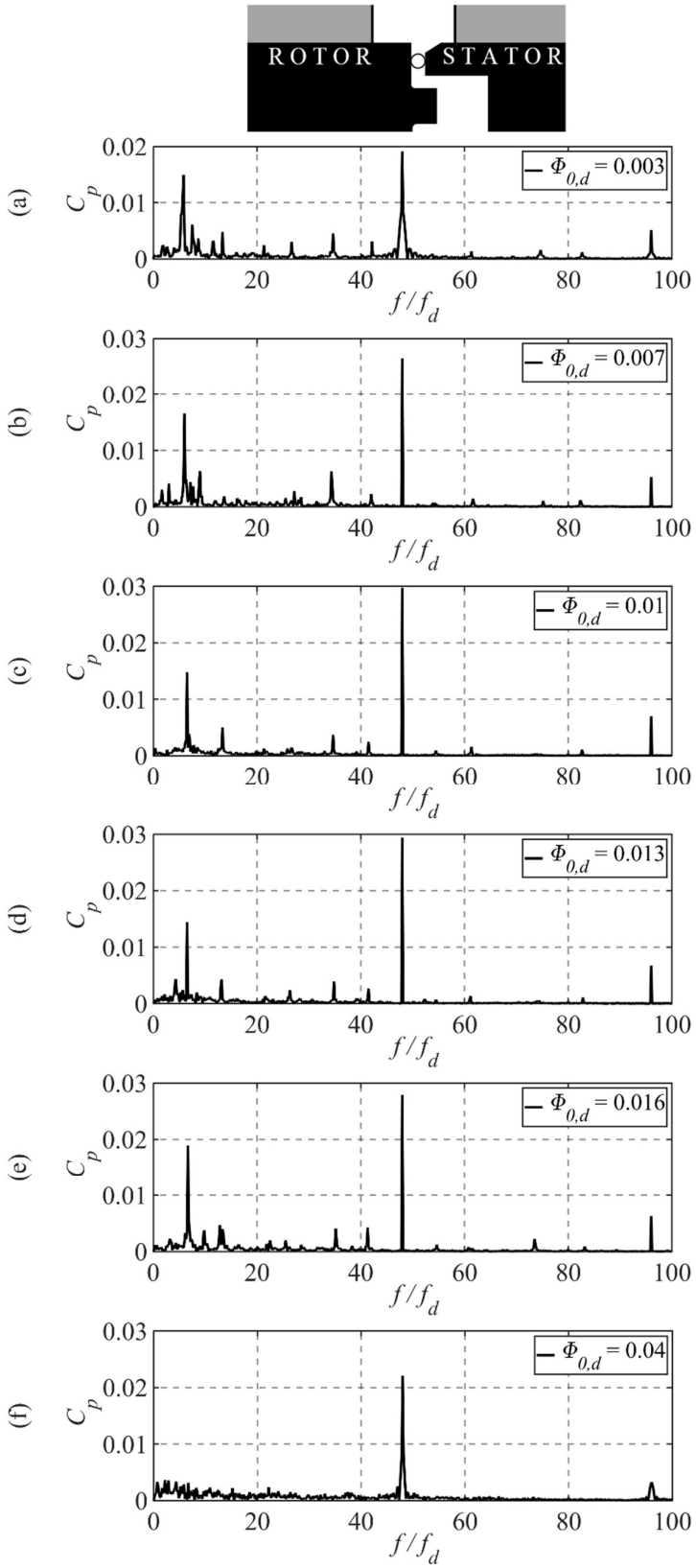

Figure 92: Fast Fourier transforms of computed pressure in the downstream rim seal

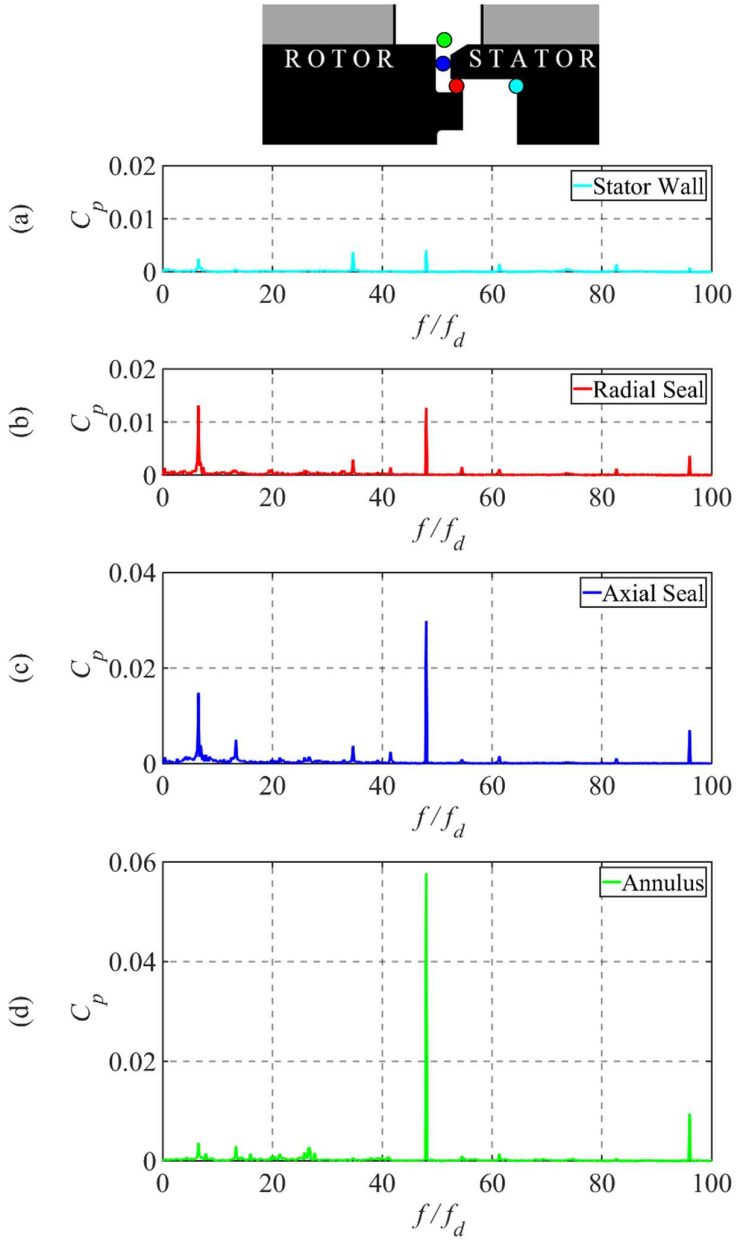

Figure 93: Fast Fourier transforms of computed pressure at four locations through the downstream seal ($\Phi_{0,d}$ = 0.010)

Table 9 details the number, N, and rotational speed, ω/Ω, of the large-scale structures computed in the downstream rim seal. Interestingly, the downstream structures rotate faster as purge levels increase. However, perhaps more significantly, the structures rotate significantly more slowly ($\omega/\Omega \sim 0.4$) than those computed upstream ($0.8 < \omega/\Omega < 0.9$). This is due to the negative swirl above the downstream seal. This is clearly visible in Figure 94, which depicts profiles of swirl through the upstream (red) and downstream (blue) rim seals at a common sealing flow rate of $\Phi_0 = 0.04$.

Non-Dimensional Sealing Parameter ($\Phi_{0,d}$)	Number of Structures (N)	Rotational speed of Structures (ω/Ω)
0.003	16	0.36
0.007	16	0.38
0.010	16	0.41
0.013	16	0.41
0.016	16	0.42
0.104	N.A.	N.A.

Table 9: Computed large-scale flow structures in the downstream rim seal

Figure 94 also illustrates a reduced overall swirl gradient across the rim seal for the downstream wheel-space versus the upstream wheel-space. It is believed this is responsible for the weaker instabilities observed in the downstream cavity (see Figure 92).

No experimental unsteady data is available to validate the existence of large-scale structures in the downstream rim seal and therefore caution must be retained in the speculative conclusions drawn. However, much of the behaviour is qualitatively similar to that measured upstream and it is reasonable to assume shear driven instabilities, which influence ingress, can occur.

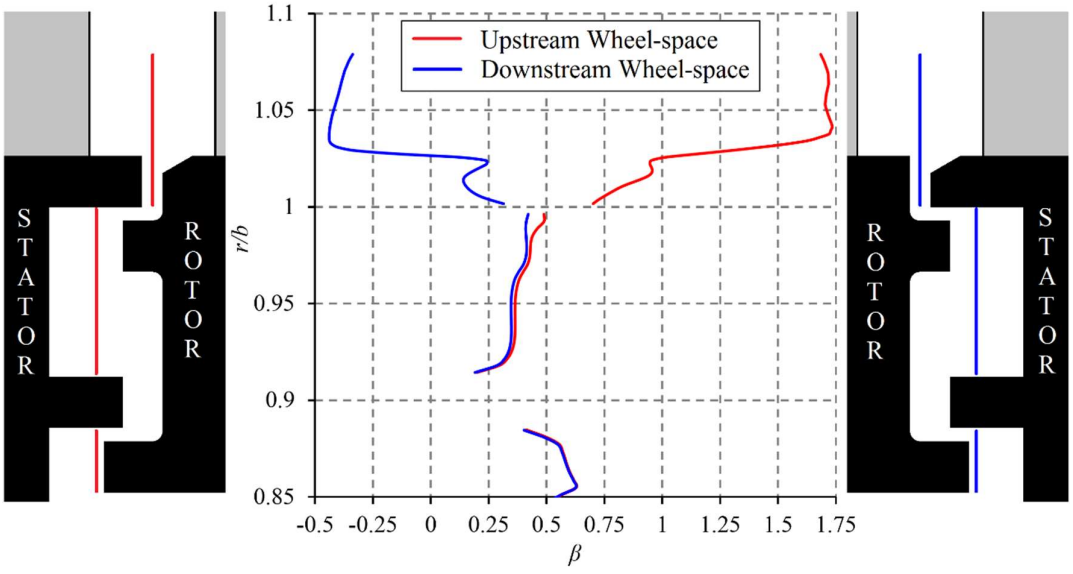

Figure 94: Variation in swirl through upstream and downstream rim seals ($\Phi_{0,u} = \Phi_{0,d} = 0.04$)

6.3 Influence of High Radius Purge

The work discussed in Sections 6.1 and 6.2 considered upstream and downstream wheel-spaces in which sealing flow was delivered through the bore of the turbine to the base of each cavity. However, in real engine architecture purge may be supplied at increased radius, either through purpose designed channels (Zhang *et al.* (2017)), or as a consequence of leakage through the interfaces between individual components, such as nozzle guide vanes and the inner carrier ring (Halila *et al.* (1982)). For simplicity, in this chapter, all purge entering through the base of the cavity is referred to as *bore* flow and all purge entering through the stator wall is referred to as *high radius* flow. The locations of the high radius injection modelled here reflect inlets built into the experimental facility, designed by Scobie (2014), and are consistent with locations present in industrial gas turbines.

Patinios *et al.* (2018) showed that in an upstream wheel-space, the injection of purge at high radius can significantly affect both the wheel-space flow structure and the sealing effectiveness (see Section 2.2.4). This section investigates the influence of high radius flows in both upstream and downstream wheel-spaces by purging cavities from discrete holes located in the stator walls. Computations modelled an upstream stator disc with 32 holes distributed at r/b = 0.82 and a downstream stator disc with 16 holes at r/b = 0.7. These additional inlets were incorporated into the design of the experimental facility, which will ultimately be used to validate the computations presented here. Experimental results were not available at time of writing.

Bore and high radius flows were supplied in combination, therefore the parameter, R_m was introduced as the ratio of the superposed flows:

$$R_m = \frac{\Phi_{0,H}}{\Phi_{0,B}} \tag{6.2}$$

where $\Phi_{0,H}$ and $\Phi_{0,B}$ represent the high radius and bore sealing flow parameters respectively, as defined in the nomenclature. It should also be noted that in real engines, the high radius purge flow occurring due to leakage between adjacent components, can typically be of a similar mass flow rate to that injected through the bore (Halila *et al.* (1982)).

To trace both the high radius and bore flows, the inlets were seeded with different passive scalars. The dilution ratio, C^*, was then defined locally as a measure of the relative concentration of bore flow, c_B, to high radius flow, c_H.

$$C^* = \frac{c_B}{c_B + c_H} \tag{6.3}$$

Figure 95 and Figure 96 depict cross-sectional planes in the upstream and downstream wheel-space respectively, with contours of time-averaged C^* and streamlines used to visualise the flow structure. In each of the figures, plots (a), (b) and (c) correspond to $R_m = 0$, 1 and ∞. The total sealing flow rates were $\Phi_{0,u} = 0.104$ and $\Phi_{0,d} = 0.04$; both wheel-spaces were almost fully sealed. For $R_m = 1$ and ∞, planes are shown at two azimuthal positions, the first aligned with a high radius hole and the second mid-way between holes. For $R_m = 0$ a single plane is shown as these computations did not model the discrete high radius inlets.

From Figure 95 and Figure 96 similar conclusions can be formed with regards to the outer wheel-space of both upstream and downstream cavities. Comparison of the streamlines show that in this region the flow structure does not change discernibly with R_m. Additionally, for $R_m = 1$ the contours in outer wheel-space show $C^* \sim 0.5$. This indicates that bore and high radius flows are fully mixed once they pass through the inner seal clearance.

The flow structure in each of the inner wheel-spaces shows a much stronger dependence upon R_m. Consider first the upstream wheel-space. In Figure 95 (a) sealing flow is applied only from the bore. A conventional Batchelor flow regime is visible, with radial in-flow and out-flow on the stator and rotor walls respectively, either side of a core. Bore flow is entrained directly into the rotor-side boundary layer. However, with $R_m = 1$ (Figure 95 (b)) high radius flow is injected across the wheel-space, disrupting the flow structure. At low radius the bore flow is entrained directly into the rotor boundary layer, however at increased radius the high radius purge flow sets up a toroidal vortex that rotates counter to the aforementioned flow regime. With $R_m = \infty$ (Figure 95 (c)) this effect is accentuated; the flow structure in the lower portion of the wheel-space is supressed further and a larger vortex forms above, driving flow radially inward on the rotor. This *vortex dominated regime* was proposed by Patinios *et al.* (2018) who also presented experimental data suggesting that the size and strength of the outer vortex increases with R_m.

The flow structure of the downstream inner wheel-space (Figure 96) is also disrupted by the high radius purge. At $R_m = 0$, a Batchelor flow regime again dominates the whole of the inner cavity. However, with $R_m = 1$ and $R_m = \infty$, the high radius flow is injected at a relatively low radius compared to the upstream cavity. A vortex, that again rotates counter to the conventional flow structure, forms in the lower part of the cavity. Above the high radius injection, the flow structure remains largely unchanged by R_m. For the case where $R_m = 1$ (Figure 96(b)), contours in the outer cavity show $C^* \sim 0.5$, again indicating that bore and high radius purge are almost fully mixed.

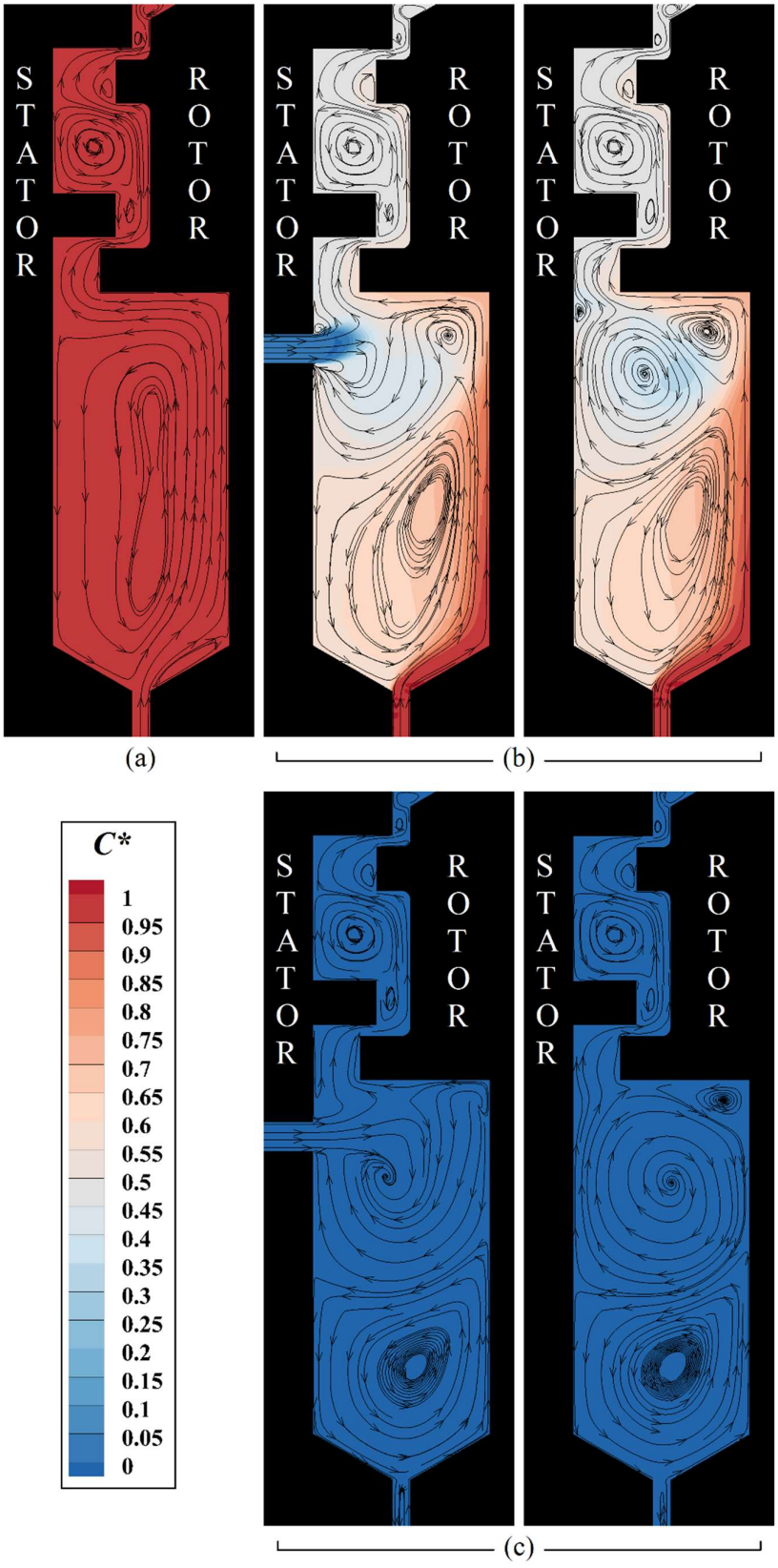

Figure 95: Time-averaged contours of the dilution ratio in the upstream wheel-space for $\Phi_{0,u}$ = 0.104 with overlaid streamlines: (a) R_m =0, (b) R_m =1, (c) R_m=∞

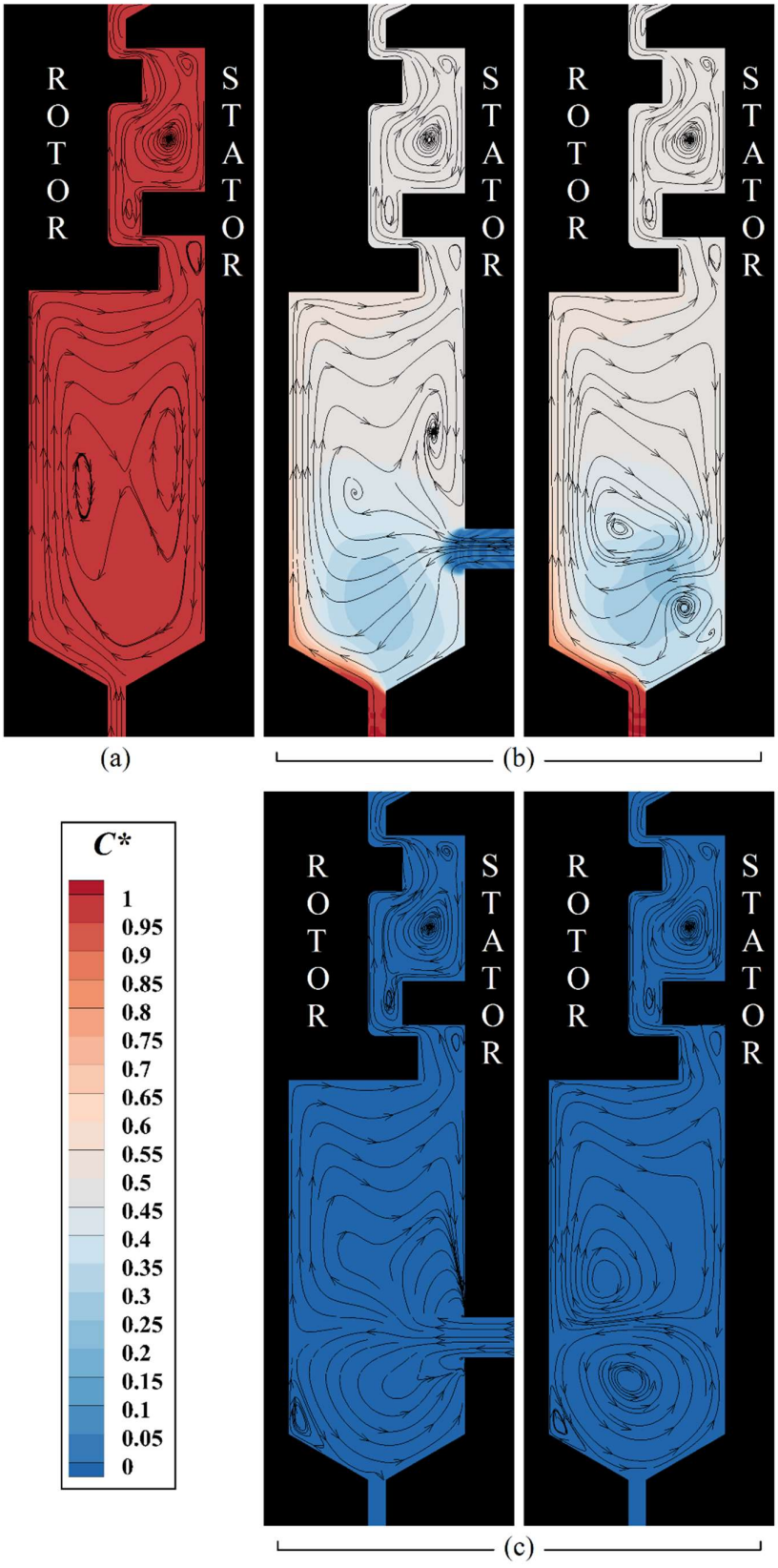

Figure 96: Time-averaged contours of the dilution ratio in the downstream wheel-space for $\Phi_{0,d}$ = 0.040 with overlaid streamlines: (a) R_m =0, (b) R_m =1, (c) R_m=∞

The streamlines in Figure 95 and Figure 96 give an indication of how axial and radial velocity components are modified by the high radius purge, however they do not show the influence on swirl. Profiles of circumferentially-averaged swirl through the core of the upstream and downstream wheel-spaces are shown in Figure 97 and Figure 98. The plots are radially aligned with the adjacent silhouettes and the blue, red and black curves represent data for R_m = 0, 1 and ∞.

High radius purge is injected perpendicular to the stator wall and therefore enters each wheel-space with $\beta = 0$. At a radius local to this, the swirl is consequently reduced. Perhaps surprisingly, in the upstream wheel-space (Figure 97) this effect appears strongest with $R_m = 1$. However, with $R_m = \infty$, the added momentum of the high radius purge was found to have a stronger influence on swirl closer to the rotor (not shown). At $r/b < 0.775$, behaviour in the upstream cavity is monotonic with R_m and shows that increasing the proportion of flow from the bore suppresses swirl. In the outer wheel-space (i.e. $0.9 < r/b < 1$), increasing values of R_m demonstrate a marginal decrease in swirl, however a similar effect was not found at lower values of $\Phi_{0,u}$, where ingress occurs.

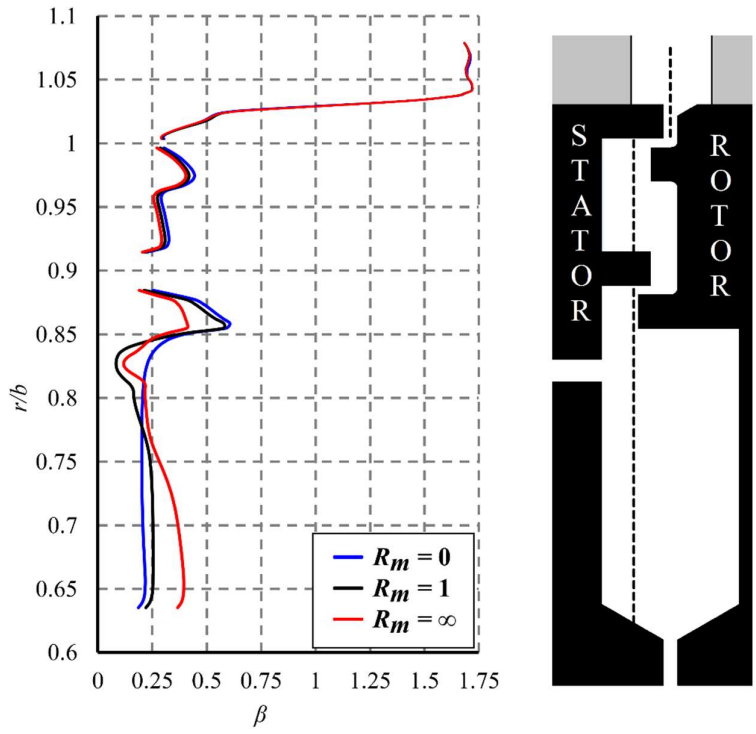

Figure 97: Variation in swirl through the upstream wheel-space with differing ratios of superposed flow ($\Phi_{0,u}$ = 0.104)

In the downstream wheel-space (Figure 98), the injection of high radius purge again supresses swirl locally. However, at $r/b > 0.725$ the effect is small and R_m had no discernible influence in

the outer wheel-space. Overall, the influence of R_m on swirl is lower in the downstream wheel-space when compared to the upstream wheel-space, but this may be largely due to $\Phi_{0,d} < \Phi_{0,u}$.

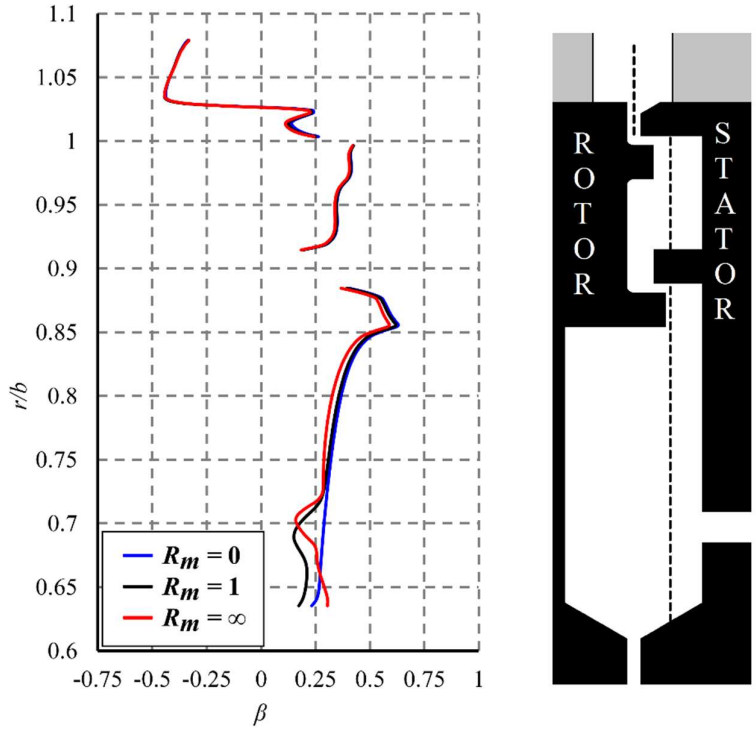

Figure 98: Variation in swirl through the downstream wheel-space with differing ratios of superposed flow ($\Phi_{0,d}$ = 0.04)

To investigate the effect of high radius purge on ingress, simulations were computed with a range of sealing flow rates used to purge each cavity. Figure 99 and Figure 100 show computed stator wall effectiveness at r/b = 0.85 (open symbols) and 0.958 (solid symbols) for the upstream and downstream wheel-spaces respectively. Blue, red and black symbols represent data for R_m = 0, 1 and ∞.

The figures do not illustrate a consistent change in ε_c with R_m in either cavity and at certain values of Φ_0, sealing effectiveness collapsed with R_m to within 0.005 (e.g. $\Phi_{0,u}$ = 0.05 and $\Phi_{0,d}$ = 0.01). This finding differs from that of Patinios *et al.* (2018), who identified a strong influence of R_m upon ε_c (see Figure 19). The principle reasons for the contrasting result are the different locations of the high radius injection and the alternative seal geometry used. Patinios injected purge at r/b = 1.03 and r/b = 0.983 and used a simple axial clearance seal. The present study injected purge flow into an inner cavity at r/b = 0.82 (upstream wheel-space) and r/b = 0.7 (downstream wheel-space), therefore the inner seal acted as a buffer, restricting the significant fluid dynamic effects resulting from the high radius purge to the inner cavity. This is also

consistent with the fact that R_m demonstrated no significant effect on the large-scale flow structures present in the outer seal.

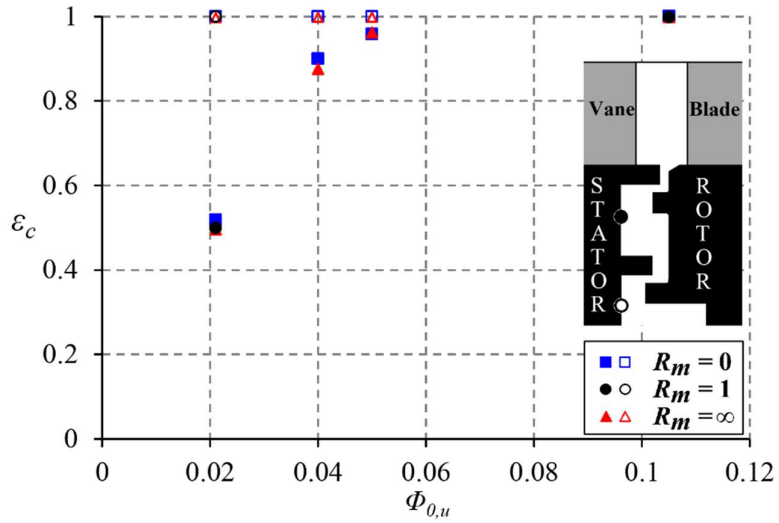

Figure 99: Variation in upstream sealing effectiveness with differing ratios of superposed flow

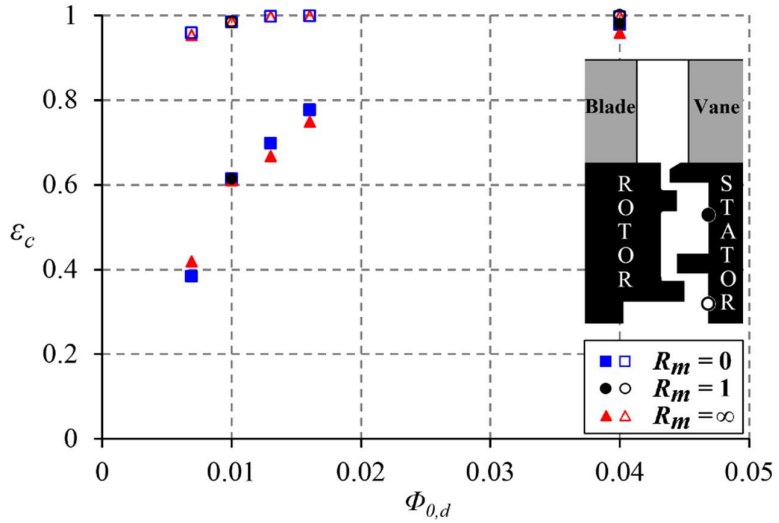

Figure 100: Variation in downstream sealing effectiveness with differing ratios of superposed flow

6.4 Summary

This chapter has investigated the ingress of annulus flow into wheel-space cavities upstream and downstream of a rotor. The turbine was geometrically similar to the baseline stage discussed in Chapter 4, however it incorporated a new blade geometry - resulting in an increased reaction - along with modified downstream vanes.

Ingress levels in the upstream wheel-space of the stage were directly compared to similar results for the baseline stage. A reduction in sealing effectiveness (~ 3%) at $\Phi_{0,u}$ = 0.021, 0.029 and 0.05 was supported by higher measured levels of ingress in the experimental facility. However, no significant difference in the distributions of non-dimensional annulus pressure, $C_{p,a}$, were identified. The higher levels of ingress were instead attributed to a slight increase in the amplitude of low-frequency (below the BPF) unsteady pressure fluctuations for the increased reaction blading. This was most apparent at $\Phi_{0,u}$ = 0.05. As discussed in Chapter 4, the large-scale structures that correspond to the low frequency unsteadiness are thought to be shear driven. The stronger instabilities were consistent with a larger shear-gradient identified across the upstream rim seal of the increased reaction stage.

Relative to the baseline stage, the peak-to-trough pressure distribution downstream of the blade row was increased by up to 40%. The circumferential distribution of pressure close to the seal also showed reasonable agreement with experiment. No significant re-ingestion of upstream egress into the downstream wheel-space was observed. This was attributed to the radial movement of upstream egress through the blade passage. Conversely, weaker secondary flow structures through the downstream vane passage showed that downstream egress remained hub-bound. Computed ingress into the downstream wheel-space was under-predicted; it is speculated that this was a result of deficiencies in the turbulence model. However, the computations did capture large-scale structures similar to those identified in the upstream wheel-space, albeit with a lower rotational speed and strength. These structures were thought to be weaker due to the reduced swirl above the seal and consequently a lower shear gradient across the rim seal, although at the time of writing experimental results were not available to validate this hypothesis.

In real engines, sealing flow can potentially enter wheel-space cavities from multiple locations at increased radius, relative to the bore. The influence of injecting purge flow from the stator wall in combination with that from the bore was investigated. The location through which purge was supplied had a strong influence on the flow structure in the lower wheel-spaces, with stator-wall purge disrupting the conventional *Batchelor flow regime* in each cavity and leading to the formation of large vortices. However, this change in flow regime did not have a clear effect on ingress, principally because the inner seal acted as a buffer, restricting any fluid dynamic effect of the high radius purge at the outer seal.

Chapter 7: Chute Seal, Twisted Blades & Stacked Vanes

This chapter presents analysis of the gas turbine configuration outlined in Chapter 3 that incorporates an engine realistic chute seal and upstream wheel-space, twisted blades, and stacked vanes. The stage is based upon geometry that was originally designed by Siemens for the experimental facility at KTH Royal Institute of Technology (Dahlqvist (2017)). However, the vanes, blades and seal from this rig were scaled for use in the Bath 1.5-stage facility, which operates at lower Mach and Reynolds numbers. Therefore, the configuration not only allows the study of ingress through a chute seal but also provides the basis for a collaboration with KTH to investigate the influence of scaling (Mach and Reynolds numbers) on ingress in gas turbines. The work reported in this thesis covers the first phase of this project which is focussed on modelling the Bath facility only.

Time-averaged results from the annulus, chute seal, and wheel-space are discussed, with validation performed against measurements from the experimental facility. The flow within the rim seal and its interaction with the annulus are studied in detail. Analysis of unsteady flow phenomena in this critical region is also included, and is compared with experiment.

A specific investigation into the influence of computational sector size is detailed, including comparison of results from 30°, 60°, 90° and 360° computations.

The experimental results in this chapter, used for validation purposes, were not measured by the present author. This chapter forms the basis of the paper "Flow Instabilities in Gas Turbine Chute Seals", which will be presented at ASME Turbo Expo 2019.

7.1 Time-Averaged Flow Characteristics

This section presents and discusses steady results, with unsteady phenomena shown in Section 7.2. Experimental and computational comparisons include interrogation of pressure, velocity and sealing effectiveness. The section is sub-divided as follows: annulus (7.1.1), rim seal (7.1.2) and wheel-space (7.1.3). Computational results are based on the 30º sector model, except where explicitly stated otherwise. Convergence of the passive scalar concentration on the stator wall was presented in Figure 47.

7.1.1 Annulus

Figure 101 illustrates the variation of time-averaged pressure coefficient ($C_{p,a}$) with normalised circumferential position across a vane passage in the annulus. The definition of $C_{p,a}$ and other

variables are included in the nomenclature. The data were collected on the hub 1.2 mm downstream of the vanes, as depicted in the silhouette. The positions for data collection are also seen in Figure 36. The experimental data were measured from two, 11.25° instrumented regions, separated by 180°. The computed values of $C_{p,a}$ (shown across four vane pitches) were determined from the 30º sector model; however, no identifiable differences were found using four sector sizes (30º, 60º, 90º, 360º). The agreement between computational and experimental results is good and provides confidence that the CFD has accurately captured the pressure distribution in the annulus. All data are presented for a non-dimensional sealing flow rate, Φ_0, of 0.075, although good agreement was found across all purge rates tested. Note there is a second-order effect of Φ_0 on the distribution of $C_{p,a}$ often referred to as the *spoiling effect* (Da Soghe *et al.* (2016)).

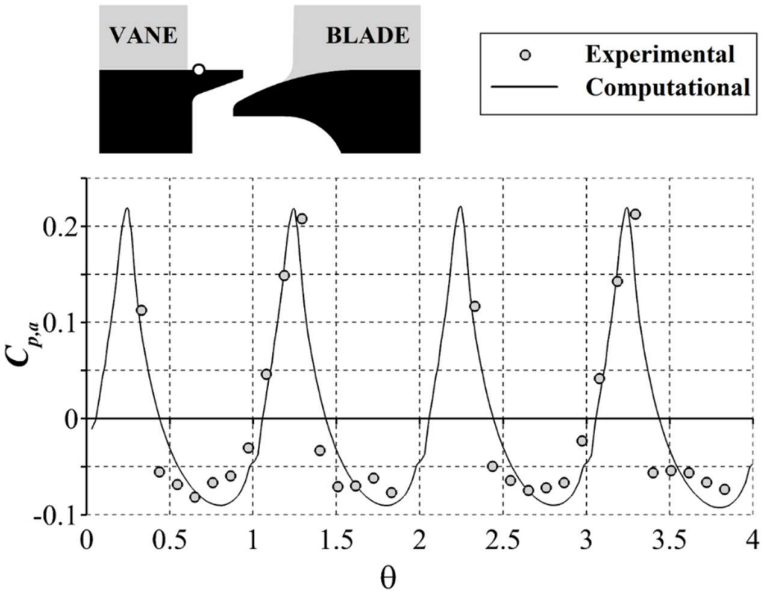

Figure 101: Circumferential distribution of time-averaged pressure coefficient over four vane pitches (Φ_0 = 0.075)

7.1.2 Chute Seal

Figure 102 illustrates time- and circumferentially-averaged profiles of computed velocity across the chute seal; the data is extracted along the dashed line. In each plot the ordinate is aligned with the angled, outer-overlap region of the stator wall and the abscissa represents the location across the seal gap with the silhouettes scaled appropriately. The ordinate represents the tangential velocity for (a) and (c), and the stream-wise velocity for (b) and (d); the velocity is normalised by the disc speed (Ωb) in all cases.

Comparisons of velocity profiles for four different domain sizes are shown in Figure 102 (a) and (b), with all sectors computed at $\Phi_0 = 0.05$. It can be seen that there is no significant effect of sector size on the tangential velocity profiles, with only a minor effect on the stream-wise velocity.

However, it should be noted that the largest discrepancy relative to the 360º computation is seen in the 60º sector model, while the smallest differences are with the 90º sector model; this is also reflected in sealing effectiveness discussed in Section 7.1.3. These dissimilarities are believed to be a result of discrepancies between the unsteady flow phenomena captured in each simulation, as discussed in 7.2.2.

The normalised tangential velocities in Figure 102 (c) illustrate the mean swirl across the seal decreasing with increasing purge flow rate. Steep velocity gradients are observed in the stator and rotor boundary layers outside the core flow, conforming to classical theory for a stator-rotor system. However, the stream-wise velocity components, seen in plot (d), indicate that the bulk flow exits the seal along the stator and the bulk flow ingested through the seal is attached to the rotor. This flow configuration challenges the conventional arrangement expected for a Batchelor flow regime, where flow is pumped radially outward in a rotor boundary layer and migrates inward in a stator boundary layer. The computed flow structure is consistent with a recirculating flow feature within the seal, referred to as a GRZ by numerous authors - see Section 2.3.2. Similar profiles of velocity were shown by Gao *et al.* (2018) who argued that the seal recirculation may be interpreted as evidence for the existence of Taylor-Couette vortices.

Figure 103 (a) shows *streamlines* on two circumferential planes, aligned with regions of peak ingress and egress. Figure 103 (b-d) shows additional *streak-lines* on the rotor hub and blade surfaces for three different purge flow rates. The contours represent sealing effectiveness with all data temporally averaged in the rotational frame over a single disc rotation. Figure 103 indicates that with increasing purge the vortex in the seal clearance is modulated circumferentially by the rotor blades and is not present in the centre of the passage where the egress flow is at its maximum (right-hand plane). The wall streak-lines indicate the gap recirculation interacts directly with the leading-edge horseshoe vortex on the blade; this suggests the proximity of the blade to the chute seal affects the seal recirculation and influences ingress. Further secondary flow features are illustrated in Figure 103, including the radial migration of the passage vortex up the suction surface of the blade (which could provide a tangible cooling effect to the blade) and the displacement of the saddle point. This saddle point (labelled S) has a clear dependence on sealing flow rate, moving further right (against the direction of rotation) with increasing purge. Surprisingly, the suction surface of the blade shows a higher sealing effectiveness at $\Phi_0 = 0.075$ (plot c), than at $\Phi_0 = 0.100$ (plot d): this is due to the egress separating from the rotor surface for conditions with higher purge momentum.

The influence of egress on both the annulus fluid dynamics and rotor surface temperature is clearly significant, indicating the importance of considering both seal geometry and purge rate when designing annulus features such as profiled end-walls.

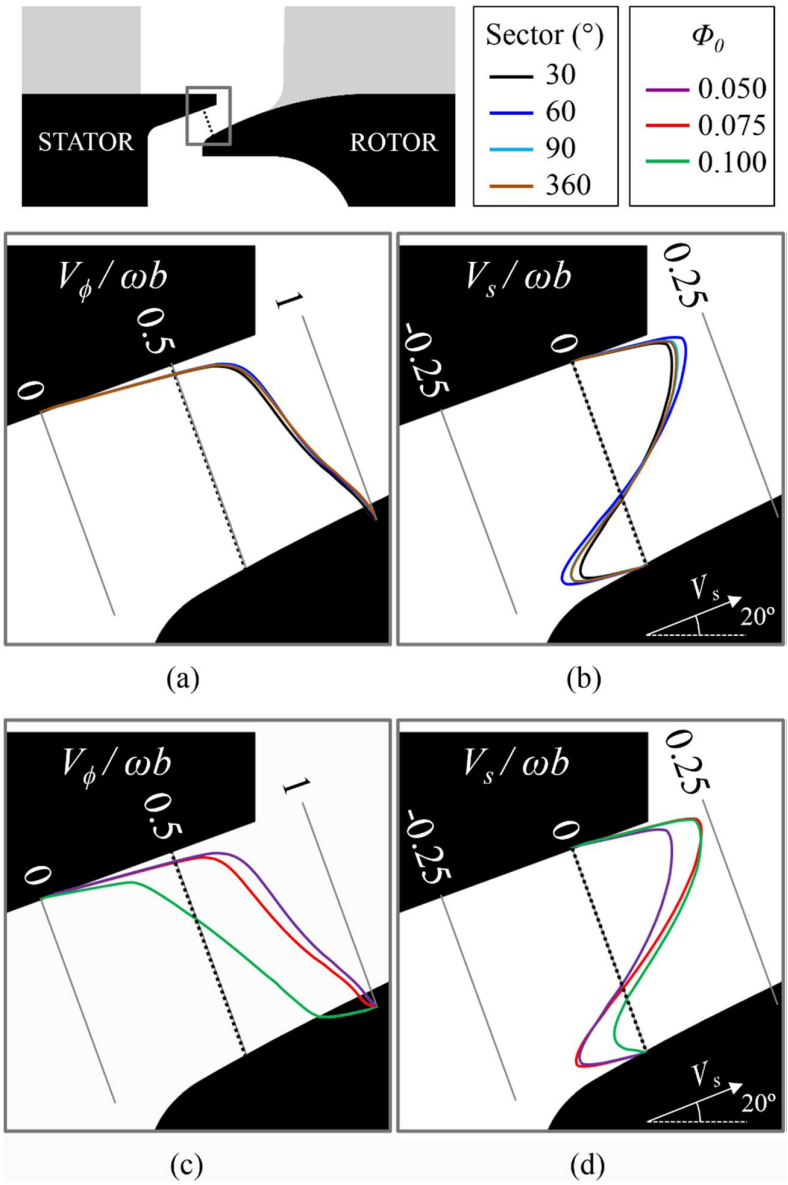

Figure 102: Computational profiles of tangential velocity (a/c) and stream-wise velocity (b/d) across the chute seal: (a/b) sector size comparison at Φ_0 = 0.05, (c/d) Φ_0 comparison with a 30° sector

Figure 103 illustrates tangential streamlines in two cross-sections of the chute seal but not the level of shear that exists in the azimuthal direction. At the exit of the chute seal, the highly-turned annulus flow downstream of the vanes encounters the relatively low swirl in the cavity. Several authors have proposed different hypotheses for the fundamental driver of large-scale structures in the seal. Two proposals are that they arise from Kelvin-Helmholtz instabilities (as discussed in Section 4.2), or from Taylor-Couette instabilities (Boudet *et al.* (2006)); both of these explanations are fundamentally a result of shear.

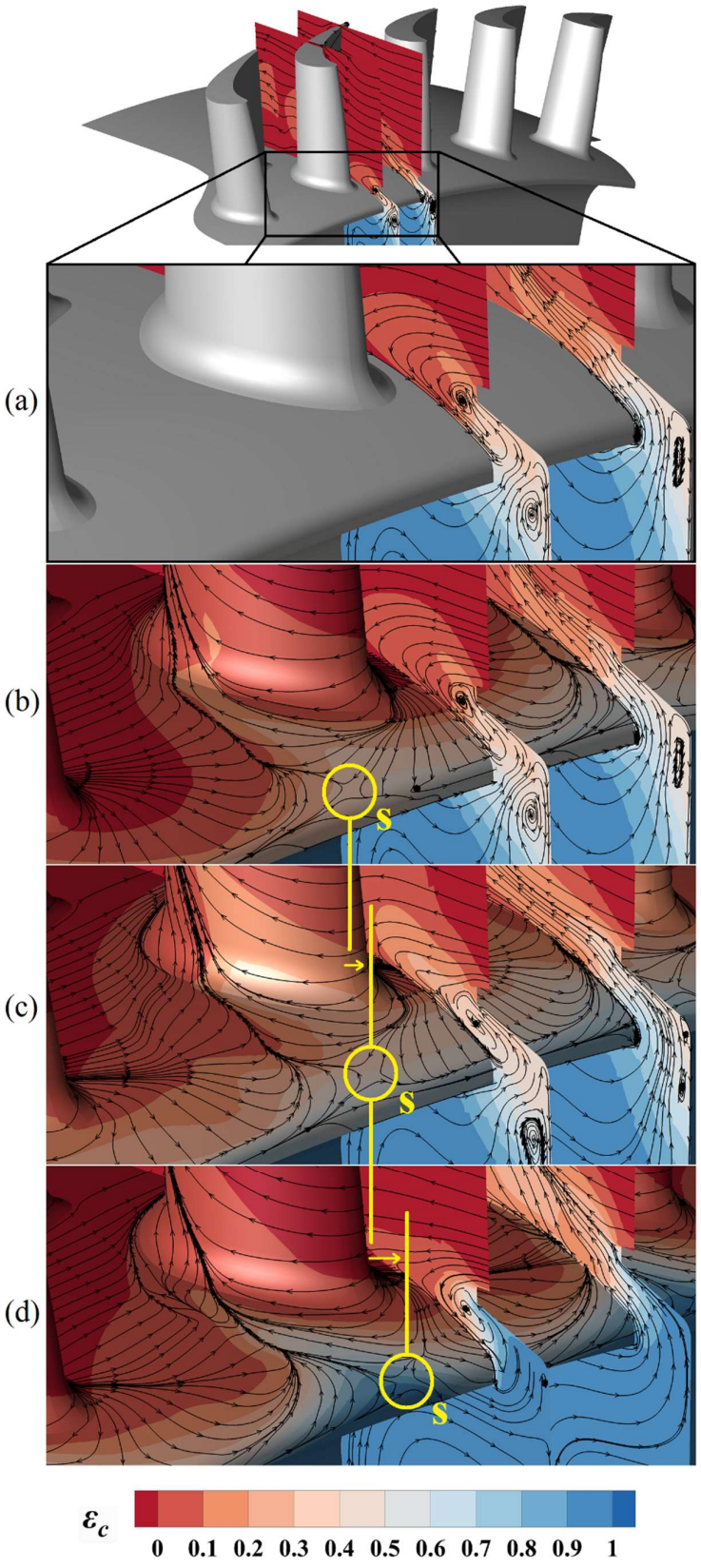

Figure 103: Time-averaged streamlines in the rotational frame from a 30° sector model, 'S' indicates saddle points: (a, b) Φ_0 = 0.050, (c) Φ_0 = 0.075, (d) Φ_0 = 0.100

Figure 104 shows time-averaged computational velocity vectors from three azimuthal locations through the seal, at three purge rates. The location of each set of vectors, time-averaged in the rotational frame, follows the dashed line in the silhouette. The vectors are shown to reverse in direction as the cavity fluid rotates more slowly than the disc and the annulus flow swirls faster than the disc.

Figure 104 (b) shows that there is a strong radial gradient in swirl extending from below the rotor platform, through the seal and into the annulus. The magnitude of the shear gradient, and radial and azimuthal position varies with purge flow. The gradient is strongest at higher purge rates and the position of maximum gradient is forced radially outwards; this is consistent with higher purge being associated with reduced momentum exchange between the annulus and wheel-space.

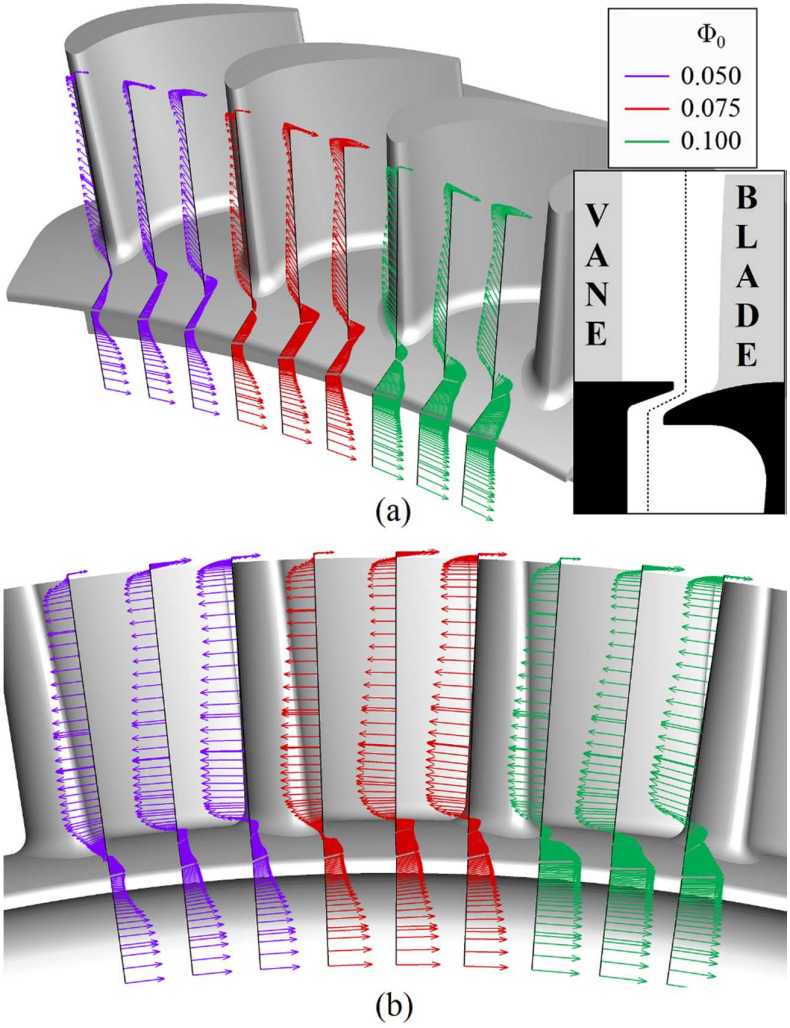

Figure 104: Velocity vectors through the seal (rotational frame) at three levels of purge

7.1.3 Wheel-Space

Figure 105 directly compares experimental and computational profiles of swirl through the wheel-space. The results are presented at four values of λ_T, the turbulent flow parameter which governs the boundary layers in the wheel-space (Owen and Rogers (1989)). The figure shows excellent agreement between experimental and computational results and provides validation that the cavity flow has been computed accurately. The figure also shows how the tangential velocity throughout the wheel-space is supressed with an increasing sealing flow rate, as expected.

Further confidence in the computation of pressure in the wheel-space flow can be gained from Figure 106, which depicts radial profiles of pressure coefficient on the stator wall in the cavity – $C_{p,s}$ is defined in the nomenclature. The data are presented at four sealing flow rates. As the wheel-space is pressurised with increasing purge, the radial variation in pressure is reduced.

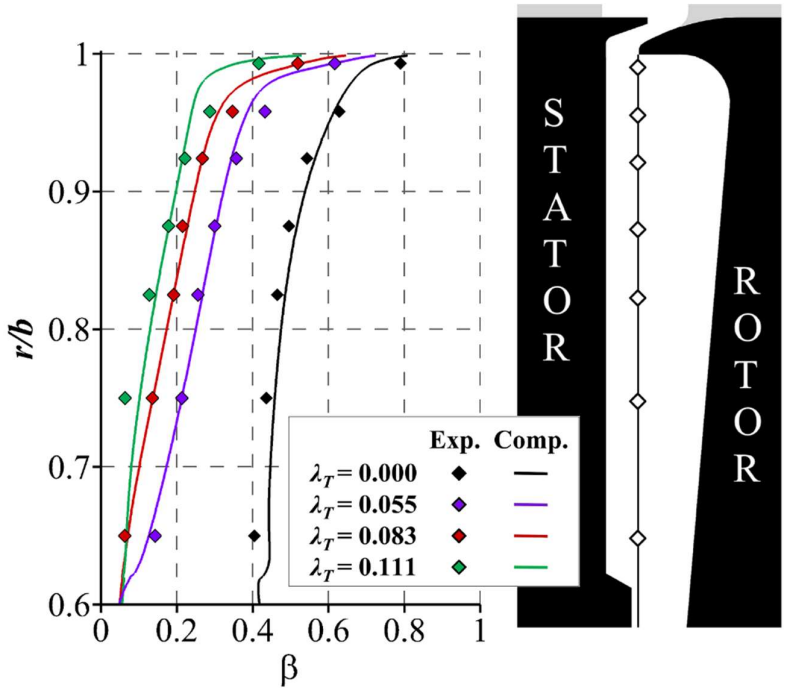

Figure 105: Radial distribution of swirl in the wheel-space at four levels of purge

Figure 107 (a/b/c) shows the radial variation of ε_c at Φ_0 = 0.050, 0.075 and 0.100 respectively (*i.e.* increasing purge). Results from the stator wall and rotating core are depicted discretely by circle and diamond symbols (respectively) for the experiments, alongside continuous solid and dashed lines (respectively) for computations. The right-hand silhouettes are aligned with the radial position of the ordinate and include superimposed contours of computed sealing effectiveness. Though not shown here, for a constant flow coefficient (C_F = 0.35) the experimental data was

found to be invariant with Reynolds number between $Re_\phi \sim 1.3\times10^6$ (as computed) and $Re_\phi \sim 9.6\times10^5$.

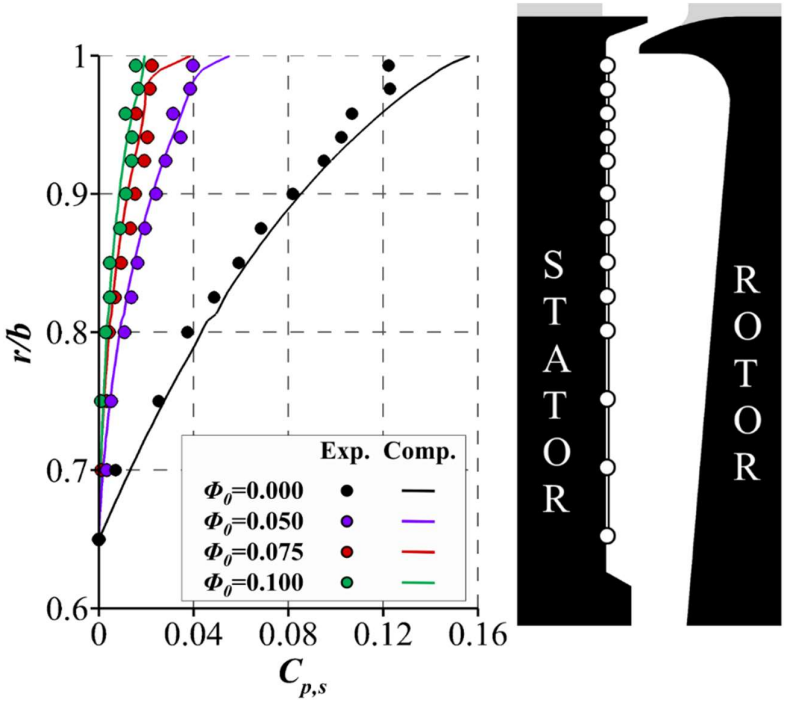

Figure 106: Radial distribution of stator-wall pressure coefficient at four levels of purge

At the two lower sealing flow rates (Figure 107 a/b) there is generally good agreement between the quantitative levels of ingress seen experimentally and computationally. The data and contours show abrupt increases in ε_c across the chute seal where the free-stream effectiveness in the annulus is zero. Relatively high gradients of sealing effectiveness exist in the wheel-space at high radius ($1 > r/b > 0.8$). This behaviour departs from the classic Batchelor-type flow structure where a fully-mixed stator wall boundary layer creates a radially-invariant distribution of effectiveness. Instead, there is a large mixing region where ingested fluid is diluted by the sealing flow pumped up the rotor boundary layer, with differences in concentration between the core and the stator. This flow structure is thought to be more prominent than in previous studies of the same rig (*e.g.* Patinios *et al.* (2016)) because the chute seal encourages the rotor boundary layer to impinge directly upon the stator wall. At $r/b < 0.8$, the radial gradient of ε_c is significantly reduced, with core and stator wall at the same concentration.

Figure 107 (c) shows a qualitatively similar flow structure, but with weaker agreement between experiment and computation at high purge. This discrepancy is discussed in the context of Figure 108 below.

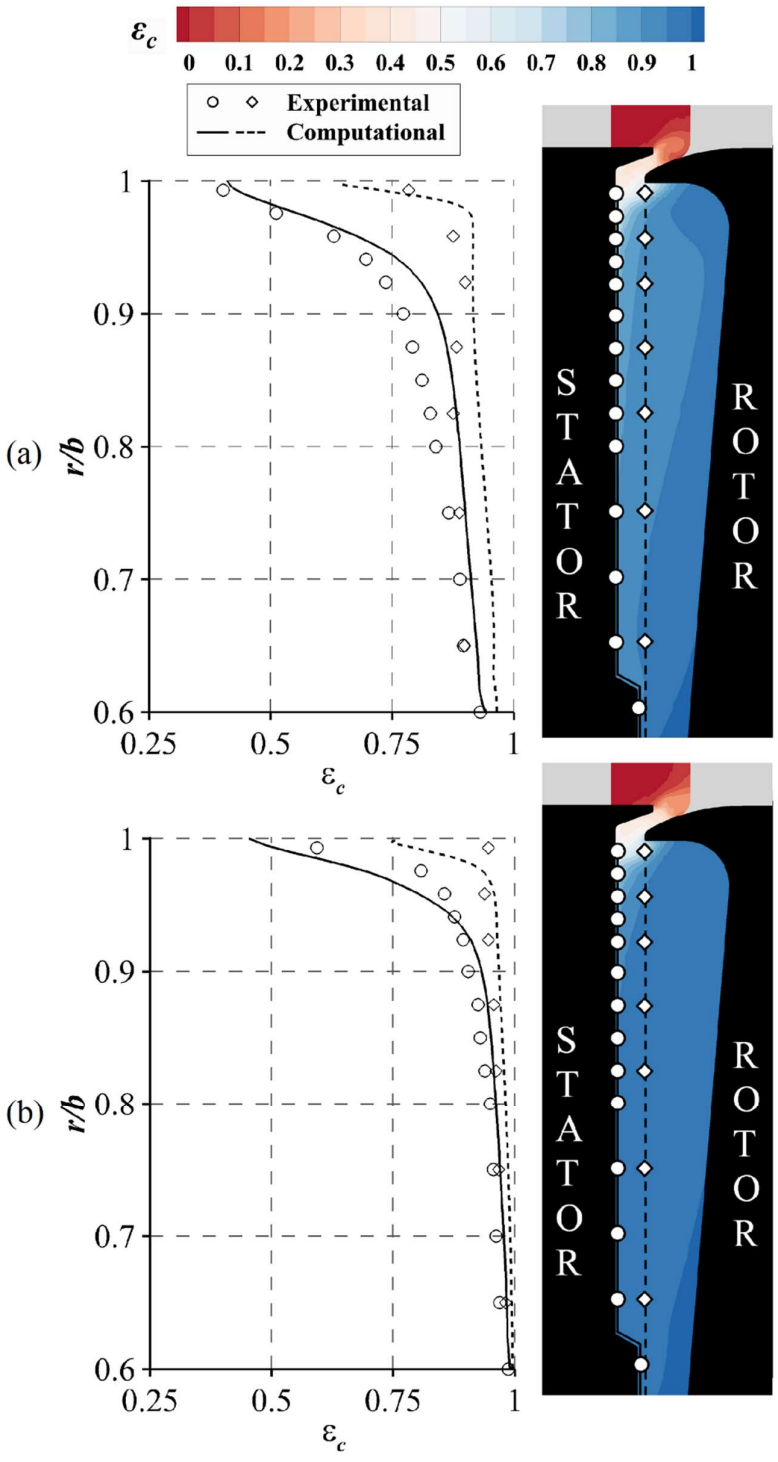
ε_c
0 0.1 0.2 0.3 0.4 0.5 0.6 0.7 0.8 0.9 1
Experimental
Computational
(a)
(b)
r/b
1
0.9
0.8
0.7
0.6
0.25
0.5
0.75
1
ε_c
STATOR
ROTOR

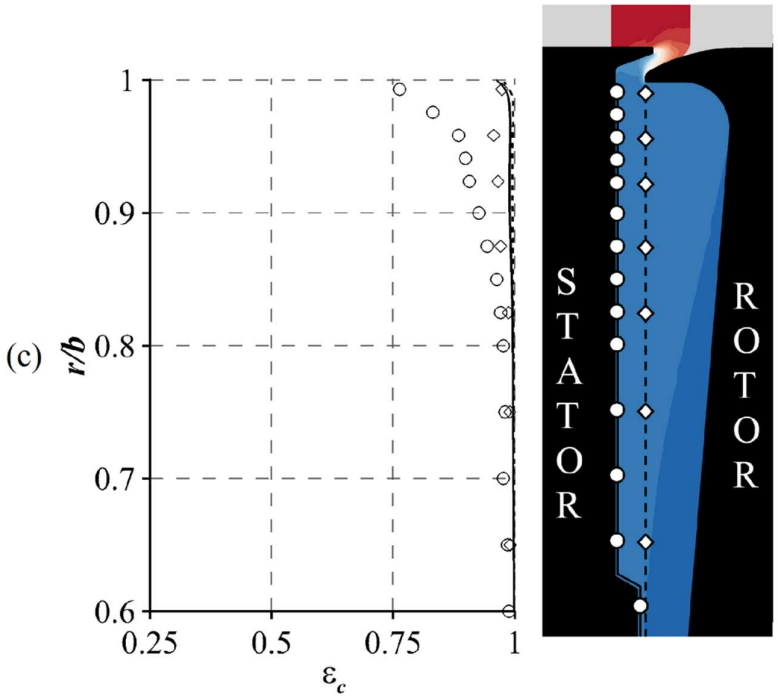

Figure 107: Radial distribution of concentration-based sealing effectiveness in the wheel-space: (a) Φ_0 = 0.050 (b) Φ_0 = 0.075 (c) Φ_0 = 0.100

Figure 108 shows the variation of ε_c on the stator wall with sealing flow parameter; the experimental and computational data is shown at r/b = 0.958 and 0.85. Generally, the sealing effectiveness increases with Φ_0 as the purge pressurises the wheel-space and reduces ingress. Experimental data are presented for two rotational speeds, demonstrating ε_c collapses with Reynolds number. There is an inflection in the experimental data for $0.06 < \Phi_0 < 0.12$, which is qualitatively similar to experimental data measured for the baseline stage (see Chapter 4) and also reported by Boudet *et al.* (2005), Clark *et al.* (2017), Gentilhomme *et al.* (2003). The degree of inflection is dependent on flow coefficient, and has again not been accurately captured computationally, leading to the mismatch in sealing effectiveness in Figure 107 (c). Here the data has been collected at a flow coefficient C_F = 0.35, which is the design point for the stage. Chapter 4 describes how the behaviour is due to the presence of the blades, and their interaction with unsteady rim seal structures. The unsteady data are discussed further for the present geometry in Section 7.2.

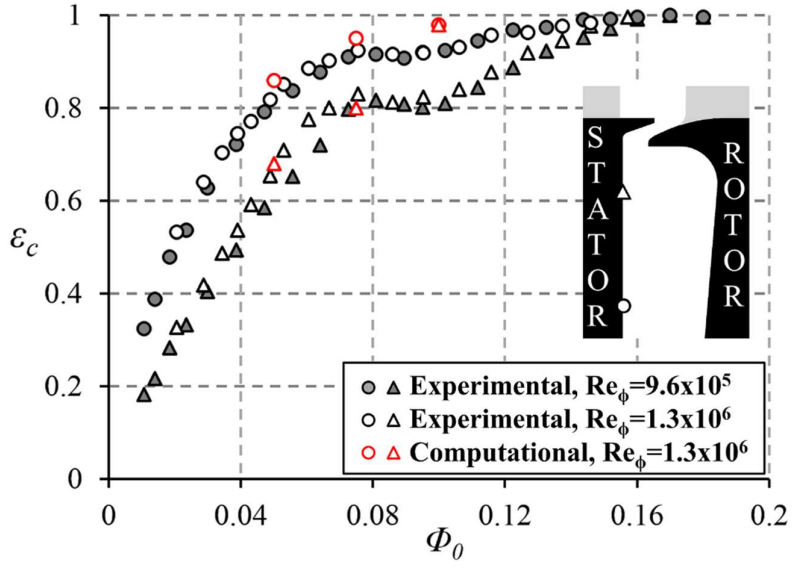

Figure 108: Variation of stator effectiveness with non-dimensional sealing parameter

Overall, the level of agreement in computed effectiveness is significantly improved over the turbine configurations studied in Chapters 4, 5 and 6. Indeed, the agreement is also improved over much of the work presented in the literature. The reason for this is not certain, however an over-prediction in the highly sensitive unsteady rim-seal flow features (discussed in Section 7.2) may be in part responsible, driving greater mixing between the annulus and wheel-space than other computations. It is also possible that the improvement is a result of the specific seal geometry itself, which lends itself to computation by incorporating a relatively short overlap and fewer 90° vertices than many other seals (including those studied in Chapter 4,5 and 6); these can result in regions of localised separation that prove difficult to accurately capture. Despite speculative reasons for the improved agreement, the author is confident in the convergence of the passive scalar for each computation (see Figure 47 for monitor data on the stator wall).

Computed profiles of the radial variation of ε_c on the stator wall for four different sector sizes are presented in Figure 109. All results are shown for $\Phi_0 = 0.05$. For $r/b > 0.9$ small differences in ε_c are apparent in all sector models when compared to the 360º case. The most pronounced differences are for the 60º sector. This feature is also reflected in the seal velocities shown in Figure 102 (b), and again can be attributed to the discrepancies between the unsteady flow phenomena captured in each simulation (see Section 7.2.1). However, at lower radii the curves collapse well and, despite the differences in unsteady structures, the degree of ingress is broadly invariant with sector size. Note that the corresponding experimental data are displayed in Figure 107 (b).

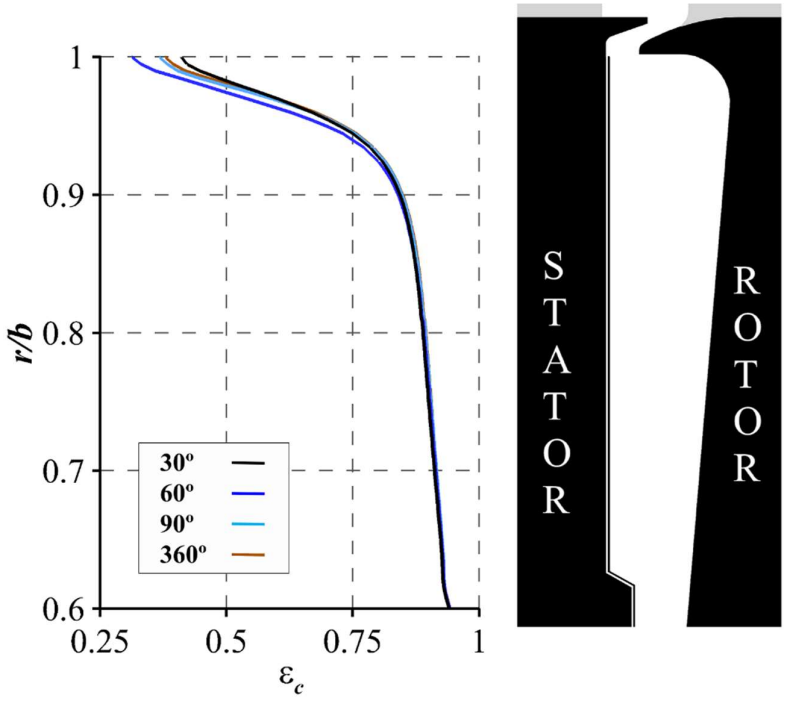

Figure 109: Radial distribution of concentration-based sealing effectiveness in the wheel-space at Φ_0 = 0.050: sector size comparison

7.2 Unsteady Flow Characteristics

This section presents unsteady computational and experimental data over a range of conditions and discusses the influence of both sealing flow rate and computational sector size on results from the turbine configuration in question.

7.2.1 Sensitivity to Sealing Flow Rate

Figure 110 and Figure 111 show Fast Fourier transformations (FFTs) of computational and experimental results respectively. The FFTs are based on unsteady pressure from the stator wall at r/b = 0.958, as shown in the silhouettes. Four purge flow rates are presented (Φ_0 = 0, 0.05, 0.075 and 0.10). All computations in Figure 110 are based on a 30º sector. Frequencies have been normalised against f_d (the rotating disc frequency) and the pressure has been normalised as C_p, as defined in the nomenclature. All results were extracted in the stationary frame: computationally this required processing data from the rotating domain over the final disc revolution using the method described for the baseline geometry in Section 4.2. Experimental results were invariant between $Re_\phi = 9.6\times10^5$ and 1.3×10^6, with data presented here at the latter case for reasons of clarity.

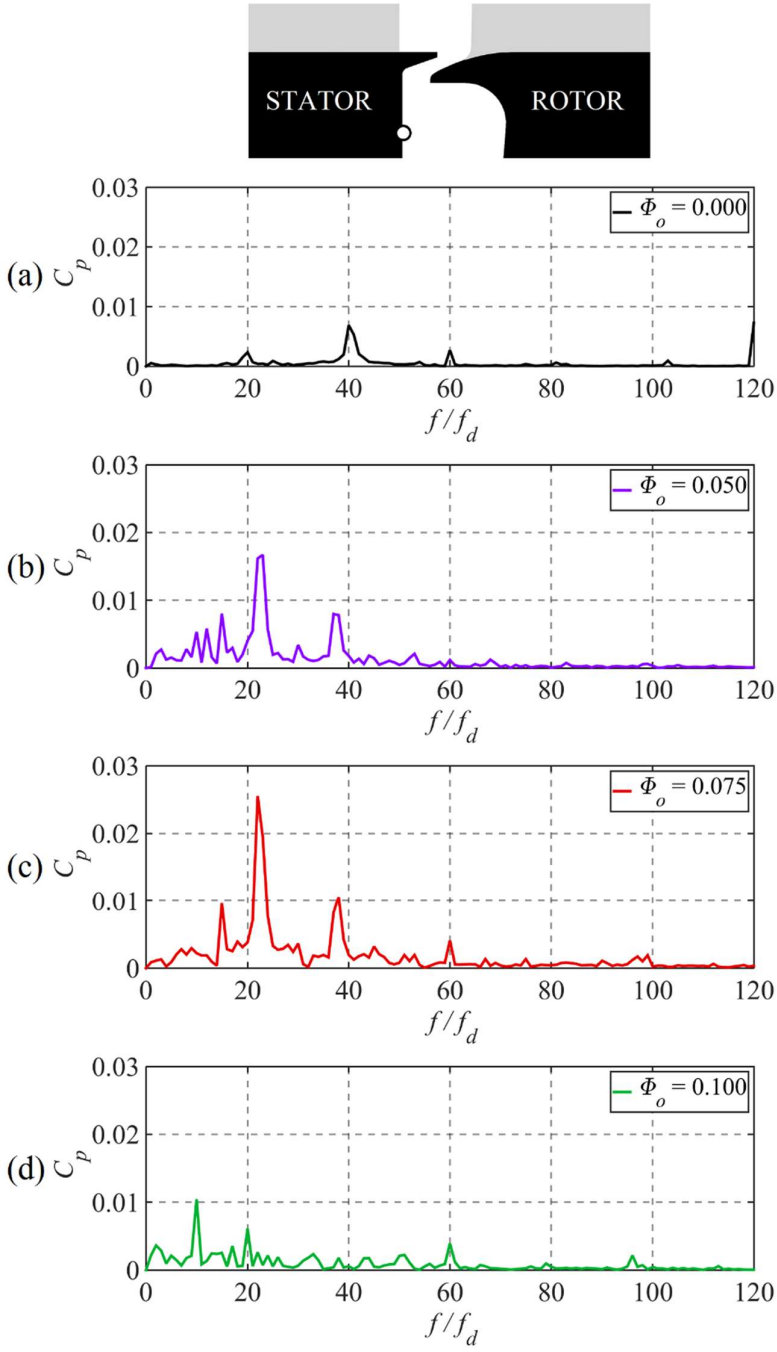

Figure 110: Fast Fourier transforms of computed stator wall pressure using a 30° sector

Consider Figure 110. Increased activity is generally observed at $f/f_d = 60$, which corresponds to the BPF. Spectral activity at frequencies below the BPF exist at all computed sealing flow rates, with the peak frequency and amplitude varying with purge. At $\Phi_0 = 0$, the peak frequency of 40 corresponds to $N = 36$ structures rotating at $\omega/\Omega \sim 1.11$. It should be noted that $\omega/\Omega > 1$ is possible given $\beta > 1.5$ immediately downstream of the vanes. This frequency reduces to 23 ($N = 24$ rotating at $\omega/\Omega \sim 0.96$) at $\Phi_0 = 0.05$; at higher purge these unsteady pressure signals are more intense. The

magnitude of the peak signal increases further at $\Phi_0 = 0.075$, while the speed of the corresponding structures reduces to $\omega/\Omega \sim 0.92$. At the highest purge ($\Phi_0 = 0.100$) there is a significant reduction in strength and frequency: $f/f_d = 10$, corresponding to $N = 12$ and $\omega/\Omega \sim 0.83$. Further peaks in each of the plots are due to harmonics and nonlinear combinations of the peak low frequency and the BPF: (a) 20 = 60 - 40, (b/c) 37 = 60 - 23, (d) 20 = 10 × 2. Note that information regarding N and ω/Ω is tabulated in Table 10 and shown in Figure 24. These structures are visualised and discussed further in the context of sector size within Section 7.2.2.

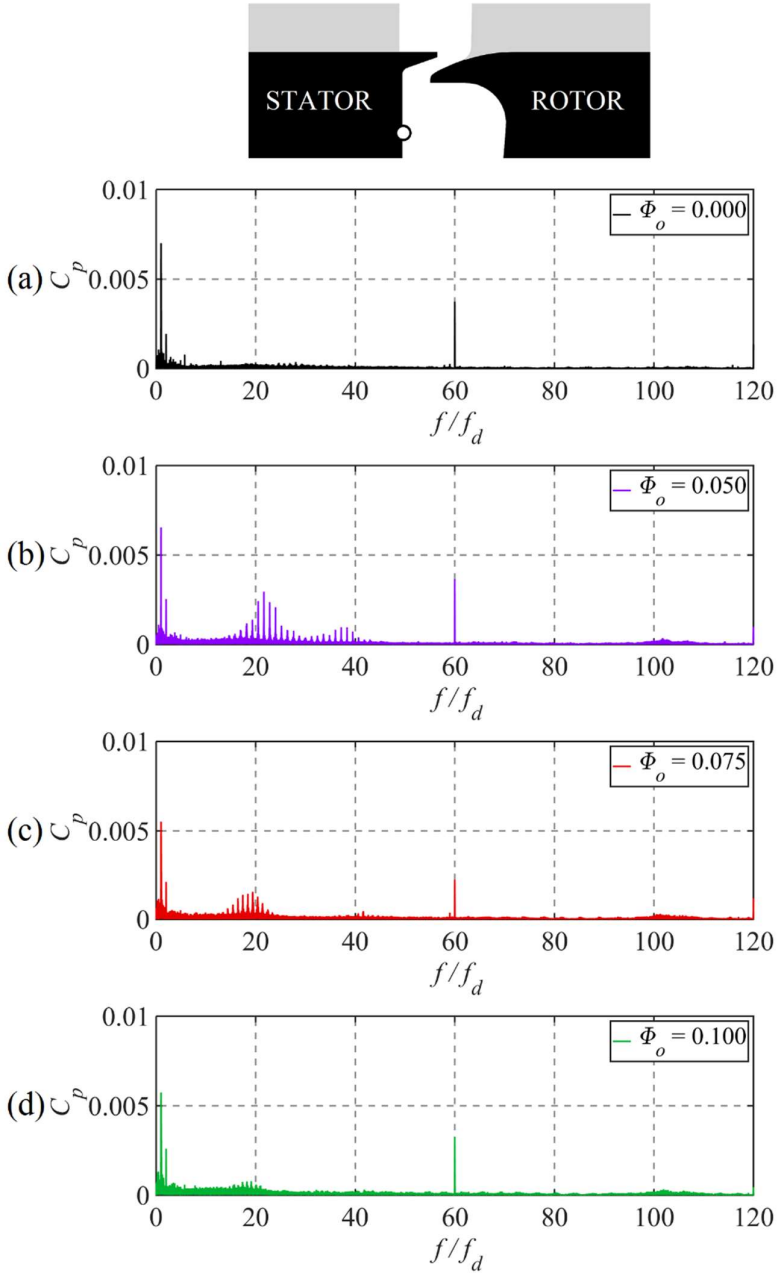

Figure 111: Fast Fourier transforms of experimental stator wall pressure

Figure 110 and Figure 111 allow a direct comparison between computational and experimental frequencies at common purge level. The experiments also clearly measure activity at the BPF for all cases. Although experimentally-determined frequencies below the BPF are largely supressed at Φ_0 = 0 and 0.1, the computations have captured numerous qualitative and quantitative similarities. There are similar peak frequencies that reduce with increasing purge and are most intense at Φ_0 = 0.05 and 0.075. It is speculated that with lower purge the intensity of the instabilities is reduced due to the relatively weak shear gradient between the annulus and wheel-space. At high purge the egress through the seal dominates the fluid dynamics, simply blowing out any large-scale structures. The experimental FFTs offer significantly higher resolution. This is a result of experimentally sampling from ~ 860 revolutions; computationally, the sampling is limited to a single disc revolution.

Phase analysis was performed over signals from two fast response pressure transducers offset by 11.25° (α) in the azimuthal direction. This allowed measurement of the number of structures (N) and their rotational speed (ω/Ω). The approach, proposed by Beard *et al.* (2017), is the same as that used for the baseline geometry and is reported in detail within Section 4.2.

The data are shown in Table 10 alongside computed values. Computationally, at Φ_0 = 0.05 and 0.075, N = 24, which compares well with the measured value, N = 21. Equally the computed speed reduces from ω/Ω ~ 0.96, to ω/Ω ~ 0.92, comparing well with the experimental speed reducing from ω/Ω ~ 1.03, to ω/Ω ~ 0.92. It should be noted that the absolute amplitudes of the computed low-frequency structures are significantly higher than those measured. This is believed to be a result of RANS turbulence modelling, where the greater viscosity term can give rise to more stable vortical structures. Despite this, the overall behaviour of the CFD is encouraging and provides clear insight into the unsteady fluid dynamics.

Several authors have proposed hypotheses for the physical origin of the large-scale structures measured and computed here. The two most compelling arguments for the driving mechanism are that they arise from Taylor-Couette or Kelvin-Helmholtz instabilities (as described in Chapter 4). Both explanations are fundamentally based on shear: caused by the overlapping stator and rotor surfaces in the case of the Taylor-Couette instabilities or by differences in the levels of swirl in the wheel-space and annulus for the case of Kelvin-Helmholtz instabilities (see Figure 104). The results here suggest the flow through the rim seal is subjected to significant three-dimensional shear and therefore neither of these explanations should be discounted.

Case	Non-Dimensional Sealing Parameter (Φ_0)	Number of Structures (N)	Rotational speed of Structures (ω/Ω)
Comp. (30°)	0.000	36	1.11
Comp. (30°)	0.050	24	0.96
Comp. (30°)	0.075	24	0.92
Comp. (30°)	0.100	12	0.83
Comp. (60°)	0.050	30	1.00
Comp. (90°)	0.050	28	0.98
Comp. (360°)	0.050	29	0.95
Exp.	0.000	N.A.	N.A.
Exp.	0.050	21	1.03
Exp.	0.075	21	0.92
Exp.	0.100	N.A.	N.A.

Table 10: Comparison of large-scale flow structures: experiment and computation

7.2.2 Sensitivity to sector size

Sector models facilitate the use of CFD at significantly-reduced cost. Section 7.2.1 presented unsteady computations using a 30º sector model not untypical of many industrial operations. However, the inherent periodicity in such simulations can influence the calculation of fluid-dynamic structures larger than a vane or blade passage.

FFTs of unsteady pressure at locations close to the rim seal are presented for sectors of 30º, 60º, 90º and 360º in Figure 112. Data is shown for $\Phi_0 = 0.05$ at three radial locations. The results are normalised using the same method described for Figure 110. Spectral peaks at $f / f_d = 60$, correspond to the BPF and increase in intensity as the monitoring point moves radially outwards through the seal clearance towards the blades. There is a range of frequencies below the BPF, indicating large-scale structures. There are differences in the characteristics of these instabilities when they are computed using different sector sizes. Across all domain sizes, the intensity of spectral activity is observed to be strongest within the chute seal, in the proximity of strongest shear.

The frequency spectra for the 90º and 360º domains show consistent behaviour at all three locations in the simulations. Flow visualisation identified was used to identify that the dominant structures in each correspond to $N = 28$ rotating at $\omega/\Omega \sim 0.98$ and $N = 29$ rotating at $\omega/\Omega \sim 0.95$

respectively. For the 30º sector the computations predict $N = 24$ rotating at $\omega/\Omega \sim 0.96$, and for the 60º sector $N = 30$ rotating at $\omega/\Omega \sim 1.00$. This data is shown in Table 10.

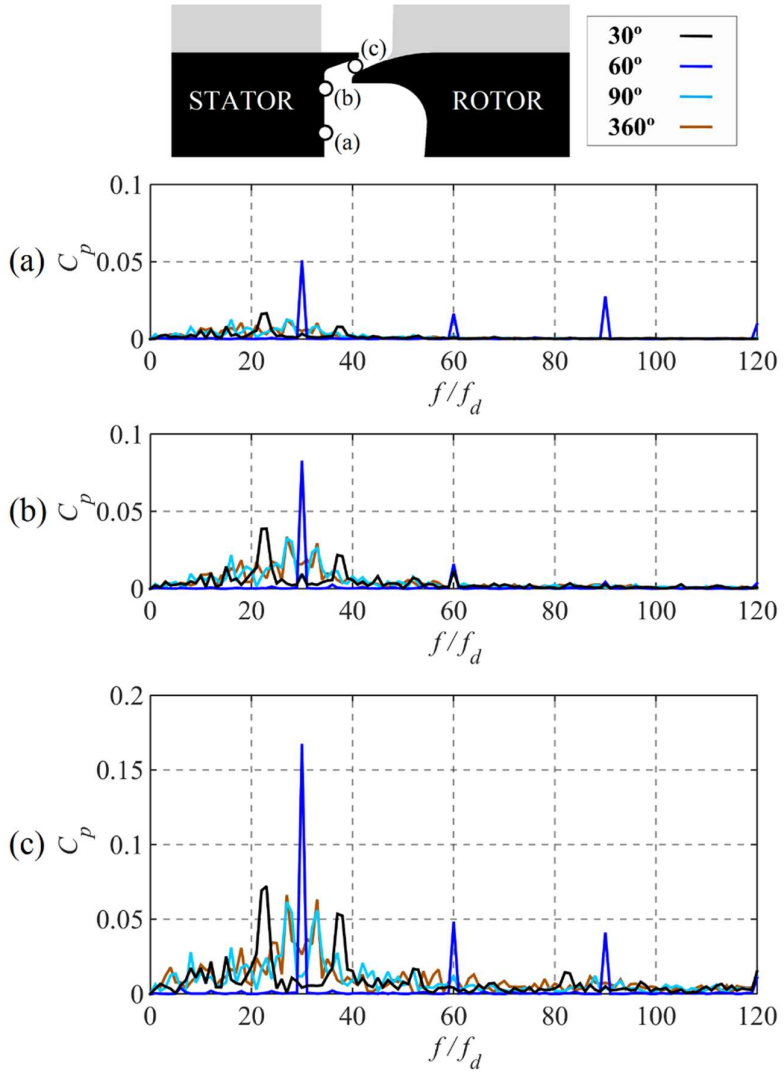

Figure 112: Fast Fourier transforms of computed wheel-space pressure at three different positions for four different sector sizes ($\Phi_0 = 0.050$)

The number of structures in each sector model converges towards that from the 360º simulation but retains an integer number of structures in each sector due to the enforced periodicity. For the 30º sector (1/12th of the full 360º) N must be a multiple of 12, and 24 is the closest value to 29. For the 60º sector (1/6th of the full 360º) N must be a multiple of 6, and 30 is the closest value to 29. For the 90º sector (1/4th of the full 360º) N must be a multiple of 4, and 28 is the closest value to the 29.

The 60º simulation exhibits behaviour which departs from that produced by other sector sizes. There is a significant peak amplitude at half the BPF, with structures rotating at precisely the disc

speed. The number of structures is enforced artificially by the 60º sector (just as it is with all sector models), however because in this case they span exactly two blade passages they are strengthened by interference with the rotor pressure field which leads to the largest discrepancies when the time-averaged results for the sector models are compared to the 360º simulations in Figure 102 and Figure 109. To prevent spurious effects of this enforced periodicity, small-sector models should avoid using an even number of blades to preclude the possibility of one structure existing per two blade passages.

The computed large-scale structures are visualised in Figure 113, using contours of instantaneous sealing effectiveness on a plane through the chute seal. Plots (a)-(d) show enlarged views of the 30º, 60º, 90º and 360º models respectively. The increased regularity of the structures that align with every second blade for the 60º sector model is clearly visible in (b), contrasting with the more similar structures for the other sectors. Figure 114 presents the 360º simulation with an additional isosurface of $\varepsilon_c = 0.025$, indicating the coupling between egress and the contoured planes shown in Figure 113.

Overall, similar unsteady structures exist across all the sector sizes used, indicating that computations from these reduced domains can model effectively much of the large-scale unsteadiness associated with rim seal flows. This is supported by broadly similar time-averaged results across different sectors, as presented in Section 7.1.2 and 7.1.3. Relative to the full 360º simulation, better accuracy was achieved with the 90º sector over the 30º sector, and a poorer prediction resulted with the 60º sector.

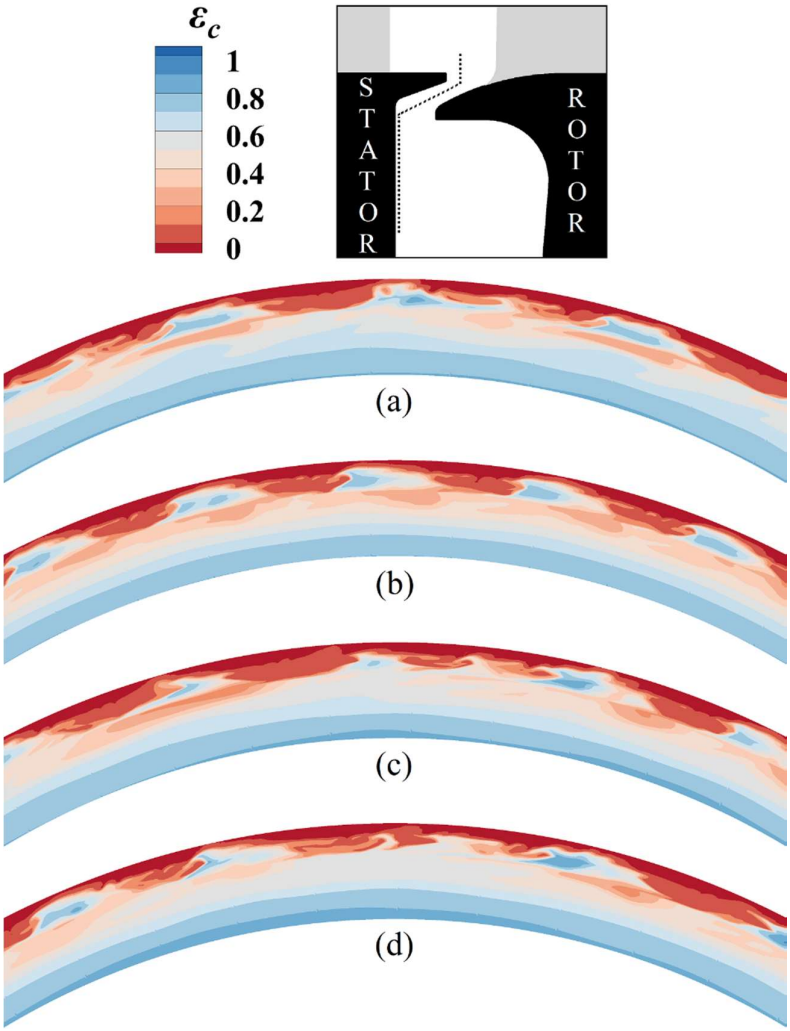

Figure 113: Contours of sealing effectiveness through the chute seal at $\Phi_0 = 0.050$, over a range sector sizes: (a) 30°, (b) 60°, (c) 90°, (d) 360°

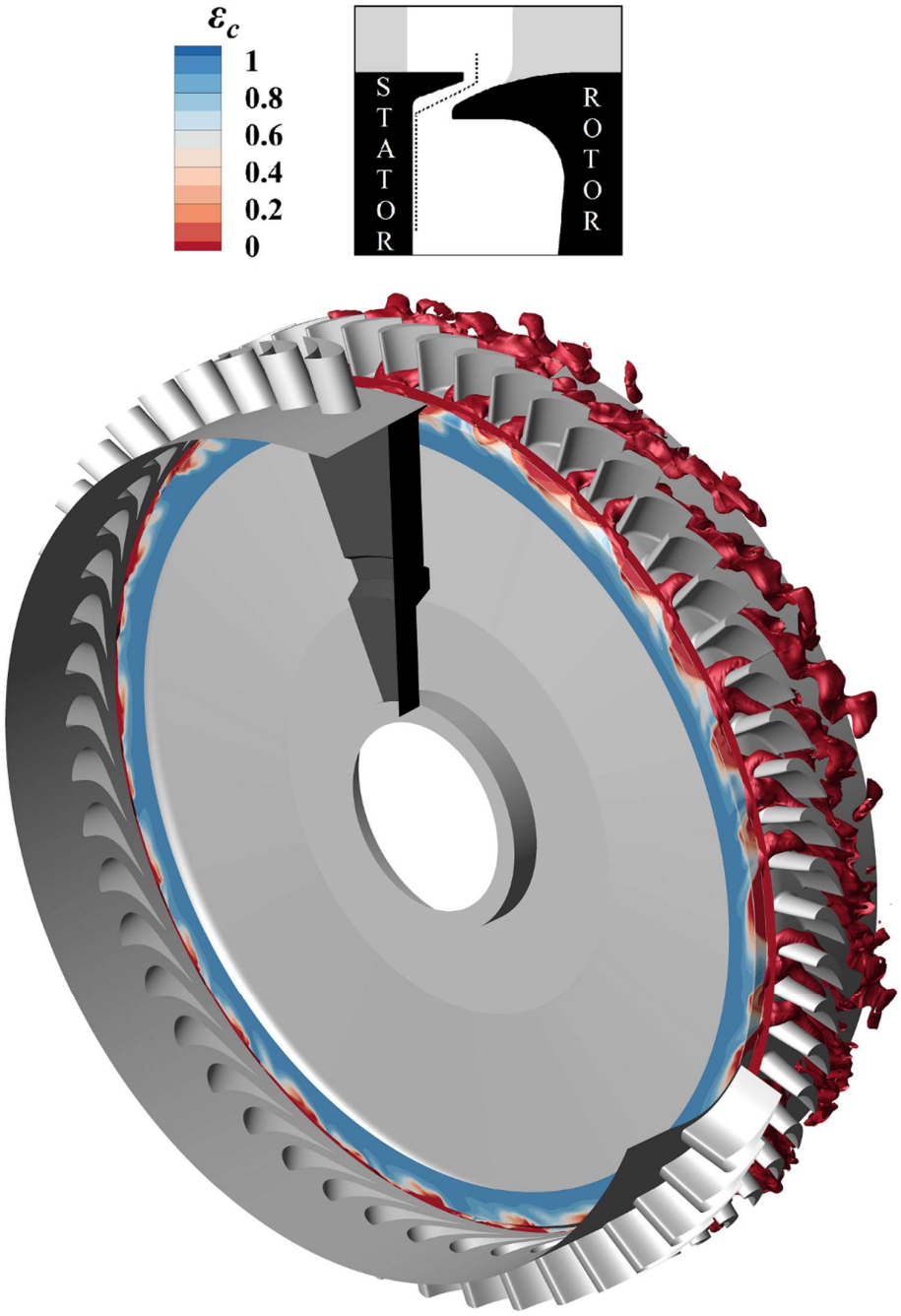

Figure 114: Contours of sealing effectiveness through the chute seal at Φ_0 = 0.050 for 360° model, with additional isosurface of ε_c = 0.025

7.3 Summary

The object of this chapter was to study the fluid dynamics of ingress in a scaled axial turbine incorporating an engine-realistic chute seal, vane and blade geometries. URANS simulations of

the geometry were validated using time-averaged and time-accurate measurements from the 1.5-stage experimental facility.

Computations showed good agreement with the time-averaged measurements of pressure, swirl and sealing effectiveness. Analysis of the computed flow field within the chute seal identified a recirculation that interacts with the blade leading edge features. Secondary flow features in the annulus also demonstrated a dependency on purge, indicating the need to include egress flows when designing blade and end-wall profiles.

High shear gradients were also identified within the seal that are believed to drive flow instabilities that influence ingress. The magnitude, and position (both radial and azimuthal) of the shear gradients were shown to vary with purge flow, becoming strongest at higher purge rates where the position of maximum gradient is forced radially outwards. Analysis correlated computed unsteady pressure to 12-30 large-scale rotating structures. These were similar in form to those observed for the baseline and increased reaction geometries discussed in Chapters 4 and 6, and demonstrated good agreement with experiment. However, an over-prediction in the magnitude of the instabilities was attributed to RANS turbulence modelling, where the greater viscosity term can give rise to more stable vortical structures.

A direct comparison of computations using 30º, 60º, 90º and 360º sectors was undertaken. Most steady features of the flow were found to be largely unaffected by the size of the computational sector. However, differences in large-scale flow structures were pronounced with the 60º sector, where structures were aligned with every second blade passage and rotated synchronously with the disc. This was enforced artificially by the periodicity and can be prevented through modelling an odd number of blades in the sector.

Chapter 8: Conclusions

This thesis reports investigations of the fluid dynamics of hot gas ingress through gas turbine rim seals. Unsteady Reynolds-averaged Navier–Stokes computations of the Bath University 1.5-stage experimental rig were used to analyse time-averaged and time-accurate features of the flow. Several turbine configurations have been studied using time-domain computations and the viability of frequency-domain for modelling ingress has also been explored.

The author considers the most important contributions of this thesis are to highlight typical unsteady flow features governing ingress and demonstrate that it is possible to quantitively compute ingress levels using relatively low-cost sector models with RANS CFD solvers.

The principal conclusions from each chapter of this thesis are outlined in Sections 8.1 - 8.4 and future work is considered in Section 8.5.

8.1 Baseline Stage

Unsteady Reynolds-averaged Navier–Stokes computations of the Bath University 1.5-stage experimental rig were undertaken based upon a baseline geometry. This incorporated prismatic vane and blade geometry alongside a double radial overlap rim seal. The simulations used sector models of the first vane and blade rows and included a wheel-space cavity upstream of the rotor. Results have been compared to experimental data from an axial turbine rig, providing insight into the fluid dynamics of ingress.

An accurate numerical simulation of the annulus pressure distribution was demonstrated. The peak-to-trough pressure difference, ΔC_p, was found not to be solely dependent upon axial distance from the vane, but showed a stronger axial decay in the presence of the rim seal and the associated ingress/egress flows. Additionally, egress was shown to be entrained into the passage vortex.

The qualitative features of the flow structure in the seal clearance and wheel-space were captured, but it is speculated that a quantitative under-prediction of ingress is due to inadequacies in the turbulence modelling.

Unsteady computational analysis determined $N = 16$ low pressure structures rotating at ~ 0.85 of the disc speed; these are identified as fundamental to ingress. It is hypothesized that the physical origin of such phenomena is the high level of shear between the annulus and wheel-space flows; similarities with Kelvin-Helmholtz instabilities were also observed. The existence and influence of the structures are highly sensitive to sealing flow rate and they were fully suppressed at the high purge. Complementary experimental data (not measured by the present author) supported the existence of the large-scale structures and showed they are largely invariant to Rotational

Reynolds number. The data showed $23 < N < 26$ rotating at 0.95 of the disc speed, and that the structures reduce in intensity with increasing purge.

Computations from an increased sector size resulted in minor changes to the strength of the large-scale unsteadiness, but no significant changes to the level of ingress.

Computations adopting a bladeless rotor showed no change in ΔC_p on the stator hub, despite corresponding to a reduction in the computed level of ingress. This reduction was also observed experimentally from $0.04 < \Phi_0 < 0.09$. Analysis of the unsteady pressure field showed that at all sealing flow rates, the spectrum of low-frequency activity present in the bladed configurations was replaced by a single distinct frequency of increased magnitude. This distinct frequency was indicative of more stable rotating structures that were higher in number. Experimentally, the presence of blades caused an inflection in the Φ_0 versus ε_c relationship; computing this feature would require accurate simulation of both the speed, ω, and the number, N, of large-scale structures around the disc.

8.2 Frequency Domain Computations

Nonlinear frequency domain computations using a harmonic balance solver have been used to model a bladeless version of the baseline configuration discussed in Chapter 4. Large-scale rotating rim seal structures have for the first time been captured using a frequency domain solver. The behaviour of these instabilities was shown to be very similar to those from a time-marching URANS case, but they were computed with a reduced computational cost.

The HB model provided a 35% reduction in computational effort over the time-domain model when both adopted the same 22.5° sector. However, computational requirements for HB models could be further reduced if a single vane/blade passage model with phase-lag boundary conditions were to be implemented and if the stability of the solution allowed increased CFL numbers.

Computations were run with the higher harmonics of the turbulence model neglected as their inclusion was found to destabilise the solution. Comparison to time-marching URANS simulations indicates that the harmonics of turbulent kinetic energy have a significant amplitude and ignoring them gave rise to a reduction in computed ingress.

The presence of blades in the computation is likely to drive further difficulties in achieving a stable solution. Additionally, if the BPF were at a different fundamental frequency to the large-scale structures – as is has been found in the majority of the time-marching simulations discussed in this thesis - the solver would neglect the nonlinear coupling between the two harmonic sets; the consequence of this is unknown.

The frequencies defined in the HB computations were informed by time-marching simulations. HB computations must be able to adopt frequency information from another source. An analytical relationship based on the geometry and flow conditions of the turbine would be most desirable, but more realistically frequency data must be drawn from experiment. The presence of blades in the computation has also been shown to drive a wider spectrum of unsteady activity, potentially rendering frequency domain computations unsuitable.

8.3 Increased Reaction Stage

Unsteady Reynolds-averaged Navier–Stokes computations of the Bath University 1.5-stage experimental rig were undertaken based upon a geometry with increased reaction blading over the baseline case. Ingress into the wheel-space cavities upstream and downstream of the rotor was investigated.

In the upstream wheel-space a small reduction in sealing effectiveness (~3%) was observed when compared to the baseline turbine configuration. The computations also demonstrated higher levels of tangential shear across the rim seal, which is believed to drive stronger large-scale rim seal structures and therefore increase ingress. No significant difference in the distributions of non-dimensional annulus pressure, $C_{p,a}$, were identified.

The circumferential distribution of pressure close to the downstream seal showed reasonable agreement with experiment. However, computed ingress into the downstream wheel-space was under-predicted; it is speculated that this was a result of deficiencies in the turbulence model. No significant re-ingestion of upstream egress into the downstream wheel-space was observed.

The downstream rim seal showed large-scale structures similar to those identified upstream of the rotor, but with a lower strength. They were thought to be weaker due to the negative swirl downstream of the blade, which resulted in a lower shear gradient across the rim seal. The reduced swirl also slowed the rotational speed of the downstream structures ($\omega/\Omega \sim 0.4$) relative to those upstream ($\omega/\Omega \sim 0.9$). At time of writing, no time-accurate experimental results were available to validate this.

The influence of injecting flow from the stator wall, in combination with regular purge from the bore was investigated. The source of the sealing flow had a strong influence on the flow structure in the lower wheel-spaces. High radius purge disrupted the conventional Batchelor flow regime in each cavity and led to the formation of large vortices. The change in flow regime did not have a clear effect on ingress; principally because the inner seal acted as a buffer, restricting any fluid dynamic effect of the high radius injection at the outer seal.

8.4 Chute Seal, Twisted Blades & Stacked Vanes

A study of the fluid dynamics of ingress has been undertaken from a scaled axial turbine incorporating an engine-realistic chute seal, vane and blade geometries. Unsteady Reynolds-averaged Navier-Stokes computations of the 1.5-stage test facility were supported by time-accurate and time-averaged measurements from the experimental rig.

Computations showed good agreement with time-averaged measurements of pressure, swirl and sealing effectiveness in the annulus and wheel-space. In particular, predictions of ingress were significantly improved relative to the baseline and increased reaction configurations. It is speculated that this is due to the chute seal geometry, through which accurate computation is less dependent upon capturing flow separation over angular vertices.

An unsteady analysis identified $12 < N < 36$ large-scale rim seal structures rotating at a fraction of the disc speed, with good agreement between computation and experiment. The intensity of these instabilities reduced in magnitude at both high and low sealing-flow rates. There is supporting evidence that flow instabilities are driven by shear gradients in the seal clearance and that they influence ingress. Shear gradients are strengthened and move radially outward with increasing purge, however, above a threshold egress dominates, blowing instabilities from the seal.

A gap recirculation within the chute seal interacts directly with the blade leading edge horseshoe vortex, circumferentially displacing features of the secondary flow such as the saddle point.

A comparison of 30º, 60º, 90º and 360º computational domains show that the steady features of the flow are largely unaffected by the size of the computational sector. Differences in large-scale flow structures were pronounced with the 60º sector and indicate that modelling an even number of blades in small sector simulations should be avoided.

8.5 Future Work and Considerations

This research programme has made progress in the understanding and modelling of steady and unsteady flow features that influence ingress, however, further research is required to address unanswered questions and some limitations of the modelling approaches adopted.

A detailed experimental investigation of the increased reaction turbine configuration is currently being undertaken, with the aim of evaluating the computed flow fields discussed in Chapter 6. This includes those surrounding the downstream wheel-space and the injection of high radius purge.

Despite encouraging agreement with experimental levels of ingress for the chute seal configuration, computed ingress in the upstream wheel-space was found to be sensitive to the geometry used and in the downstream wheel-space showed a significant under-prediction. It is speculated that a chute seal geometry may allow improved predictions of ingress downstream of the rotor, but methods that are robust and reliable for all geometries are ultimately desired. To this end, further investigation of advanced CFD methodologies, such as LES should continue. It is believed this may also address the tendency to over-predict the strength of the large-scale rim seal instabilities, which is thought to result from the RANS turbulence modelling approach.

Experimental data has shown that there is no significant dependence of the large-scale structures upon rotational Reynolds number. However, further computations at the elevated conditions representative of a real engine should be undertaken to determine whether this holds across a wider range of conditions. The influence of scaling flow conditions should also be investigated experimentally, through the collaboration with KTH Royal Institute of Technology. Additionally, work is required to gain a deeper understanding of the unsteady driver for the inflection in the experimental ε_c versus Φ_0 relationship and how to capture this computationally.

Numerous significant challenges must be addressed for the harmonic balance method to reliably compute ingress with the same fidelity as time-domain simulations. These are detailed in Section 5.4.

References

Abe, T., Kikuchi, J., and Takeuchi, H., 1979, "An Investigation of Turbine Disk Cooling (Experimental Investigation and Observation of Hot Gas Flow Into a Wheel Space)," CIMAG - 13th International Congress on Combustio Engines.

ASME, 1988, "The World's First Industrial Gas Turbine Set at Neuchâtel (1939)," ASME International Historic Mechanical Engineering Landmark, H135.

Bakken, L. E., Syverud, E., Jordal, K., and Veer, T., 2004, "Centenary of the first gas turbine to give net power output: A tribute to AEgidius elling," ASME Paper GT2004-53211.

Batchelor, G. K., 1951, "Note on a class of solutions of the Navier-Stokes equations representing steady rotationally-symmetric flow," Quarterly Journal of Applied Mathematics, 4 (1), pp. 29-41.

Bayley, F. J. and Owen, J. M., 1970, "Fluid Dynamics of a Shrouded Disk System With a Radial Outflow of Coolant," ASME J. Eng. Power, 92 (3), pp. 335-341.

Beard, P. F., Gao, F., Chana, K. S., and Chew, J., 2017, "Unsteady Flow Phenomena in Turbine Rim Seals," ASME J. Eng. Gas Turb. Power, 139 (3).

Bohn, D., Johann, E., and Krüger, U., 1995, "Experimental and Numerical Investigations of Aerodynamic Aspects of Hot Gas Ingestion in Rotor-Stator Systems With Superimposed Cooling Mass Flow," ASME Paper 95-GT-143.

Bohn, D., Rudzinski, B., Sürken, N., and Gärtner, W., 1999, "Influence of Rim Seal Geometry on Hot Gas Ingestion Into the Upstream Cavity of an Axial Turbine Stage," ASME Paper 99-GT-248.

Bohn, D., Rudzlnskl, B., Surken, N., and Gartner, W., 2000, "Experimental and Numerical Investigation of the Influence of Rotor Blades on Hot Gas Ingestion into the Upstream Cavity of an Axial Turbine Stage," ASME Paper 00-GT-284.

Boudet, J., Autef, V., Chew, J., Hills, N., and Gentilhomme, O., 2005, "Numerical Simulation of Rim Seal Flows in Axial Turbines," Aeronautical Journal, 109 (1098), pp. 373-383.

Boudet, J., Hills, N. J., and Chew, J. W., 2006, "Numerical Simulation of the Flow Interaction Between Turbine Main Annulus and Disc Cavities," ASME Paper GT2006-90307.

Boutet-Blais, G., Lefrancois, J., Dumas, G., Julien, S., Harvey, J.-F., Marini, R., *et al.*, 2011, "Passive Tracer Validity for Cooling Effectiveness Through Flow Computation in a Turbine Rim Seal Environment," ASME Paper GT2011-45654.

Brack, S. and Muller, Y., 2014, "Probabilistic Analysis of the Secondary Air System of a Low-Pressure Turbine," ASME J. Eng. Gas Turb. Power, 137 (2), p. 022602.

Cao, C., Chew, J. W., Millington, P. R., and Hogg, S. I., 2004, "Interaction of Rim Seal and Annulus Flows in an Axial Flow Turbine," ASME J. Eng. Gas Turb. Power, 126 (4), pp. 786-793.

Chew, J. W., Dadkhah, S., and Turner, A. B., 1992, "Rim Sealing of Rotor–Stator Wheelspaces in the Absence of External Flow," ASME J. Turbomach., 114 (2), pp. 433-438.

Chew, J. W., Green, T., and Turner, A. B., 1994, "Rim Sealing of Rotor-Stator Wheelspaces in the Presence of External Flow," ASME Paper 94-GT-126.

Childs, P. R. N., 2011, *Rotating flow*, Oxford: Butterworth-Heinemann.

Chilla, M., Hodson, H., and Newman, D., 2013, "Unsteady Interaction Between Annulus and Turbine Rim Seal Flows," ASME J. Turbomach., 135 (5), p. 051024.

Clark, K., Barringer, M., Johnson, D., Thole, K., Grover, E., and Robak, C., 2017, "Effects of Purge Flow Configuration on Sealing Effectiveness in a Rotor-Stator Cavity," ASME Paper GT2017-63910.

Custer, C. H., Weiss, J. M., Subramanian, V., Clark, W. S., and Hall, K. C., 2012, "Unsteady Simulation of a 1.5 Stage Turbine Using an Implicitly Coupled Nonlinear Harmonic Balance Method," ASME Paper GT2012-69690.

Da Soghe, R., Bianchini, C., Sangan, C. M., Scobie, J. A., and Lock, G. D., 2016, "Numerical Characterization of Hot-Gas Ingestion Through Turbine Rim Seals," ASME J. Eng. Gas Turb. Power, 139 (3), p. 032602.

Dadkhah, S., Turner, A. B., and Chew, J. W., 1992, "Performance of Radial Clearance Rim Seals in Upstream and Downstream Rotor–Stator Wheelspaces," ASME J. Turbomach., 114 (2), pp. 439-445.

Dahlqvist, J., 2017, "Cavity Purge Flows in High Pressure Turbines," KTH Royal Institute of Technology, PhD Thesis.

Dahlqvist, J. and Fridh, J., 2017, "Experimental Investigation of Turbine Stage Flow Field and Performance at Varying Cavity Purge Rates and Operating Speeds," ASME J. Turbomach., 140 (3), p. 031001.

Daily, J. W. and Nece, R. E., 1960, "Chamber Dimension Effects on Induced Flow and Frictional Resistance of Enclosed Rotating Disks," Journal of Basic Engineering, 82 (1), pp. 217-230.

Diakunchak, I., Kiesow, H. J., and McQuiggan, G., 2008, "The History of the Siemens Gas Turbine," ASME Paper GT2008-50507.

Eastwood, D., Coren, D. D., Long, C. A., Atkins, N. R., Childs, P. R. N., Scanlon, T. J., *et al.*, 2012, "Experimental Investigation of Turbine Stator Well Rim Seal, Re-Ingestion and Interstage Seal Flows Using Gas Concentration Techniques and Displacement Measurements," ASME J. Eng. Gas Turb. Power, 134 (8), p. 082501.

Eisfeld, B., 2004, "Implementation of Reynolds stress models into the DLR-FLOWer code," DLR Internal Report, Report No. 124-2004/31.

Erdos, J. I., Alzner, E., and McNally, W., 1977, "Numerical Solution of Periodic Transonic Flow Through a Fan Stage," AIAA Journal, 15 (11), pp. 1559-1568.

Feiereisen, J., Paolillo, R., and Wagner, J., 2000, "UTRC Turbine Rim Seal Ingestion and Platform Cooling Experiments," AIAA Paper 2000-3371.

Frey, C., Ashcroft, G., Kersken, H.-P., Schonweitz, D., and Mennicken, M., 2017, "Simulation of Indexing and Clocking with Harmonic Balance," Proceedings of 12th European Conference on Turbomachinery Fluid dynamics & Thermodynamics, ETC2017-135.

Frey, C., Ashcroft, G., Kersken, H.-P., and Voigt, C., 2014, "A Harmonic Balance Technique for Multistage Turbomachinery Applications," ASME Paper GT2014-25230.

Gao, F., Chew, J., Beard, P. F., Amirante, D., and Hills, N. J., 2017, "Numerical Studies of Turbine Rim Sealing Flows on a Chute Seal Configuration," Proceedings of 12th European Conference on Turbomachinery Fluid dynamics & Thermodynamics, ETC2017-284.

Gao, F., Poujol, N., Chew, J. W., and Beard, P. F., 2018, "Advanced Numerical Simulation of Turbine Rim Seal Flows and Consideration for RANS Turbulence Modelling," ASME Paper GT2018-75116.

Gentilhomme, O., Hills, N. J., Turner, A. B., and Chew, J. W., 2003, "Measurement and Analysis of Ingestion Through a Turbine Rim Seal," ASME J. Turbomach., 125 (3), pp. 505-512.

Giampaolo, T., 2002, *Gas Turbine Handbook: Principles and Practice*, New York: Fairmont Press.

Giles, M. B., 1988, "Calculation of unsteady wake/rotor interaction," AIAA Journal of Propulsion and Power, 4 (4), pp. 356-362.

Graber, D. J., Daniels, W. A., and Johnson, B. V., 1987, "Disc Pumping Test, Final Report," Air Force Wright Aeronautical Laboratories, Report No. AFWAL-TR-87-2050.

Green, B. R., Mathison, R. M., and Dunn, M. G., 2014a, "Comparison of Harmonic and Time Marching Unsteady Computational Fluid Dynamics Solutions With Measurements for a Single-Stage High-Pressure Turbine," ASME J. Turbomach., 136 (1), p. 011005.

Green, B. R., Mathison, R. M., and Dunn, M. G., 2014b, "Time-Averaged and Time-Accurate Aerodynamic Effects of Forward Rotor Cavity Purge Flow for a High-Pressure Turbine - Part I: Analytical and Experimental Comparisons," ASME J. Turbomach., 136 (1), p. 011004.

Green, T. and Turner, A. B., 1994, "Ingestion into the upstream wheelspace of an axial turbine stage," ASME J. Turbomach., 116 (2), pp. 327-332.

Halila, E. E., Lenahan, D. T., and Thomas, T. T., 1982, "High Pressure Turbine Test Hardware Detailed Design Report," National Aeronautics and Space Administration, Lewis Research Center, Technical Report No. NASA-CR-167955.

Hall, K. C. and Crawley, E. F., 1989, "Calculation of Unsteady Flows in Turbomachinery Using the Linearized Euler Equations," AIAA journal, 27 (6), pp. 777-787.

Hall, K. C., Ekici, K., Thomas, J. P., and Dowell, E. H., 2013, "Harmonic Balance Methods Applied to Computational Fluid Dynamics Problems," International Journal of Computational Fluid Dynamics, 27 (2), pp. 52-67.

Hall, K. C., Thomas, J. P., and Clark, W. S., 2002, "Computation of Unsteady Nonlinear Flows in Cascades Using a Harmonic Balance Technique," AIAA Journal, 40 (5), pp. 879-886.

He, L., 1990, "An Euler Solution for Unsteady Flows Around Oscillating Blades," ASME J. Turbomach., 112 (4), pp. 714-722.

He, L., 1992, "Method of Simulating Unsteady Turbomachinery Flows with Multiple Perturbations," AIAA journal, 30 (11), pp. 2730-2735.

He, L., 2010, "Fourier Methods for Turbomachinery Applications," Progress in Aerospace Sciences, 46 (8), pp. 329-341.

He, L. and Ning, W., 1998, "Efficient Approach for Analysis of Unsteady Viscous Flows in Turbomachines," AIAA journal, 36 (11), pp. 2005-2012.

Hills, N. J., Chew, J. W., and Turner, A. B., 2002, "Computational and Mathematical Modeling of Turbine Rim Seal Ingestion," ASME J. Turbomach., 124 (2), pp. 306-315.

Horwood, J. T. M., Hualca, F. P., Scobie, J. A., Wilson, M., Sangan, C. M., and Lock, G. D., 2018, "Experimental and Computational Investigation of Flow Instabilities in Turbine Rim Seals," ASME J. Eng. Gas Turb. Power, 141 (1), p. 011028.

Hualca, F. P., Horwood, J. T. M., Sangan, C. M., Lock, G. D., and Scobie, J. A., 2019, "The Effect of Vanes and Blades on Ingress in Gas Turbines," ASME Paper GT2019-90987.

Hunt, R. J., 2011, "The History of the Industrial Gas Turbine (Part 1 The First Fifty Years 1940-1990)," IDGTE Paper 582.

Jakoby, R., Zierer, T., Devito, L., Lindblad, K., Larsson, J., Bohn, D. E.*, et al.*, 2004, "Numerical Simulation of the Unsteady Flow Field in an Axial Gas Turbine Rim Seal configuration," ASME Paper GT2004-53829.

Johnson, B. V., Jakoby, R., Bohn, D. E., and Cunat, D., 2009, "A Method for Estimating the Influence of Time-Dependent Vane and Blade Pressure Fields on Turbine Rim Seal Ingestion," ASME J. Turbomach., 131 (2), p. 021005.

Julien, S., Lefrancois, J., Dumas, G., Boutet-Blais, G., Lapointe, S., Caron, J.-F.*, et al.*, 2010, "Simulations of Flow Ingestion and Related Structures in a Turbine Disk Cavity," ASME Paper GT2010-22729.

Junge, L., Ashcroft, G., Jeschke, P., and Frey, C., 2015, "On the Application of Frequency-Domain Methods to Multistage Turbomachinery," ASME Paper GT2015-42936.

Ko, S. H. and Rhode, D. L., 1992, "Thermal Details in a Rotor–Stator Cavity at Engine Conditions With a Mainstream," ASME J. Turbomach., 114 (2), pp. 446-453.

Kozulovic, D., Röber, T., Kuegeler, E., and Nürnberger, D., 2004, "Modifications of a Two-Equation Turbulence Model for Turbomachinery Fluid Flows," Deutscher Luft-und Raumfahrtkongress, Dresden, Germany.

Kügeler, E., Geiser, G., Wellner, J., Weber, A., and Moors, A., 2018, "On the Simulation of Unsteady Turbulence and Transition Effects in a Multistage Low Pressure Turbine, Part III: Comparison of Harmonic Balance and Full Wheel Simulation," ASME Paper GT2018-76749.

Laitone, E. V., 1951, "New Compressibility Correction for Two-Dimensional Subsonic Flow," Journal of the Aeronautical Sciences, 18 (5), pp. 350-350.

Laskowski, G. M., Bunker, R. S., Bailey, J. C., Ledezma, G., Kapetanovic, S., Itzel, G. M.*, et al.*, 2011, "An Investigation of Turbine Wheelspace Cooling Flow Interactions With a Transonic Hot Gas Path—Part II: CFD Simulations," ASME J. Turbomach., 133 (4), p. 041020.

Liu, J., Weaver, A., Shih, T. I.-P., Sangan, C., and Lock, G., 2015, "Modelling and Simulation of Ingress into the Rim Seal and Wheelspace of a Gas-Turbine Rotor-Stator Configuration," AIAA Paper 2015-1445.

Marpu, R. P., Custer, C. H., Subramanian, V., Weiss, J. M., and Hall, K. C., 2015, "Comparison of Numerical Methods for the Prediction of Time-Averaged Flow Quantities in a Cooled Multistage Turbine," ASME Paper GT2015-43717.

McMullen, M., Jameson, A., and Alonso, J. J., 2002, "Application of a Non-Linear Frequency Domain Solver to the Euler and Navier-Stokes Equations," AIAA Paper 2002-0120.

Menter, F. R., Kuntz, M., and Langtry, R., 2003, "Ten Years of Industrial Experience with the SST Turbulence Model," Turbulence Heat and Mass Transfer, 22 (3), pp. 625-632.

Mirzamoghadam, A. V., Giebert, D., Molla-Hosseini, K., and Bedrosyan, L., 2012, "The Influence of HPT Forward Disc Cavity Platform Axial Overlap Geometry on Mainstream Ingestion," ASME Paper GT2012-68429.

Mirzamoghadam, A. V., Heitland, G., Morris, M. C., Smoke, J., Malak, M., and Howe, J., 2008, "3D CFD Ingestion Evaluation of a High Pressure Turbine Rim Seal Disk Cavity," ASME Paper GT2008-50531.

Mirzamoghadam, A. V., Kanjiyani, S., Riahi, A., Vishnumolakala, R., and Gundeti, L., 2014, "Unsteady 360 Computational Fluid Dynamics Validation of a Turbine Stage Mainstream/Disk Cavity Interaction," ASME J. Turbomach., 137 (1), p. 011008.

Ning, W. and He, L., 1998, "Computation of Unsteady Flows Around Oscillating Blades Using Linear and Nonlinear Harmonic Euler Methods," ASME J. Turbomach., 120 (3), pp. 508-514.

NUMECA-International. (2019a, accessed on 27/09/19). *AutoGrid5*. Available: https://www.numeca.com/product/autogrid5

NUMECA-International. (2019b, accessed on 27/09/19). *IGG*. Available: https://www.numeca.com/product/igg

O'Mahoney, T., Hills, N., and Chew, J., 2012, "Sensitivity of LES Results From Turbine Rim Seals to Changes in Grid Resolution and Sector Size," Progress in Aerospace Sciences, 52 pp. 48-55.

O'Mahoney, T. S. D., Hills, N. J., Chew, J. W., and Scanlon, T., 2011, "Large-Eddy Simulation of Rim Seal Ingestion," Proc. IMechE Part C: J. of Mechanical Engineering Science, 225 (12), pp. 2881-2891.

Owen, J. M., 2011a, "Prediction of Ingestion Through Turbine Rim Seals-Part I: Rotationally Induced Ingress," ASME J. Turbomach., 133 (3), p. 031005.

Owen, J. M., 2011b, "Prediction of Ingestion Through Turbine Rim Seals-Part II: Externally Induced and Combined Ingress," ASME J. Turbomach., 133 (3), p. 031006.

Owen, J. M. and Rogers, R. H., 1989, *Flow and Heat Transfer in Rotating-Disc Systems, Volume 1 - Rotor Stator Systems.*, Taunton: Research Studies Press Ltd.

Patinios, M., Ong, I. L., Scobie, J. A., Lock, G. D., and Sangan, C. M., 2018, "Influence of Leakage Flows on Hot Gas Ingress," ASME J. Eng. Gas Turb. Power, 141 (2), p. 021010.

Patinios, M., Scobie, J. A., Sangan, C. M., Michael Owen, J., and Lock, G. D., 2016, "Measurements and Modeling of Ingress in a New 1.5-Stage Turbine Research Facility," ASME J. Eng. Gas Turb. Power, 139 (1), p. 012603.

Phadke, U. P. and Owen, J. M., 1988, "Aerodynamic Aspects of the Sealing of Gas-Turbine Rotor-Stator Systems, Part 3: The Effect of Nonaxisymmetric External Flow On Seal Performance," International Journal of Heat and Fluid Flow, 9 (2), pp. 113-118.

Pogorelov, A., Meinke, M., and Schröder, W., 2018, "Large-Eddy Simulation of the Unsteady Full 3D Rim Seal Flow in a One-Stage Axial-Flow Turbine," Flow, Turbulence and Combustion, 102 (1), pp. 189–220.

Rabs, M., Benra, F. K., Dohmen, H. J., and Schneider, O., 2009, "Investigation of Flow Instabilities Near the Rim Cavity of a 1.5 Stage Gas Turbine," ASME Paper GT2009-59965.

Rolls-Royce, 2005, *The jet engine*, London: Rolls-Royce.

Roy, R. P., Zhou, D. W., Ganesan, S., Wang, C. Z., Paolillo, R. E., and Johnson, B. V., 2007, "The Flow Field and Main Gas Ingestion in a Rotor-Stator Cavity," ASME Paper GT2007-27671.

Sangan, C. M., Lalwani, Y., Owen, J. M., and Lock, G. D., 2014, "Fluid Dynamics of a Gas Turbine Wheel-Space with Ingestion," Proc. IMechE Part A: J. of Power and Energy, 228 (5), pp. 508-524.

Sangan, C. M., Pountney, O. J., Zhou, K., Owen, J. M., Wilson, M., and Lock, G. D., 2013a, "Experimental Measurements of Ingestion Through Turbine Rim Seals-Part II: Rotationally Induced Ingress," ASME J. Turbomach., 135 (2), p. 021013.

Sangan, C. M., Pountney, O. J., Zhou, K., Wilson, M., Michael Owen, J., and Lock, G. D., 2013b, "Experimental Measurements of Ingestion Through Turbine Rim Seals-Part I: Externally Induced Ingress," ASME J. Turbomach., 135 (2), p. 021012.

Saravanamuttoo, H. I. H., Rogers, G. F. C., Cohen, H., Straznicky, P. V., and Nix, A. C., 2017, *Gas Turbine Theory, Seventh Edition*, Harlow: Pearson.

Savov, S. S. and Atkins, N. R., 2017, "A Rim Seal Ingress Model Based on Turbulent Transport," ASME Paper GT2017-63531.

Savov, S. S., Atkins, N. R., and Uchida, S., 2017, "A Comparison of Single and Double Lip Rim Seal Geometries," ASME J. Eng. Gas Turb. Power, 139 (11), p. 112601.

Schadler, R., Kalfas, A. I., Abhari, R. S., Schmid, G., and Voelker, S., 2017, "Modulation and Radial Migration of Turbine Hub Cavity Modes by the Rim Seal Purge Flow," ASME J. Turbomach., 139 (1), p. 011011.

Schreiner, B. D. J., Wilson, M., Li, Y. S., and Sangan, C. M., 2019, "Effect of Purge on the Secondary Flow-Field of a Gas Turbine Blade Row," Submitted to ASME J. Turbomach.

Scobie, J., 2014, "An Experimental Study of Gas Turbine Rim Seals," University of Bath, PhD Thesis.

Scobie, J. A., Hualca, F. P., Patinios, M., Sangan, C. M., Michael Owen, J., and Lock, G. D., 2018, "Re-Ingestion of Upstream Egress in a 1.5-Stage Gas Turbine Rig," ASME J. Eng. Gas Turb. Power, 140 (7), p. 072507.

Scobie, J. A., Sangan, C. M., Owen, J. M., and Lock, G. D., 2015, "An overview of hot gas ingestion research at the University of Bath," Proceedings of 11th European Conference on Turbomachinery Fluid dynamics & Thermodynamics, ETC2017-050.

Scobie, J. A., Teuber, R., Li, Y. S., Sangan, C. M., Wilson, M., and Lock, G. D., 2016, "Design of an Improved Turbine Rim-Seal," ASME J. Eng. Gas Turb. Power, 138 (2), p. 022503.

Siemens-AG, 2018, "Siemens HL-Class Factsheet," Siemens Article No. PGGT-T10031-00-7600.

Stewartson, K., 1953, "On the Flow Between Two Rotating Coaxial Disks," Mathematical Proceedings of the Cambridge Philosophical Society, 49 (2), pp. 333-341.

Subramanian, V., Custer, C. H., Weiss, J. M., and Hall, K. C., 2013, "Unsteady Simulation of a Two-Stage Cooled High Pressure Turbine Using an Efficient Non-Linear Harmonic Balance Method," ASME Paper GT2013-94574.

Sultanian, B. K., 2018, *Gas Turbines: Internal Flow Systems Modeling*, Cambridge: Cambridge University Press.

Teuber, R., Li, Y. S., Maltson, J., Wilson, M., Lock, G. D., and Owen, J. M., 2013, "Computational Extrapolation of Turbine Sealing Effectiveness from Test Rrig to Engine Conditions," Proc. IMechE Part A: J. of Power and Energy, 227 (2), pp. 167-178.

Town, J., Averbach, M., and Camci, C., 2016, "Experimental and Numerical Investigation of Unsteady Structures Within the Rim Seal Cavity in the Presence of Purge Mass Flow," ASME Paper GT2016-56500.

Valencia, A. G., Dixon, J. A., Da Soghe, R., Facchini, B., Smith, P. E. J., Muñoz, J., *et al.*, 2012, "An Investigation Into Numerical Analysis Alternatives for Predicting Re-Ingestion in Turbine Disc Rim Cavities," ASME Paper GT2012-68592.

Wang, C.-Z., Mathiyalagan, S., Johnson, B. V., Glahn, J. A., and Cloud, D. F., 2014, "Rim Seal Ingestion in a Turbine Stage from 360 Degree Time-Dependent Numerical Simulations," ASME J. Turbomach., 136 (3), p. 031007.

Wilcox, D. C., 1988, "Reassessment of the Scale-Determining Equation for Advanced Turbulence Models," AIAA journal, 26 (11), pp. 1299-1310.

Zhang, F., Wang, X., Li, J., and Zheng, D., 2017, "Numerical Investigation on the Effect of Radial Location of Sealing Air Inlet and its Geometry on the Sealing Performance of a Stator-Well Cavity," International Journal of Heat and Mass Transfer, 115, Part B, pp. 820-832.

Zhou, D. W., Roy, R. P., Wang, C. Z., and Glahn, J. A., 2011, "Main Gas Ingestion in a Turbine Stage for Three Rim Cavity Configurations," ASME J. Turbomach., 133 (3), p. 031023.

Zhou, K., Wilson, M., Owen, J. M., and Lock, G. D., 2013, "Computation of Ingestion Through Gas Turbine Rim Seals," Proc. IMechE Part G: J. of Aerospace Engineering, 227 (7), pp. 1101-1113.

Zlatinov, M. B., Tan, C. S., Little, D., and Montgomery, M., 2016, "Effect of Purge Flow Swirl on Hot-Gas Ingestion into Turbine Rim Cavities," AIAA Journal of Propulsion and Power, 32 (5), pp. 1055-1066.

Appendix A: Harmonic Balance Methodology

The steps below outline the *Non-linear Frequency Domain* method proposed by McMullen *et al.* (2002). An earlier harmonic balance approach was proposed by Ning and He (1998), however their method neglected the coupling between high order harmonics and unsteadiness was not considered in the turbulence model.

First consider the discretised form of the URANS equations expressed as

$$V\frac{\partial U}{\partial t}+R(U)=0 \tag{A.1}$$

where V is the volume of the cell, U is the vector of conservation variables, t denotes time and R is the residual term where

$$R(U)=\sum_{j=1}^{m}\vec{F}_j\cdot\vec{S}_j \tag{A.2}$$

In equation A.2, $\vec{S}_j$ are the areas of each of the m faces, $\vec{F}_j$ are the corresponding fluxes normal to the faces.

If the conservation variables are assumed to be periodic over a known period, A.1 can be approximated by a Fourier series of the form

$$U=Re\left[\sum_{n=0}^{N_f}\widehat{U}_n\, e^{in\omega t}\right] \tag{A.3}$$

Note that it is assumed a truncated Fourier series with a finite number of harmonics (n = 0, ..., N_f) adequately approximates the unsteady flow. It then follows that the residual term may be approximated in a similar fashion, such that

$$R(U)=Re\left[\sum_{n=0}^{N_f}\widehat{R}_n\, e^{in\omega t}\right] \tag{A.4}$$

Following these Fourier transformations, equation A.1 becomes

$$\sum_{n=0}^{N_f}\left[in\omega V\widehat{U}_n+\widehat{R}_n\right]e^{in\omega t}=0 \tag{A.5}$$

However, because each of summands cannot be expressed as a sum of the others (i.e. they are linearly independent), each harmonic term must be equal to zero, therefore

$$in\omega V\hat{U}_n+\hat{R}_n=0 \qquad \textbf{A.6}$$

Equation A.6 is then solved through the introduction of a pseudo time derivative term, which is numerically integrated over the volume of the cell to form equation A.7.

$$V\frac{d\hat{U}_n}{d\tau}+in\omega V\hat{U}_n+\hat{R}_n=0 \qquad \textbf{A.7}$$

However, $\hat{R}_n$ cannot be computed directly from $\hat{U}_n$ due to its nonlinear dependency on all harmonics of U. Therefore, the conservation variables are transferred to a number of independent timesteps using an inverse fast Fourier transform. The residuals are then calculated at the individual timesteps before being transferred to the frequency domain using a fast Fourier transform. This process in shown in Figure 31. A similar harmonic balance approach was proposed by Hall *et al.* (2002). Referred to as the *Time-spectral* harmonic balance method, this approach stores conservation variables in the time domain rather the frequency domain between iterations, however both approaches require the calculation of the solution at $2N_f+1$ equally spaced time instances.

Unlike the original method of Ning and He (1998), the *Time-spectral* method and *Non-linear Frequency Domain* methods allow the transport equations for turbulence to be solved just like the other flow equations. The *Non-linear Frequency Domain* method proposed by McMullen *et al.* (2002) is the basis of the method implemented in the DLR's industrial CFD solver TRACE.